The University Of Sheffield.

The Enhancement of the Ammonium Bicarbonate Synthesis Using Non-Thermal Plasma

Muwafaq Mahdi Abd Al-Shammari

A thesis

Submitted to the University of Sheffield for the degree of Doctor for the

Philosophy in the Faculty of Engineering

Department of Chemical and Biological Engineering

December 2020

Dedication

To my mother and my wife,

…… to my daughters and sons,

…… to my brothers, and my unique sister

……. and to the wonderful memory of my father.

Muwafaq

ACKNOWLEDGEMENTS

The utmost thanks and gratitude is for my God for the help, great graces, and conciliation;

"*And that the human being attains only what he pursued for. And that his efforts will be witnessed. Then he will be rewarded for it with the fullest reward.*" *The Holy Quran. An-Najm (39-41).*

Firstly, I would like to express my deep thanks my supervisors Professor William Zimmerman for his outstanding guidance, supervision, and continuous support throughout my PhD, who was, persistently, advising, motivating, and directing me. I'm also very grateful to Dr. Thomas D. Holmes, for his help in part of my work (simulation part), who worked in the microplasma team.

I am thankful to the technical staff of the departmental workshop that made a lot of effort to construct the custom designed equipment for the research requirements. I should also thank the technical staff of laboratories for their kind assistance.

I am also great thankful to the ***Ministry of Higher Education and Scientific Research***/Iraq, Iraqi cultural attaché/London, and the ***University of Diyala*** for the financial support.

My exclusive appreciation goes to my parents. My gratitude to my wife, my daughters and sons, for their continuous, unconditional support and endless patience. They always made my life delighted.

Abstract

A kinetic study of carbon dioxide activated by non-thermal plasma (NTP), injected as a fine bubbles, to produce highly energetic species is shown to enhance reaction yield. The study shows the yield of the reaction of CO_2 and aqueous ammonia to produce ammonium bicarbonate is enhanced by 36% relative to the conventional staging process i.e. in absence of non-thermal plasma. The ratio of captured CO_2 by the reaction estimated to be better than that reported (15-20 %) by Mani et al. (2006).

A chemical kinetics model for NTP to activate CO_2 molecules is developed using the fine element method, implemented in the Comsol Multiphysics software package. The model dynamically evaluates vibrationally excited levels and associated species concentrations evolution. Furthermore, thermogravimetric analysis (TGA) study is conducted to determine kinetic parameters of thermal decomposition under non-isothermal conditions for three ammonium solid salts. The TGA data is combined with pseudo-inverse method (PIM) to infer the composition of an unknown binary mixture of ammonium salts, in order to develop a reliable estimate of the composition of ammonium salts. Results of the PIM for the bicarbonate /carbamate characterization show a good agreement between the modelling and experimental data, while other mixtures results are not sufficiently well inferred from the approach.

The influence of operating parameters of the reaction CO_2 with aqueous ammonia solution are studied. Empirical models based on the process operating parameters are developed to show the significance of the parameters through the response surface methodology. At an applied voltage of 3.5 kV, CO_2 flow rate of 0.8 LPM with 3.4 M. $NH_{3\,(aq.)}$ concentration, and reaction time of 40 minutes, the maximum electrical conductivity of 167 mS and 60 % process yield are achieved.

The difference between the theoretical value of liberated heat during the reaction and the experimental value in this study is about 1.6 kJ that can represent a temperature range of 2-3 °C. This indicates negligible losses are incurred by plasma joule heating and sensible heating.

Table of contents

Dedication i
ACKNOWLEDGEMENTS ii
Abstract iii
Table of contents iv
List of figures viii
List of Tables xiv
Nomenclature xvi
Abbreviations xvii
1 Chapter One 1
General introduction and study goals 1
1.1 Introduction 1
1.2 Importance of the ammonium bicarbonate 2
1.3 Research objectives 4
1.4 Research hypotheses 5
1.5 Structure of the thesis 6
2. Chapter Two 9
Literature review 9
2.1 Introduction 9
2.2 Basic plasma definition: 9
2.3 Classification of plasma 10
2.4 Applications of plasma 11
2.5 Discharges at Atmospheric Pressure 13
2.5.1 Corona Discharges: 14
2.5.2 Dielectric barrier discharge 15
2.6 Plasma microreactor /microscale plasma 17
2.7 Small bubbles features 19
2.7.1 Characteristics and applications of microbubbles 19
2.7.2 Microbubble cloud generation 23
2.7.3 Developed microbubble generation methods 25
2.8 Gas –liquid reactions 27
2.8.1 Film theory 27
2.8.2 Penetration theory 28
2.8.3 The surface renewal theory 30
2.9 Reaction kinetics and reactor design 31
2.10 Carbon dioxide gas dissociation using non-thermal plasma 33
2.11 Absorption of CO_2 in hydroxide solutions 36

2.12 Absorption of CO_2 in aqueous ammonia 37
2.13 Identification methods of the reaction process output 39
2.13.1 The detection in aqueous solutions 39
2.13.2 Determination method of kinetic parameters 39
2.14 Conclusion 41
3. Chapter Three 44
Materials and Methodology 44
3.1 Introduction 44
3.2 Chemicals 44
3.3 Experimental Apparatuses: 44
3.3.1 Plasma generation equipment: 45
3.3.2 Non-thermal plasma generator 48
3.3.3 The chemical reactions zone: 50
3.4 Measuring devices and sensors: 52
3.4.1 The Arduino circuit: 52
3.4.1 Temperature sensor (thermocouples) and thermometer: 52
3.4.2 Weight Scale 52
3.4.3 The pH probe 53
3.4.4 Electrical conductivity: 53
3.5 The electrical conductivity measurement: 54
3.5.1 The calibration curves of the electrical conductivity of pure aqueous ammonia solution: 55
3.5.2 The calibration curves of the E.C. of aqueous ammonia / ammonium ion solution 57
3.6 Experimental design using response surface methodology: 61
3.7 The reaction process of the CO_2 and $NH_{3\,(aq.)}$ 62
3.8 Experimental work set up 64
3.8.1 The experimental protocols for the CO_2 / $NH_{3\,(aq.)}$ reaction: 65
3.8.2 Experimental procedure 65
3.8.3 The control experiment: 67
3.9 The main analytical devices 67
3.9.1 Thermogravimetric analyzer (TGA): 67
3.9.2 Fourier Transform Infrared Spectrophotometer: 68
3.9.3 Nuclear magnetic resonance spectrometers 71
3.10 Conclusions 72
4. Chapter Four 75
Kinetic modelling of CO_2 reaction dynamics with in Dielectric Barrier Discharges in an atmospheric pressure plasma reactor 75
4.1 Summary 75
4.2 The role of the non-thermal plasma 75
4.3 CO_2 molecule behaviour in the presence of plasma 77

4.4 Silent discharges formation theory 79
4.5 Model Description 81
4.5.1 The modelling equations and chemical species nature 82
4.5.2 Microdischarge plasma and discharge physics 83
4.6 The behaviour of species concentration with time 87
4.6.1 Rate coefficient computation 87
4.6.2 Vibrational excited levels of CO_2 behaviour 89
4.6.3 The behaviour of charged and neutral species 90
4.6.4 The behaviour of oxygen species 91
4.7 The influence temperatures on species concentration 94
4.7.1 Electron temperature (T_e) 94
4.7.2 Gas temperature (T_g) 95
4.8 Model validation 96
4.9 Conclusion 97
5. Chapter Five 101
Thermogravimetric analysis of ammonium salts: development of a chemometrics model 101
5.1 Introduction 101
5.2 Kinetics modelling 102
5.3 The thermal dissociation reactions and thermogravimetric curves: 104
5.4 Kinetic parameters: 106
5.4.1 Ammonium carbonate: 106
5.4.2 Ammonium bicarbonate 109
5.4.3 Ammonium carbamate 112
5.5 Pseudo-inverse method (PIM) to estimate initial solid state mixture composition 116
5.5.1 Computational procedure: 117
5.5.2 Modelling assumptions: 119
5.5.3 Ammonium carbonate / bicarbonate system (A/B) 120
5.5.4 Carbonate / Carbamate System (A/C) 123
5.5.5 Bicarbonate / Carbamate System (B/C) 126
5.6 Conclusions: 130
6. Chapter Six 133
Response surface method for modelling the aqueous NH_3 reaction mediated by submerged, CO_2 small bubbles injected with non-thermal plasma 133
6.1 Introduction 133
6.2 The hypotheses of the effects of parametric variation 134
6.3 Mathematical Model 135
6.4 Estimating the polynomial coefficients 135
6.5 Effect of the selected variables on the electrical conductivity 139
6.5.1 Effect of individual parameters on the electrical conductivity of the final solution 140

6.5.2 The interaction effects of the variables on the electrical conductivity 145
6.6 Effect of studied variables on the process yield of $CO_2/NH_{3\,(aq.)}$ reaction 151
6.6.1 Effect of individual parameters on the yield of the process 153
6.6.2 The interaction influences of the variables on the process yield 158
6.6.3 CO_2 captured ratio: 164
6.7 The behavior of temperature and pH value during the reaction process 164
6.7.1 The temperature of reaction behavior 164
6.7.2 The pH value of the reaction behaviour 166
6.7.3 Thermal Calculations: 167
6.8 Absorption calculation 169
6.9 The effect of absence of non-thermal plasma (the control experiment) 170
6.10 Analysis of the precipitated solid 171
6.10.1 Analysis using C^{13} nuclear magnetic resonance (NMR): 171
6.10.2 Analysis using infrared spectrum: 172
6.11 Conclusion 172
7. Chapter Seven 176
Conclusion and recommendation future work 176
7.1 Introduction 176
7.2 Conclusions 176
7.3 Recommendations for future work 178
References 180
Appendix A 194
Appendix B 197
Appendix C 203
Appendix D 209
Appendix E 211
Appendix F 215
Appendix G 217

List of figures

Figure 1- 1. Ammonium bicarbonate salt with its chemical formula. 2
Figure 1- 2. Pie chart show the ammonium bicarbonate grade in the global market. (Market.Biz Company, 2017). 4
Figure 1- 3.The structure of the thesis composition in each chapter. 7

Figure 2- 1. The major components of plasma; electrons, photons, positive and negative ions, excited and neutral particles (atoms or molecules) 11
Figure 2- 2. Non-thermal plasma uses in variant field of the industry, environment and biomedical application. 13
Figure 2- 3.The DBD electrodes arrangement design -a- planar reactor and -b- cylindrical reactor 16
Figure 2- 4. Different designs schemes of microdischarge (Tachibana, 2006) 18
Figure 2- 5.The relation between pressure with both electron temperature and gas temperature (Tachibana, 2006) 19
Figure 2- 6. A unit volume when divided into very small parts, equalized two units in sizes, but provide additional surface area (W. B. Zimmerman et al., 2008). 21
Figure 2- 7. For a single bubble (a) the relation of bubble size (l), surface area and transfer rate as function tor bubble radius. (b) the total transfer rate is enhanced by subdivision of (n) number of bubbles to smaller bubbles leading to greater transfer (at con constant total volume).(W. B. Zimmerman et al., 2008) 21
Figure 2- 8. The behaviour of micro-bubbles, (a) the macro size bubbles are rapidly rising and the blast occurs at the surface of the liquid, meanwhile, the microbubbles suffer from a reduction in their radius and could be disappeared (Temesgen et al., 2017), (b): the rising velocity versus the diameter of the microbubbles in distilled water (Takahashi, 2005). 23
Figure 2- 9. The relation of microbubble diameter with the pressure difference (Edzwald, 1995) 25
Figure 2- 10. The Fluidic amplifier used (W. B. Zimmerman et al., 2008) used for microbubbles generation. The pressure difference between the feedback loop (connects the two control terminals of the amplifier) generates the flow in the loop than causes the main air flow from the supply terminal to switch from one Coanda-effect attachment wall to the opposite one. 26
Figure 2- 11. A schematic sketch represents two films theory (Norouzbahari, et al., 2015) 28
Figure 2- 12. The penetration theory (a) model for systems of the gas film to liquid bulk. (b) A schematic representation of the penetration theory 29
Figure 2- 13. Schematic representation of the surface renewal theory (Liao and Lucas, 2018). 30
Figure 2- 14. A simple sketch for the CO_2/aqueous ammonia reaction system. The non-thermal plasma-activated the CO_2 microbubble before the entry to the reactor. 33

Figure 3- 1. A simple flow diagram for the reaction system of CO_2 with aqueous ammonia, which is divided into two parts: (1) the non-thermal plasma generation zone, (2) the absorbed CO_2 molecules (excited) reacted with the

aqueous ammonia solution, after that a set of steps are conducted such as electrical conductivity measuring, cooling the solution, the separation by filtration and finally the weight of the precipitate solid. 46
Figure 3- 2 the power supply 48V DC-AC-Generator 50 kHz 500W – Germany. 47
Figure 3- 3. the PicoScope (a) 5242A 60 MHz 2 channel with two voltage probe sensors (b & c) are connected with an oscilloscope, which is connected with PC by a USP cable, to measure the voltage. In bottom of the sketch the electrical connection circuit (d) of the plasma generation system (Wagner, 2003). 47
Figure 3- 4 A preliminary experiments using ozone generator, which is consist from an electrodes of aluminium foils 48
Figure 3- 5 Sketch of reactor and the shell of plasma generator, the dimension of both reactor vessel, plasma shell tube, the ground electrode, the quartz barrier cylinder, and the high voltage electrode are shown. 49
Figure 3- 6. Electrodes arrangement of the dielectric barrier discharge (DBD) set-up to generate the non-thermal plasma. 50
Figure 3- 7. (a) reactor and the shell of plasma generator dimensions, (b) diffuser which inserted in the reactor to form the babble at the surface, with thickness S = 4.5 mm (±1 mm), and the diameter B =50 mm. (c) the position of the reactor in the whole system. 51
Figure 3- 8 . Arduino circuit for measuring the pH value and the temperature. 52
Figure 3- 9 .Temperature sensor (thermocouples) in left-side, and infrared thermometer in right-side. 52
Figure 3- 10. The electrode pH meter with BNC connector from VWR pHenomenal® 111. 53
Figure 3- 11. Calibration curve of pH with different buffer solutions 53
Figure 3- 12. Model 4510 Conductivity meter with range 0 to 1999 µS Accuracy ±0.5%±2 digits 54
Figure 3- 13 the electrical conductivity and pH value of the aqueous ammonia versus the concentrations. 56
Figure 3- 14 the electrical conductivity of the aqueous ammonia and ammonium carbonate versus the concentrations. 58
Figure 3- 15 the electrical conductivity of the aqueous ammonia and ammonium bicarbonate versus the concentrations. 58
Figure 3- 16 the electrical conductivity of the aqueous ammonia and ammonium carbamate versus the concentrations. 58
Figure 3- 17. Electrical conductivity of pure ammonium carbonate against the molar concentration. 60
Figure 3- 18. Electrical conductivity of the pure ammonium bicarbonate salt against the molar concentration. . 60
Figure 3- 19. The electrical conductivity of the pure ammonium carbonate salt against the molar concentration 60
Figure 3- 20 A schematic sketch for system of the carbon dioxide /aqueous ammonia reaction. 66
Figure 3- 21.Thermogravimetric analyser (a) shows the sketch of connections between the furnace, the balance and temperature control, (b) the computer and the screen connected to the e analyser to show the results progress while, (c) the furnace and sample position. 68
Figure 3- 22. Fourier Transform Infrared Spectrophotometer type IRAFFINITY-1S, Shimadzu. (https://www.shimadzu.co.uk/iraffinity-1s) 69
Figure 3- 23. Fourier transform infrared spectroscopy (FTIR) analysis of standards ammonium salts (carbonate, bicarbonate, and carbamate) (Lingyu Meng et al., 2005) 70
Figure 3- 24. FTIR spectrum of NH_4HCO_3 standard at room temperature (Meng, 2004). 70

Figure 3- 25. ^{13}C NMR spectra of the carbamate and bicarbonate/carbonate ions, Carbon resonances at various pH values in four liquid ammonia with increase the carbon dioxide gas loaded (Mani, et al. 2006). 72

Figure 4- 1. The activation energy diagram represents the maximum energy (the peak) and reaction progresses from reactant to product formation due to this activation barrier 77
Figure 4-2. Vibrational modes of CO_2 molecule (a) symmetric stretching v1, (b) doubly degenerate bending mode v2, and (c) asymmetric stretching v3. Taken from (Moreno Wandurraga, 2015). 77
Figure 4- 3. A simple schematic graph of CO_2 very fine bubble in aqueous ammonia solution. 79
Figure 4- 4. DBD electrodes arranged in planar and cylindrical geometries. 80
Figure 4- 5. The time scale for plasma reaction adapted from (Sakiyama et al., 2012)..... 84
Figure 4- 6. The chemical reaction (R) scheme of CO_2 splitting and further reactions between O, O_2 and O_3, as predicted by the model. The labels of the arrows are explained in the text. (Adapted from (Bogaerts et al., 2015b) 85
Figure 4- 7. Fractional energy losses of CO_2 molecule, taken from (Eliasson, et al., 1994)..... 86
Figure 4- 8. Cross-sections of electron / CO_2 molecule collision, taken from (Anzai et al., 2012) 86
Figure 4- 9. The relation of rate coefficients of vibrational excited levels of CO_2 as a function of the mean electron energy, where; k9, k10, k11, k12 are related to the reactions 9, 10, 11and 12 as shown in table B2 appendix B 88
Figure 4- 10. Concentration-time variations of vibrationally excited species of CO_2 with a pulses of discharge. 89
Figure 4- 11. Concentrations of a selected charged and neutral species as a function of time with a pulse of discharge. 90
Figure 4- 12. Concentrations of O_2, O_3, and their excited levels, positive and negative ions as a function of time with a pulse discharge..... 92
Figure 4- 13. Concentrations of all ions, neutral and excited species of CO_2 in plasma as a function of time with a pulse discharge in a single microdischarge streamer. 93
Figure 4- 14. Concentration of vibrational excited CO_2 levels as function of electron temperature 95
Figure 4- 15. Concentration of the vibrational excited CO_2 levels as function of gas temperature, (a) illustrates the vibrational excitation modes CO_2 v_1 and CO_2 v_3 while (b) shows the vibrational excitation modes CO_2 v_2 and CO_2 v_4..... 96
Figure 4- 16. The effect of the input high voltage of the non-thermal plasma on exciting CO_2 molecules to react with aqueous ammonia. The yield of reaction process studied at interaction of parameters; high voltage with CO_2 flowrate. 97

Figure 5- 1. Dissociation reaction curves of ammonium carbamate, bicarbonate, and carbonate vs. temperature 105
Figure 5- 2. Activation energy of ammonium carbonate decomposition reaction versus the reaction order at different heating rates. 107
Figure 5- 3. Pre-exponential factor of ammonium carbonate decomposition reaction with different heating rates and reaction orders assumed. 108

Figure 5- 4. Activation energies of ammonium bicarbonate decomposition reaction versus the reaction order at different heating rates. 110
Figure 5- 5. Pre-exponential factor of ammonium bicarbonate decomposition versus reaction orders with different heating rates. 111
Figure 5- 6. Activation energies of ammonium carbamate decomposition reaction versus the reaction order at different heating rates. 115
Figure 5- 7. Pre-exponential factor of ammonium carbamate decomposition versus reaction orders with different heating rate. 115
Figure 5- 8 shows the mass loss fraction of A/B salts versus the temperature, the ratio: 0.2/0.8 122
Figure 5- 9 shows the mass loss fraction of A/B salts versus the temperature, the ratio: 0.4/0.6 122
Figure 5- 10 shows the mass loss fraction of A/B salts versus the temperature, the ratio: 0.5/0.5 122
Figure 5- 11 shows the mass loss fraction of A/B salts versus the temperature, the ratio: 0.6/0.4 122
Figure 5- 12 shows the mass loss fraction of A/B salts versus the temperature, the ratio: 0.8/0.2 122
Figure 5- 13 shows TGA and PIM calibration results for the mass loss fraction (A/B) 122
Figure 5- 14. Weight loss fraction versus temperature at heating rate 5 C/min. for a different mixtures of ammonium carbonate (A) and ammonium bicarbonate (B), as well as the pure salt. 123
Figure 5- 15. Total gas pressure as a function of temperature for ammonium carbonate and ammonium carbamate, (Fulks et al., 2009). 124
Figure 5- 16 shows the mass loss fraction of A/C salts versus the temperature, the ratio: 0.2/0.8 125
Figure 5- 17 shows the mass loss fraction of A/C salts versus the temperature, the ratio: 0.4/0.6 125
Figure 5- 18 shows the mass loss fraction of A/C s alts versus the temperature, the ratio: 0.5/0.5 125
Figure 5- 19 shows the mass loss fraction of A/C salts versus the temperature, the ratio: 0.6/0.4 125
Figure 5- 20 shows the mass loss fraction of A/C salts versus the temperature, the ratio: 0.8/0.2 125
Figure 5- 21 shows TGA and PIM calibration results for the mass loss fraction (A/C) 125
Figure 5- 22. Weight loss fraction versus temperature at heating rate 5 C/min. for a different mixtures of ammonium carbonate (A) and ammonium carbamate (C), as well as the pure salt 126
Figure 5- 23 shows the mass loss fraction of B/C salts versus the temperature, the ratio: 0.2/0.8 127
Figure 5- 24 shows the mass loss fraction of B/C salts versus the temperature, the ratio: 0.4/0.6 127
Figure 5- 25 shows the mass loss fraction of B/C salts versus the temperature, the ratio: 0.5/0.5 127
Figure 5- 26 shows the mass loss fraction of B/C salts versus the temperature, the ratio: 0.6/0.4 127
Figure 5- 27 shows the mass loss fraction of B/C salts versus the temperature, the ratio: 0.8/0.2 127
Figure 5- 28 shows TGA and PIM calibration results for the mass loss fraction (B/C) 127
Figure 5- 29. Weight loss fraction versus temperature at heating rate 5 C/min. for a different mixtures of ammonium bicarbonate (B) and ammonium carbamate (C), as well as the pure salt 128
Figure 5- 30 represents the weight loss fraction versus temperature at heating rate 5 C/min. for unknown mixtures of solid separated from reaction of the carbon dioxide and liquid ammonia (the deposits produced from experiments number 9 and 17 in chapter 6). 129

Figure 6- 1. The comparison between the predicted and observed data for electrical conductivity at the end of the experiment. 138

Figure 6- 2. Correlation between the predicted and observed data of the yield of the process from the separated solid substance. 139
Figure 6- 3. The influence of the high voltage on the electrical conductivity of the solution at a aqueous ammonia concentration (3.4M), CO_2 flow rate (0.8 LPM), and time of the reaction (40 min.). 141
Figure 6- 4. The influence of CO_2 flow rate on the electrical conductivity of solution at constant aqueous ammonia concentration (3.4 M), high voltage (3.5kV) and time of reaction (40 min.) 142
Figure 6- 5. The influence of aqueous ammonia concentration on the electrical conductivity of the solution at high voltage (3.5 kV), CO_2 flow rate (0.8 LPM)) and time of reaction (40 min.) 143
Figure 6- 6.Influence of reaction time on the electrical conductivity of solution at at high voltage (3.5 kV), CO_2 flow rate (0.8 LPM)) and NH_4OH concentration (3.4 M)..... 144
Figure 6- 7. The combined effects of the high voltage and flow rate of CO_2 on the electrical conductivity of the solution. 146
Figure 6- 8. The combined effects of the high voltage and aqueous ammonia concentration on the electrical conductivity of the solution. 147
Figure 6- 9 .The combined effects of the high voltage and reaction time on the electrical conductivity of the solution 148
Figure 6- 10. The combined effects of the CO_2 flow rate and aqueous ammonia concentration on the electrical conductivity of the solution. 149
Figure 6- 11. The combined effects of the CO_2 flow rate and reaction time on the electrical conductivity of the solution. 150
Figure 6- 12. The combined effects of the aqueous ammonia concentration and reaction time on the electrical conductivity of the solution. 151
Figure 6- 13. The influence of high voltage on the yield of the process at a aqueous ammonia concentration (3.4 M), CO_2 flow rate (0.8 l/min) and time of reaction (40 min)..... 154
Figure 6- 14. The influence of CO_2 flow rate on the yield of the process at constant high voltage (3.5kV), NH_4OH concentration (3.4M), and time of reaction (40 min.). 155
Figure 6- 15. The influence of NH_4OH concentration on the yield of the process at constant high voltage (3.5 kV), CO_2 flow rate (0.8 LPM) and time of reaction (40 min.)..... 156
Figure 6- 16 . The influence of reaction time on the yield of the process at constant high voltage (3.5 kV), CO_2 flow rate (0.8 LPM), and NH_4OH concentration (3.4 M)..... 157
Figure 6- 17. The influence of high voltage and CO_2 flow rate on the yield of the process at constant NH_4OH concentration and time of reaction..... 158
Figure 6- 18. The influence of High voltage and NH_4OH concentration on the yield of the process at constant CO_2 flow rate and time of reaction. 159
Figure 6- 19. The influence of high voltage and time of reaction on the yield of the process at constant CO_2 flow rate and NH_4OH concentration. 160
Figure 6- 20. The influence of CO_2 flow rate and NH_4OH concentration on the yield of the process at constant high voltage and time of reaction. 161

Figure 6- 21. The influence of CO_2 flow rate and time of reaction on the yield of the process at constant High voltage and NH_4OH concentration. 162
Figure 6- 22. The influence of NH_4OH concentration and time of reaction on the yield of process at constant high voltage and CO_2 flow rate..... 163

List of Tables

Table1-1. Specifications physical properties of the ammonium bicarbonate (Market.Biz, 2017). 3

Table 2- 1. Non-thermal discharge types and their common applications, taken from (Pârvulescu, et al., 2012). 15

Table 2- 2. The typical parameters of a Microdischarge 18

Table 3. 1 shows the main devices and tools which are used in the process. 45

Table 3. 2 illustrates the range of real and coded values of variables that will be used in experiments of CO2 / aqueous ammonia solution reaction 63

Table 3. 3 the experiments and experimental real and coded variables using rotatable experimental design (the factorial points) 63

Table 3. 4 the experiments and experimental real and coded variables using rotatable experimental design (the axial points). 64

Table 3. 5 the experiments and experimental real and coded variables using rotatable experimental design (the centre points). 64

Table 3. 6 .The positions and intensities of Infrared absorption Bands of ammonium bicarbonate (Miller and Wilkins, 1952). 71

Table 4- 1. Dielectric barrier discharges with typical operation conditions adapted from (Wagner et al., 2003). 81

Table 4- 2. The main species which included in model ions, neutral and excited species. 83

Table 4- 3. The vibrational levels considered in this model with their notations and energy. 87

Table 4- 4. illustrates the energy of some positive ions of carbon dioxide. Adapted from (Itikawa, 2002). 93

Table 5- 1 illustrates the heating rate of ammonium carbonate decomposition reaction, conversion percentage, against temperature range with standard deviation. 108

Table 5- 2. Kinetic parameters of ammonium carbonate decomposition reaction data: heating rate β °C/min, activation energy E (kJ/mole), pre-exponential factor (A 1/min.) and correlation coefficient R2. 109

Table 5- 3. Heating rates of ammonium bicarbonate decomposition reaction, conversion percentage, against temperature range with standard deviation. 110
Table 5- 4 Kinetic parameters of ammonium bicarbonate decomposition reaction data: where heating rate β °C/min, activation energy E (kJ/mole), pre-exponential factor (A 1/min.) and correlation coefficient R^2. 112
Table 5- 5 illustrate the heating rate of ammonium carbamate decomposition reaction, conversion percentage, against temperature range with standard deviation. 114
Table 5- 6. Kinetic parameters of ammonium carbamate decomposition reaction data: where heating rate β °C/min, activation energy E (kJ/mole), pre-exponential factor (A 1/min.) and correlation coefficient R^2. 116

Table 6- 1 shows the F-test results for the mathematical model coefficients of the electrical conductivity of the solution at the end of the experiment. (S: significant, NS: insignificant) 136
Table 6- 2 shows the F-test results for the mathematical model coefficients of the electrical conductivity of the solution at the end of the experiment. (S: significant, NS: insignificant) 138

Nomenclature

ΔH	The enthalpy change
(g)	Gas phase
(s)	Solid phase
n	Charged particle density
N_A	The molar mass flux of species A in mol.cm^{-2} s^{-1}
Q	Heat flux (Watts.m^{-2})
R_A	Rate of absorption of component A
k_l	The mass transfer coefficients in liquid phase
h	The coefficients of heat transfer
D_A	The diffusivity (cm^2.s^{-1}) of component A
a (equation 2.2)	The surface area of heat transfer
ΔC, C_{Ab}, C_{AI}	Concentration difference, bulk & interface concentrations
ΔT, T_H, T_C	Temperature difference, hot and cold temperatures
g	The gravitational acceleration (m.s^{-2})
U_t	(is the terminal velocity of rising microbubble (m.s^{-1})
$\Delta\rho$	The density difference kg m^{-3}
μ	The dynamic viscosity of liquid kg m-1 s-1
d	Diameter of the bubble m
r	The radius of the bubble
ΔP	The pressure difference (inside and outside) bubble
σ	The surface tension of bubble
ΔF	Change in free energy
P_A	The dissolved gas pressure
$P_\circ$	The atmospheric pressure
H_E	Henry's law constant
x_g	Molar fraction of gas at dissolved pressure
δ	Thickness of the film
W	Mass fraction decomposed at a time **t**.
$d\alpha/dt$	Rate of conversion
k (T)	Rate constant (k) depend on temperature
A	The pre-exponential factor min^{-1}
E	The activation energy J. mol^{-1}
R	The universal gas constant
C	Capacitance C
κ	Conductivity (S/cm)
(Y)	Observed response
X_i	Independent variables
B_i	The coefficients parameters
N	The number of experiment
‹ε›	The mean elecron energy
β	Heating rate
(n)	Reaction order
R^2	The correlation coefficient
S_b	The estimated variance of coefficients
S_r^2	The estimate of experimental error variance

Abbreviations

DBD	Dielectric barrier discharge
STP	Standard temperature and pressure
TGA	Thermogravimetric analysis
MEA	Monoethanolamine
eV	A quantity of energy (1eV= 1.602 *10 $^{-19}$ J)
T_e	The temperature of the electron
$\mathbf{T_g}$	Gas temperature
ICP	Inductively coupled plasma
TP	Thermal plasmas
RF	Radio frequency
NTP	Non-thermal plasmas
kV	kilo-volt
kHz	kilo-hertz
USB	Universal Serial Bus
PC	Personal computer
TDS	Total dissolved salts
RSM	Response surface methodology
HV	High voltage
IR	Infrared
UV	Ultraviolet
FTIR-ATR	Fourier Transform Infrared -Attenuated total reflectance
NMR	Nuclear magnetic resonance
EEDF	Electron energy distribution function
E/n	Reduced field (input energy/ particles density)
PIM	Pseudo-inverse method
(A)	Ammonium carbonate
(B)	Ammonium bicarbonate
(C)	Ammonium carbamate
GHG	Greenhouse gas
EC	The electrical conductivity

Department of Chemical and Biological Engineering

Chapter One

General introduction and study goals

Chapter One

General introduction and study goals

1.1 Introduction

One of the most significant current global challenges is environmental stress. As population grows continually, the demand for energy increases. In other words, fossil fuels burning and carbon dioxide emission will continue to increase at least in the next few years (O'Neill et al., 2010). Although numerous alternative routes suggested for reducing of CO_2 emission, still the most effective remediation technology is reactive absorption (Chakma, 1995). There are several aqueous alkaline solutions which are utilized as absorbents such as sodium hydroxide, potassium carbonate, some specified amines, and ammonia (Chen and Yu, 2018). One of the disadvantages of NaOH as absorbent is poor regeneration due to the formation of sodium bicarbonate as a final product, which possesses a high solubility in water (Yoo, et al., 2013). While monoethanolamine (MEA), is a common system to remove CO_2 industrially, it has many problems such as low absorption capacity, high cost, and corrosion of equipment (Bai and Yeh, 1997). Recently, aqueous ammonia has gained attention as a solvent to absorb CO_2 by scrubbing. This process has excellent features compared to MEA: lower costs, more suitable for recycling, and higher loading capacity (Mani, et al., 2006). In spite of these essential features, the absorption process is, overall, highly energy-consuming due to the successive separation processes by heating of a massive quantity of the dilute aqueous solutions.

On the other hand, a critical goal that could positively impact the global carbon balance is transforming CO_2 into usable materials using non-thermal plasma. The carbon dioxide molecule has a high kinetic stability, so it requires high activation energy to overcome on this stability (Yap, et al., 2015). These authors show sinusoidal AC excitation for CO_2 dissociation to carbon monoxide by non-thermal plasma is better than that produced by pulse generation. The results show a CO_2 conversion improvement from 7.5% to 13.5%, respectively, in presence of the helium gas.

Additionally, using the non-thermal plasma in conversion of CO_2 to dimethyl ether and methane is reported (Hayashi, et al., 2006). Their results show that, under the effect of additive gases (H_2, H_2O vapor), the conversion of CO_2 is about 15% and a ratio of conversion to dimethyl ether of not more than 5% at maximum is achieved. In addition, a study about CO_2 conversion to hydrocarbons (CH_4, C_2H_4, and C_2H_6) and CO was reported (Yoshida, et al., 2001). They explored the effect of the electrode material (Fe, Cu) and plasma reaction on the

conversion efficiency, but the results of conversion efficiency for CO and hydrocarbons were less than 20% and 0.3% respectively. Therefore, to avoid high energy-consuming (high pressure, temperatures) and the thermodynamic limitations of species equilibrium, the plasma may be the solution to overcome some of these limitations. The high temperatures and catalysts would still be necessary since methane and hydrocarbon reforming requires high energy to reach the ionization state (12kV (Hayashi, et al., 2006)). Furthermore, Xiang et al., (2012) shows another CO_2 conversion route for chemical synthesis. They used negative corona discharge to perform a gas-gas reaction between CO_2 and ammonia to produce urea. They achieve high conversion at ambient conditions, but still gas-gas reaction has high risks with the presence of the high voltage plasma. All the above issues make upgrading essential with new technology for carbon dioxide capturing and at same time produce valuable chemicals with both low capital and low operational expenditure. Unfortunately, this goal cannot be simply achieved through traditional technologies because highly endothermic CO_2 conversions, with high activation energies, have high consumption intrinsically. For sustainable, large-scale utilization of CO_2, commodity products of CO_2 conversion processes should be economically viable and in high demand. In this study we intend to enhance the reaction of a CO_2 with aqueous ammonia solution using non-thermal plasma and small bubbles to prepare ammonium bicarbonate, with the aim to address these essential features for sustainability and viability.

1.2 Importance of the ammonium bicarbonate

Ammonium bicarbonate is an inorganic compound with the formula $NH_4\ HCO_3$. It is a colorless to white solid as shown in figure (1.1), which decomposes readily to carbon dioxide and ammonia.

Figure 1- 1. Ammonium bicarbonate salt with its chemical formula.

Molecular weight of (79.06), and density of 1.58 g/cm^3. It is the only ammonium compound dissolves in water without decomposition some other physical properties as illustrated in table (1.1).

Table1-1. Specifications physical properties of the ammonium bicarbonate (Market.Biz, 2017).

Physical State	**Solid**
Color:	colourless to white
Odour:	ammonia-like - weak odour
pH:	7.8 At 0.1N.
Vapor Pressure	60 mm Hg at 25 °C
Boiling Point	Decomposes.
Freezing/Melting Point	60 °C (140.00°F)
Solubility in water	17.4 % at 20°C in water
Specific Gravity/Density	1.586
Molecular Formula	NH_4HCO_3
Molecular Weight	79.06

The reaction forming of NH_4HCO_3 is exothermic (Kauffman, 1996):

$$NH_{3\,(g)} + CO_{2\,(g)} + H_2O \rightleftharpoons NH_4HCO_{3\,(s)} \quad \Delta H = -126.5\ kJ/mol \qquad (1.1)$$

Although possessing a low ratio of nitrogen content (18%) compared to urea (46%), it is still used as a fertilizer by Chinese farmers. Zhuang, *et al*., (2012) referred to significant improvement economically and technologically for fertilizer production particularly the ammonium bicarbonate in China. The scale of production per annum consumes 3000–12,000 tons of ammonia. This technology is highly integrated and optimized. Nitrogen (N) is considered the motive of plant growth. The N_2 source is down from the soil. It absorbs in the form of nitrate (NO_3^-) or ammonium (NH_4^+) (FAO, 2000).

The decomposition reaction of the ammonium bicarbonate is characterized by no solid residue after the end of the reaction (NH_3, CO_2, H_2O all species in gas phase). Every 10 grams of NH_4HCO_3 if heated to 150 °C produce a volume of 13 litres of gas at STP (Kauffman, 1996). This merit makes it a suitable choice in food industry as a raising agent in most baked products. It is also effective in removal of deposits by dissolving the thin layers of calcium sulphate in tubes of the heat exchangers.

Global sales market share of ammonium bicarbonate by types in 2016 as shown in Pie chart (1.1) the main consuming ratio (83%) for the agriculture, and 10.5% as a food grade while rest 6.5% is used in technical field. This product, has standards specifications that are similar to the fertilizer class but lower nitrogen content. In generally 17% or less in nitrogen content, and

is mainly used in the leather, softening the leather, and rubber industry (Market.Biz company, 2017).

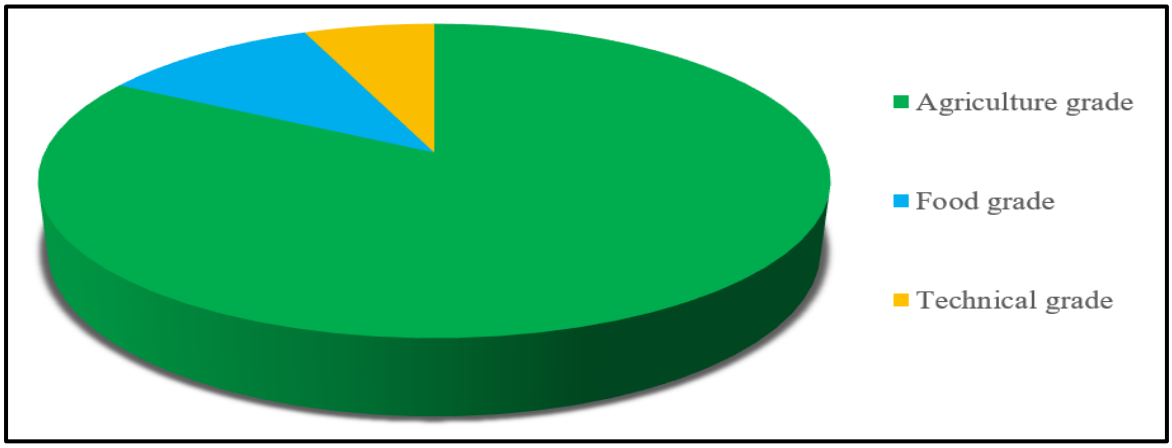

Figure 1- 2. Pie chart show the ammonium bicarbonate grade in the global market. (Market.Biz Company, 2017).

1.3 Research objectives

The absorption of carbon dioxide into aqueous ammonia solutions to produce ammonium bicarbonate is an attractive route to capture CO_2, which is well known as one of the fundamental species that contributing to the greenhouse effect. The major objectives of this study are focused on enhancing the reaction method to activate the CO_2 molecules before the contact occurs between the reactants, and the product of ammonium bicarbonate is formed. The goals of this study are:

1. Investigate the effect of activation the CO_2 gas molecules into enhancing a gas-liquid reaction by exploiting features of non-thermal plasma to generate high energy species at ambient conditions.
2. Investigate the small bubble clouds not only provide the high surface area to bulk volume ratios but also act on surface renewal internal due to quick internal change. Furthermore, it is an important factor in enhancing the mass transfer and reaction rate.
3. Explore and discuss the ability to design an efficient and low power consumption method for producing a valuable chemical (ammonium bicarbonate as a fertilizer) by adapting a non-thermal plasma combined with the small bubbles.
4. Establish a kinetics model for CO_2 reactions and their related species as a function of time using Comsol Multiphysics® Reaction Engineering Laboratory, with a key role in providing a deep understanding of CO_2 (excitation of vibrational species) behaviour, and will support finding the processing optimum conditions.

5. Characterize the reaction products using thermogravimetric analysis data and determine a new strategy for estimating the components of the solid sample, using a pseudo-inverse method.
6. Due to the high dimensionality of process parameters, determining an efficient design of experiments using the Box-Wilson method (a response surface methodology) to facilitate empirical mathematical modelling. By applying this technique, the relationship between controlled experimental parameters and observed response variables can be evaluated.
7. Investigate the effect of selected parameters including high applied voltage, CO_2 flow rate, initial aqueous ammonia concentrations, and reaction time on the conversion of CO_2 to ammonium bicarbonate and solution conductivity.

1.4 Research hypotheses

The current study investigates the application of non-thermal plasma technology to prepare a valuable chemical compound from carbon dioxide gas and aqueous ammonia solution. The performance of the non-thermal plasma effect for ammonium bicarbonate synthesis with the presence of small bubbles to enhance chemical reaction will be explored. It is hypothesized that heterogeneous reaction between the reactants occurs on the gas-liquid interface. The plasma species, which are usually generated with a high electrical field, influence the mode of activation of CO_2 molecules. Within the classes of excited species of CO_2 in particular, the vibrational modes should tend to react near the bubble interfaces due to carrying extra energy. Moreover, microbubbles themselves possess high Gibbs free energy per unit area due to high curvature. In addition, the small internal volume of the small bubbles supports internal mixing. The mixing process is a surface reaction driver, so the rapid surface renewal, according to Danckwerts' surface renewal theory, occurs. Since the reaction surface area is a dominant factor, small bubbles can create a large interfacial-area to promote the total mass transfer. The reaction rate should be selectively enhanced by targeting the excitation of vibrational modes, whereby the principle of resonance achieving minimum wastage of applied energy. So the small bubbles will increase the mixing efficiency due to increasing interfacial reaction area and mass transfer. Furthermore, as ammonium bicarbonate synthesis is controlled by the contact time of excited CO_2 microbubble at the interface, this study proposes to characterize the kinetics of NH_4HCO_3 reaction process.

Primarily, this study will focus on building a model providing a fundamental framework for investigating the non-thermal plasma effects on carbon dioxide chemical behaviour in a dielectric barrier discharge (DBD). Although there are many simulation studies related to CO_2

dissociation in plasmas media, we think the effect of non-thermal plasma on excitation of vibrational modes is necessary for the current study. So the concentrations during very short residence, and thus contact times, will be explored.

Moreover, in this work, a thermogravimetric analysis (TGA) study for three ammonium compounds (carbonate, bicarbonate, and carbamate) is explored to characterize the kinetic parameters of the predicted products of $CO_2/NH_{3\ (aq.)}$ reactions. This study will answer the question. "Are the values of kinetic parameters (activation energy, pre-exponential factor) fixed or changed under non-isothermal conditions, conversion, and temperature?" Consequently, the effect of changing the heating rates on the kinetics decomposition parameters will be investigated. This study aims to find a relationship linking the pure component TGA profiles with an unknown mixture of two product species, relying on the TGA mixture profile, by using the pseudoinverse method (PIM) to determine the composition of the unknown sample.

The research hypothesis for the steps of the reactions by non-thermal plasma route comprises the following mechanism:

- Non-thermal plasma activates the CO_2 molecules to form excited species, through the temperature of the energetic electrons of higher than 10000 K while the gas temperature remains near ambient temperature.
- Absorption of the excited CO_2 species (electron acceptor i.e. Lewis acid) near the interface of the microbubble and the aqueous ammonia solution.
- Acid-base reaction on the liquid-side bubble film of excited CO_2 with ammonium ions to form ammonium bicarbonate compound.

1.5 Structure of the thesis

The structure of the thesis is organized in seven chapters in the following order as illustrated in the figure (1.3):

Chapter one includes a general introduction to the research, ammonium bicarbonate uses and importance, the objectives of the study, and the research hypotheses. Followed by the ***Chapter two*** the previous work available in the literature is assessed and analysed in light of the hypothesis for this study. Plasma classification, bubble cloud generation, and gas-liquid reactions are incorporated in this chapter. CO_2 dissociation using non-thermal plasma and treatment by the absorption technology are evaluated from the same perspective. ***Chapter three*** describes the materials and the methodologies utilized to complete the project. The description contains the method of experimental design which is focused on the non-thermal plasma and

small bubbles in the excitation of CO_2 gas to react with aqueous ammonia solution. The procedure of the experiments, the chemical characterization of the reaction product, and analytical equipment used are explained and outlined. ***Chapter four*** discusses the results of the simulation of the kinetic reaction of CO_2 using *Comsol Multiphysics* software. The concentration of vibrational species and the effect of the gas and electron temperatures are studied.

Then in ***Chapter five***, an attempt is made to understand the kinetics behaviour with variation of heating parameters. The chapter also discusses the thermogravimetric data for the binary system of pure salts to estimate the composition of the unknown solid sample using the pseudo-inverse method (PIM). **Chapter six** presents the experimental results which explore the influence of the non-thermal plasma technique for the activation of CO_2 molecules. The main studied parameters are high voltage input, CO_2 flow rate, aqueous ammonia concentration, and reaction time. An experimental, factorial design by applying response surface methodology is used to find the optimum operating parameters for "the electrical conductivity of the solution and the yield of the solid crystals" of the process. Eventually, **Chapter seven** draws the study conclusions. Some ideas are recommended for the future work. In **Appendices**, there are some data which give furthermore information (additional results).

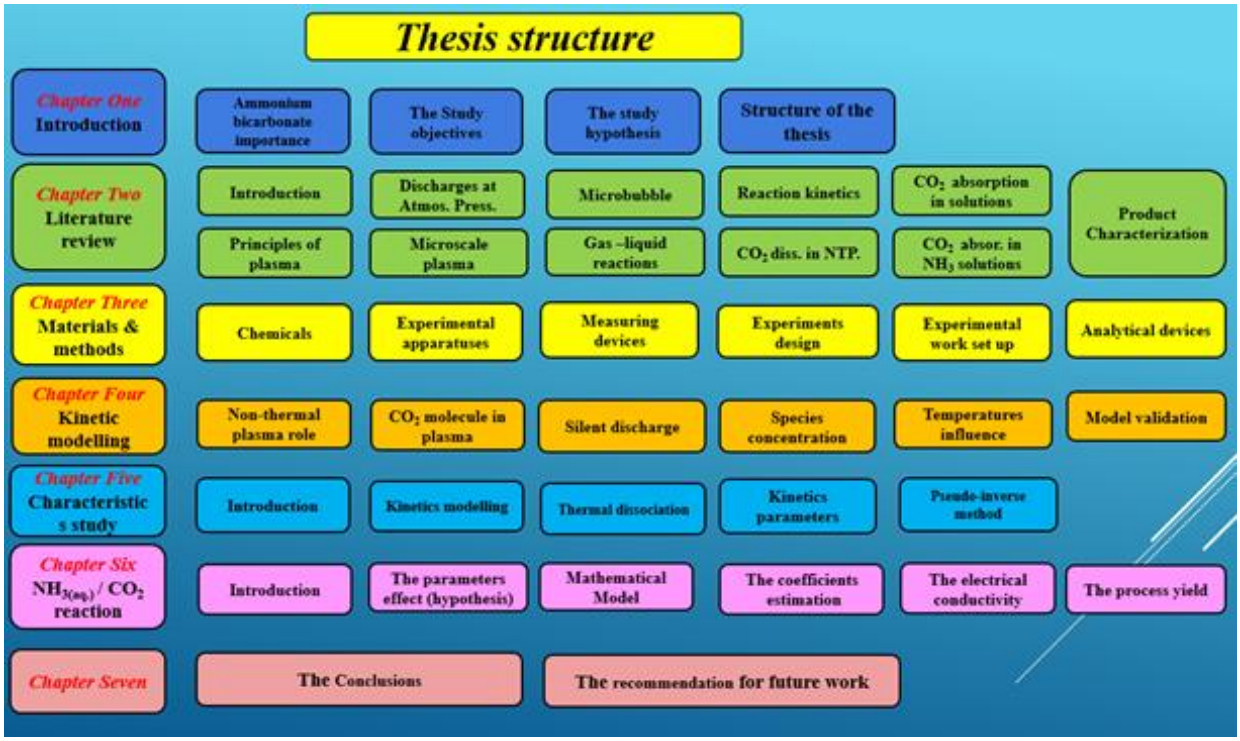

Figure 1- 3.The structure of the thesis composition in each chapter.

Department of Chemical and Biological Engineering

Chapter Two

Literature review

Chapter Two

Literature review

2.1 Introduction

There many industrial gas streams which emit CO_2 to the atmosphere. Many studies have been performed in the field of CO_2 capture for the purpose of minimizing the contribution of CO_2 in the global warming. Even though chemical absorption has the appropriate efficiency for carbon dioxide capture by amines, for instance, monoethanolamine (MEA), it still faces some problems such as high cost, solvent degradation, and corrosion of the equipment. In recent times, the usage of aqueous ammonia has gained significant attention due to its distinctive characteristics as an efficient absorbent to overcome most of the above problems with amines. The major merits of the aqueous ammonia as an absorbent are low cost, a high loading capacity of CO_2, the high capability to react with the acidic gases, and the low energy requirement for the processing.

Non-thermal plasma excitation is a new enhanced technology to activate CO_2 molecules. High activation energy of CO_2 is the major drawback for its utilization. This technology is supported by another technology, which is the CO_2 gas inserted as very small bubbles in order to increase the surface area of mass transfer and improve the yield of the process. The desired product of the reaction is ammonium bicarbonate. It could be a useful and valuable compound in converting and removing CO_2 emission and at the same time useful in agriculture fertilizer (18% N_2) and in food and pharmaceutical industries uses.

The outlines of this chapter include the plasma, their classes and uses, small bubble technology features and their benefits. In addition, the importance of gas-liquid reactions is discussed. Finally, the CO_2 absorption using aqueous ammonia and the reaction conditions are explained and other related subjects.

2.2 Basic plasma definition:

The term plasma was introduced by Irving Langmuir in 1928, by which he referred to an electrically neutral collection of ions and electrons. These collections may or may not contain a background neutral gas, and which is capable of responding to electric and magnetic fields (Roth, 1995). Typically, the element's state changes depending on its energy content. The material states are either solid, liquid, gas, or plasma. This arrangement is usually concerning energy levels, in other words, adding enough energy to solid-state will transform it into the

liquid phase. Adding heat or removing it into/from the liquid phase can cause changing its state to the gas phase or solid-state respectively, also adding or removing pressure can do the same job. If the kinetic energy of the gas molecules increased by adding more energy through an electric potential then the molecular collisions will become highly intense. Collisions repetition leads to gas ionization as a result of increasing electrons energy so, the gas converts into the plasma state (Fridman, 2008). Generally, the plasma also may be defined as an ionized gas or a conglomeration of different species charged particles. These charged particles are comprised of free electrons, ions, and atoms or even molecules. The plasma state may be fully ionized or may be contains neutral particles, consequently a plasma is independent of the degree of ionization (Nasser, 1971).

The degree of ionization represents the ratio of gaseous atoms or molecules that are decomposed into charge carrier to those initially present. Nishikawa and Wakawtani (2000) have reported the degree of ionization increases as the temperature rises. The quantity of energy that required to transition from one phase to another for each particle is, on average 10^{-2} eV (1eV= 1.602×10^{-19} J) while the amount of energy needed to change the state from gas phase to plasma state is 1-30 eV/ particle, depending on the gas type. The main two important characteristics of plasma are the temperature of the electron T_e and charged particle density (n). Typically, for laboratory plasma n is about $\approx 10^{-9}$ particle/m^3 and $T_e \approx 10^5$ $^{\circ}$K (Kettani and Hoyaux, 1973). The ionized gas is consist of a large number of negatively charged electrons "light" and positively charged "heavy" ions. Other elements of plasma are photons, neutrals, excited (atoms or molecules) as shown in figure 2.1.

2.3 Classification of plasma

Electric discharges can be classified according to some specific features and their physical characteristics. For example: Fridman *et al.,* (2005) classified the plasmas into two major categories: thermal and non-thermal ones, characterized by their specific advantages and disadvantages. Thermal plasmas (TP) included inductively coupled plasma (ICP), arcs, and radio frequency (RF), which are characterized by thermal ionization, Joule heating, and transition of high power at high pressures. The disadvantages of the TP involve very high gas temperature, high risks of the quenching requirements, as well as the electrodes problems. All these factors lead to limited energy efficiency. In contrast, non-thermal plasmas (NTP) comprise the low-pressure glow, microwave, and RF. The NTP possesses many advantages,

for instance, high selectivity in plasma chemical reactions, high energy efficiency, and no need for quenching since it operates effectively at low temperatures (Fridman, et al., 2005).

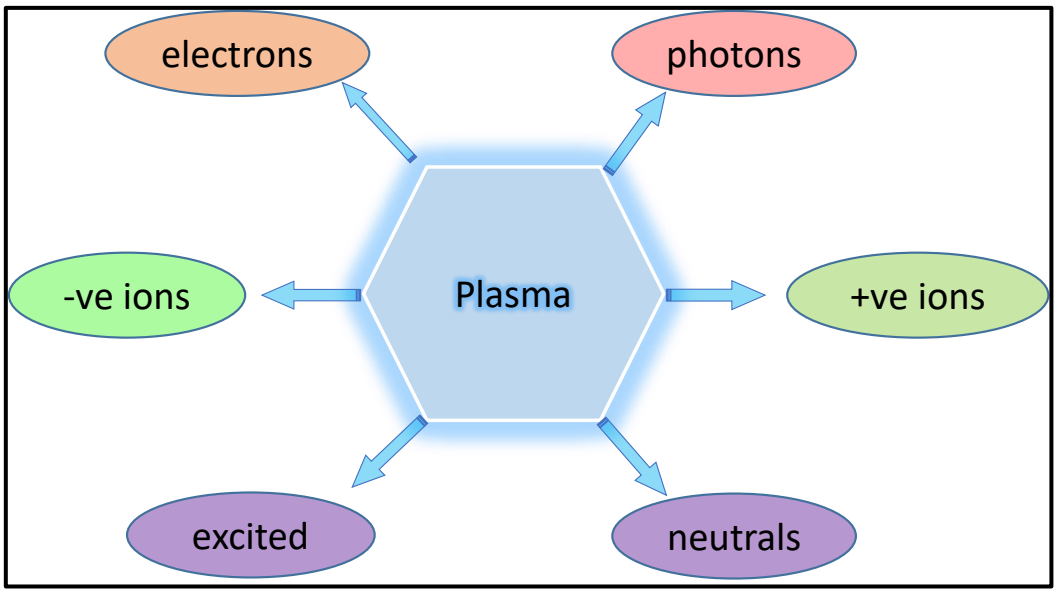

Figure 2- 1. The major components of plasma; electrons, photons, positive and negative ions, excited and neutral particles (atoms or molecules)

2.4 Applications of plasma

The plasma applications are recently extended in quite different areas of daily life, industrial and medical fields. However, the fields of science and engineering in which plasma can be applied are dramatically increasing, so a plasma has a great promise for practical applications in the following fields as reviewed (Samukawa *et al.*, 2012; Kim *et al.*, 2016), such as:

i. Plasma-etching processes: Plasma etching is a processes applied in microelectronic circuit fabrication. The aim of etching process is to remove material from surfaces (Eliasson and Kogelschatz, 1991), either by chemically selective (remove unwanted material) or anisotropic etching which involves removing material at the bottom of a channel and leaving the sidewalls unaffected. It can fabricate trenches in silicon films of wide 0.2 μm and 5 μm deep. In last years, a technologies of high-density plasma sources, such as inductively coupled plasma (ICP) and electron-cyclotron resonance plasma used to develop a precise etching processes.

ii. Plasma deposition processes: Applications of plasma for film deposition (Kushner, 1988) are related to chemical vapor deposition by forming amorphous carbon films. There many research and development on plasma polymerization techniques to produce materials which have different applications in variant fields such tribology, biomaterials, photovoltaics.

iii. Microplasmas: Numerous microcavity plasma devices (Kushner, 2005) have been developed during the last decade in various applications, such as micro-fabrication processes, use of microplasmas as microreactors for gas phase chemistry as the synthesis of ozone, or synthesis of nanoscale particles and biomedical treatments, and also other application in the manufacturing of microfluidic devices for functionalizing internal surfaces (Becker, *et al.*, 2006).

iv. Plasmas in and in-contact with liquids: There is a great research work that dealing with the interaction of plasmas and liquids was done last years (Bruggeman and Leys, 2009). However, the main focus in the field of plasmas was in water purification to produce radicals such $^{\bullet}OH$, $O^{\bullet}$, as well as H_2O_2, and ultraviolet radiation (Joshi *et al.*, 2009). Plasma species have a strong ability to destroy the organic and inorganic compounds in water. The research focus in plasma contact with liquid did not stop at this point, but took other direction such as biological, chemical, material and environmental applications (Locke *et al.*, 2006). In general, plasmas in liquids are still more complicated than that which in the gas phase.

v. Plasma in medicine: Plasma health care or plasma medicine (Stalder, *et al*., 2005) may provide an efficient and quick new path for hospital staff helping to contain and prevent diseases that are gaining ground as resistance of pathogens to antibiotics grows. At present, plasma medicine is at research and development stages. Academic and clinical experiments have yielded very promising results. However, the fundamental understanding of the interaction between the plasma and living cells, tissues and organisms is need more and more discussion to reach maturity stage.

vi. Plasma catalysis: The use of a catalyst into a plasma reactor has many advantages (Hessel *et al.*, 2013) through enhance yield of desired product and high selectivity or by other word, it work on minimize the reaction path of undesired species. The main application of plasma - catalyst is clearly appear in environmental field to remove common pollutants such as nitrogen oxides and other volatile organic compounds (Morent *et al.*, 2007) also may be use to synthesis valuable materials. Certain benefits such as operation at ambient conditions, high selectivity and improved efficiency of energy are clearly emerging.

Non-thermal plasma has numerous branches and a numerous applications as shown in figure (2.2), which illustrates the most important non-thermal plasms applications.

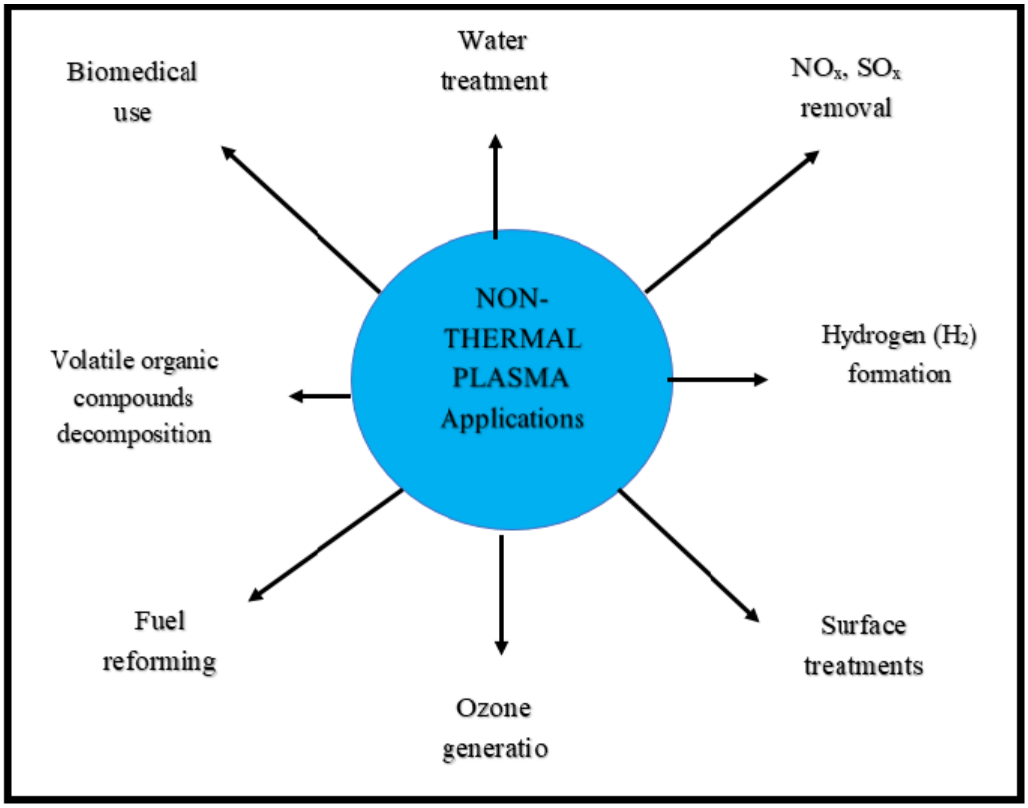

Figure 2- 2. Non-thermal plasma uses in variant field of the industry, environment and biomedical application.

However, although a some applications are mentioned above, there are many others such as; Thermal plasma applications (Boulos, 1991), plasma for environmental applications (Morent *et al.*, 2007), plasma lighting, and other applications, more details in (Kogelschatz, 2007) . The most important type of plasma for our proposed research will be the non-thermal plasma (microdischarge) so we will address it in more details in the next sections.

2.5 Discharges at Atmospheric Pressure

Recently, non-thermal plasma is used for gases processing such as combustion exhaust treatment, the generation of the ozone, and CO_2 conversion into value-added chemicals (Bogaerts *et al.*, 2015). These plasmas are not in thermal equilibrium due to, firstly, applying an electromagnetic field easier than regularly heating and confining the plasma, i.e. the electromagnetic field transfers the charged species, so their concentrations and energies are varying in space, in particular, close to the container walls. In general, the species of this type of plasmas are not in thermal equilibrium. The second reason is the degrees of freedom of the energy distribution. In thermal plasma, energy is equally partitioned into the rotation, and vibration of neutral molecules. Conversely, with non-thermal plasma, it is possible efficiently to control the desired reaction products for a specific application. Hence it is better to energize

electrons to high velocities in order to excite and ionize molecules by collision, meanwhile, the ionized gas temperature remains close to the ambient conditions (Bogaerts *et al.*, 2015).

Through this technique, the nature of non-thermal plasmas possesses many unique advantages. More energy can be controlled for a particular reaction or molecules excitation by changing specific parameters, such as circuit characteristics, the components of gases, electrodes material, and their configuration. There are many techniques are usually utilized in the nonequilibrium discharge (Eliasson and Kogelschatz, 1991) such as glow, RF, and microwave. In the next paragraphs, the corona discharge and the barrier discharge will be addressed in brief due to proximity to our research field.

2.5.1 Corona Discharges:

Corona discharges (discharges between uncovered metal electrodes or without insulation materials) are characterized by weak illumination at atmospheric pressure when a high electric field is applied close to thin wires, sharp edges or other strongly curved surfaces. At this region (sharp or curved ends) the gas breakdown occurs under specific conditions. The corona discharge (negative or positive) possesses specific features like non-uniform ionization process, strong electric field, and luminosity. Within the negative corona and away from the wire electrode (cathode) a rapid drop in the electric field occurs. The secondary emission from cathode provides the continuity of electric current from the electrode (cathode) to the plasma. The low energetic electrons in the drift region could be attached by neutral particles and form negative ions. While positive corona discharge starts near the other electrode (anode) by streamer mechanism "which are the earliest stage of electric breakdown of large non-ionized regions" away from the wire in low electric field region mainly positive ions are present (Dinklage *et al.*, 2005). This type of discharge is mainly used in plasma chemical gas cleaning and treatments of surfaces. It works at atmospheric operating condition with the ability of scaling-up as shown in table (2.1). The low continuous corona discharge power is undesired for some applications because it characterized by very low power. If the voltage is increased, sparks (arcing) will be formed (Fridman, et al., 2005; Rehman, et al., 2013). Therefore to prevent this corona-to-arcing transition, nanosecond pulsed power supplies should be used. Typically, the corona discharge in industrial applications is limited, only when there is need for relatively small concentrations of charged species (Kostov *et al.*, 2009). For example, the common applications are high- speed printing devices, electrostatic precipitators, dry-ore separation systems, and copying machines. For this reason the corona discharge was not the best choice reactor in our study. We searched for another reactor type with specific features.

Table 2- 1. Non-thermal discharge types and their common applications, taken from (Pârvulescu, et al., 2012).

Type of discharge	Gap (mm)	Plasma	Energization	Typical application
Corona	10-300	Filaments	Pulsed / DC	Gas cleaning/ dust precipitation
Corona with barrier	10-30	Filaments	Pulsed	Gas and water cleaning
Plate/cylinders with barrier	1-5	Filaments	AC	Ozone generation /large surface treatment/excimer lamp
Barrier with packed bed	3-10	Filaments	AC	Chemical conversion
Plates with barrier	1-5	Diffuse	AC	Surface treatment / deposition surface
Surface discharge	1-5	Filaments	AC	Surface treatment / deposition surface
Surface barrier	1-5	Filaments	Pulsed	Aerodynamic control
Plasma jets	0.5-10	Diffuse	AC/ RF	Local surface
Microdischarge	0.1-1	Diffuse	AC/RF	Chemical conversion / light generation

2.5.2 Dielectric barrier discharge

Barriers are employed in plasma reactors to overcome the problem of the spark transition in a corona discharge, which forms in the streamer channels. Inserting a dielectric barrier between the plasma electrodes system generates dielectric barrier discharges (DBD), referred to as silent discharges. DBD reactors have found numerous applications in industry. For instance, applications include ozone generation (Pietsch and Gibalov, 1998), CO_2 lasers (Cenian, *et al*., 1995), excimer radiation in excimer lamps, processes of pollution control and surface treatment (Kogelschatz, 2010), hydrogen gas production from water vapor at atmospheric pressure (Rehman, *et al*., 2012), (Rehman, *et al.*, 2013), and analytical chemistry for mercury detection in water (Abdul-Majeed, *et al., 2011).*

The discharge process occurs between two separated electrodes with small gap. One or both electrode surface is covered with dielectric (insulation material). Figure (2.3) illustrates a typical electrode arrangements planar reactor (a) and cylindrical reactor (b) designs.

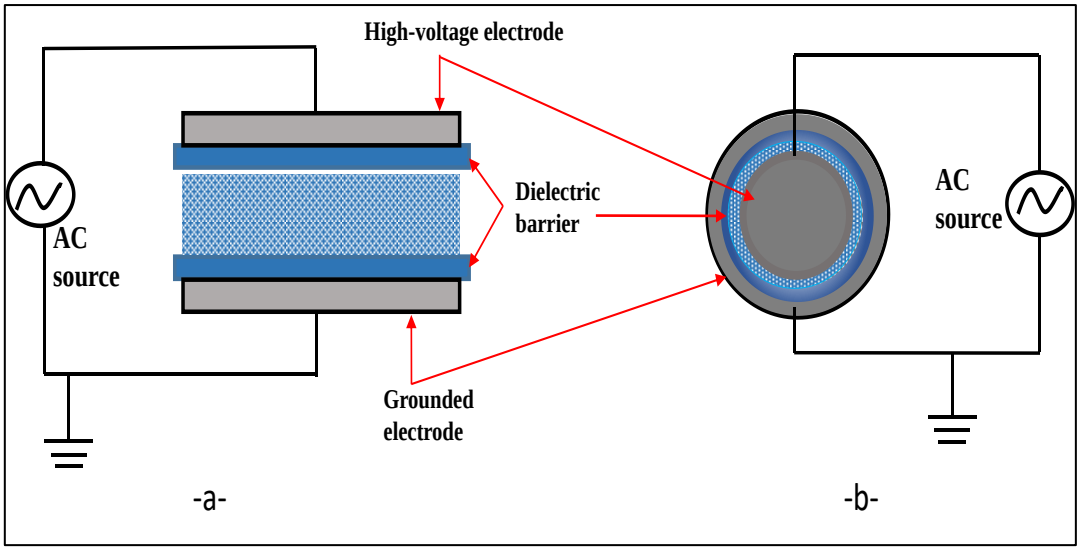

Figure 2- 3.The DBD electrodes arrangement design -a- planar reactor and -b- cylindrical reactor

Li-Fang *et al.*, (2001) identified the self-organized filaments in DBD at atmospheric pressure, which depend on the voltage nature which is applied to the electrodes surface either a sinusoidal or square-wave shape at a few hundred kilohertz of the frequency. They stated that the DBD is the best choice for generating plasma at atmospheric pressure. That is due to the dielectric layers, which insulate the electrodes and prevents an arc formation but allow the current to pass with specific limitation.

The most important features (Kogelschatz, Eliasson and Egli, 1997; Wagner *et al.*, 2003) of the DBD are:

- The non-thermal plasma conditions at low gas temperatures and at elevated electron temperature.
- The ability to generate atoms, radicals and excited particles because DBD provides high-energy electrons.
- It is characterized by the design flexibility, especially with respect to operation parameters, geometrical configuration, and operating medium. All these merits are unique to DBD.
- The capability to upscale from laboratory conditions to industrial conditions
- The availability of the efficient power supplies with a low cost even for the large powers.

When those above characteristics are combined well with other parameters, originated from scaling down of reactor dimensions, the process efficiency for excitation of CO_2 molecules will be enhanced. Zimmerman (2011) concluded that electrochemical microfluidic reactors are started to achieve progress through the " scaling -out" by exploiting microscale processing features and the major success lies in the characterization and information discovery. These features were exploited into the reactor design to excite the CO_2 gas and to improve the process efficiently. Tachibana echoed this assertion in the review article of " The 2012 Plasma

Roadmap" when he states the spatial smallness “microdischarges” has an ability to make new different chemistry, physical or science from that of the large scale of plasma as a result of the increase in the surface area to the volume ratio (Samukawa *et al.*, 2012).

2.6 Plasma microreactor /microscale plasma

Plasma microreactors are very small devices having a size within sub-millimeter to micrometer length scale in at least one dimension, and are attracting much attention in recent years (Tachibana, 2006). Microplasmas innovations, if integrated with other technologies like microelectronics and microfluidics, provide numerous advantages for scientific and engineering fields, and can create many advances in different application areas. The hypothesis of this study will based on both micro-discharge and microbubbles characteristics (Al-Mashhadani, et al., 2012; Ying *et al.,* 2013) to exploit its merits in providing a large a surface area comparing to the volume. Before considering characteristics of microreactors, it is important to note the difficulties to control a uniform temperature, concentration and residence time distribution in traditional scales of reactors (Hessel, 2015). Miniaturization of plasma reactors included many important factors which promise to enhance control and spatially precise through using of microfluidic to get a selectivity for desired product or intermediate compounds in chemical processing for valuable chemicals such as fine chemicals and pharmaceuticals (Lozano-Parada and Zimmerman, 2010). The typical characteristics of the DBD microdischarges in a 1 mm air gap at atmospheric pressure are shown in table (2.2). Furthermore, producing microplasma as shown in figure (2-4) by miniaturization technique involves reduction in voltage values comparing with the traditional reactors and that leads to improvement in power efficiency of production. An equally significant aspect of the design stage is decreasing the distance between electrodes to increase the electric field strength as well as increase the surface-to-volume ratio. The plasma reactor design is considered one of the significant objectives for study, to know the influence of the NTP discharge on CO_2 molecules activation. Microplasma can be distinct from conventional plasma by many features such as non-equilibrium chemistry, high-pressure operation, and micro-scale geometry. Consequently, microplasmas can be sustained at virtually lower power which means low operating costs. The plasma micro-reactors can provide 10^6 micro discharges cm^{-2} s^{-1}, as detected by Coogan and Sappey (1996). Their density depends on the power dissipated in the discharge. On the other hand, plasma microreactors offer the possibility to preserve non-equilibrium state for gas mixture, leading to high reaction rates, and enabling a large number of fast and efficient high productivity processes.

Table 2- 2. The typical parameters of a Microdischarge

	Filament radius	50/100 μm	Current density	0.1/1 kA cm^{-2}
	Peak current	0.1 A	Electron energy	1–10 eV
	Electron density	$10^{14}/10^{15}$ cm^{-3}	Electron energy field	*E/n = (1/2)(E/n) Paschen*
	Total transported charge	0.1–1 nC		
	Total dissipated energy	5 μJ	Gas temperature	Close to average, about 300 K
	Overheating 5 K	5 K		

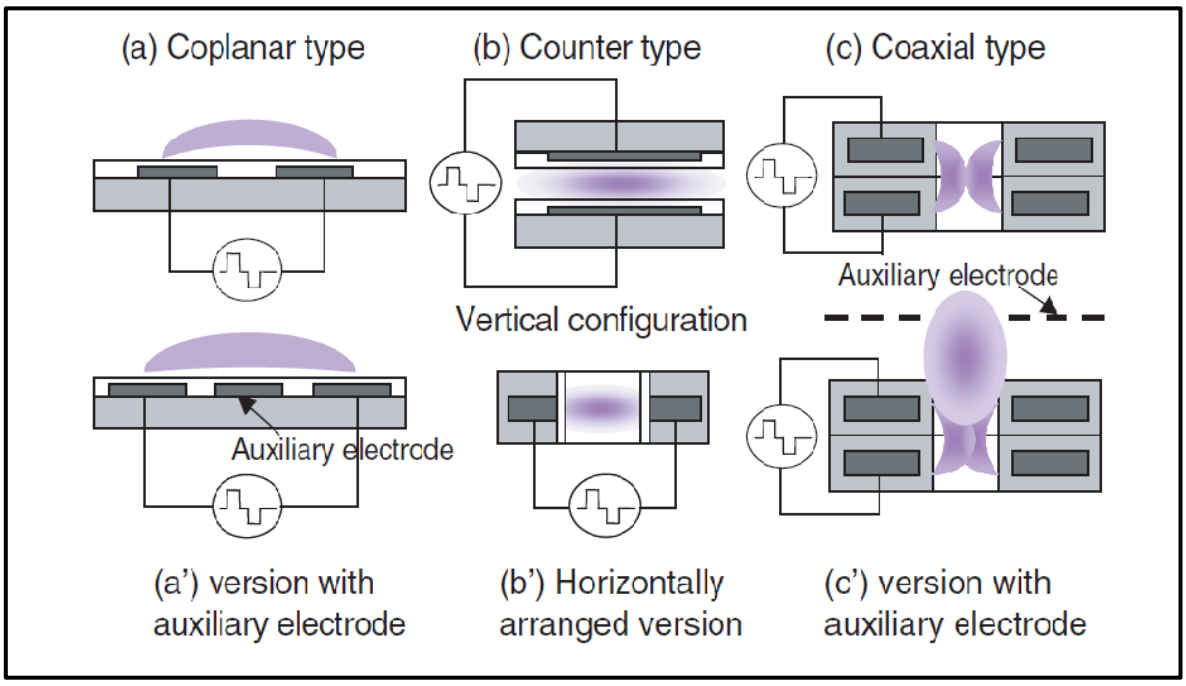

Figure 2- 4. Different designs schemes of microdischarge (Tachibana, 2006)

In traditional plasma low pressure reactors, the gas temperature is much lower than the electron temperature, causing the non-equilibrium state (Mariotti, 2008). Then, the pressure is gradually increased through reaction of the process, so the temperatures of gas and electrons tend to be approach to each other as shown in figure (2.5), leading to equilibrium. While, in microplasma reactors the non-equilibrium state is one of the best features, because the reduction of volume and increase the area (area / volume ratio is large) dissipates any excess heat come from the power supply.

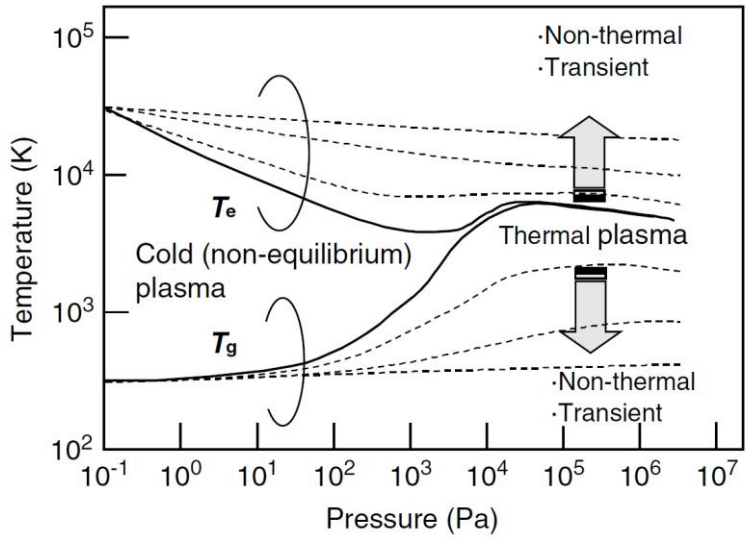

Figure 2- 5.The relation between pressure with both electron temperature and gas temperature (Tachibana, 2006)

Another reason is the efficient energy exchange between the electrons and the radicals by the collisions. The miniature scale of plasma leads to an increase in the rate of collisions, and the average energy exchanged rises. Thus, an increase in the electron temperature results from plasma size reduction at a fixed pressure.

There are a substantial number of factors that have an effect on features of microplasma such as electron energy distribution functions, electron temperature, electron density, gas temperature (Lin and Wang, 2015). Also other parameters for instance, the gas flowrate, pressure, dimensions of electrode, electrode material, and their arrangement, applied power, and frequency. Also the residence time of plasma microreactor are influenced on reduction of power consumption (Rehman, *et al.*, 2016). Generally, more details will be discussed in chapter four of this study, which is related to the non-thermal plasma effect on CO_2 chemistry and the other substantial parameters.

2.7 Small bubbles features

2.7.1 Characteristics and applications of microbubbles

From the basic hypotheticals for the mass transfer principles, one of the major effective factors which contribute to enhance the process performance is the increasing contacting surface area. The interfacial surface area plays an important role in improving either the mass and heat transfer or even the rate of absorption (include reaction) between the phases at the contact region (Temesgen *et al.*, 2017), as shown in equations (2-1 to 2-3). When a system contains

two components with different concentrations from point to point, then the system has a natural tendency for the mass transfer, leading to minimize the concentration variation in the system:

$$N_A = k_l \ (C_{Ai} - C_{A\,l}) \qquad (2\text{-}1)$$

Where N_A, is the molar-mass flux of species A in mole per unite area, k_L the coefficients of mass transfer in liquid phase, C_{Al} and C_{Ai}, represent the driving force of concentration at the interface and the bulk of liquid respectively.

The heat flux Q from a body at a temperature T_H according to Newton's law of cooling is:

$$Q = \frac{q}{a} = h\ (T_H - T_C) \qquad (2\text{-}2)$$

Where a local heat loss is q, and T_C is the surrounding air temperature, h is the heat transfer coefficient.

The rate of absorption component A per unit area,

$$R_A = -D_A \frac{\Delta C}{\Delta x} \qquad (2\text{-}3)$$

Where R is rate of absorption component *A* per unit area, D_A is the diffusivity (m^2/s) of component *A*, ΔC is the concentration change at the interface and the bulk of liquid respectively, Δx is the distance change from the interface. The transport of mass or heat within a fluid mixture or across a phase boundary is a process that fundamentally depends on the surface area. The surface area plays a significant role in many applications in industrial processes to improve efficiency. The above equations for chemical and physical phenomena refer to the importance of the surface area in the processes of transferring.

There are many variables which influence by the efficiency of "gas-liquid" operations design process, for example, the fluid properties at the contact area and contacting operations type. The main importance of small bubbles emanate from their ability to provide large surface area to volume ratio as shown in figure (2.6) which is exploited in direct contact evaporation (Zimmerman, *et al.*, 2013) and in purification of bioethanol (Abdulrazzaq *et al.*, 2016). Another important property of small bubbles is the ability to decrease their size and may be dissolved inside the liquid, while on the opposite end the large bubbles, go up to the surface and burst (Takahashi *et al.*, 2003).

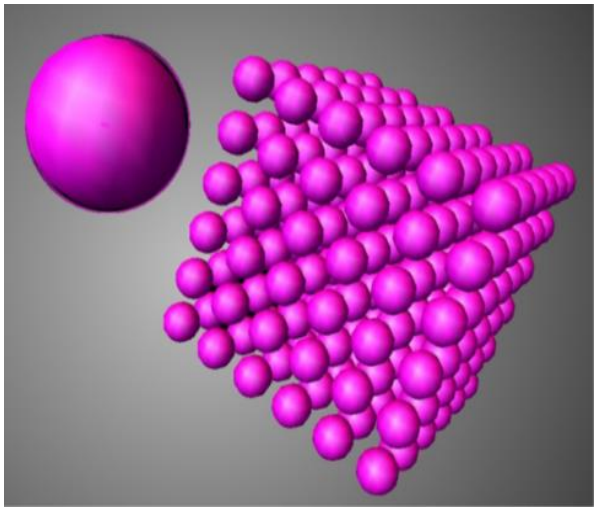

Figure 2- 6. A unit volume when divided into very small parts, equalized two units in sizes, but provide additional surface area (W. B. Zimmerman et al., 2008).

Particularly noteworthy is the induction of interfacial area which offered by microbubbles will improve the liquid mixing (Al-Mashhadani, *et al.*, 2015) process at low energy cost (Al-Mashhadani, *et al.*, 2012). Not only may mixing control the amount of surface available for a reaction for example, but it will raise the gradient of the concentration in the bulk of liquid that might enhance diffusion and mass transfer. The exploitation of the microbubbles characteristics particularly when introduced as a uniform cloud of the gas, occurs in many chemical processes, separations processes, flotation, air-lift of wastes and oil recovery (Zimmerman *et al.*, 2009).

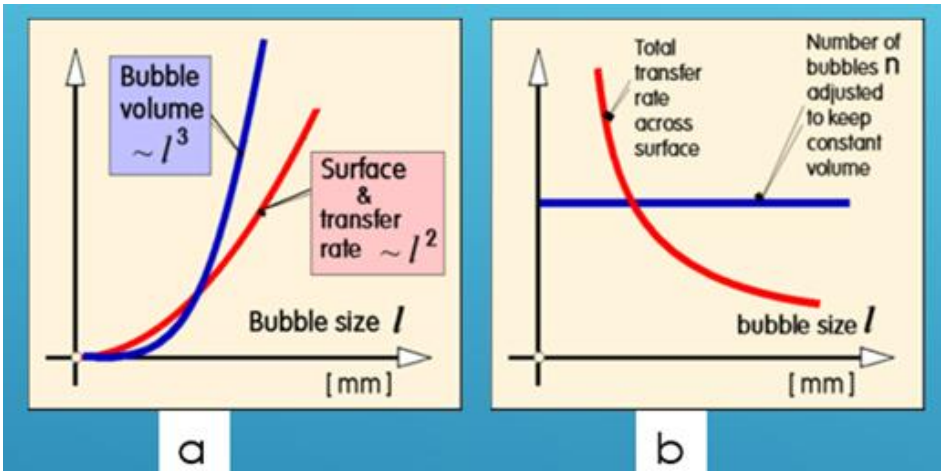

Figure 2- 7. For a single bubble (a) the relation of bubble size (l), surface area and transfer rate as function tor bubble radius. (b) the total transfer rate is enhanced by subdivision of (n) number of bubbles to smaller bubbles leading to greater transfer (at con constant total volume).(W. B. Zimmerman et al., 2008)

Figure (2.7) describes the main features of high surface area to volume ratio. The surface area and transfer rate are correlated with square of the bubble radius, while, the volume related with its cube. Basically, in every phase transition starts with the forming of a tiny spherical particle

named a nucleus. The interface separates the two phases, the particle and the matrix are characterized by the existence of surface energy. In case of a gas bubble, there is a pressure inside the bubble. The same is true for a nucleus of a solid particle when it precipitates. The pressure inside the bubble can be specified in terms of the surface tension (N/m). Bubble radius is correlated with pressure difference and surface tension according to the Young-Laplace equation (Takahashi, *et al.*, 2007), which will discuss in next section.

Moreover, there are other benefits of small bubbles. For instance, it has a high residence time (smaller bubble rise slower than a larger bubble). This highlights that the small bubbles possess the capability to stay in liquid phase extra time and contact with the reactant. If that occurs then an improvement in the yield will be gained and the losses in gas will be reduced. Figure (2.8-a) illustrates a large bubble rise faster than a small bubble with other characteristics. It has been demonstrated that the rising velocity of microbubble can be roughly calculated by the theoretical values of Stokes' Law (Takahashi, 2005) with equation (2.4), and Zimmerman, *et al.*, (2013) improve on this with the Hadamard drag law.

$$U_t = \frac{gr^2}{3\mu} \Delta\rho \qquad (2.4)$$

Where: U_t (m/s), is the terminal velocity of rising microbubble, g is the gravitational acceleration (m/s^2), μ (kg m^{-1} s^{-1}) is the dynamic viscosity of liquid, density difference Δρ (kg m^{-3}) is the density difference and d (m) is the diameter of the bubble. So the small bubbles have a tendency to decrease in size and eventually breakdown due to long-stagnant state and dissolution of the inner gases into the surrounding liquid.

This study will be an important attempt to use these features of small bubbles in reaction of CO_2 gas with aqueous ammonia. Exploitation small bubble characteristics in chemical reaction of valuable chemical synthesis will open extensive application across many other reactions.

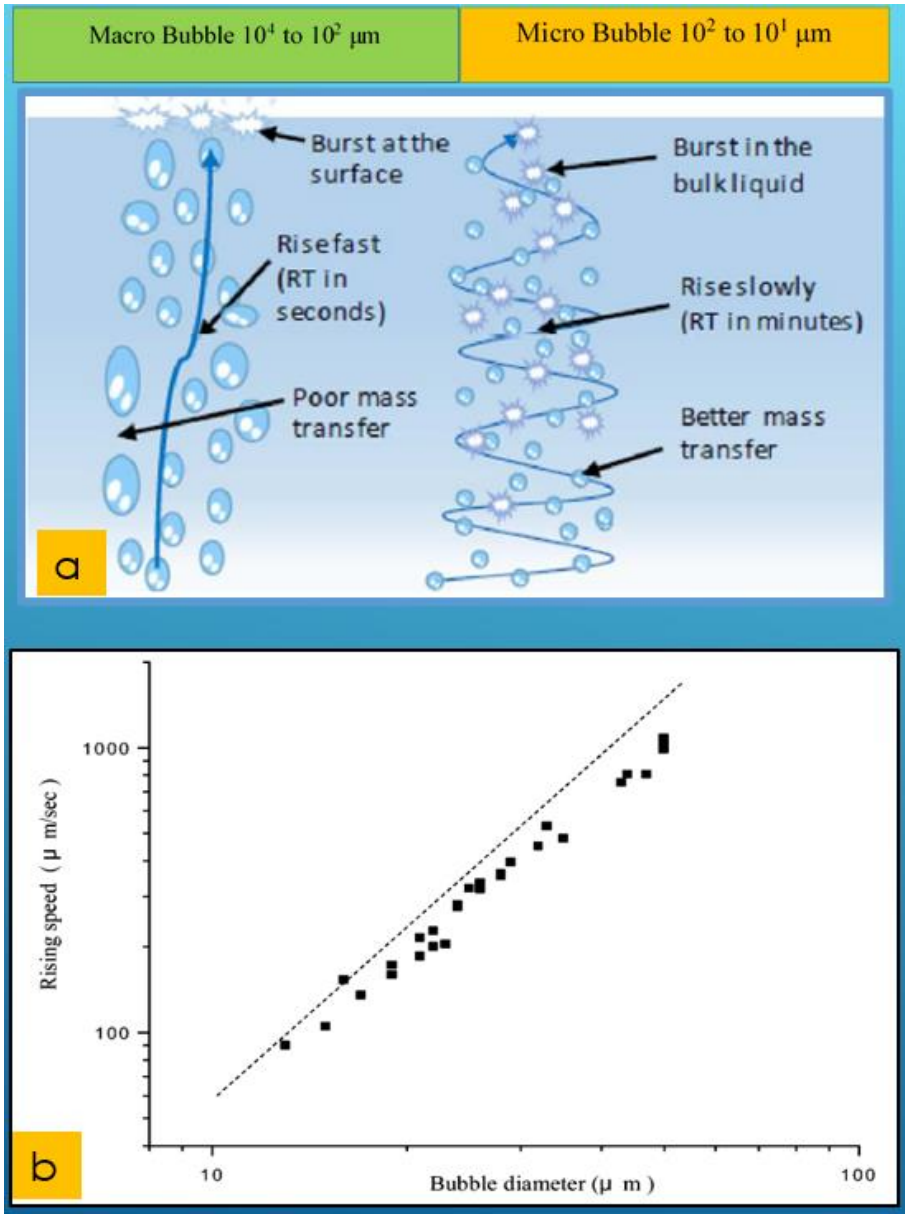

Figure 2- 8. The behaviour of micro-bubbles, (a) the bubble sizes as a proposed range and their major properties. The macro size bubbles are rapidly rising and the burs occurs at the surface of the liquid, meanwhile, the microbubbles exhibit a reduction in their radius and can be vanish, if wholly consisting of soluble gas in the solution (Temesgen et al., 2017), (b): the rising velocity versus the diameter of the microbubbles in distilled water. The microbubble aerator generated very fine bubbles in the water reservoir. (Takahashi, 2005).

2.7.2 Microbubble cloud generation

The generation process of bubbles mainly occurs in the two-stage; static or quasi-static process followed by a dynamic process or the bubble dispersion. Generally, these stages depend on the gas flow rate (Hanotu, *et al.*, 2017). There are many conventional methods of producing bubbles. However, different studies applied variant technologies to generate fine and ultrafine bubbles, below some of these method according to (Temesgen *et al.*, 2017):

i. Hydrodynamic cavitation (Agarwal, *et al*., 2011)
ii. Acoustic or sonication (Xu *et al.*, 2008; Agarwal, *et al*., 2011)
iii. Mechanical agitation (Xu *et al.*, 2008)
iv. Electrochemical cavitation (Wu *et al.*, 2008)

The cavitation term is often used to refer to the formation, growth, and collapse of the microbubbles. Furthermore, the method of bubble generation could be classified into four divisions; hydrodynamic, particle cavitation, acoustic, and optic as addressed by *(*Agarwal, *et al.*, 2011). The cavitation is formed due to the pressure drop in the injection device or nozzle leads to form bubble. (Edzwald, 2010) indicated that the process of microbubble formation include two steps which are a bubble nucleation and bubble growth. Bubbles cannot separated from pores when formed unless, it overcomes a force balance. So, it continue to grow until buoyant force and the force exerted by downstream portion of the nozzle orifice or pores exceeds the forces of wetting of the aperture surface.

The increased internal pressure of microbubble can be achieved by injecting compressed air through a porous material, which creates the pressure difference between inside and outside bubble. The bubble radius is correlated with pressure difference and surface tension by the Young-Laplace equation as follows:

$$r = 2\sigma/\Delta P \qquad (2.5)$$

Where: r: is the radius of the bubble, σ: is the surface tension of bubble ΔP: is the pressure difference between inside and outside bubble. From equation (2.5), it can be seen that the size of bubble is inversely proportional to the pressure difference and the figure (2.9) shows clearly this relation. Edzwald (1995) reported that "In supersaturation system of clean water the large pressure difference across the nozzle produce bubble nuclei spontaneously according to the thermodynamic principle of minimizing the free energy change".

The change in free energy as a result of the microbubble generation can be estimated (Takahashi, *et al*., 1979) by the following equation :

$$\Delta F = \left(P_\circ + \frac{2\sigma}{r}\right)\frac{4}{3}\pi r^3 \ln\left(\frac{P_\circ + \frac{2\sigma}{r}}{P_A}\right) + \frac{4}{3}\pi r^2\sigma^2 \qquad (2\text{-}6)$$

Where:

ΔF: is the change in free energy, r: radius of bubble, $P_\circ$: is the atmospheric pressure, P_A: is dissolved gas pressure, σ: surface tension

On the other hand, Henry's law gives that the saturated concentration of gas dissolved in the liquid is proportional to the pressure of gas outside the surface of liquid:

$$P_A - P_\circ = H_E x_g \qquad (2\text{-}7)$$

Where: P_A: is the dissolved gas pressure, $P_\circ$: is the atmospheric pressure, H_E: Henry's law constant, x_g: molar fraction of gas at dissolved pressure

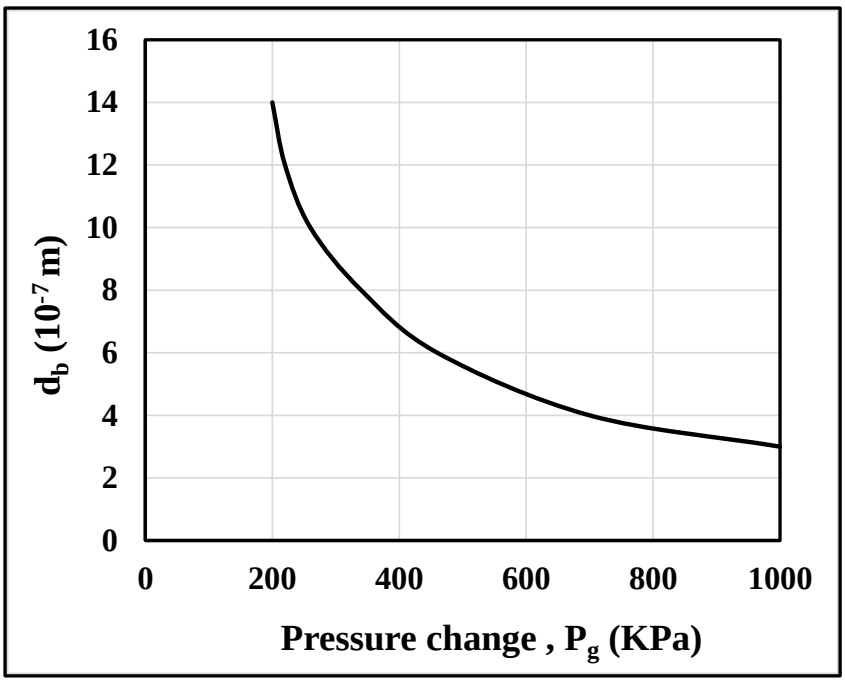

Figure 2- 9. The relation of microbubble diameter with the pressure difference (Edzwald, 1995)

Agarwal (2011) used the Young–Laplace equation (2.5) to estimate the internal pressure of 1 μm bubble diameter, it was 390 kPa, i.e. four times greater than the atmospheric pressure. Whenever the pressure of dissolved gas in the bubble is increased, the gas diffuses to the lower pressure area, i.e., transfer from the bubbles to the liquid bulk. Consequently, the bubble shrinks and internal pressure increase, and so that lead to further decrease in bubble size.

2.7.3 Developed microbubble generation methods

Traditionally, the diffuser of a very fine pore is utilized in specific industries particularly in water treatment, but the generated bubbles size is still much larger than the pore size. This variance can be attributed to the mechanism of bubble growth. The formation of bubbles mainly depends on three forces, the surface tension, and the inertial forces which tend to keep the bubble stagnant down on the diffuser surface. While the third force is the buoyancy which

pushes the bubble toward the surface of the liquid. Zimmerman et al. (2008) explained the bubble detachment from the surface of the diffuser depends on the wetting properties of the solid surface. If the solid surface is hydrophobic the bubble contacts the surface over a larger region comparing when the surface is hydrophilic. Another factor is the nature of intermediate distances among the bubbles, usually irregular leading to quick coalescence between any neighbor bubbles.

Most of the above methods (section 2.7.2) of bubble generation have substantial energy requirements thus spurring Zimmerman and coworkers to develop a new design of fluidic oscillator to generate micro-bubbles with desirable bubble size distribution and nearly uniform spacing to oppose coalescence as shown in figure (2.10).

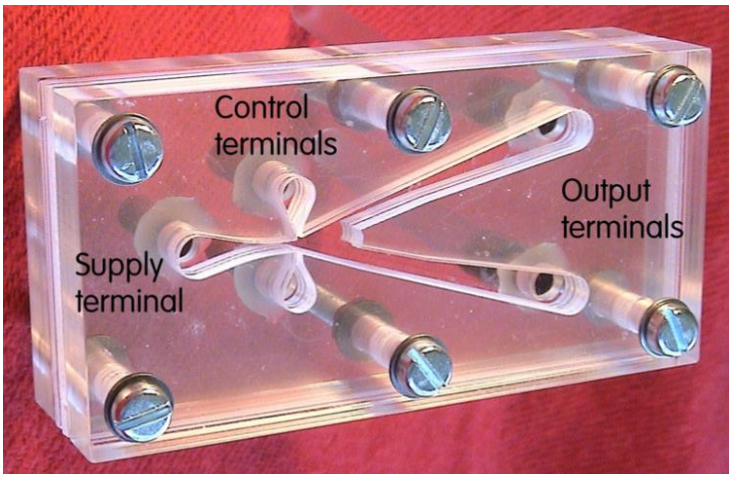

Figure 2- 10. The Fluidic amplifier used (Zimmerman et al., 2008) used for microbubbles generation. The pressure difference between the feedback loop (connects the two control terminals of the amplifier) generates the flow in the loop than causes the main air flow from the supply terminal to switch from one Coanda-effect attachment wall to the opposite one.

The fluidic oscillator was appropriate to provide significant improvements for mass transfer coefficients, mixing and energy efficiencies of the microbubble generation. The method could offers considerable economic savings in the water treatment plants and in the ecological troubles (Rehman *et al.*, 2015). Unfortunately, we have not been able to take advantages of the characteristics of this distinctive method, due to this work being conducted in very low flow. If we use fluidic oscillation for small scale applications, we vent a large proportion of the gas to the atmosphere, due to the onset flowrate for oscillation. So we will suggest use it in next-stage, for instance, the pilot-scale (Zimmerman *et al.*, 2011), or multiplex multiple vessels / diffusers with one oscillator (Ying, *et al*., 2014).

2.8 Gas –liquid reactions

There are a number of various physical models which are used to explain the gas-liquid reaction processes, e.g. Film theory, penetration theory, surface renewal, film-penetration, etc. Most of these models are described by (Danckwerts, 1970). These theories give a comparatively different physical view of the reaction process, but the final required rate of absorption of gas in the presence of a liquid phase is the same. The film theory and penetration theory are most commonly used and with many applications. We will briefly reviewed these applications. The combination of the reaction with gas absorption in bulk liquid enhances the rate of gas transfer compared to the absorption without reaction (Aieta and Roberts, 1986).

2.8.1 Film theory

The film theory was originally proposed by Whitman, while Hatta, was the first to apply it on the analysis of gas absorption accompanied by a chemical reaction (Shah, 1979). This theory is designated for a steady-state. It proposes that there is a thin film in each side of the two phases. The mass-transfer a cross the interface is restricted due to the resistances of these thin films as shown in figure (2.11). The gas moves from the gas bulk region to the gas-liquid interface. The interface region is split into two films, one is the gas film and the liquid film, each one has a thickness of a $\boldsymbol{\delta}$. The concentration of gas decreases across the distance from the gas to liquid due to the resistances. The absorbed gas moves across the interface and overcomes the liquid film resistance and goes through the bulk liquid. Henry's law is applied at the interface region. If there are more species, the theory presumes that the thickness of the film at the interfaces is the same for all species (reactants and products) (Chen, 2012). The equations which govern this theory can be written in a following form as:

$$D_i \frac{d^2 W_i}{dx^2} - R_i^* = 0 \qquad i=1, 2, .n \qquad (2.8)$$

Where D_i, W_i, and R^*_i are the diffusivities, concentrations, and rate of the species *i* generated (or depleted) in the reaction medium, respectively. The absorption rate is obtained as

$$R_i = - D_i \frac{dW_i}{dx}\Big]_{x=0} \qquad (2.9)$$

In condition without reaction, the theory only involves the mass flux across the film is given by the following equation:

$$R_i = K_i \Delta W_i \qquad (2.10)$$

Where W_i is the concentration difference at the two boundaries of the film and K_i, is represent the coefficient of the mass-transfer for the i^{th} species. K_i in equation (2.10) could be expressed as (D_i/δ), where δ is the thickness of the film.

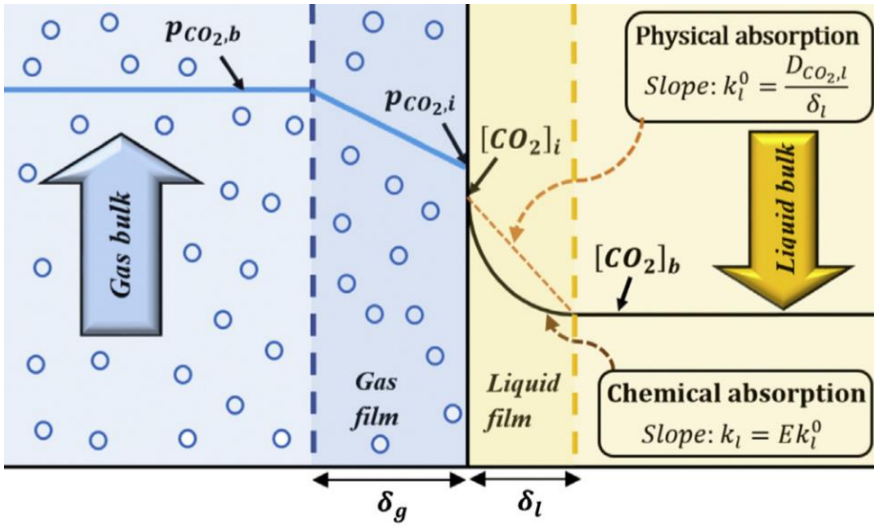

Figure 2- 11. A schematic sketch represents two films theory (Norouzbahari, et al., 2015)

The K_i values usually related to the fluid properties and hydrodynamic conditions, as well as the diffusion properties of the species during the reaction process. The film theory has some weakness according to Khan, (1990), which leads to erroneous prediction because the transport mechanism was unrealistic. He based his argument on the Danckwerts claim, which the substantial conditions for sustaining *stagnant layers* in *mixing* systems not actually occur.

2.8.2 Penetration theory

Generally the mass transfer from a gas phase to a liquid phase occurs through the interfacial area. The penetration theory by Higbie, (1935) is considered more realistic than film theory because it takes into account the transiemt mass transfer conditions. It does not state further assumptions in related to the depths of penetration of the different reacting species. So the main assumption focuses on the interface, which is always replaced via eddies. The transfer in region with eddies is controlled by unsteady-state molecular transfer. The penetration theory is considered more accurate in particular for the calculations of absorption and desorption rates especially when the reaction species possess dissimilar diffusivities as shown in figure (2.12)

The general form equations which govern the theory can be expressed as follows

$$\frac{\partial^2 W_i}{\partial x^2} - R_i^* = \frac{\partial W_i}{\partial t} \qquad i = 1, 2, \dots, n \qquad (2.11)$$

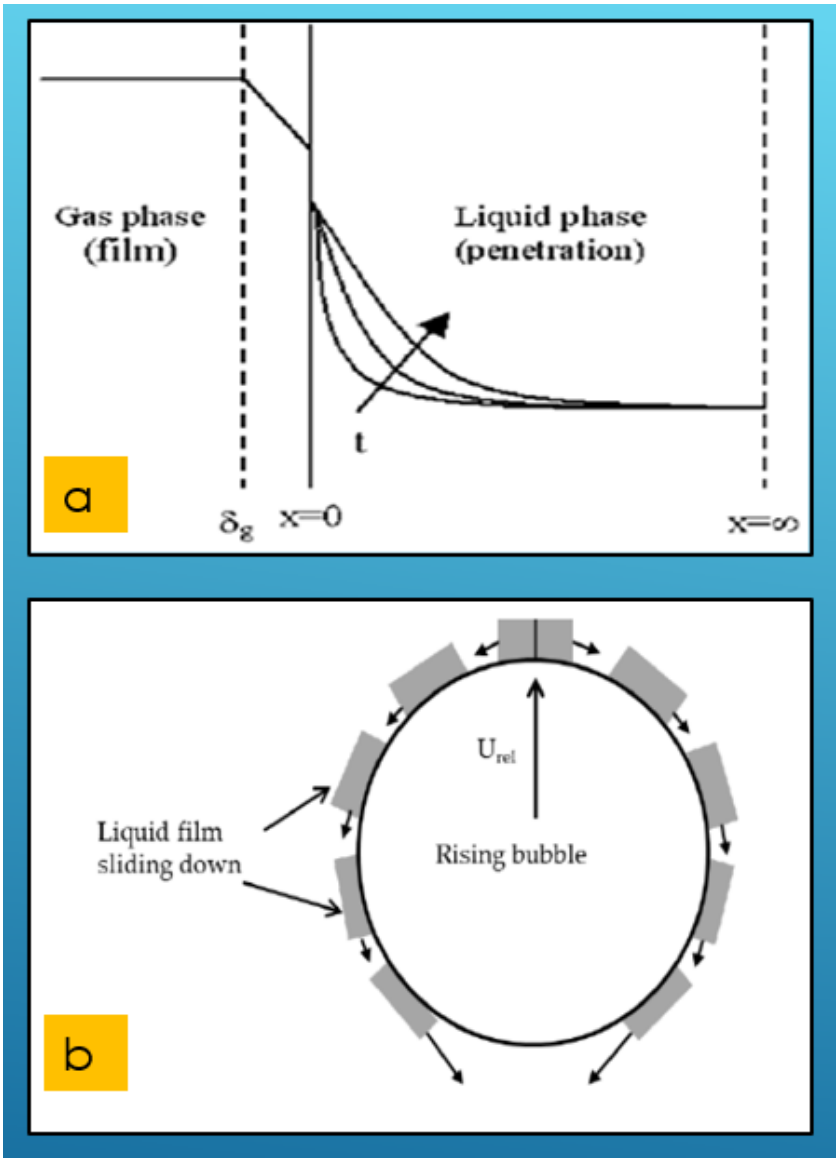

Figure 2- 12. The penetration theory (a) model for systems of the gas film to liquid bulk. (b) A schematic representation of the penetration theory

Penetration theory distinctly takes into account the influence of contact time between the two phases (gas-liquid) compared to the film theory, as shown in right hand side in equation (2.11). The purpose of applied the above theories is to find solutions for the following problems (Toor and Marchello, 1959):

i. The solid-fluid transfer, with turbulent flow.
ii. The fluid -fluid transfer, one of them is in a turbulent flow.
iii. The transfer between two fluids in specific column design such as packed tower

2.8.3 The surface renewal theory

Danckwerts explained why the assumption of a “stagnant film" should be abandon at the interface. He proposed instead another assumption, the surface renewal theory which based on mass-transfer across turbulent interfaces, so that surface are replaced continuously with a fresh layer of liquid (Danckwerts, 1951). Many surface renewal models were then developed to characterize mass-transfer gas-liquid (Perlmutter, 1969). Absorption into surface of the turbulent liquid usually happens when the motion of liquid is turbulent. One could imagine how turbulent manifest eddies a new fresh surface mixing material from the bulk of the liquid to the gas. This process of drifting and mixing of the liquid layers offers contact with the gas for different intervals of time. In general, surface renewal theory proved more practical and realistic to elucidate the phenomenon of the interface mass-transfer (Sarkar *et al.*, 2012). Due to internal circulation inside the liquid segments, intense inter-phase mixing becomes possible in addition to molecular diffusion. Hence, excellent mixing is accomplished in the liquid bulk, which imposes short residence time requirements. The small eddies (see figure 2.13) are more active in interphase transfer for the surface renewal (Liao and Lucas, 2018)

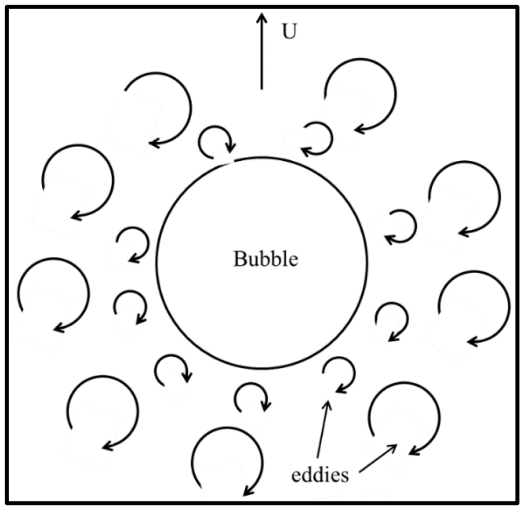

Figure 2- 13. Schematic representation of the surface renewal theory (Liao and Lucas, 2018).

In this study, the renewable surface theory more convenient appropriate to apply in case of very fine bubbles transfer than the film or penetration theories. This follows from the assumption that mass transfer is controlled by a bubble boundary layer that is turbulent. The bubble maintains in random boundary layers movement until reaching the surface of the liquid.

2.9 Reaction kinetics and reactor design

Multiphase reactions have received considerable attention in many industrial processes. Operations involving phase changes with chemical reactions require familiarity with other topics such as molecular diffusion, chemical reaction kinetics, and fluid mechanics, etc. The phase-related processes include gas-liquid operations such as chemical and petrochemical industries, wastewater and water treatment technologies, and food processing industries. These reactions occur between gas, liquid and solid phases. The most widely investigated class is the reactions of gas-liquid, and have received considerable attention (Danckwerts, 1970). However, the complex reactions occur by migration of substances to interfaces. In many cases the chemical affinity and physical factors affect the rate of mass transfer between phases as well as affect overall rate of reaction. Walas, (1989) determined that the physical factors can be outlined as follows:

i. Interfacial surface amount: its effect on the rate of mass transfer and rate of reaction, may be proportional under some conditions. The interfacial surface can be increased by different technologies depending on phases (grinding solids, dispersion of fluids…etc.).

ii. Diffusion rate of fluids to interfacial film and across it: several parameters influenced on diffusion rate such as relative velocity of two phases, pressure, temperature, physical properties of reactants and geometric design of the system

iii. Product diffusion rates outside of the reaction zone: which is related to reversible reaction, unless products concentrations are sufficient to influence the diffusivities of reactants.

Many chemical reactions processes must take into account the kinetics by two contributions: mass-transfer and chemical reaction rates. Sometimes one of the rates, mass or reaction, is much smaller than the other and it becomes the controlling step. Particularly, noteworthy is the creation of turbulence due to bubble mixing as this may control the amount of surface available for the reaction. It could be lead to eliminate bulk concentration gradients that might, on the other hand, hinder the boundary layer diffusion rate.

The dominant mechanism can be detected experimentally by determining the effects of operating conditions on certain changes. For instance, when an increase/decrease in temperature leads to an increase/decrease in the overall rate in accordance with the Arrhenius law (reaction rate constant assumed to be depends only on temperature), then the chemical rate

becomes the controlling step. While if the gas injection flowrate or amount interfacial surface fluctuated affecting the overall rate, correlate with the rate of mass transfer.

According to Metcalfe (2002), tubular reactors are utilized in many gases reactions for the large-scale in homogeneous or heterogeneous reactions. The design equation which is govern tubular reactor may be written:

For reactants: $r_A = -{dn_A}/{dV}$ or for products: $r_B = {dn_B}/{dV}$ (2.12)

Where r_A: is the reaction rate (moles of substance A disappeared / unit time * unit volume), and n_A, n_B: is the molar flow rate of component A and B (mol s^{-1}) respectively. In general, the reaction rate in tubular reactors are inversely proportional to the length of reactor or its volume. Therefore, as we pass along the length of the reactor (increase volume of reactor), the conversion of the reactants to products increases, but the reaction rate will decreased due to the concentration of reactants depleting.

The relationship between the tubular reactor volume and the conversion can be given by integration of the above design equation (2.12):

$$\int_0^V dV = -\int_{n_{A0}}^{n_A} \frac{dn_A}{r_A} \qquad (2.13)$$

The differential form for the conversion definition can be written in molar flow rate term:

$$dx_A = -\frac{dn_A}{n_{A0}} \qquad (2.14)$$

By gathering the equation 2.14 and equation 2.13 and perform the integration we get the relation which connect reactor volume and the conversion of the reactant:

$$V = \int_0^{x_A} \frac{n_{A0} dx_A}{-r_A} = n_{A0} \int_0^{x_A} \frac{dx_A}{-r_A} \qquad (2.15)$$

$$or\ V = F_{A_0} \int_0^{x_A} \frac{dx_A}{-r_A} \qquad (2.16)$$

Where F_{A0} is the molar flow rate mol/unit time.

This study will focus on the most important variables that influence the chemical reaction rate and mass transfer rate. In particular, variables are identified to determine the optimum conditions of the CO_2/aqueous ammonia reaction. The system will be built as shown in figure (2.14) to carry out gas-liquid reaction of the carbon dioxide /aqueous ammonia. The system include plasm generation (non-thermal plasma) as the activation mechanism for CO_2

molecules. The gas will be injected in the form of very small bubbles and combined with molecular excitation activation processes using non-thermal plasma. The hypothesis focuses on the combination of both two factors to improve the reaction process. Since multiphase reactions are usually limited by mass transfer and mixing, the large interface of the phases facilitates chemical reactions between the phases. That is the crucial role of very fine bubbles, while the non-thermal plasma role is excitation the (inert) CO_2 molecules energetic electrons and reactive species (Bogaerts *et al.*, 2015).

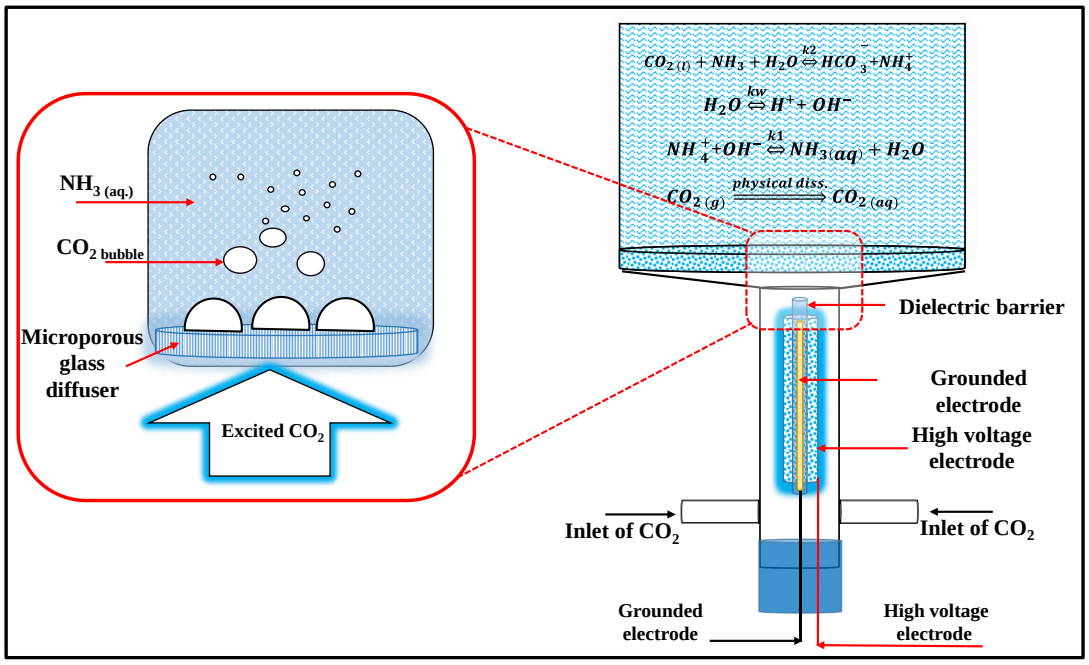

Figure 2- 14. A simple sketch for the CO_2/aqueous ammonia reaction system. The non-thermal plasma-activates CO_2 microbubble before the entry to the reactor.

2.10 Carbon dioxide gas dissociation using non-thermal plasma

Climate change is one of the most hazardous global risks that stresses the economy and threatens life. Thus there is an urgent need to reduce the average temperatures rise, widespread melting of snow and ice, and a rising global average sea level. Hence, it is incumbent on the researchers to find feasible technologies for utilizing CO_2 as a carbon source for the manufacture of fuels (Hayashi, *et al.*, 2006) and valuable chemicals (Xiang *et al.*, 2012). Only high volume products for which demand is not plastic can significantly impact CO_2 emissions levels by carbon capture and utilization. Traditional technologies of carbon dioxide utilization have many disadvantages because of their operating requirements such as high temperatures, high pressure, undesired products like, deposits of solid carbon and requirement of catalysts (Wang *et al.*, 1999). By non-thermal plasma, this objective could be achieved because it has many pertinent features, for example low temperature, low cost, no needed for catalysts, and

plasma creates species of high energy enhance reaction rate and able to initiate chemical process (Yap, *et al.*, 2015). Generally, the widely used common patterns of plasma which focus on CO_2 conversion are dielectric barrier discharges (Mei *et al.*, 2015), (Taylan and Berberoglu, 2013), gliding arc plasma(Indarto *et al.*, 2007), microwave plasma (Vesel *et al.*, 2011), microhollow cathode discharge (Taylan and Berberoglu, 2015), and plasma discharge within packed bed reactors (Butterworth, Elder and Allen, 2016). Fridman, (2008) reported that the highest energy efficiency (80-90 %) is achieved by non-thermal microwave discharges under moderate pressure and supersonic gas flow. It is important but, it is not easy to apply the above condition industrially, in most cases the energy efficiency is about 40% at atmospheric pressure and normal gas flowrate conditions (Bogaerts *et al.*, 2015). The energy efficiency of the process could be calculated by the relation ($\eta = \Delta H / E_{CO}$.) where, ΔH is the dissociation enthalpy (ΔH = 2.9 eV/mol.), and E_{CO} is the actual energy of one CO molecule produced in a plasma system.

Undoubtedly, non-thermal plasma has unique features to induce physical and chemical transformations at ambient temperatures, while the electrons temperature may be reach 1-10 eV (10000-100000 K) (Harling *et al.*, 2008). The high electron temperature has a key role in non-thermal plasma to create unusual chemical reactions. In general non-thermal plasma can be classified based on its generation process and it involves several types (Petitpas *et al.*, 2007);

i. **Glow discharge**: This type of plasma discharge is characterize by the following features; operate under low pressure (less than 1000 Pascal), flat electrodes commonly used, their electrons with high energy, used in fluorescent tubes as a result of their excited neutral species generate a high glow, not convenient for chemical synthesis because the low pressure requirements. However, Wang *et al.*, (1999) use this type of plasma to decompose CO_2, they had referred the maximum conversion and maximum efficiency were less than 14%, 16% respectively. The CO_2 decomposition with low energy efficiency (3.5%) in the existence of metal catalyst in fan-type AC glow discharge was performed. (Brock *et al.*, 1998).

ii. **Corona discharge**: it is characterized by non-homogeneous discharge, used different shapes of electrodes such as wire - plate, operates at atmospheric pressure and its requires a high electric field to ionize the neutral molecules. Wen and Jiang, (2001) studied the combine the pulsed corona discharge in a packed reactor with porous γ-Al_2O_3 pellets, their results were CO_2 conversion, CO yields 23 and 15% respectively.

iii. **Dielectric barrier discharge**: it has large volume excitation of the glow discharge, high-pressure characteristics of discharge, at least one of electrodes covered with dielectric material, the current pulse duration relates to properties of gases, the dielectric material used, and the pressure. The most important reactor investigated for the conversion (Bogaerts *et al.*, 2015a), splitting (Aerts, *et al.*, 2012; Kozák and Bogaerts, 2014; Aerts, *et al.*, 2015), decomposition in packed bed (Butterworth, *et al.*, 2016) or modelling (De Bie *et al.*, 2011) the plasma chemistry of the carbon dioxide. This type of discharge is gaining more attention due to its advantageous characteristics, so it adopted in this study.

iv. **Microwave discharge**: it can be used in a broad pressure domain and runs with very high frequencies for instance in the range of microwaves 2.45 GHz, so in this oscillations of the electric field, only light electrons can operate. Thus, the discharge is far away from thermodynamic equilibrium. Microwave plasma used to dissociate carbon dioxide molecules with power range of 200 to 1200 W, the dissociation fraction reached 13% at pressure of 20 Pa. (Vesel *et al.*, 2011).

v. **Gliding arc discharge**: it is a collection of non-thermal plasmas of preferable selectivity and discharge of high power equilibrium arc, reported to be used in field of reforming application. The Gliding arc plasma has a high selectivity, energy efficiency and specific productivity, which applied a wide range of chemical industries. The CO_2 dissociation by gliding arc plasma was performed under a condition of supersonic flow and 4000 K which provide a selectivity up to 90% from the total discharge power in carbon monoxide (Fridman *et al.*, 1999). While under conditions of adding N_2, O_2, H_2O, and air, the conversion was 18% at total gas flow rate 0.8 l/min.(Indarto *et al.*, 2007).

One of the main CO_2 dissociation mechanisms is the electron-impact dissociation as equation (2.16), as well as attachment reactions, and the dissociative ionization (Kozák and Bogaerts, 2014). However, CO_2 dissociation is mainly occurred by electrons impact reactions and the electron impact ionization.

$$CO_2 + e^- \rightarrow CO + O + e^- \qquad (2.16)$$

The conversion of CO_2 increases at rising input energy, which is logically correct, as a result of the electron energy is enhanced. The energetic electrons undoubtedly have an effect to activate the CO_2 dissociation. Increasing the electron energy amount is gained through increases the applied electric field on a constant flow rate of gas or through decrease the gas flow rate at constant electric field power. On the other hand, to reveal the fundamental reaction

paths of stimulating CO_2 molecules by plasmas, the whole chemical thermodynamics of carbon dioxide dissociation should be reviewed. Indeed, the CO_2 dissociation chemistry is complicated, especially when taking into account the various plasma dynamics. The reaction is actually a two-step process that start with breaking down carbon dioxide to carbon monoxide and atomic oxygen:

$$CO_2 \rightarrow CO + O \qquad \Delta H = 5.5\ \text{eV/mol.} \qquad (2.17)$$

The oxygen atom (O) reacts with other oxygen atoms or CO_2 to form O_2

$$2O \rightarrow O_2 \qquad \Delta H = -5.16\ \text{eV/mol.} \qquad (2.18)$$

$$O + CO_2 \rightarrow O_2 + CO \qquad \Delta H = 0.34\ \text{eV} \qquad (2.19)$$

The full reaction contains CO and O_2 as the main products of dissociation in the plasma system:

$$CO_2 \rightarrow \frac{1}{2}O_2 + CO \qquad \Delta H \sim 283.3\ \text{kJ/mol.} = 2.94\ \text{eV} \qquad (2-20)$$

The producing of carbon monoxide from CO_2 decomposition using non-thermal plasma has gained a lot of interest due to the difficulties facing this reaction at ambient temperature through conventional methods. However, the main challenge is how to overcome the highly stable state of the carbon dioxide molecules, and the high energy requirements provide for breaking the OC=O bonds to execute the dissociation process as shown in equations(2.17). The second reason could be the low conversion of the dissociation process and low power plant efficiency to 34% (Wang *et al.*, 1999). That also could be attributed to the largest fraction of ions recombining to form CO_2 (Bogaerts *et al.*, 2015). Thus, high consumption of energy is required for endothermic CO_2 conversions occur (Hu, *et al.*, 2013). In addition to this, most modeling studies of CO_2 focus on the dissociation state as mentioned above. Eventually, this study will concentrate on the vibrational excitation of CO_2 molecules to increase their energy, and investigate the plasma effect on the reaction process. This task will be discussed in more details in chapter four. The crucial task is to find more efficient methods of carbon dioxide conversion into valuable chemicals. As a consequence of all these factors, we posit it as the main objective of this study.

2.11 Absorption of CO_2 in hydroxide solutions

Environment pollution reduction through the absorption process of the CO_2 into aqueous alkaline solutions has acquired important significant in two directions. Firstly, in research, such

as Danckwerts' method, which is related to the equilibrium measurements at the interfacial boundary. Secondly, in industry, such as the purification of gas streams in the chemical and petrochemical industries (Pohorecki and Moniuk, 1988). On the other hand, the aqueous waste streams for some chemical industries often comprise weak electrolytes of ammonia or the ammonia gas emission from the landfills. These solutes should be treated. The distillation process as a traditional method is usually used. (Kawazuishi and Prausnitz, 1987). The chemical absorption of CO_2 by alkaline liquids and the separation process by distillation requires high energy input and solvent consumption. However, the absorption rate of CO_2 into several aqueous solutions of potassium hydroxide, sodium hydroxide, and lithium hydroxide is well studied by many investigators (Gondal *et al.*, 2015). The results of the studies of aqueous electrolyte solution containing Li^+, Na^+, and K^+ of (0.01–2.0 Kmol. /m^3) at a temperature range of 25 to 64 °C show the reaction to be pseudo-first-order. The reaction rate constant dependence on the concentration strength and temperature, for the CO_2 reaction with hydroxyl ions is verified. But in general, the experimental data indicates that the loading change of CO_2 is limited. Nevertheless, studies persisted; for instance, a spray dryer techniques absorb CO_2 into NaOH (Tavan and Hosseini, 2017). While some studies focused on the simulation of the reactive mass transfer during the absorption (Krauß and Rzehak, 2018), absorption in carbonate/bicarbonate at elevated pressure (Cents, *et al.*, 2005) or to calculate absorption rates (Bontozoglou and Karabelas, 1993) .

Much of the CO_2 chemical removal research has focused on identifying and evaluating processes using monoethanolamine (MEA). It has been successfully used in chemical plants for carbon dioxide recovery. What we know about the MEA process is a promising system for the control of CO_2 emissions, but unfortunately, it is an expensive option (Chakma, 1995). The performance of the MEA as a solvent has considerable problems in terms of CO_2 absorption capacity (Bai and Yeh, 1997) removal efficiency (Yeh and Bia, 1999), and volatility. In order to improve the above weak points, various studies suggested the requirement to find a new solvent with properties of high efficiency, removal capacity, and low operation costs (Niu *et al.*, 2013).

2.12 Absorption of CO_2 in aqueous ammonia

Inorganic chemical compounds such as sodium or potassium carbonate and aqueous ammonia as alternative system have been proposed to absorb CO_2 (Cullinane and Rochelle, 2005). Some publications that concentrate on using aqueous ammonia as a solvent to reduce CO_2 emissions

from the power generation plants, have gained sensational attention. The aqueous ammonia/ carbon dioxide system possesses unique merits such as; lower material costs, a high loading capacity of CO_2, and no problems of the solvent degradation. As Mani *et al.*, (2006) state the speciation of the products of the $CO_2/NH_{3\ (aq.)}$ system is driver of "paramount importance to optimize the process in term of loading capacity, reaction temperature, and the ammonia concentration ". The nature of the products are usually a soluble chemical in reaction media such as ammonium carbonate, bicarbonate, and carbamate as following reactions occur in the system of CO_2-NH_3-H_2O:

$$NH_3 + H_2O \leftrightarrow NH_4^+ + OH^- \quad (2.21)$$

$$CO_2 + 2H_2O \leftrightarrow HCO_3^- + H^+ \quad (2.22)$$

$$NH_{3\ (aq,)} + HCO_3^- \leftrightarrow H_2O + NH_2COO^- \quad (2.23)$$

$$HCO_3^- \leftrightarrow CO_3^- + H^+ \quad (2.24)$$

The CO_2/ $NH_{3\ aq.}$ reactions are exothermic, so the temperature of the reaction medium increases with increasing the concentration of aqueous ammonia. A detailed analysis of equilibria in a NH_3-CO_2-H_2O system is discussed in (Edwards *et al.*, 1978). They present an appropriate method from a thermodynamically view to calculate the equilibria compositions of liquid /vapor system at various temperatures and concentrations. Bai and Yeh, (1997) carried out a number of investigations into the removal of flue-gas by ammonia scrubbing. The overall efficiency of the process was about 95% and the absorption capacity of ammonia was 0.9 kg of carbon dioxide /kg ammonia. The same authors in 1999 performed another study in this field, a comparison between MEA and ammonia solvents to absorb CO_2 (Yeh and Bia, 1999). The results illustrate that removal efficiency for CO_2 via NH_3 and MEA are 99% and 94% respectively, while the absorption capacities for the two solvents were 1 and 0.4 kg CO_2/kg of the solvent respectively. In the experimental results, they mentioned white crystalline ammonium bicarbonate could be precipitated, forming a visible plume in the flue gas. In general, the processes of regeneration of ammonia through heating the aqueous solutions to recycle of NH_3 from the absorbed CO_2 gas is considered a high energy consumption process. So in this piece of work, we will propose producing ammonium bicarbonate as a main product from a $CO_2/NH_{3\ aq.}$ reaction to avoid more energy consumption.

2.13 Identification methods of the reaction process output

2.13.1 The detection in aqueous solutions

The characterization of the salts as expected mixture which may be formed from CO_2 /$NH_{3\,(aq.)}$ reaction such as ammonium carbonate, bicarbonate, and carbamate is an important part of this study. Many investigation focus on the analysis methods of the CO_2/aqueous ammonia reaction system. Wen and Booker (1995) applied Raman spectroscopy to analyse the aqueous solutions for the above three compounds. The study shows the presence of the three compounds in the region of 850 to 1100 cm^{-1}. This indicates that intermediate compounds such as carbonic acid or carbamic acid are formed, but are unstable, due to a decomposition for these compounds into carbon dioxide and ammonia may occur. Development of an analysis method for the CO_2-NH_3-H_2O equilibrium system using Raman spectroscopy is reported by (Halstensen *et al.*, 2017). They offered a novel approach to provide rapid and reliable inferences of the carbonate, bicarbonate, and carbamate content in the above system. By using Infrared spectra to identify carbamate and bicarbonate frequencies, (Gal'perin and Finkel'shtein, 1972) found the wavelength of the ammonium bicarbonate is 1620 to 1300 cm^{-1}, while 1120 and 3420-3450 cm^{-1} for ammonium carbamate, also they expected the characteristic band 860-890 cm^{-1} for the ammonium carbonate.

On the other hand, Carbon-13 nuclear magnetic resonance (^{13}C NMR) spectroscopy used as a simple and reliable method to evaluate the reaction products for CO_2 /$NH_{3\,(aq.)}$, i.e. the three ammonium salts (carbonate, bicarbonate, and carbamate) (Mani, *et al.*, 2006). The carbamate ion signal at 166 ppm is attributed, while the carbon atoms of the CO_3^{-2} and HCO_3^{-1} ions attribute at lower frequencies of $165.23 \leq \delta \leq 161.5$ ppm.

2.13.2 Determination method of kinetic parameters

The decomposition of the solid-state salts of ammonium (carbonate, bicarbonate, and carbamate) confers interesting data to investigate reaction compounds and the nature of the reaction products. Thermogravimetric analysis (TGA) is a common technique used to characterize the decomposition reaction behavior. The decomposition reactions of the three compounds can be studied by either isothermal or non-isothermal kinetic experiments. The isothermal process includes the change of mass of the sample with time at a constant temperature. In contrast, the sample heating at a constant heating rate i.e., linearly with time, allows the observation of the change of mass with time, and temperature, i.e., by the non-

isothermal process (Hillier, *et al.*, 2010). Most kinetic methods use the rate of thermal conversion as a function of the temperature and the extent of conversion by the reaction:

$$\frac{d\alpha}{dt} = k(T)f(\alpha) \qquad (2.25)$$

Where dα/dt is rate of conversion, k (T) is the term represents the reliance of the process rate on temperature expressed by rate constant (*k*), and *f* (α) is the dependence of the process conversion on the reaction formula (Vyazovkin *et al.*, 2011). The rate constant depends on the temperature as illustrated by Arrhenius equation:

$$k(T) = A\exp(\frac{-E}{RT}) \qquad (2.26)$$

Where *A* is the pre-exponential factor, *E* is the activation energy, and *R* is the universal gas constant. The TGA curve generated using mass (or conversion) versus time to determine the activation energy, pre-exponential factor, and reaction order. The decomposition reaction of the ammonium bicarbonate, carbonate, and carbamate are:

$$NH_4HCO_3 \rightarrow NH_{3\,(g)} + H_2O_{(g)} + CO_{2\,(g)} \qquad (2.27)$$

$$(NH_4)_2CO_3 \rightarrow 2NH_{3\,(g)} + H_2O_{(g)} + CO_{2\,(g)} \qquad (2.28)$$

$$NH_4COONH_2 \rightarrow 2NH_{3\,(g)} + CO_{2\,(g)} \qquad (2.29)$$

Both carbonate and bicarbonate release water. The carbonate and carbamate are similar in releasing two molecules of ammonia when heated. Fulks *et al.*, (2009) reported that the ammonium carbamate could be decomposes in two steps. The first releases one molecule of ammonia while forming carbamic acid (unstable intermediate compound).

$$NH_4COONH_2 \rightarrow NH_{3\,(g)} + HCOONH_2 \qquad (2.30)$$

$$HCOONH_2 \rightarrow NH_{3\,(g)} + CO_{2\,(g)} \qquad (2.31)$$

In general, according to the study requirement and in order to cover the reaction process; the reactant materials, the products, and reaction conditions, the following questions should be taken into account through the research:

- What is the influence of changing the non-thermal process conditions (heating rate) on the kinetic parameters, in particular the activation energy?

- Are the kinetic parameters remain unchanged? as reported by (Popescu and Segal, 1994). Or it matched with the conclusions of Vyazovkin, (2000) of acceptance of the concept of variable activation energy, which is more consistent with the concept of the multiple-step nature (Vyazovkin *et al.*, 2011) of the solid-state reactions .

In addition, the need to find a method to estimate the unknown quantities of components in the solid-state samples compels using the pseudo-inverse method (PIM). PIM is widely applied because it allows a brief-expression for linear mathematical systems in an n-dimensional space (Stewart, 1977). For more details and discussion see chapter five. However, the studying of the (solid-state) products of the reaction $CO_2/NH_{3\ (aq.)}$ can provide an increased understanding of the reaction mechanisms. Finally, one task of this study motivates the analysis research of sensors in the field of solid-state chemistry to estimate the unknown quantities of the components in a sample using PIM.

2.14 Conclusion

The absorption of gases in aqueous solutions in particular, when synchronized with the chemical reaction process, is a common and significant aspect of chemical engineering. Many studies have been done as a theoretical simulation or experimental work mainly by chemist and chemical engineers. One of the most important industrial applications for this branch of science is CO_2 emissions treatment and other toxic gases. The treatment of CO_2 emissions takes many paths depending on the chemical and physical absorption methods, biological fixation, or conversion processes (methane or syngas). Generally, it can be noticed that CO_2 dissociation by various plasmas types has been growing in the recent years experimentally and theoretically. At the same time, the chemical capturing of CO_2 by scrubbing with amines has gained some attention.

However, the two lines have drawbacks, including low energy efficiency and low conversion efficiency. The dissociation in presence of plasmas for CO yield only removes to 0.1 kg of CO_2 per kW. h. of the applied power (Brock *et al.*, 1998). While the second path of (monoethanolamine) CO_2 capture suffer several problems, like the high cost, low loading capacity, corrosion problems for the technical equipment, and the regeneration cycles.

A new path suggested by this study is based on the non-thermal plasma role to increase the electronic excitation of CO_2 molecules, not dissociation. The non-thermal plasma combines with injection the gas as very small bubbles to increase the surface area of mass transfer. These two technologies promise to enhance the reaction process between the “plasma activated” CO_2

and aqueous ammonia to produce the ammonium bicarbonate. Therefore, likely with the low activation energy of the plasma excitation, and the staging of the reaction at or near very fine bubbles interfaces has a catalytic effect.

Before the reaction process is performed, a simulation study using multiphysics software COMSOL for the CO_2 reactions in a plasma is conducted. It can provide more insights to understand CO_2 plasma chemistry in particular the vibrational excitation state. In addition, a characterization study for the reaction products is essential to determine the kinetic parameters. Therefore the need to find a new method to estimate the amount (mass fraction) in an unknown sample, by thermogravimetric analysis (TGA) data using the pseudo-inverse method (PIM) will be discussed. So in this piece of work, we will propose a novel path to proceed the $CO_2/NH_{3\ aq.}$ reaction, to produce a pure ammonium bicarbonate and avoid more energy consumption.

Department of Chemical and Biological Engineering

Chapter Three

Materials and Methodology

Chapter Three

Materials and Methodology

3.1 Introduction

The materials and methods, which are used to carry out the experimental work of this study are presented and explained in this chapter. The chemicals, equipment, and sensors which are used in recording data are described. In general the plasma reactor is addressed in more details as it is the heart of the process. The design of electrodes, manufacture material selection, and assembly protocol to evaluate the study objectives are highlighted. Box-Wilson factorial experimental design is used to determine the effects of operating parameters on the electrical conductivity of CO_2 / $NH_{3\,(aq.)}$ reaction and on the quantity of precipitated solid (yield). Finally, analytical equipment and their accessories are illustrated, with the protocols for their application to this project described.

3.2 Chemicals

The chemicals are used analytical grade. The main substances are carbon dioxide gas, ammonium hydroxide, ammonium carbamate, ammonium bicarbonate, Ammonium carbonate, and deionized water. All the chemicals which are used in this study are explained and their specification are determined in appendix (A1).

3.3 Experimental Apparatuses:

In this section, the equipment and the instruments which are used in this study will addressed to facilitate the reaction of CO_2 with aqueous ammonia solution in presence a non-thermal plasma. The main devices and tools are summarized in table (3.1). More details will be given in next sections. In general, the framework of the reaction system can be divided into two parts. Firstly, the non-thermal plasma generation zone, where the carbon dioxide molecules are excited under the influence of high voltage. Secondly the chemical reaction between the absorbed CO_2 molecules (excited) with the aqueous ammonia solution, as shown in a simple flow diagram in the figure 1.

In addition to the chemical reaction, there are other steps which require specific devices and instruments. These apparata are used to provide either an ability to control the process conditions or to measure values for the desired parameters.

Table 3. 1 shows the main devices and tools which are used in the process.

no.	*Item*	*The purpose and specification*
1	Cylinder of carbon dioxide	It is provided with a pressure of 50 bar
2	Pressure regulator on-line for CO_2 gas system	It used to preserve the pressure at 2 bar, a ball valve was used for safety protection
3	Carbon dioxide flowmeter	It is supplied from *PLATON* Company with range 0.1 to1.0 litter per minute.
4	Pressure regulator on-line for air system	To preserve the pressure at 2 bar, as well as a ball valve was used for safety protection
5	Air flowmeter	MR3000 Key Instruments with flow scales in litter per minute air, the range (1_5)
6	High voltage power source	A custom made high voltage power supply (48V DC-AC-Generator 50 kHz 500W - Germany)
7	Digital oscilloscope	PicoScope 5242A 60 MHz 2 channel, used to measure the high voltage
8	Plasma generator	Glass cylindrical shell supplied with two electrodes separated with a dielectric barrier of a quartz glass (to generate the non-thermal plasma).
9	Chemical Reactor	A cylindrical glass vessel. A Diffuser of a glass inserted in the reactor to generate a bubbles of carbon dioxide.
10	The Arduino circuit	Arduino board is a device which allows to build an electrical circuit interact with sensors and controllers.
11	Temperature sensor	K-type thermocouples from RS Components are used. Infrared thermometer also used for checking.
12	The pH probe	A pH electrode with BNC connector from VWR. Connected to Arduino circuit
13	Electrical conductivity	A bench meter Model 4510 Conductivity/TDS.

3.3.1 Plasma generation equipment:

a. High voltage power source: A custom made high voltage power supply (48V DC-AC-Generator 50 kHz 500W - Germany) was used. The power supply works from 48VDC, delivered by a Switching power supply, Type Meanwell SP500-48. The power source has been designed to supply high voltage up to 4 kV with a frequency 50 kHz as shown in figure (3.2). The device is provided with a manual control of voltage and current with separated unite as a transformer. Values of both voltage and current are displayed using a digital oscilloscope.

b. Digital oscilloscope**:** (PicoScope 5242A 60 MHz 2 channel), PC connectivity: USB 2.0 hi-speed, Software/PC requirements Windows 10.The high voltage supplied at the load is measured using a high voltage probe (Testec, HVP-15HF) the maximum working high voltage is 10 kV. The ground voltage at the load was measured by TA008 60 MHz with attenuation ratio 10X PicoScope probe. The maximum working voltage 600 V peak to peak. The connection circuit as shown in figure (3.3).

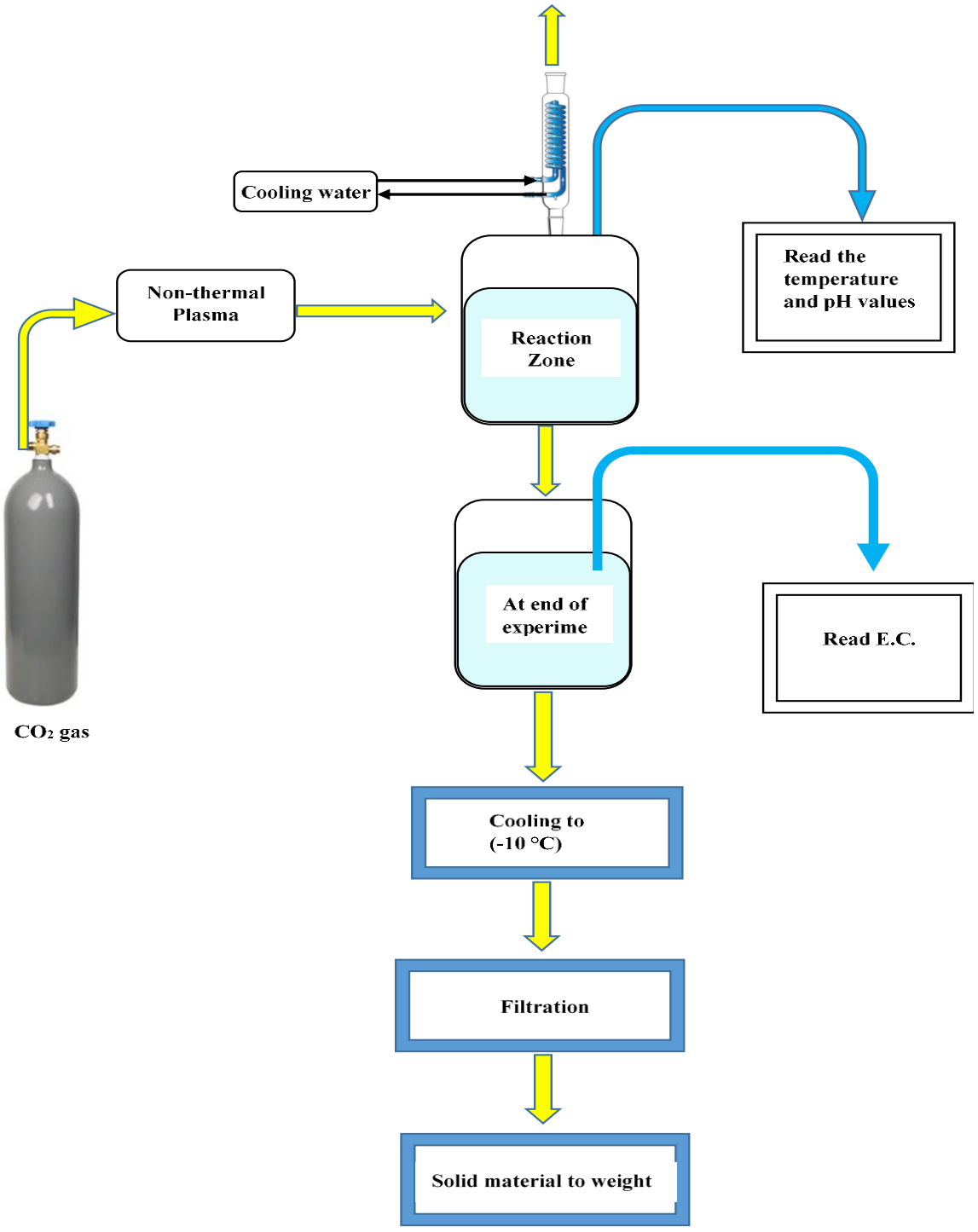

Figure 3- 1. A simple flow diagram for the reaction system of CO_2 with aqueous ammonia, which is divided into two parts: (1) the non-thermal plasma generation zone, (2) the absorbed CO_2 molecules (excited) reacted with the aqueous ammonia solution, after that a set of steps are conducted such as electrical conductivity measuring, cooling the solution, the separation by filtration and finally the weight of the precipitate solid.

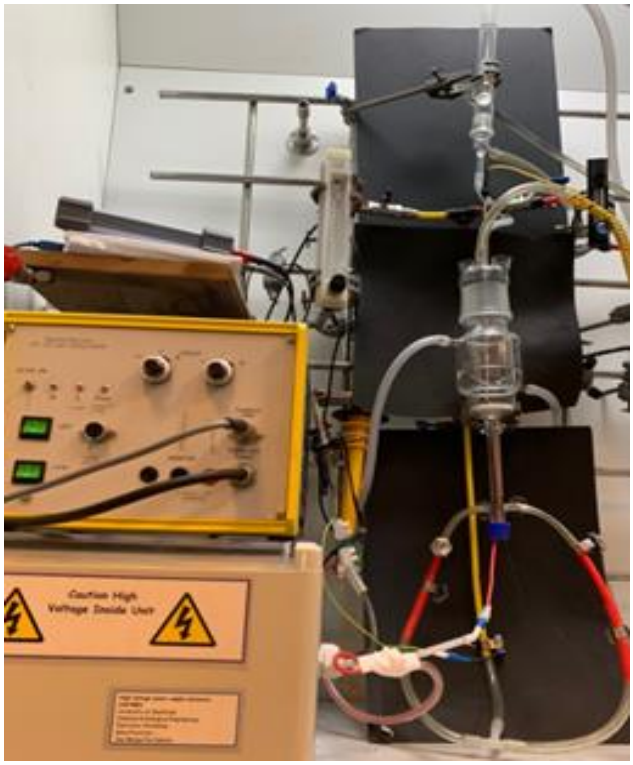

Figure 3- 2 the power supply 48V DC-AC-Generator 50 kHz 500W – Germany.

c. Ceramic Disc capacitor: the charge-voltage characteristic can be registered alternatively using a capacitance C (C10 nano-Farad) by means of an oscilloscope with maximum working voltage 3kV.

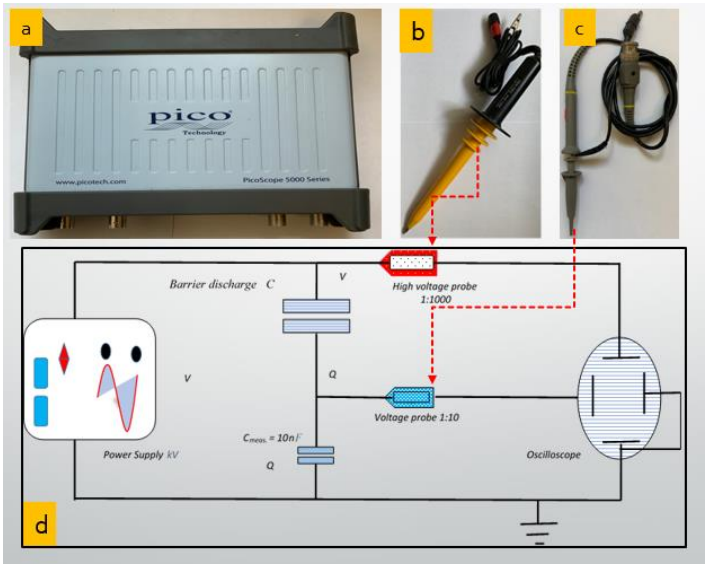

Figure 3- 3. the PicoScope (a) 5242A 60 MHz 2 channel with two voltage probe sensors (b & c) are connected with an oscilloscope, which is connected with PC by a USP cable, to measure the voltage. In bottom of the sketch the electrical connection circuit (d) of the plasma generation system (Wagner, 2003).

3.3.2 Non-thermal plasma generator

Some preliminary experiments are carried out prior to start design of the plasma generator. A rectangular reactor fitted with a flat plate of aluminium foils as electrodes separated by a thin (1mm) glass sheet tested, as shown in figure 3.4. The design is suitable for ozone generation, then inject the ionized gas for treating the water slightly under the surface.

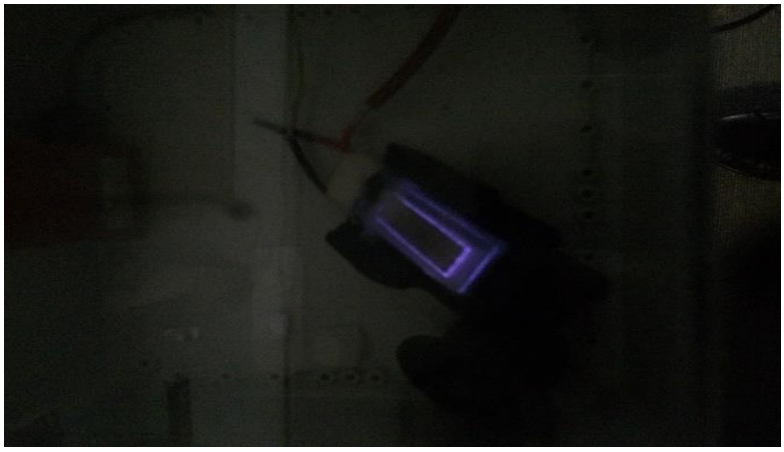

Figure 3- 4 A preliminary experiments using ozone generator, which is consist from an electrodes of aluminium foils.

The design has many problems if used in CO_2 /$NH_{3\,(aq.)}$ system, especially when desired to tight the reactor directly with the plasma generators. Problems to overcome include: (i) such a long distance between plasma generator and reactor, the differences in dimensions between the plasma generator (rectangular) reactor (tubular) while, (ii) the electrical terminals connections (sparks lead to damage the aluminium foils). So we must find another system design to solve these points. The material used in fabricating the reactor was a thin Perspex sheets, and that could be undesired if there is (moderate) heat in the system. Therefore, the glass was the best choice for the laboratory experimental system.

The copper metal has distinct electrical mechanical properties and has been recommended by many of researcher to use it as electrodes. On the other hand, the tubular shape is more flexible and easily in tighten and screwing to prevent the gas leakage. The gap distance between the electrodes can be controlled depending on the barrier thickness which is selected.

Dielectric barrier discharge (DBD) plasma reactor was designed and fabricated with cooperation of glass workshop and mechanical and electronic workshop in the University of Sheffield. The plasma generator consists from the following parts as (figure 3.5):

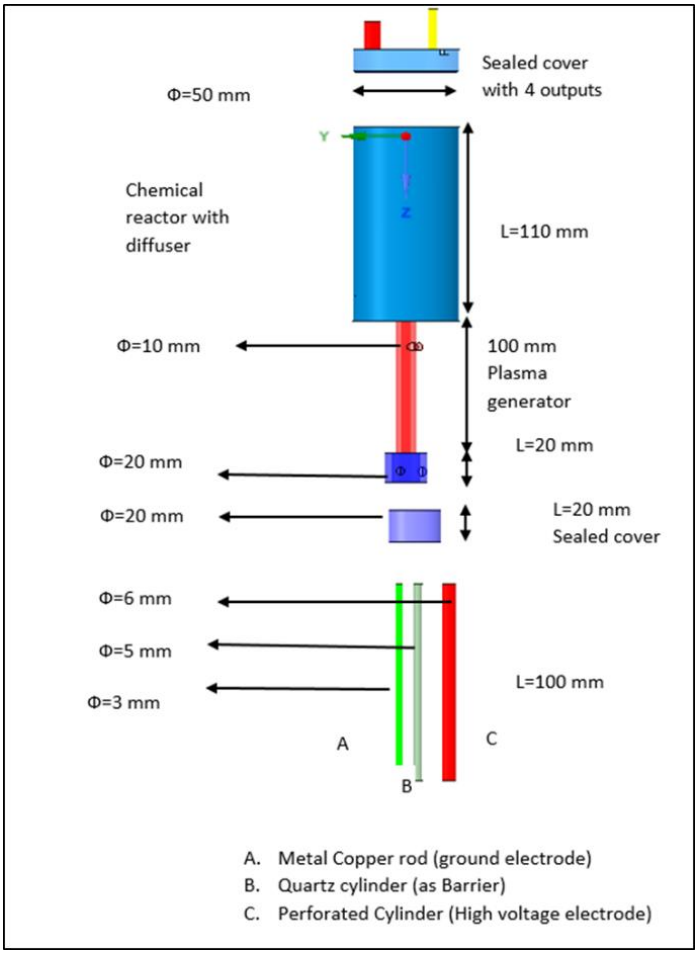

Figure 3- 5 Sketch of reactor and the shell of plasma generator, the dimension of both reactor vessel, plasma shell tube, the ground electrode, the quartz barrier cylinder, and the high voltage electrode are shown.

Glass cylindrical shell: The glass tube works as a gas flow channel where the CO_2 is ionized before contacting and reaction process with aqueous ammonia. This shell is contained the electrodes unit, which is fixed on the sealed cover at the lower tube end, where the wires of the high voltage electrode and the ground electrode are passed across the cover. The glass tube of plasma generation has a dimensions; **140 mm** length, **10 mm** inside diameter provided with four apertures on sides of the shell, two at bottom used for feeding carbon dioxide gas while the upper could be used to measure the temperature and pressure inside the plasma generator. The base of cylinder shell was designed to permits introduce the electrodes units with sealed cover. The upper part of cylindrical shell (plasma generator) was welded with the lower part of the reactor vessel.

The electrodes of plasma generation: which are consists from the following parts as illustrated in figure (3.6):

a- A high voltage electrode; a cylindrical shape with dimensions; **5 mm** inside diameter and 10 mm length. The electrode made of pure copper perforated with a mesh **1 mm**; thickness **2 mm**; round holes **3.5 mm** pitch.

b- Dielectric barrier; a quartz glass with cylinder shape has a dimensions **100 mm** length and inside diameter **4 mm** (**0.5 mm** thickness).

c- Ground electrode: a brass rod **3 mm** diameter and **100 mm** length

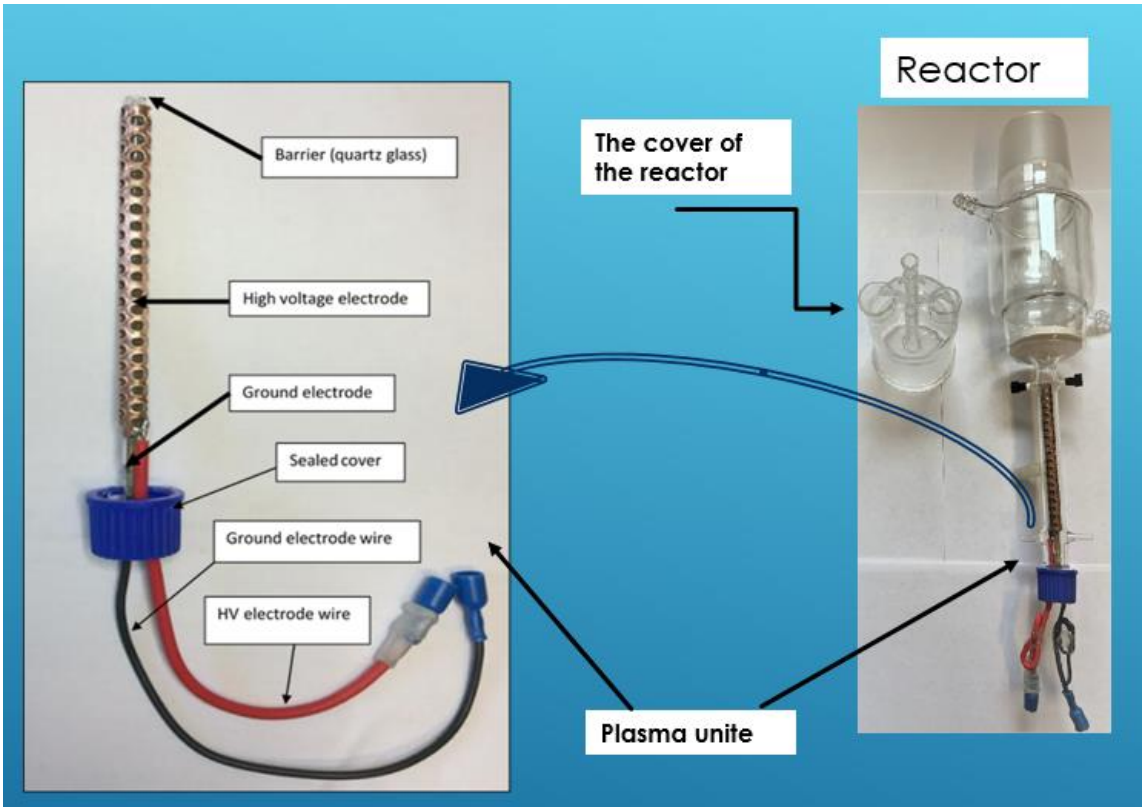

Figure 3- 6. Electrodes arrangement of the dielectric barrier discharge (DBD) set-up to generate the non-thermal plasma.

3.3.3 The chemical reactions zone:

Chemical Reactor: a cylindrical glass vessel has a 100 mm length and 50 mm inside diameter. The reactor was provided with a lid (quick fit cover 55/44) contained four orifices to insert thermocouple and pH probe while the other used as a vent and returning of the condensate. The lower part of the reactor was welded with vessel cylindrical shell (plasma generator) as shown in figure (3.7). The lid and the reactor overlap together by height of 4 cm. The reactor provided with a jacket for cooling or heating, but we did not use cooling system in this study, maybe we recommend to did it by separated work in the future.

Diffuser: a glass disc of *a grade 4* was used to generate a very fine bubbles of carbon dioxide gas on its surface. Its dimensions was 4.5 mm thickness (S) ±1mm and with a diameter (B) 50 mm. Its porosity number 4 and pore diameter is 10-16 micrometres as shown in figure (3.7, b).

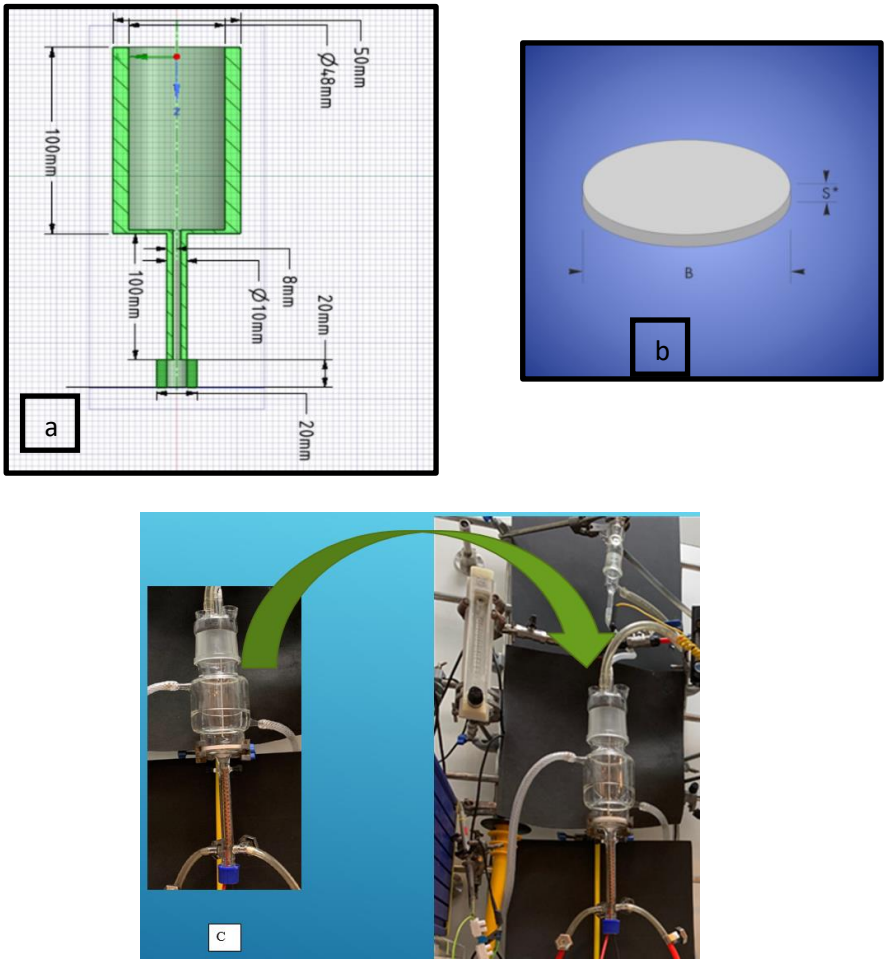

Figure 3- 7. (a) reactor and the shell of plasma generator dimensions, (b) diffuser which inserted in the reactor to form the babble at the surface, with thickness S = 4.5 mm (±1 mm), and the diameter B =50 mm. (c) the position of the reactor in the whole system.

The volume of the aqueous ammonia solution used is **150 cm^3** for each experiment, while the total reactor volume was about 220 cm^3 measured from the upper diffuser surface to upper point near the lid. So the head volume before bubbling is 63 cm3 (28% of the total volume of the reactor). Hence, the phase ratio (head volume to the liquid volume) is 42%. The head volume is necessary due to the gas hold-up in liquid phase lead to increase the liquid height may be more than 15 %. In addition, foam formation occasionally occurs when a high flow rate is used, in particular at the end of experiment, which can fill most of the head volume.

3.4 Measuring devices and sensors:

3.4.1 The Arduino circuit:

The Arduino board is a device which allows the building of electrical devices which interact with the tangible things through sensing and controlling. The temperature sensor and pH probe are constructed which to incorporate a cost-effective, single-board microcontroller, Arduino board as presented in figure (3.8). The Arduino Data interface is shown in the appendix (A2)

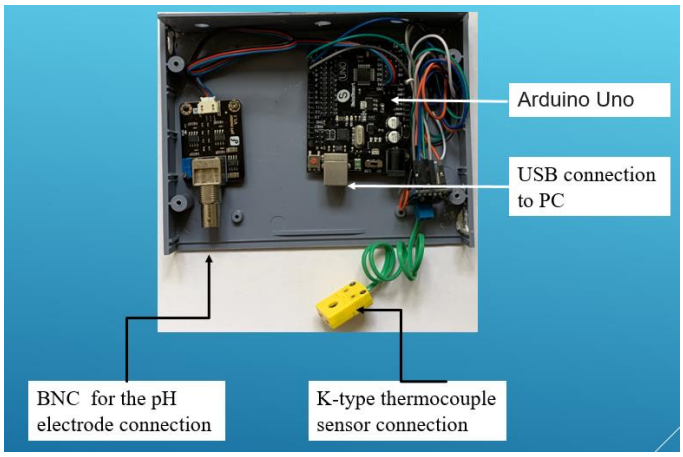

Figure 3- 8 . Arduino circuit for measuring the pH value and the temperature.

3.4.1 Temperature sensor (thermocouples) and thermometer:

K-type thermocouples from RS Components (figure 3.9 in left side) are used which have an operating range of -50 °C to 750 °C. Connected to Arduino circuit. The infrared thermometer also used for checking. It has a temperature range of -50 to 350 °C and accuracy ±1.5 °C.

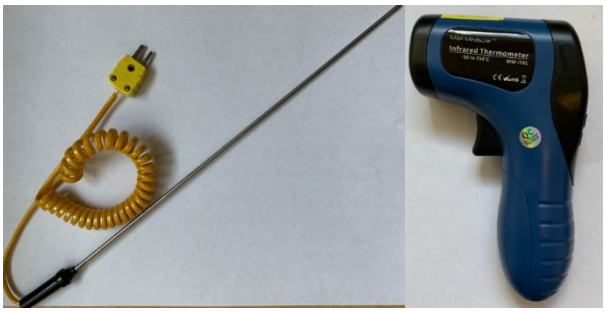

Figure 3- 9 .Temperature sensor (thermocouples) in left-side, and infrared thermometer in right-side.

3.4.2 Weight Scale

The Fisherbrand analytical balance has a capacity 210 g. and readability precision of 0.1mg, is used to weight the solid samples which precipitate from the chemical reaction process.

3.4.3 The pH probe

The pH of the solution is directly measured using pH probe/electrodes with BNC connector from VWR pHenomenal® 111. It is supplied, tested, and ready for use as shown in figure (3.10). The characteristic data show that the offset voltage at zero point pH 7 (25 °C) is less than 20 mV and the electrode slope is larger than 95% of the theoretical value. The calibration curve as shown in figure (3. 11).

Figure 3- 10. The electrode pH meter with BNC connector from VWR pHenomenal® 111.

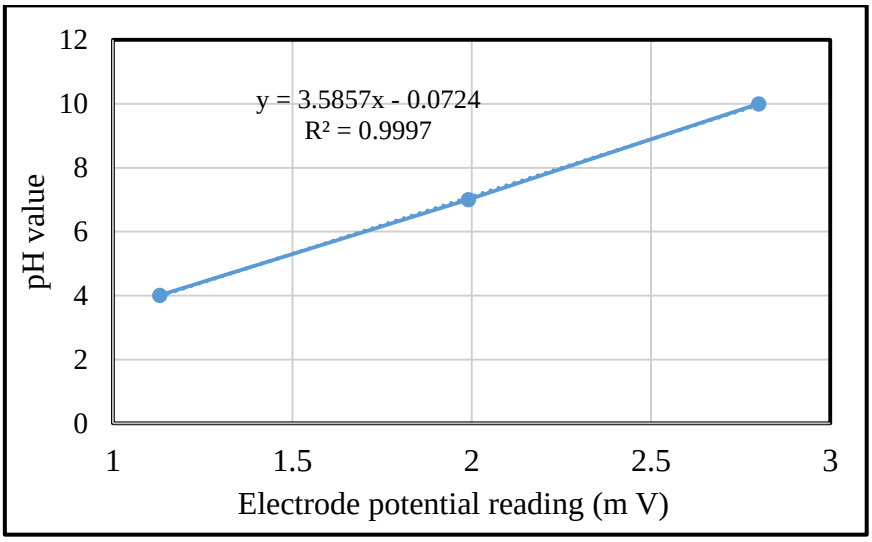

Figure 3- 11. Calibration curve of pH with different buffer solutions

3.4.4 Electrical conductivity:

A bench meter for the electrical conductivity measurements is used. Model 4510 Conductivity/TDS Meter with range 0 to 1999 µS. Accuracy ±0.5% ±2 digits, temperature range -10 to +105°C as present in figure (3.12) with the cell constant (cm^{-1}) of the electrode is equal to 0.99.

The conductivity is defined as the ability of a solution to conduct an electrical current, or the reciprocal of the solution's ability to resist the current flow, for more information see (Horvath, 1985). The current is conducted by electrically charged particles (ions), which are present in

almost all solutions. Although a conductivity reading provides an overall measurement of the ionic strength of a solution, it is not possible to distinguish the specific amounts of individual ions. For this reason, conductivity is often used to measure the total dissolved solids (TDS) of a solution.

Figure 3- 12. Model 4510 Conductivity meter with range 0 to 1999 µS Accuracy ±0.5%±2 digits

The conductivity value of a sample is changed with temperature, concentration, mobility of ions and valence of ions. Conductivity is measured using a probe which has two parallel plates separated by a fixed distance. When a voltage from the meter is applied across the electrodes, the ions in the solution conduct a current that flows between the two electrodes. The greater the concentration of ions in the solution, the larger the current generated and the higher the conductivity.

In next section, a set of preliminary experiments are done to determine the electrical conductivity curves for the three pure ammonium salts (carbamate, bicarbonate, and carbonate) according to their concentration and the solubility in the water.

3.5 The electrical conductivity measurement:

Measuring method: The electrical conductivity of aqueous ammonia/ammonium salts mixtures over a specific range of concentrations is studied and analysed. The process involves preparing aqueous ammonia and the three ammonium salts solutions (carbonate, bicarbonate, and carbamate) with specific concentrations (1.6, 2.2, 2.8 and 4.0 mol/L). The solutions are maintained at the lab temperature. The sample solutions were prepared from 28% aqueous ammonia concentrated solution as weight fraction.

The process involves mixing of two components with equal solution volumes (2ml for each sample) using different concentrations. The experimental cell of the electrical conductivity was

calibrated with standard solution (12.88 mS/cm KCl Calibration Solution). The cell constant is equal to 1 cm^{-1}, and it was checked from time to time to control for any possible deviation. The estimated uncertainty for electrical conductivity was about (0.5%). Most the experimental conductivity values are the average of three measurements.

The mixing step takes 2-3 minutes before measuring the pH value, which also needs additional 1-2 minutes to achieve a stable reading. After that, the electrical conductivity of the solution is measured at constant temperature (the solution temperature is controlled via a water bath at 23°C (±0.5°C). The measuring of EC also takes 2-3 minutes for a stable reading. The entire time of measuring EC process is about 5 to 8 minutes. This period of time could be enough for the components inside the solution to reach the equilibrium state.

3.5.1 The calibration curves of the electrical conductivity of pure aqueous ammonia solution:

Figure (3.13) shows the electrical conductivity and pH values of the aqueous ammonia versus the concentrations. The EC of solution decreases with increasing concentration. The aqueous ammonia concentration range of 1.6 – 4.0 mol/L is studied, which shows an electrical conductivity range of 1.33 - 0.94 mS, respectively. The results of the electrical conductivity of the pure aqueous ammonia agree with the results of Shcherbakov, *et al.* (2009). They reported the behaviour of the EC for the ammonia-water system versus the concentration range 0.1–10 mol/L ammonia and the temperature range 15 – 60 °C. Their results show that the EC of the ammonia–water system, decreases with increasing aqueous ammonia concentration.

In general, and according to Shcherbakov, some EC contributions can be attributed to solvent molecules, which are insufficient to complete the ionization process of the concentrated ammonia (weak electrolyte solution consists of mostly neutral molecules, so there are a diminished in the charge carriers). While at low concentrations, the ionization process is accomplished (100% ionization) and the ions (charge carriers) possess more mobility inside the solution, hence the electrical conductivity is higher. Furthermore, they show the electrical conductivity of the aqueous ammonia increases with increasing the temperature, which could be interpreted according to the viscosity reduction of the solution and that could increase the ion mobility.

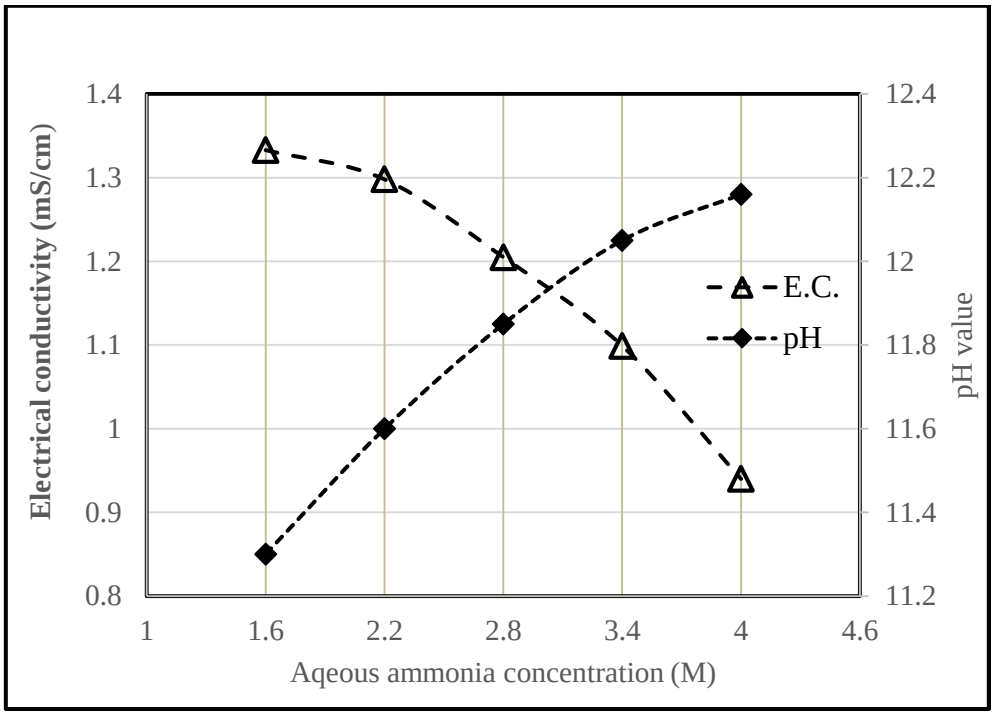

Figure 3- 13 the electrical conductivity and pH value of the aqueous ammonia versus the concentrations**.**

The EC for the pure water is 34 μS cm^{-1} which represents the value for a solution containing no ions, as the neutral molecules are not anticipated to produce ions. Another example, sodium hydroxide, classified as an ionic compound at 100% ionization has an electrical conductivity of a (21.5 mS cm^{-1}) for a concentration solution of a 0.1 mol/L. (Sanger, and Danner, 2010). Sanger and Danner state that the electrical conductivity for the NH_3/NH_4OH solution is only 496 μS cm^{-1}. This value is greater than the non-conducting solutions (pure water) and at the same time much smaller than the value for the completely ionization solution, i.e. (NaOH). Hence, it is likely that the NH_3/NH_4OH solution is composed of predominantly neutral molecules such NH_3 and H_2O and very few NH_4^+ and OH^- ions.

On the other hand, in this study the pH value for the same range of the concentrations of aqueous ammonia is measured. The results show that the pH of the solution increases with increasing the concentration as shown in Figure 3.12. The values of pH is 11.3 to 12.16 at concentration 1.6 and 4.0 mol /L respectively. In general, the rising concentration of the aqueous ammonia that usually points to an increase in the alkalinity of the solution (pH value) is due to the increase in hydroxide ions.

3.5.2 The calibration curves of the E.C. of aqueous ammonia / ammonium ion solution

The electrical conductivity of an aqueous ammonia/ammonium ion solutions (carbonate, bicarbonate, and carbamate) is determined by the same method just described at the same temperature and concentration range (1.6 to 4.0 mol/L) as shown in Figures 3.14 to 3.16.

Figure 3.14 illustrates the EC of the aqueous ammonia /ammonium carbonate solutions at a total molarity of 4.4. The EC is measured for five points two of these points represent the pure compounds; aqueous ammonia 4.4 mol/L and ammonium carbonate (3.3 mol/L (maximum solubility in water, so cannot get the 4.4 mol/L)). While the three points represent a mixture of both compounds with concentration: 2.8/1.6, 2.2/2.2, and 1.6/2.8 mol/L aqueous ammonia /ammonium carbonate). The mean value of EC for the three salts and the deviation bars are calculated, to assess whether the calibration is reasonably estimated. Also the deviations of the each concentration ratio are outlined. The first impression which draws the attention is the substantial differences in electrical conductivity of pure compounds. For example, the EC of aqueous ammonia is less than 1 mS /cm while the electrical conductivity of the *ammonium carbonate* is higher than 150 mS/cm at 3.3 mol/L. The similar concentrations ratio of the aqueous ammonia/ammonium carbonate (2.2/2.2 mol/L) has a conductivity of 113.5 ±19 mS. While at higher aqueous ammonia concentration (2.8/1.6 mol/L), the solution conductivity decreases to 87±14 mS. It is clear that the increase of the ammonium carbonate concentration leads to increasing the electrical conductivity of the solution to 129 ±18 mS, if we increase concentration ratio to 1.6/2.8 mol/L.

Figure 3-15 shows the electrical conductivity of the aqueous ammonia/ammonium bicarbonate solutions. It is 66.4±5 mS for the concentration ratio 2.8/1.6 mol/L and increased to 85.2±8 and 96.2±11 mS at concentration ratios of 2.2/2.2 mol/L and 2.8/1.6 mol/L respectively. However, the EC of the pure salt of the ammonium bicarbonate was 127 mS at 2.8 mol/L (represents the highest concentration due to the solubility restrictions). Generally, all the concentrations of the $NH_{3\,(aq.)}$ / bicarbonate possess EC values less than the EC of the $NH_{3\,(aq.)}$ / carbonate salt. The variation in EC could be attributed to the differences in valence of CO_3^{-2} and HCO_3^{-1} ions.

As is observable from Figure 3.16, electrical conductivity increases with increasing concentration ratio of the aqueous ammonia to ammonium carbamate solution. However, conductivity measurements of the liquid solution was 63.4±8 mS at concentration ratio (2.8/1.6) mol/L.

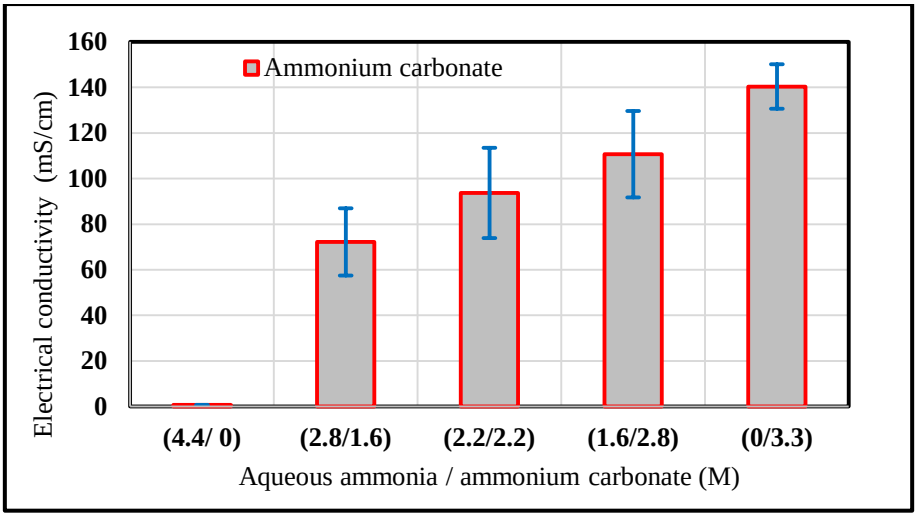

Figure 3- 14 the electrical conductivity of the aqueous ammonia and ammonium carbonate versus the concentrations.

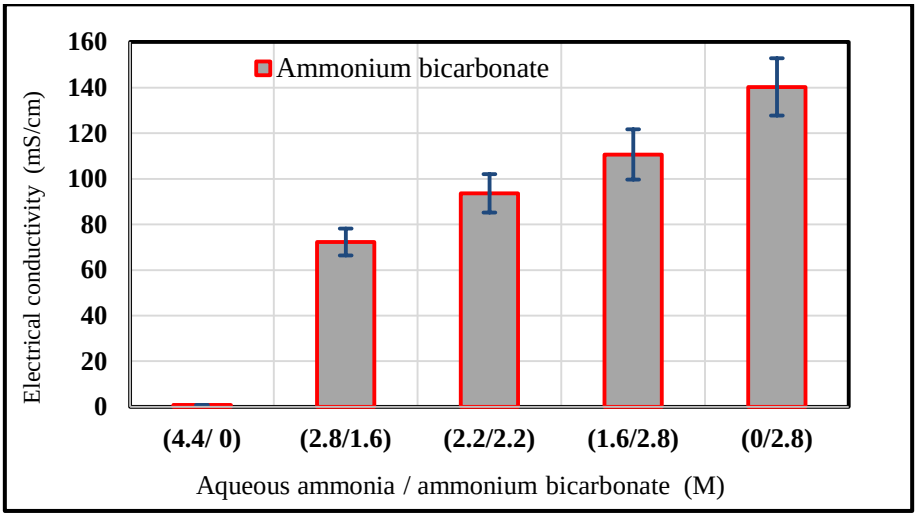

Figure 3- 15 the electrical conductivity of the aqueous ammonia and ammonium bicarbonate versus the concentrations.

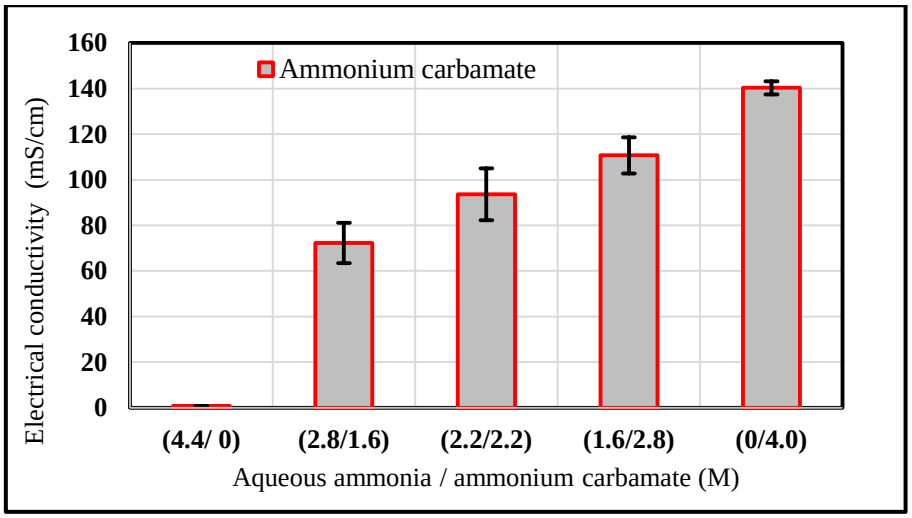

Figure 3- 16 the electrical conductivity of the aqueous ammonia and ammonium carbamate versus the concentrations.

Thereafter EC becomes 82.3±11 mS at the concentration ratio of (2.2/2.2) mol/L. The increasing the ammonium carbamate concentration and decreasing the aqueous ammonia concentration to the ratio (1.6/2.8 mol/L) yields EC slightly higher than one hundred ±8 mS.

In general, the electrical conductivity of the solution mixtures of the ammonium salts with aqueous ammonia decreases with increasing of aqueous ammonia concentrations. On the other hand, increasing of the carbon species in the solutions as carbonate, bicarbonate and carbamate ions increase the EC of the solutions. So, one could estimate qualitatively that the ammonia calibration for extent of reaction is different depending on the selected salt, hence there is no unique calibration. In other words, these solutions are far from an ideal mixture, where molar effects on EC are expected to be linearly additive. This conclusion may be attributable to the equilibration of ammonia salts in solution is slow, hence the EC alone cannot be used for kinetic purposes. The electrical conductivity of the calibrated solutions are apparently linked to the concentration of aqueous ammonia with one of the ammonium salts in this study. While in the actual reaction of $CO_2/NH_{3\,(aq.)}$ there are many intermediate reactions occurring (Diao, et al., 2004). Therefore the conductivity of the fraction of aqueous ammonia in such a solution cannot represent the actual reaction medium. The key feature distinguishing these electrolytic mixtures is the reversible reactions that occurs between the carbonate and bicarbonate as in reaction (1) and between the bicarbonate ions and carbamate ions as in reaction (2).

$$HCO_3^- \Leftrightarrow CO_3^{-2} + H^+ \qquad (3.1)$$

$$NH_{3\,aq.} + HCO_3^- \Leftrightarrow NH_3COO^- + H_2O \qquad (3.2)$$

Therefore such system is considered a complex for the binary components, and certainly will be more complex if there are three components or more in the electrolyte solution.

The calibration curves of the pure ammonium salts are shown in figures 3.17 to 3.19. These curves represent the electrical conductivities of the salts, which are proportionate to the salt solubility in the water. The electrical conductivity of the aqueous ammonia / ammonium ions is less than the pure salts at the same concentrations. The order of salts solubility is bicarbonate, carbonate, and carbamate: 220, 320 and 790 g/L respectively. In figures (3.17 and 3.18) the EC of ammonium carbonate and ammonium bicarbonate are plotted against the concentration respectively. The maximum solubility for the NH_4HCO_3 and $(NH_4)_2CO_3$ are correlate with the highest values of the electrical conductivity (150, 122) mS respectively.

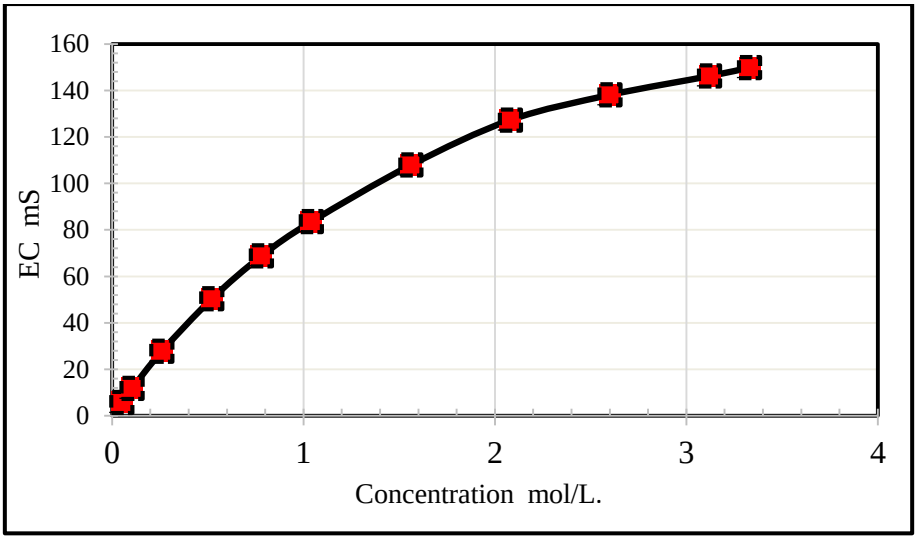

Figure 3- 17. Electrical conductivity of pure ammonium carbonate against the molar concentration.

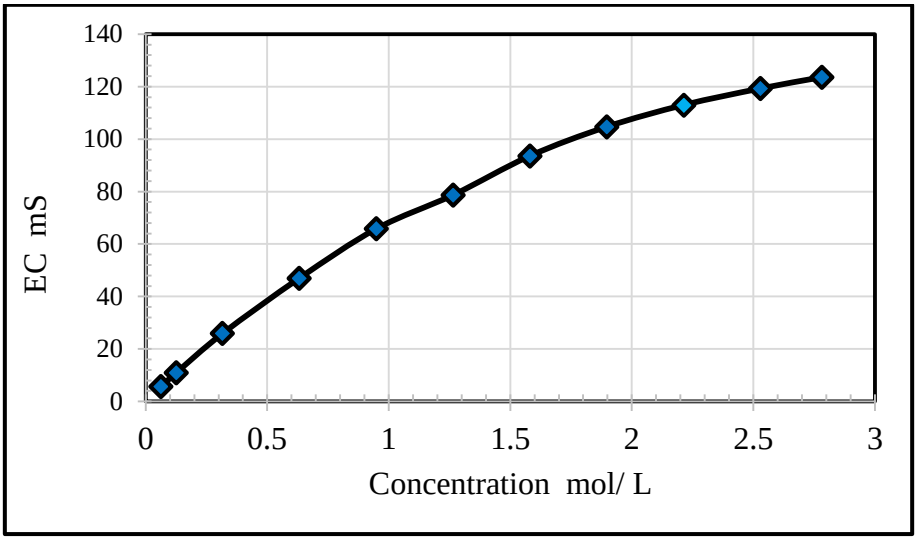

Figure 3- 18. Electrical conductivity of the pure ammonium bicarbonate salt against the molar concentration.

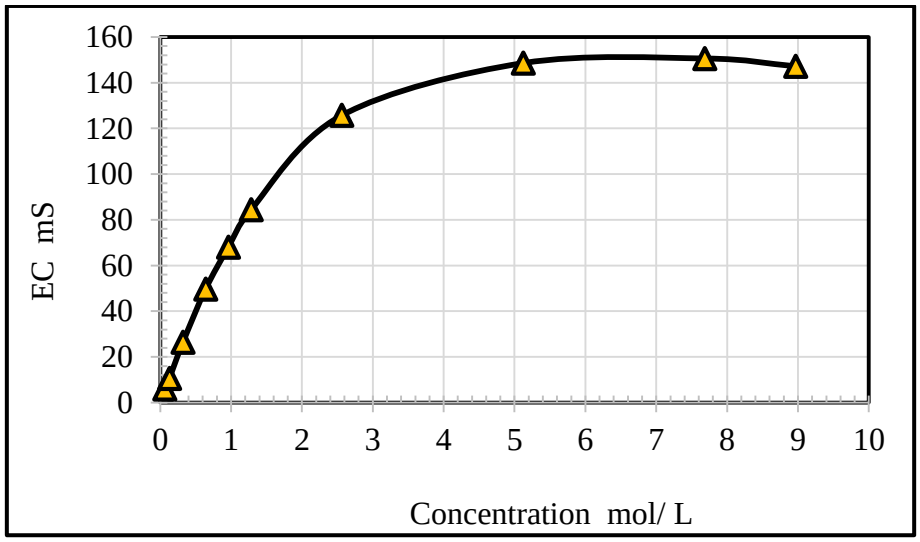

Figure 3- 19. The electrical conductivity of the pure ammonium carbonate salt against the molar concentration

Figure 3.19 shows the electrical conductivity (EC) of the ammonium carbamate behaviour as function for the concentration. The EC increases sharply till 2.0 mole/L to become slightly less 120 mS. However, the curve tends to be flat at 4.0 mole/L to the concentration of 9.0 mole/L, so that the EC is changed slightly at this range.

3.6 Experimental design using response surface methodology:

Response surface methodology, RSM, is a technique combining the mathematical and statistical tools for experimental design with a high dimensionality of control parameters. RSM is useful for analyzing problems where several independent variables influenced on one or more dependent variables (responses) (Montgomery, 2001). The independent variables can be denoted as X_1, X_2, X_3 …X_K. It is assumed that these variables are continuous and controllable by the experiment with negligible error. The response (e.g. Y) is assumed to be a random variable(Cavazzuti, 2013). The observed response (Y) as a function of the levels of variable (X_1) and variable (X_2) may be expressed as:

$$Y = f(X_1, X_2) \; + \; \varepsilon \qquad (3-3)$$

Where ε represents random error which is assumed to be normally distributed with mean zero and standard deviation. If the response is well modelled by a linear function of the independent variables, (Simpson *et al.*, 1997) then the approximating function of the first- order model is: -

$$Y = B_O \; + \; B_1X_1 + \; B_2X_2 + \cdots . + B_KX_K + \varepsilon \qquad (3-4)$$

While if there is curvature in the system, then a polynomial of higher degree such as the second-order model must be used:-

$$Y = B_O + \sum_{i=1}^{n} Bi\, X_i + \sum_{i=1}^{n} B_{ii}X_i^2 + \sum_{i=1}^{n}\sum_{i=1}^{n} B_{ij}X_iX_j \quad _{i<j} + \varepsilon \qquad (3-5)$$

Almost all RSM problems utilize one or both of these approximation polynomials (Box and Wilson, 1951). The minimization of least squared error is used to estimate the parameters in the approximating polynomials. If the fitted surface is an adequate approximation of (f) the analysis of the fitted surface will be approximately equivalent to analysis of the actual system. The most widely used design for fitting a second-order model is the central composite design. This design consist of a 2^k fractional, i.e., coded to (0, ± α, 0 ….0), (0, 0, ±α, 0) …, (0, 0…., ± α) and center points (0, 0… 0). A central composite design is made rotatable by the choice of f (x). The value for relatability depends on the number of variables k (i.e., for two variables

k=2, α= $\sqrt{k}$ = $\sqrt{2}$ =1.414 and for k = 4; α = $\sqrt{4}$ = 2). A first step is to setup the relationships between the coded levels and the corresponding real variables. The relationship is as follows:-

$$X_{coded} = \frac{(X_{actuai} - X_{Center})}{\left[\frac{(X_{center} - X_{minimum})}{\sqrt{k}}\right]} \qquad (3-6)$$

The number of experiment (N) needed is estimated according to the following equation: -

$$N = 2^k + 2k + 1 \qquad (3-7)$$

Thus for four variables, the number of experiments needed according to equation (3.6) is 25 plus 3 to 5 experiments at the center point to estimate the experimental error.

3.7 The reaction process of the CO_2 and NH_3 (aq.)

The effect of discharge power (kV), carbon dioxide flowrate (liter/min.), liquid ammonia concentration (Molar) and the time of reaction (min.) on the electrical conductivity and weight precipitated will be examined by using central rotatable composite design. In order to design the experiments, the operating range (Table 3.1) of each variable is fixed as follows: -

X_1: High voltage: (2.0 – 4.0) kV,

X_2: CO_2 gas flowrate: (0.2 – 1.0) litter/min,

X_3: concentration of aqueous ammonia: (1.6 – 4) M,

X_4: Time of reaction (10.0 – 50) min

The levels of each variables are selected to be five, because a small number of levels do not give a good interpolation on the design space. According to equation (3.7) the total number of experiments (N) is: N = 2^4 +2 × (4) +1 =25. Where 2^4 represents the factorial points as in table (3.3), 2*4 are the axial points as in table (3.4) and one center point as in table (3.5). The coded and real values of level and range for independent variables are calculated according to equation (3-6) as shown in table (3.2). While the total experiments will be 25. Last experiment no. 25 is the center point repeated three times to estimate the experimental error, so 28 experiments are required.

Table 3. 2 illustrates the range of real and coded values of variables that will be used in experiments of CO_2 / aqueous ammonia solution reaction

Main Parameters	Units	Symbol	Coded values				
			-2	-1	0	+1	+2
			Real values				
Discharge power	kV	X_1	2.0	2.5	3.0	3.5	4.0
CO_2 gas flowrate	Lit./min.	X_2	0.2	0.4	0.6	0.8	1.0
Conc. of liquid ammonia	Molar	X_3	1.6	2.2	2.8	3.4	4
Time of reaction	Minute	X_4	10	20	30	40	50

Table 3. 3 the experiments and experimental real and coded variables using rotatable experimental design (the factorial points)

Exp. No.	Coded independent variables				Real independent variables			
	X_1	X_2	X_3	X_4	High voltage (kV)	CO_2 flowrate (lit. /min.)	Conc. of aqueous ammonia (M)	Reaction time (min.)
1-	1	1	1	-1	3.5	0.8	3.4	20
2	-1	1	1	-1	2.5	0.8	3.4	20
3-	1	-1	1	-1	3.5	0.4	3.4	20
4-	-1	-1	1	-1	2.5	0.4	3.4	20
5-	1	1	-1	-1	3.5	0.8	2.2	20
6-	-1	1	-1	-1	2.5	0.8	2.2	20
7-	1	-1	-1	-1	3.5	0.4	2.2	20
8-	-1	-1	-1	-1	2.5	0.4	2.2	20
9-	1	1	1	1	3.5	0.8	3.4	40
10-	-1	1	1	1	2.5	0.8	3.4	40
11-	1	-1	1	1	3.5	0.4	3.4	40
12-	-1	-1	1	1	2.5	0.4	3.4	40
13-	1	1	-1	1	3.5	0.8	2.2	40
14-	-1	1	-1	1	2.5	0.8	2.2	40
15-	1	-1	-1	1	3.5	0.4	2.2	40
16-	-1	-1	-1	1	2.5	0.4	2.2	40

Table 3. 4 the experiments and experimental real and coded variables using rotatable experimental design (the axial points).

Exp. No.	Coded independent variables				Real independent variables			
	X_1	X_2	X_3	X_4	High voltage (kV)	CO_2 flowrate (lit. /min.)	Conc. of aqueous ammonia (M)	Reaction time (min.)
17-	2	0	0	0	4	0.6	2.8	30
18-	0	2	0	0	3	1	2.8	30
19-	0	0	2	0	3	0.6	4	30
20-	0	0	0	2	3	0.6	2.8	50
21-	-2	0	0	0	2	0.6	2.8	30
22-	0	-2	0	0	3	0.2	2.8	30
23-	0	0	-2	0	3	0.6	1.6	30
24-	0	0	0	-2	3	0.6	2.8	10

Table 3. 5 the experiments and experimental real and coded variables using rotatable experimental design (the centre points).

Exp. No.	Coded independent variables				Real independent variables			
	X_1	X_2	X_3	X_4	High voltage (kV)	CO_2 flowrate (lit. /min.)	Conc. of aqueous ammonia (M)	Reaction time (min.)
25-	0	0	0	0	3	0.6	2.8	30
26-	0	0	0	0	3	0.6	2.8	30
27-	0	0	0	0	3	0.6	2.8	30
28-	0	0	0	0	3	0.6	2.8	30

3.8 Experimental work set up

The experimental work can be divided into two parts. The first part is the reaction of carbon dioxide with aqueous ammonia solution. Four parameters are studied in this part of the experimental work. The work was done depending on testing five levels of each independent variables (input high voltage, the flow rate of CO_2 gas, the concentration of aqueous ammonia, and the reaction time). The electrical conductivity of the final solution, yield of solid deposited, pH values, and temperature of the system are observed and measured. The second activity

focuses on the characterization of the compounds of reaction products. The characterization of the chemicals such as ammonium carbonate, ammonium bicarbonate, and ammonium carbamate are performed using thermogravimetric analysis technique. Thermal profile studies using thermogravimetric analysis (TGA) are an excellent tool to calculate kinetics parameters of many chemicals using thermal decomposition process. The data collected from TGA experiments are utilized to determine kinetic parameters, through an assumption of the reaction order of ammonium salts decomposition (carbonate, bicarbonate, and carbamate) then find the activation energy and pre-exponential factor.

3.8.1 The experimental protocols for the CO_2 / $NH_{3\,(aq.)}$ reaction:

A solution of ammonium hydroxide 28-30% is used as a stock solution to prepare the reaction medium which is purchased from EMSURE®. The initial concentration of the stock solution was 7.19 mol/L. It has a specific density (0.9), formula weight (35.05) g/mol., and the concentration of 28% by weight. The required concentration of each experiment is calculated as mentioned in Appendix (A1). Compressed air is circulated within the system piping to check piping connection and leaks, as well as for setting up and testing the plasma generation. Thermocouple sensor (type K) and the pH probe are fixed on the reactor cover. They are connected to the Arduino board, which is connected by USP cable to the data logging PC. The pH electrode is calibrated using three buffer solutions before each experiment.

Two voltage probe sensors are connected to an oscilloscope, which is connected with PC by a USP cable. The HV probe (Testec, HVP-15HF) is used to measure the high voltage which is loaded on the outer electrode, by the power source. It was calibrated using another high-voltage probe in order to match the real values at the load. The ground voltage at the inner electrode is measured by TA008 60 MHz with attenuation ratio 10X PicoScope probe. The oscilloscope provides an option on the current pulses passing through a capacitance of 10 nano F which was putted on ground voltage line as shown in figure (3.20).

3.8.2 Experimental procedure

The schematic diagram for generating a cloud of very fine bubbles of CO_2 gas to react with aqueous ammonia solution, excited by the non-thermal plasma unit, is shown in figure 3.20. A solution of **150 ml** is added to the reactor with a specific concentration as illustrated in tables (3.2, 3.3, 3.4, and 3.5) in section 3.7 for all 28 experiments. The solution addition step was performed with the presence of very low compressed air flow. The purpose of airflow was to prevent the solution flow down due to gravity through the diffuser to the plasma generator. The

next steps were the CO_2 gas valve was opened (the flow should be set on to a specific value using CO_2 flowmeter), the air valve closed, and the power switched on. The required magnitudes of high voltage are set on the power source by changing the voltage and current values through the power source knobs, making a priority to keep the high voltage value at the plasma generator (DBD) within the defined amplitude. The High voltage, the voltage of ground electrode, are monitored through the double-headed USB 2.0 cable to provide the power and to connect the oscilloscope with the PC screen. Furthermore, the Arduino screen shows the parameters such as the time of reaction, temperature and pH value inside the reactor.

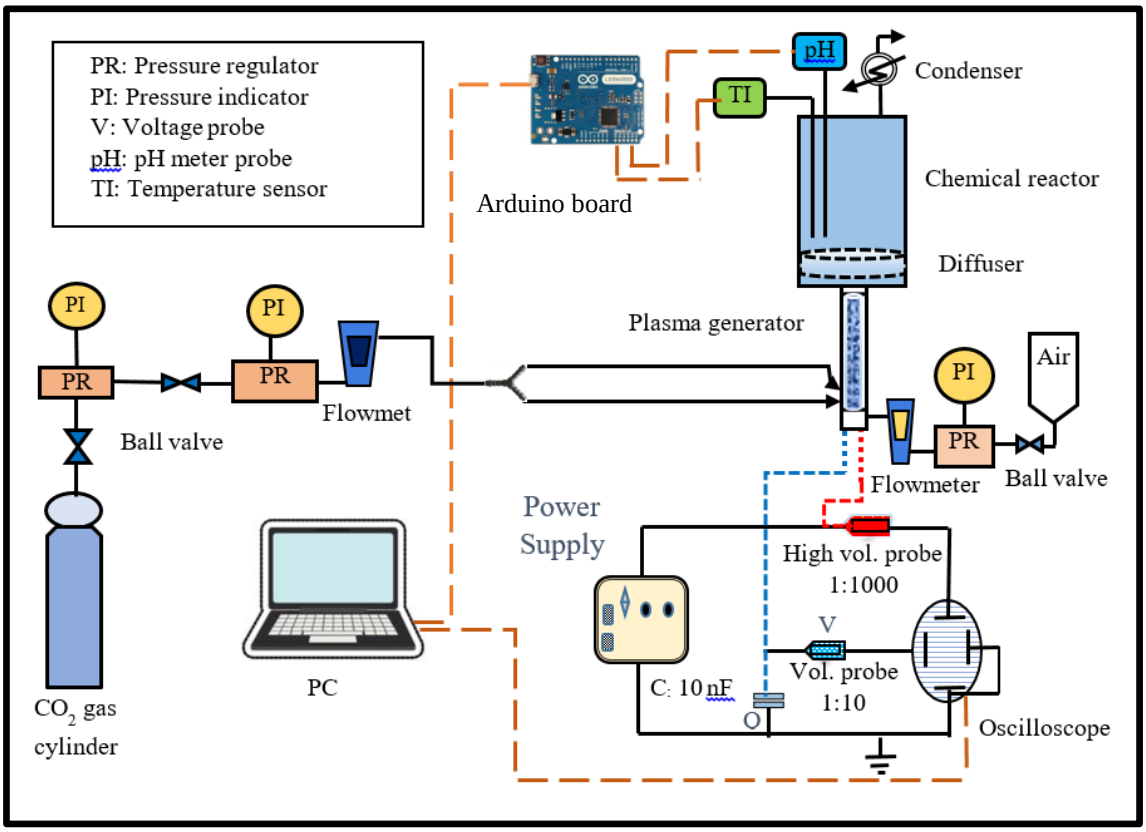

Figure 3- 20 A schematic sketch for system of the carbon dioxide /aqueous ammonia reaction.

A reaction usually started smoothly at first five-to-ten minutes with sharply increasing in temperature. Generally, the mid-time of the reaction could be identified by the highest temperatures during the reaction time. Thereafter, the behavior of temperature tends to decrease at the end of an experiment. By decreasing the ammonia content (or dissolving the acid CO_2 gas), the pH values are usually reduced to a range of 8.1 to 8.5 by the end of the reaction. At the end of each experiment the CO_2 gas flow is closed, the power is switched off, and the solution withdrawn to a beaker. Thereafter, electrical conductivity of the solution is measured at 38-40 °C. The solution subsequently is shifted to a closed container and put in a refrigerator

for quenching, for at least 4 hours, so that its temperature reaches -10 °C. The precipitate is separated using Buchner funnel to carry out the separation process. Additionally, the precipitate is weighted using a precise digital scale. Finally, a few samples from the precipitate are withdrawn and send to the NMR spectrum to check the composition.

3.8.3 The control experiment:

When gas is flowing through the liquid as a current of bubbles, for example, on a bubble-plate or in a sparged vessel a diffusion, convection, and reaction proceed together. And during gas-liquid contact, a complicated system is formed. Absorption characterised by a chemical reaction can enhance the absorption rate and reduce the height of scrubber (Levenspiel, 1999). The highest yield of the reaction process of $CO_2/NH_{3\ (aq.)}$ that achieved in Chapter 6 for the bicarbonate production is chosen to conduct a control experiment. The yield process enhancement in presence / absence of non-thermal plasma should be tested according to the reaction (3.8).

$$NH_{3\ (aq.)} + H_2O + CO_{2\ (g)} \Leftrightarrow NH_4HCO_3 \quad \text{---------- (3-8)}$$

The conditions of experiment number 9 gave the highest yield. This experiment reduplicated again with same parameters value except the high voltage was switched off. So the CO_2 flow rate of 0.8 LPM, aqueous ammonia concentration of 3.4 M, and reaction time of 40 min is selected. This experiment will be used to judge on the yield process enhancement due to the non-thermal plasma, which activates the CO_2 species to participate in reaction.

3.9 The main analytical devices

3.9.1 Thermogravimetric analyzer (TGA):

Thermogravimetric analysis is defined as a technique in which the mass of a substance is monitored as a function of temperature or time. The specimen is subjected to a controlled temperature programme in a controlled atmosphere. A TGA is composed of a sample pan that is supported by a high accuracy weight scale. That pan is stabilized in a furnace and is heated during the experiment. The weight of the sample is plotted during the experiment as a graph against time or temperature. The sample environment is controlled by a certain purging gas. This gas flows over the sample and exits through an exhaust. The nature of this gas might be inert or a reactive gas depending on the tested sample.

Perkin Elmer TGA 7 Analyser**:** this analyser includes a standard furnace assembly (up to 1000C). The Perkin-Elmer TGA-7 thermogravimetric analyser measures the weight loss of

samples upon heating as shown in figure 3.21. The samples could be heated in a nitrogen or an air atmosphere, the gas being selectable via data system control.

The heating temperature range of the samples in the furnace is started from room temperature to 900°C. The balance of TGA is sensitive to 0.1 microgram. The equipment screen continuously shows weights reductions curve during the experiment. So that, the X-axis could be represented either as a decomposition time of sample or temperature of the sample, while the Y-axis is represented the sample weight (mg) or weight percent (%). Temperature programme should be set on starting temperature T_1°C to final temperature T_2 °C with a specific heating rate with units (°C/minute) in the Nitrogen or air atmosphere with a particular flow rate of the gas mL/minute. There are six operating variables that contribute to reproducibility of the TGA: (Calibration, Furnace Cleanliness, Sample Preparation, Temperature Range, Temperature Scanning Rate, and Sample Atmosphere).

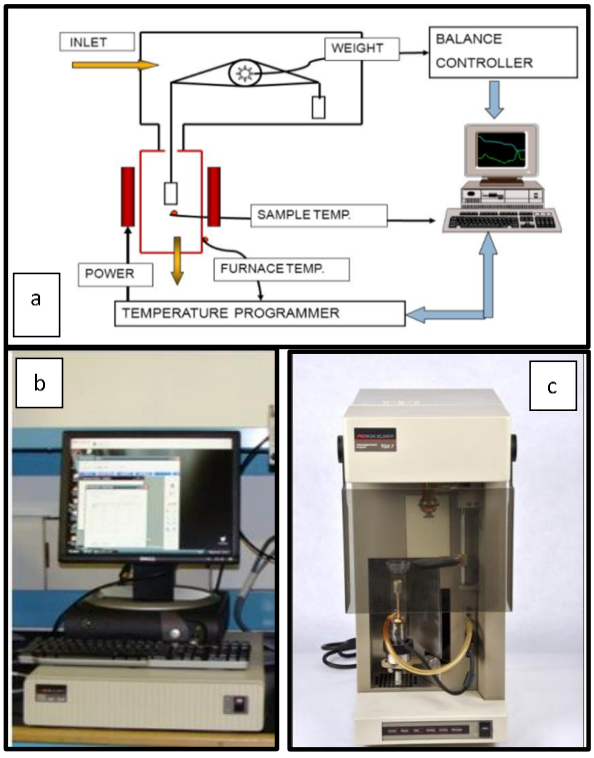

Figure 3- 21.Thermogravimetric analyser (a) shows the sketch of connections between the furnace, the balance and temperature control, (b) the computer and the screen connected to the e analyser to show the results progress while, (c) the furnace and sample position.

3.9.2 Fourier Transform Infrared Spectrophotometer:

One of the most common techniques used in organic chemistry is Infrared (IR) spectroscopy, used to identify the structural characteristics of various substances. Electromagnetic radiation in a specific ranges of infrared frequency has an ability to excite organic compounds as a result of molecules absorbing energy. The resonance frequencies are led an increase in the bonds activity of these molecules through the stretch, bend or rotate. The strength of the bonds is

influenced by the resonant frequency, the atoms connected by the bond, bonds type and the condition around each bond.

Figure 3- 22. Fourier Transform Infrared Spectrophotometer type IRAFFINITY-1S, Shimadzu. (https://www.shimadzu.co.uk/iraffinity-1s)

Fourier Transform Infrared Spectrophotometer-attenuated total reflectance (FTIR-ATR figure 3.22) is used to investigate the components of precipitate (solid) and filtered (liquid). However, the results are listed as a function of the infrared radiation which absorbed by the molecule versus of wavenumber (cm^{-1}). The samples were analyzed using IRAFFINITY-1S, Shimadzu. The measurement system was absorbance, with a number of scans 100 and resolution 4. The range of mid-infrared frequencies was 800-4000 cm^{-1} most useful in the characterization of bicarbonate peaks.

Diao et al. (2004) analyzed a crystalline solids of ammonium bicarbonate using FTIR spectrometer. They are proved that the NH_4HCO_3 is the main product of the wet reaction CO_2-NH_3-H_2O comparing to a powder of standard ammonium bicarbonate. The FTIR spectra peaks of the three standards ammonium salts (carbonate, bicarbonate, and carbamate) are discussed (Lingyu Meng *et al.*, 2005) as shown in figure (3.23) and figure (3.24). The figures show the region of wavelength 1200-1450 cm^{-1} as the asymmetric CO stretch of the bicarbonate ion, while the peak nearly1600 cm^{-1} region is the symmetric of CO stretch.

The spectrum of ammonium carbonate and ammonium bicarbonate, have the same peaks in range 1200-1700 cm^{-1}, also at 3098 cm^{-1} which represents the ammonium ion but the peaks in the region 1300-1600 cm^{-1} are the CO_3^{-1} ion asymmetric C-O stretch. Whereas, the ammonium carbamate could be distinguished by a peak at region 3472 cm^{-1} in the spectrum which does not appear in spectra of the other two compounds. Miller and Wilkins (1952) analyse the IR spectra of 159 pure inorganic compounds, most of which are salts containing polyatomic ions.

One of these salt is the ammonium bicarbonate as shown in table (3.6), which is illustrates the wavelength peaks and their intensities. They were pointed out a band at 2500 -2600 cm^{-1} it attributes to frequencies of O-H stretching of the hydroxyl groups, which is connected to the central atom.

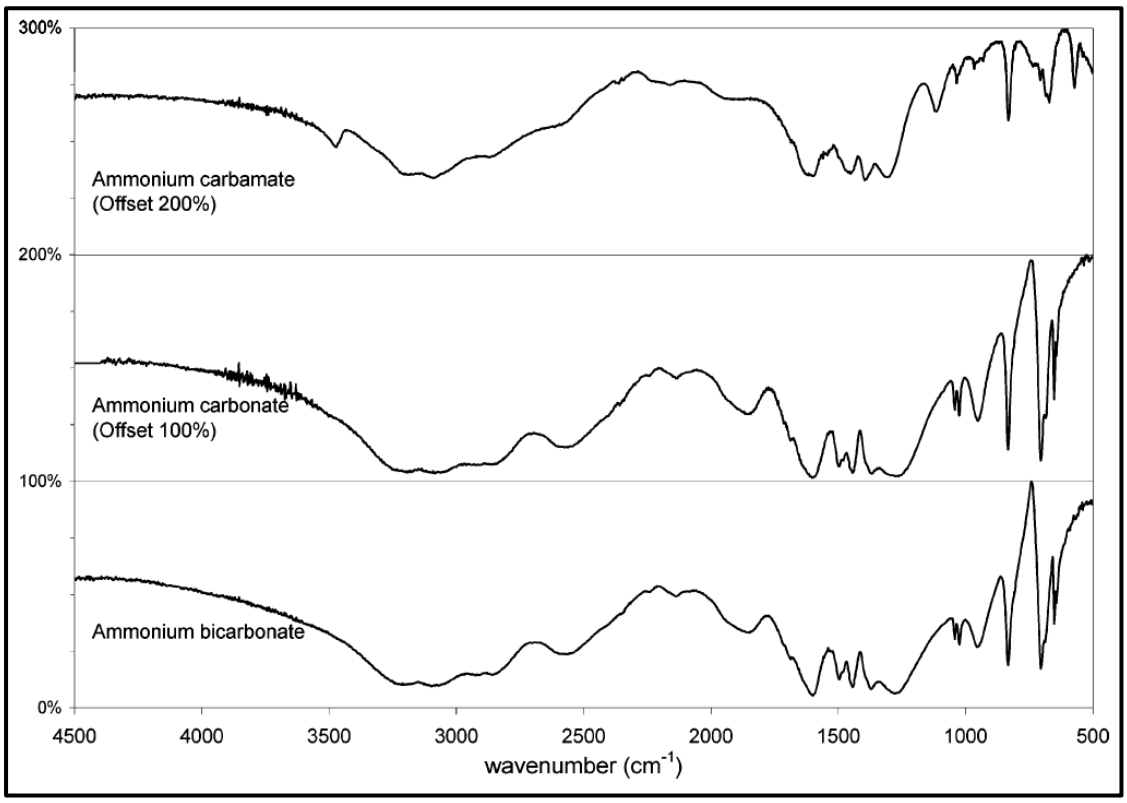

Figure 3- 23. Fourier transform infrared spectroscopy (FTIR) analysis of standards ammonium salts (carbonate, bicarbonate, and carbamate) (Lingyu Meng et al., 2005)

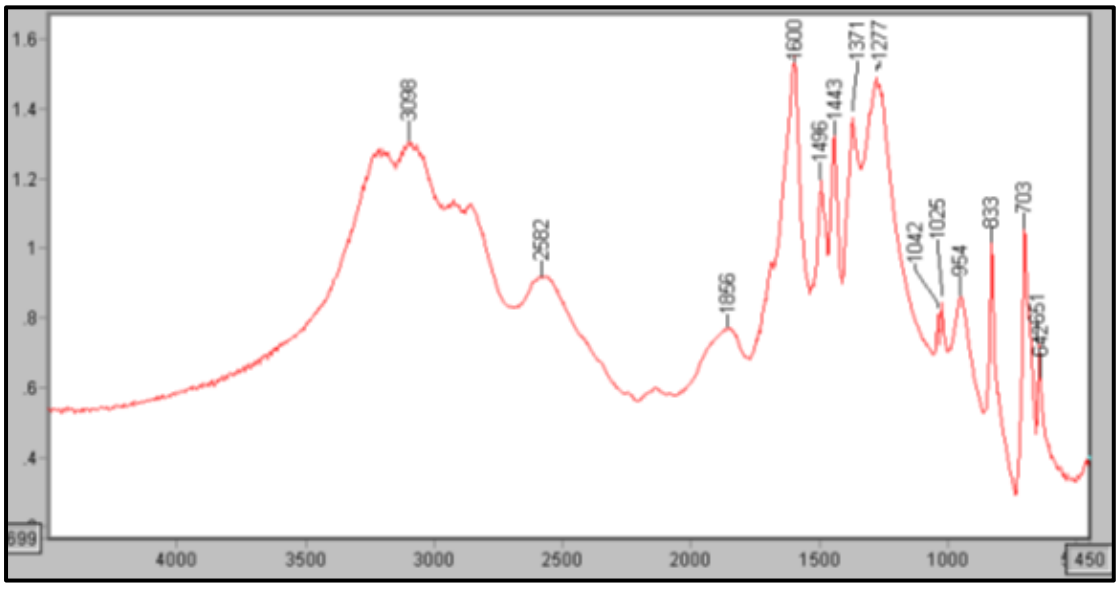

Figure 3- 24. FTIR spectrum of NH_4HCO_3 standard at room temperature (Meng, 2004).

Table 3. 6 .The positions and intensities of Infrared absorption Bands of ammonium bicarbonate (Miller and Wilkins, 1952).

	cm $^{-1}$	Microns	intensity
1	703	14.25	*strong*
2	832	12.02	*strong , sharp*
3	993	10.08	*strong*
4	1030	9.7	*weak , sharp*
5	1045	9.58	*weak , sharp*
6	1325	7.55	*very strong , broad*
7	1400	7.15	*very strong , sharp,*
8	1620	6.17	*strong*
9	1655	6.05	*strong*
10	1890	5.3	*weak*
11	2550	3.92	*medium*
12	3060	3.27	*very strong , sharp*
13	3160	3.17	*very strong , sharp*

3.9.3 Nuclear magnetic resonance spectrometers

Nuclear magnetic resonance spectrometers have currently become very useful instruments to perform an almost unlimited number of a high degree of complexity experiments. NMR is used to analyze samples of solid state and liquid to confirm its identity and its composition. However, the main important parts of the spectrometer are not very complex, and it is certainly useful when using the spectrometer to have some basic principles of how it operates (Keeler, 2005). The spectrometer consists of the following components:

• **Magnetic field:** should be homogeneous, an intense and stable

• **The probe:** which enables the coils to excite and detect the signal to be placed close to the sample

• **The radiofrequency transmitter:** which generates the pulses with a high-power

• **A sensitive receiver** to amplify the NMR signals, the place of amplifier is usually put adjoining to the probe. So, that the weak signal is boosted before being sent down to spectrometer console.

• **A digitizer: or** analogue to digital converter a device is used to convert the NMR signals into a binary number which can be stored in computer memory.

• **A pulse programmer:** The pulse programmer is a very complex part of computer hardware to control and set all of the functions of the spectrometer. It produces very precisely timed events, often in rapid succession, it is usual for it to run independently of the main computer.

• **A computer** to control everything and to process the data.

(Pelkie, et al. (1992) proposed using the ^{13}C NMR spectra to establish the concentrations of all the ions of the solid compounds, which form in the gaseous $CO_2/NH_3/ H_2O$ reaction to validate the assumptions used in the conductivity analysis. The solution of ammonium carbonate, bicarbonate, and carbamate was investigated by Wen and Brooker (1995) using Raman and ^{13}C-NMR spectroscopic. The study with NMR spectroscopy shows that the carbonate/bicarbonate ions have a singular peak due to fast proton exchange, while the carbamate has a separated peak.

Mani, et al. (2006) reported that the nuclear magnetic resonance spectrometer provides a precise and reliable method to estimate the reaction products of ammonia solution with carbon dioxide gas. The ^{13}C NMR spectra of different concentration of aqueous ammonia are studied at various loaded quantities carbon dioxide gas and their effect on pH value as illustrated in figure (3.25). In general, to understand the CO_2/NH_3 system behaviour, it is necessary to utilize ^{13}C NMR technology because it provides deep and quick information about the experimental method and the reaction conditions.

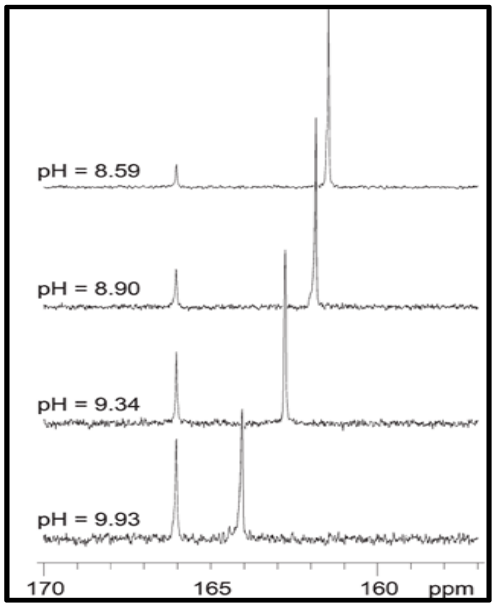

Figure 3- 25. ^{13}C NMR spectra of the carbamate and bicarbonate/carbonate ions, Carbon resonances at various pH values in four liquid ammonia with increase the carbon dioxide gas loaded (Mani, et al. 2006).

3.10 Conclusions

Through using $NH_{3\,(aq.)}$ solutions to capture the CO_2 could produce a cheap nitrogen fertilizer of ammonium bicarbonate as a practical method to sequestration of carbon dioxide. In general the influence of changing the conditions of reaction and reactants concentration could yield different ammonium compounds. Generally, the calibration curves show the increasing of the

carbon species in the solutions as carbonate, bicarbonate and carbamate ions increase in the EC of the solutions. So, one could estimate qualitatively that the ammonia calibration for extent of reaction is different depending on the selected salt, hence there is no unique calibration. In other words, these solutions are far from an ideal mixture. Therefore, to achieve the efficient process of CO_2/ $NH_{3\ (aq.)}$ reaction the choice of ammonium bicarbonate will be one of the suitable options. Consequently, the reaction products should be specified via one of the analytical method. Although electrical conductivity has not shown a correlation with the extent of reaction, i.e. aqueous ammonia transformed into amine functional groups within the salts, it has shown in the calibration studies monotonicity and sensitivity with composition of binary salt mixtures dissolved in aqueous solution. Jeanmeure et al. (2001a,b) for multiphase flow regime identification and Zimmerman et al. (2004) for rheology, respectively, demonstrated that with moments of response profiles for sensitive measurements alone (even non-monotonic profiles) are sufficient factors for multimodal inversion.

The sensor design methodology is to identify other modes of physico-chemical response that are complementary, such as UV and IR fibre-optic spectrometry and pH. Al-Mashhadani et al. (2012) found that pH alone was sufficient to infer dissolved CO_2 aqueous concentration, even though it has reversible and fast equilibrated carbonate and bicarbonate salt formation pathways. The distinct difficulty with the ammonium salts explored here is that they precipitate and sediment, thereby breaking the equilibration. Hence liquid phase measurements alone will not capture the phase change at supersaturation. However, the monotonicity and sensitivity for the binary calibration curves with EC make electrical conductivity a strong candidate for inclusion in a multimodal, fast-response monitoring system for ammonia/CO_2 salt characterisation. The utilization of the on-line sensors has an importance in industry in particular the low cost and in an instantaneous data collection. The electrical conductivity and pH value will be used to measurements directly on the lab-bench.

The other techniques also will be used for more results validation such as FTIR and ^{13}C NMR. Additionally, the TGA will be used to characterize the decomposition reaction of the some ammonium compounds. The experiments will performed via using response surface methodology (RSM), because it is most useful in building an empirical mathematical model linking between multi-input parameters and output responses. So it provides a better understanding for each influence of the individual variables and the mutual interaction. In addition it requires less number of the experiments, which save on the chemicals consumptions and labour and hence maintains low cost.

Department of Chemical and Biological Engineering

Chapter Four

Kinetic modelling of CO_2 reaction dynamics with in Dielectric Barrier Discharges in an atmospheric pressure plasma reactor

Chapter Four

Kinetic modelling of CO_2 reaction dynamics with in Dielectric Barrier Discharges in an atmospheric pressure plasma reactor

4.1 Summary

In nonequilibrium plasma, fast electrons created by the discharge mechanism mainly initiate plasma chemical reactions. These electrons collide with gas molecules exciting them to higher energy levels. The excited molecules can now, as a result of their high internal energy initiate other chemical reactions. One of the main aims of this study is to understand chemical reactions in plasma states, then use these assumptions to carrying out the CO_2/ aqueous NH_3 reactions at the interface of the fine bubbles. Exciting molecules of gas by the dielectric barrier discharge reactors promises energy efficiency process because the transfer of energy by electrons to the species which take part in reactions can be tuned to be highly specific to quantum transitions.

Modelling carbon dioxide kinetics predicts that the main species with high concentrations and possess stability are charged ions and neutrals. These excitation levels of the CO_2 molecule occur at low concentrations in milliseconds, the region of the effective concentrations is ranged from 10^3 to 10^4 cm^{-3} then decreased with the time to very tiny values, while coinciding with increasing O_2 and CO concentration in the same period of time.

This model would be useful for investigating the conditions and parameters that influence the carbon dioxide reaction process. Many reactions may occur in the plasma microreactor with many species having different lifetimes and metastable states, which play significant roles in plasma chemical reactions. Finally, the model provides additional understanding of the CO_2 chemistry under plasma excitation. This knowledge will facilitate the selection of the optimum conditions for the reaction with aqueous ammonia solution in the next step of this study.

4.2 The role of the non-thermal plasma

Carbon dioxide is a greenhouse gas formed from different human and industrial activities as a by-product of the combustion of fuels such as coal, oil and gas. Recently, considerable attention has focused on different technologies to utilise CO_2 and contribute to recycling carbon with diverse chemical processes. Emission reduction and environmental hazard management require complementary strategies such as adaptation and mitigation. Some categories for CO_2

utilization are reported by Aerts et al., (2015) to address the emission issue through: chemicals production, fuel production and biomass utilization. Omae (2012) shows a detailed review of carbon dioxide used as feedstock in industrial fields, its main substrates and their products such as: oxygen-containing compounds such as epoxides and alcohols (to produce cyclic carbonates); nitrogen-containing compounds such as ammonia and amines (to produce urea); carbon-carbon unsaturated compounds, e.g. aromatic, alkynes, alkenes and dienes (to produce carboxylic acids and esters,…); and finally hydrogen substrate to produce formic acid and methanol.

De Bie *et al.,* (2011) reported the conversion process of greenhouse gases into value-added chemicals using dielectric barrier discharges, earning more attention in environmental applications. Their modelling study on the conversion of methane to higher hydrocarbons or oxides by partial oxidation with CO_2 or O_2, shows that the reaction products as a function of residence time in the reactor, for different gas mixing ratios are found to be important reaction products such as syngas and higher hydrocarbons. However, the carbon dioxide molecule as a dissociative process or laser techniques has also been studied and more details, including a discussion and references, can be found in references(Hokazono and Fujimoto, 1987; Cenian, ea al., 1995)

There has been much interest in how to obtain maximum power efficiency, high conversion rate of the CO_2 molecules and the reduction of the excitation power. Indeed, CO_2 molecules at room temperature are very stable, with a high energy of dissociation 5.5 eV. Fridman (2008) reported that CO_2 decomposition mechanisms in quasi-equilibrium thermal plasma require high *plasma temperature* T_e (2500-3000 K). According to Arrhenius the high kinetic energy of activated molecules of reactants determines the reaction rates. From figure 4.1 there are two plateaus in energy, representing reactants and products. The diagram illustrates a maximum peak called the activation barrier or transition state, which is the energy that activate molecules must have to proceed from reactants to products. The plasmas can lower the activation energy for a certain reaction and enhance the formation of desired end products. Two factors limiting the conversion and energy efficiency are correlated in the quasi- equilibrium systems: the dissociation products may undergo reverse reactions unless there are very fast cooling rates of about 107–108 ºK/s; and the dissociation of CO_2 in thermal plasmas is only 43% (maximum value of energy efficiency).

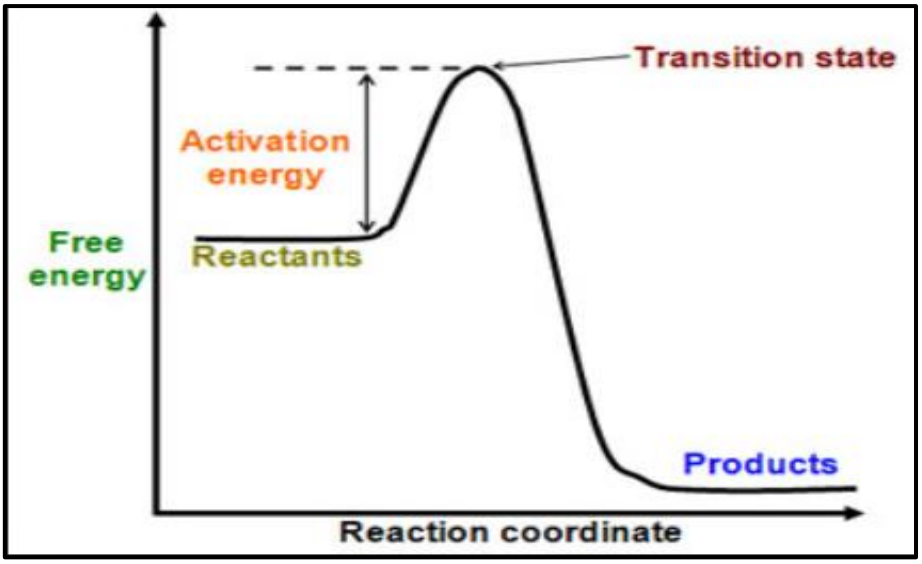

Figure 4- 1. The activation energy diagram represents the maximum energy (the peak) and reaction progresses from reactant to product formation due to this activation barrier

Therefore, thermal plasma application is not necessarily very effective in that most of the energy is used in heating molecules, ions, and all particles to achieve the required high temperature. These two problems can be overcome with non-thermal plasma systems, because it is possible to enhance or suppress specific reaction channels by controlling gas temperature, electron temperature and electron density (Fridmam, 2008).

4.3 CO_2 molecule behaviour in the presence of plasma

Carbon dioxide molecules at ground state are described as triatomic linear molecules have three modes of vibrations. The vibrations would be classified as: symmetric stretching, symmetric bending, and asymmetric stretching (Fridman and Kennedy, 2011) as illustrated in figure 4.2

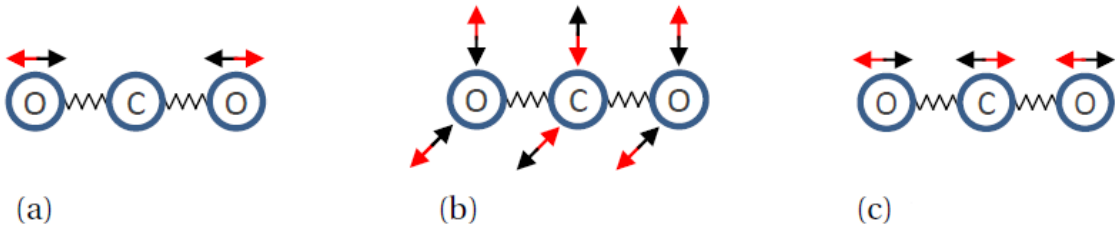

Figure 4-2. Vibrational modes of CO_2 molecule (a) symmetric stretching v1, (b) doubly degenerate bending mode v2, and (c) asymmetric stretching v3. Taken from (Moreno Wandurraga, 2015).

Generally, in plasma physics and chemistry of molecular gases, the vibrational excitation of molecules plays an important role. Undoubtedly, the types of molecular symmetry illustrate common features of vibrational modes of the triatomic molecules. At low energy of the vibrational excitation, the interference of the vibrational modes is weak and the structure of the vibration levels possess a discrete structure (Kitajima *et al.*, 2001). The energized electrons in

plasma media at a range of 1 to 2 eV stimulate mainly the lower vibrational levels of CO_2 and the asymmetric mode of the vibrations. The highly excited state molecules will be involved in chemical reactions (Fridman and Kennedy, 2011). An electron impact vibrational excitation is considered the most effective pathway (reactions 1 and 2) for CO_2 conversion in non-thermal plasmas and up to 97% of the plasma energy can be transferred from electrons to vibrational excitation at an electron temperature of 1–2 eV, or a reduced electric field (E/N) of (20–40) Td.

$$e^- + CO_2 => CO_2^+ + 2e^- \quad ------(4.1)$$

$$e^- + CO_2^* => CO + O + e^- \quad ------(4.2)$$

CO^*_2 is the vibrational excited state. However, Aerts et al., (2012); Kozák and Bogaerts, (2015) developed chemical kinetic models to explore the plasma chemistry and the role of electron vibrational excitation in the splitting of the CO_2 molecules. Both authors used a dielectric barrier discharge (DBD) reactor with an average electron temperature (2–3 eV). Their results showed that 94% of the CO_2 conversion occurs by electron impact dissociation reactions with ground state CO_2. Aerts found only 6% splitting reactions is achieved from the vibrational excited CO_2 state. However, they suggested increasing the frequency of pulses per unit time to improve the efficiency of splitting from the path of the vibrationally excited molecules.

The study focuses on activated CO_2 molecules (electron acceptor or proton donor i.e. Lewis acid) by non-thermal plasma in order to enhance the reaction with aqueous of ammonia thereafter. The nitrogen atom in ammonia molecules has a lone electron pair, which makes ammonia a base and a proton acceptor or electron donor. So the contact of gas-liquid at the interface of the small-bubbles leads to CO_2 gas simultaneously dissolving in liquid phase as shown in figure (4.3). Thereby, there is an excess of aqueous ammonia and CO_2 exactly at the bubble interface; ammonium carbamate, ammonium carbonate, and ammonium bicarbonate, can be form. The main products of the CO_2/ aqueous ammonia reactions are expected as shown in equations (4.3 to 4.5):

$$2NH_{3\,(aq.)} + CO_{2(g)} \rightarrow NH_{4(aq)} + NH_2COO_{(aq)} \quad ----------(4.3)$$

$$2NH_{3\,(aq.)} + CO_{2\,(g)} + H_2O \underset{\leftarrow}{\rightarrow} (NH_4)_2CO_{3\,(s)} \quad ----------(4.4)$$

$$NH_{3\,(aq.)} + CO_{2\,(g)} + H_2O \underset{\leftarrow}{\rightarrow} NH_4HCO_{3\,(s)} \quad ----------(4.5)$$

The small bubbles will be responsible for enhancing the reaction efficiency through the increased surface area between the gas/liquid interfaces. The reaction process of gas/liquid will

depend on the quantity CO_2 dissolved and then on the removal of the reaction products. These two factors will drive the main reaction towards products and improve the yield of the process.

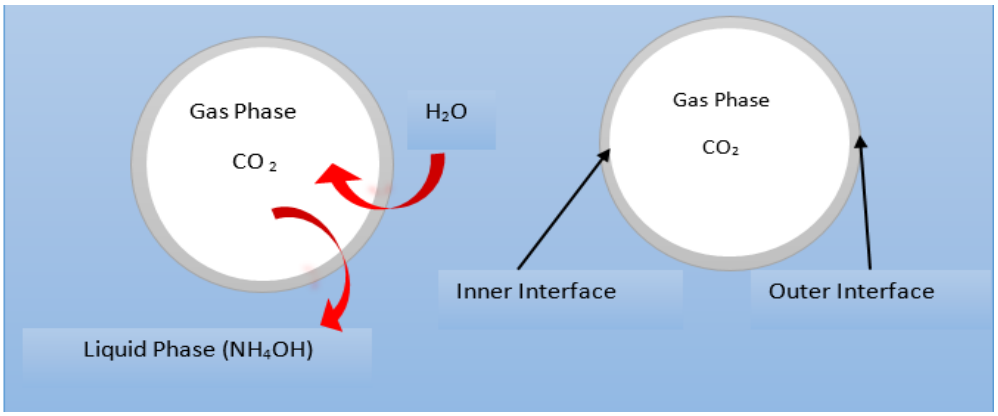

Figure 4- 3. A simple schematic graph of CO_2 very fine bubble in aqueous ammonia solution.

4.4 Silent discharges formation theory

Dielectric-barrier discharges or silent discharges are non-equilibrium discharges that can be used over an extensive pressure and temperature range. Dielectric barrier discharges (DBD) have many uses including light generation for plasma and LCD displays, ozone generation, hydrogen production (Rehman, et al., 2013) and surface modification (Konelschatz, 1997). Furthermore, DBD has found an increasing interest for plasma chemical gas cleaning and surface treatment due to their operation at atmospheric pressure and their good scaling-up to industrial applications. There are many arangments for the DBD as shown in figure 4.4. The operating principle for a dielectric barrier discharge based on small gap in between two dielectric electrodes filled with a gas. This gap or the distance is typically less than one millimetre. At one of the DBD electrodes, a high voltage is applied. The other electrode is electrically grounded. As the voltage applied to the live electrode (high voltage) increases, the electric field increases.

Any free electrons in the gap will be accelerated. If the electric field is strong enough they may acquire enough energy to cause ionization. This can lead to a cascade effect where the number of energized electrons in the gap increases exponentially in a nanosecond time scale. Electrons created via electron impact ionization drift toward one of the DBD electrodes in each pulse, in the opposite direction to the electric field. An equal number of ions are also generated during electron impact ionization (Eliasson and Kogelschatz, 1991).

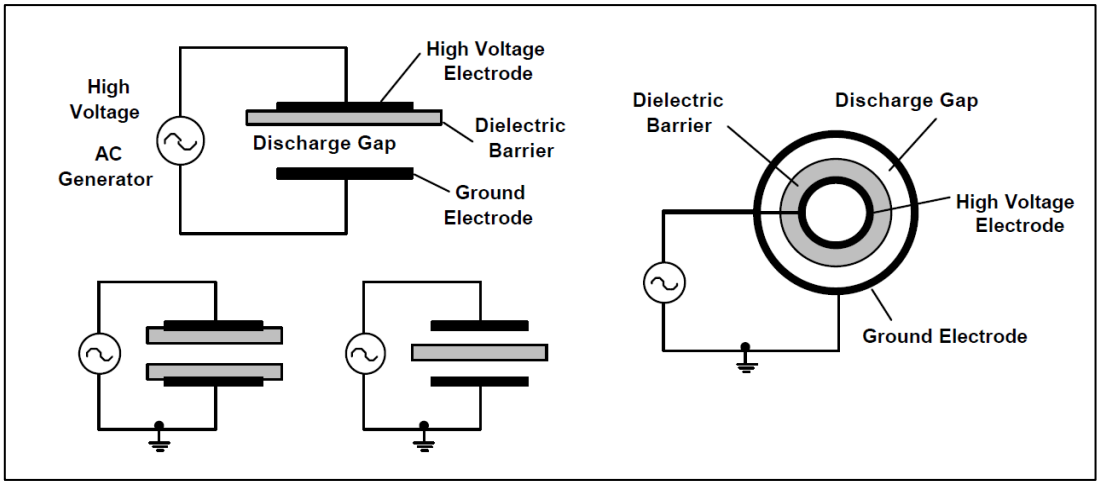

Figure 4- 4. DBD electrodes arranged in planar and cylindrical geometries.

The moment that ionization begins at any position in the gap between the electrodes, transported charge accumulates on the dielectric. Accumulated charges reduce the field in the gap and interrupts the current flow after a few nanoseconds. Therefore the current pulse durations depend on the gas ionization characteristics, the pressure, and on the dielectric properties. In fact, the electric field across the gap cannot exceed the breakdown electric field, which is highly dependent on the gas and background pressure. The breakdown electric field is also a function of the surface properties of the dielectric material. Surface charge accumulation temporarily terminates the discharge until the field reverses direction. Subsequently, this process repeats in the opposing direction. Dielectric barrier discharges typically operate in the pressure range of 0.1–3 atm. with an applied voltage of 1–100 kV and a frequency of kHz up to MHz. The dielectric barriers are usually made of quartz, glass, or ceramic material. A quartz dielectric is used in a CO_2 plasma generator in this study due to it is transparency thus allowing optical observation. Also, the literature reports other types of barriers which enhance the CO_2 reactivity, while increasing the density of the filaments in the plasma (Aerts, et al., 2015). The dielectric role is usually to limit the charge carrier supply, producing a local electric field by charging the dielectric (Dinklage *et al.*, 2005). Electrode spacing is typically small, ranging from 100 μm up to several mm. Table 4.1 shows the main parameters and operation conditions of DBD. Typically, a large number of short-lived discharge filaments can be observed.

The micro-discharges have duration of 1to 10 ns, with a diameter about 0.1 mm, and current density of 10^2 to 10^3 Acm^{-2}. Discharge voltage in wide range of 3 kV to more than 20 kV and frequency of between 50 Hz to more than 10 kHz are applied. It is important to note, however,

that plasma due to micro-discharge is non-thermal and characterized by density of 10^{14} to10^{15} cm $^{-3}$ and $T_e \approx 1$ to10 eV.

Table 4- 1. Dielectric barrier discharges with typical operation conditions adapted from (Wagner et al., 2003).

No.	*parameter*	*value*
1	Electric field strength E of first breakdown	150 Td (p=1bar, T=300 K)
2	Voltage V_{pp}	3–20 kV
3	Repetition frequency *f*	50 Hz–10 kHz
4	Pressure p	1–3 bar
5	Gap distance g	0.2–5mm
6	Dielectric material	glass, Al_2O_3, ferroelectrics
7	Thickness d	0.5–2mm
8	Relative dielectric permittivity ε_r	5–10 (glass)… 7000 (ferroelectrics)

4.5 Model Description

The chemical kinetics model for CO_2 species includes processes of excitation of electronic states, dissociation and ionization of heavy particles by electron impact, associative ionization, electron attachment and detachment, electron-ion and ion-ion recombination, ion conversion and chemical transformations of neutral particles for ground and excited electronic states. The model is assembled and computed using Comsol Multiphysics (version 5.2a)-Chemical Reaction Engineering Module. This software yields automatic sensing of stiff systems as well as an algorithm for adaptive time-stepping with relative tolerance set to 10^{-6} (Rehman, et al., 2012). A zero-dimensional (well mixed vessel) plasma chemistry kinetic model for CO_2 dissociation at atmospheric pressure and under non-thermal plasma conditions is modelled. All plasma parameters are assumed to be spatially homogeneous. By using the zero-dimensional model, we focus specifically on the reaction kinetics. Therefore, we assume all variables are spatially uniform. We also neglect heat conduction. Most chemical reactions of plasma species and their rate constants are adopted from literature (Aerts et al., 2015) and, (Beuthe and Chang, 1997) while the remaining rate reactions coefficients are calculated by the using Boltzmann equation for electron impact reactions, based on electron energy and cross sections, as shown in appendix B (figure B1). The kinetic model for CO_2 excitation by non-thermal plasma is desired since advanced scenario modelling facilitates the optimization of engineering parameters in the design stage, as well as physical performance during the operation stages. So the main aim of the kinetic model is to investigate the carbon dioxide plasma chemistry. It

would be useful to use the kinetic model to provide initial conditions for the interfacial reaction that is spatially i*nhomogeneous* in chapter six. Our hypothesis is that the interfacial region is where the carbon dioxide and aqueous ammonia reacts in particular conditions, involving plasma effects on the process output.

4.5.1 The modelling equations and chemical species nature

The reactions in appendix B table (B2) are irreversible and the concentration gradient of the species will varied with time as shown in equation (4.6):

$$\frac{dC_i}{dt} = r_i \qquad (4.6)$$

Where C_i is concentration of species *i* in particles.cm^{-3}; t: is time in seconds, and r_i is the rate reaction of species *i* in (mol.cm^{-3} s^{-1}).

Reaction rate for these reactions (r) is calculated by the following equations:

$$r_j = k_j^f \prod_{i=1}^{Q_r} C_i^{-vij} - k_j^r \prod_{i=1}^{Q_p} C_i^{vij} \qquad 4.7)$$

Where k_j^f and k_j^r in equation (4.7) are rate coefficients for forward and reverse reactions, respectively. The rate coefficient is a function of electron temperature for electron reactions as; k =*f* (T_e) where: T_e is an electron temperature. The second term in right-hand side in equation (4.7) is neglected because all the reactions are taken to be irreversible reactions and due to the dilute levels of the products. The gas temperature was 300°K and the computation information as follows; CPU Intel(R), Core(TM)i7-6700HQ CPU @ 2.60 GHz, 4 cores. The model focuses on carbon dioxide, carbon monoxide and oxygen species as shown in table (4.2), seven of these species are a neutral species CO_2, CO, C_2O, C, O, O_2, and O_3, while the others are charged species such as the electrons, CO_2^+, O_2^- and O^- and fourteen excited species of CO_2 , CO, and O_2. Indeed, this model included excited levels of carbon dioxide, carbon monoxide and oxygen molecules, though the excited levels play an effective role in CO_2 molecule discharge and stimulate in DBD plasma.

Table 4- 2. The main species which included in model ions, neutral and excited species.

Neutral and excited	Negative ions	Positive ions
CO_2, O, O_2, CO, CO_2 v_1, CO_2 v_2, CO_2 v_3, CO_2 v_4, CO v_1, CO e_1, CO e_2, CO e_3, CO e_4, C, O_2 v_1, O_2 v_2, O_2 v_3, O_2 e_1, O_2 e_2, O_3, C_2O,	CO_3^-, O_3^- ,CO_4^- , O_4^- , O_2^- O^-	CO_2^+, CO^+, O^+, C^+, C_2^+, O_2^+, $C_2O_2^+$, $C_2O_3^+$, $C_2O_4^+$,O_4^+

4.5.2 Microdischarge plasma and discharge physics

In a simulation of plasma, many species react due to the impact of electron collision. Excitation occurs with the duration of single filaments (~1–10 ns), while neutrals and ions have much slower time scale to proceed the reactions (>1000 s) as shown in figure 4.5. The main challenge here is to develop a computationally efficient model that captures the essential elements of interest from the point of view of the chemical reaction (Sakiyama *et al.*, 2012). Plasma has three special features which are appealing for some related disciplines and chemistry applications: firstly, energy density and temperatures of some species can significantly exceed those in conventional chemical technologies, secondly, by plasma it is possible to produce very high concentrations of energetic and chemically active species (e.g., electrons, ions, atoms and radicals, excited states, etc.), and thirdly non-thermal plasma systems are far from thermodynamic equilibrium, providing high concentrations of the chemically active species while the gas remains at nearly ambient temperature. All these features make plasma more attractive than conventional chemical processes, increases of their efficiency and facilitate some chemical reactions which are impossible to achieve by conventional chemistry (Fridman, 2008).

The breakdown starts at many points followed by the development of filaments, if the local electric field strength in the gap achieves ignition level, these filaments are called microdischarges (Wagner *et al.*, 2003). The plasma processes initiated by energetic electrons mainly depend on initial phases of microdischarge formation which are characterized by a multiplicity of factors such as spatial charge distribution formation and ionization, excitation and dissociation. Chemical reactions are initiated by the excited and ionized species (atoms and molecules) that finally cause the synthesis of a desired products or chemicals (methanol,

ozone, etc.) or pollutant destruction, for example nitrogen oxides, sulfur oxides, hydrogen sulfide, etc. (Eliasson *et al*., 1994).

In the majority of DBD applications, charged particles disappear or decay before any major chemical changes happen, therefore free radical chemistry involving neutral species like atoms, molecules and excited molecules will be more effective. Microdischarges have the main role for discharge and energy dissipation, so set the primary conditions for resulting chemical reactions. Eliasson (1994) mentioned that the homogeneous discharges of plasmas can be obtained at high pressures (1 bar) if using a large concentration of some noble gases He or Ne, or using some special additves or using a pulsed discharge. Lozano-Parada and Zimmerman (2010) show that for any plasma reaction that is sufficiently fast, the microfluidic plasma reactor can achieve low power consumption at low voltages and atmospheric pressure by suitable choice of gap thickness and operating conditions.

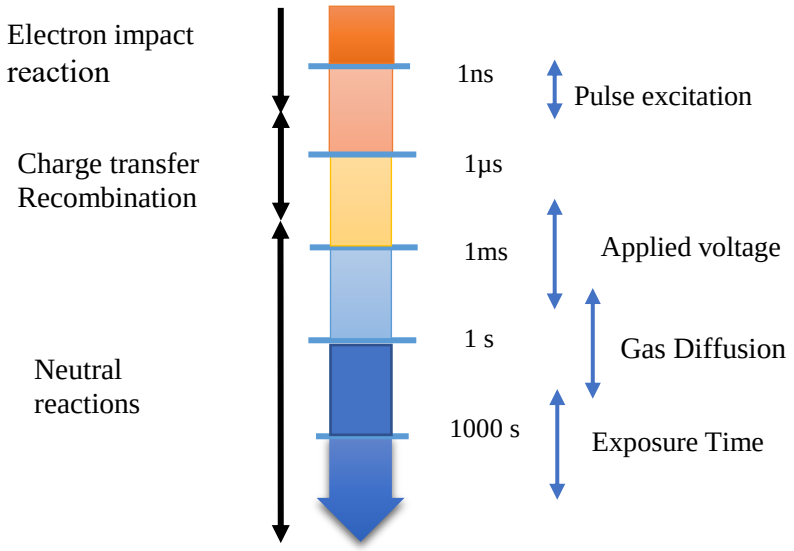

Figure 4- 5. The time scale for plasma reaction adapted from (Sakiyama et al., 2012)

The great potential of plasma technology for CO_2 conversion is due to the presence of energetic electrons. As the electrons are much less massive than the other plasma species, they gain the most energy from the electric field, and they do not lose their energy so readily by collisions with the other plasma species, explaining their persistently higher energy. So several researchers have compiled modelling for CO_2 plasma (Taylan and Berberoglu, 2013; Bogaerts *et al.*, 2015) to investigate in detail the role of the various processes contributing to CO_2 splitting. Bogaerts et al. (2015) show a simplified reaction scheme of carbon dioxide as illustrated in figure 4.6.

Dielectric barrier discharge accords the electrons a non-stationarity and inhomogeneity. These characteristics are not obtained by microwave or glow discharges. Although the corona discharge is usually inhomogeneous, but it may be either stationary or nonstationary. The single transition of a microdischarge causes spatial inhomogeneity for the DBD discharge. The microdischarge initiation usually depends on favourable conditions like high local field strength, nature of electrode surface and initial electrons. Microdischarges eventually become "self-propagating" more or less independent to their surrounding environment. So the nature of this kind of discharge is inhomogeneous. The random distribution of microdischarges leads to filling the available space moderately over time, so the inhomogeneity of dielectric barrier does not imply negative effects.

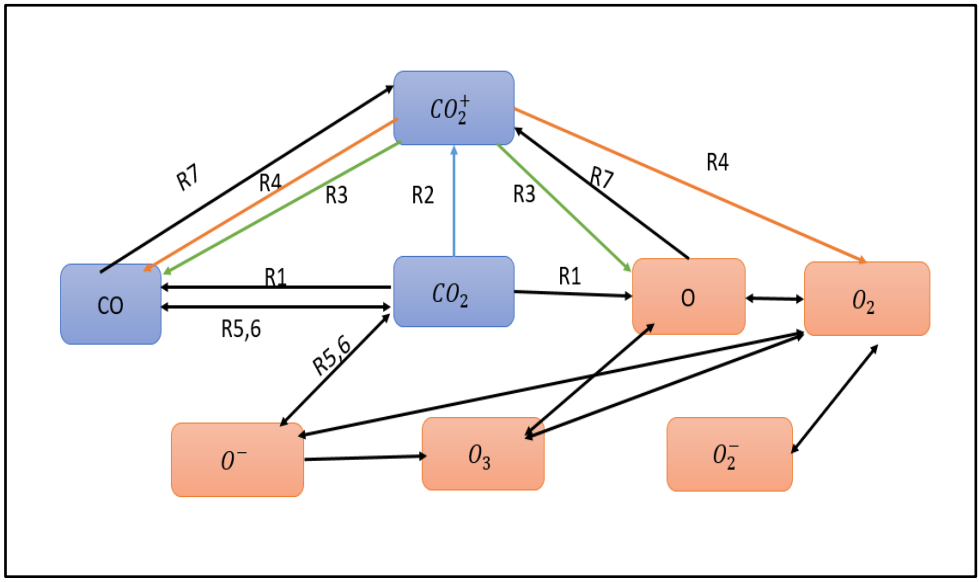

Figure 4- 6. The chemical reaction (R) scheme of CO_2 splitting and further reactions between O, O_2 and O_3, as predicted by the model. The labels of the arrows are explained in the text. (Adapted from (Bogaerts et al., 2015b)

In general, this could explain the underlying reaction paths of CO_2 species. The main reactions of CO_2 are electron impact dissociation into $O^{\cdot}$ as a radical and CO (R1), also electron impact ionization into CO_2^+ (R2). This ion reacts with oxygen molecule or an electrons to form carbon monoxide (R4). At shorter residence times, singlet O atoms recombine into oxygen molecules or ozone. The CO_2 molecules take part in different reaction paths: dissociation, ionization as well as excitation in DBD discharge. On the other hand, Eliasson (1994) indicates that 40 % of the electron energy, could be utilized for the dissociation process, while about 70 %, 97 % for the excitation and vibration respectively as shown in figure 4.7. The efficiency of any processes of the plasma reactions depends on two factors; the electron energy distribution function and on their cross sections for electron collisions. The updated cross-section data set for CO_2 is

shown in figure 4.8. The energy loss spectrum for electron is measured at various energies of 30 to 200 eV, for the scattered electron angle range from 3.5° to 130°(Anzai *et al.*, 2012). The electron energy influenced by changing the product of (*nd*) where *n*, is gas density and *d* is the gap width between the electrodes.

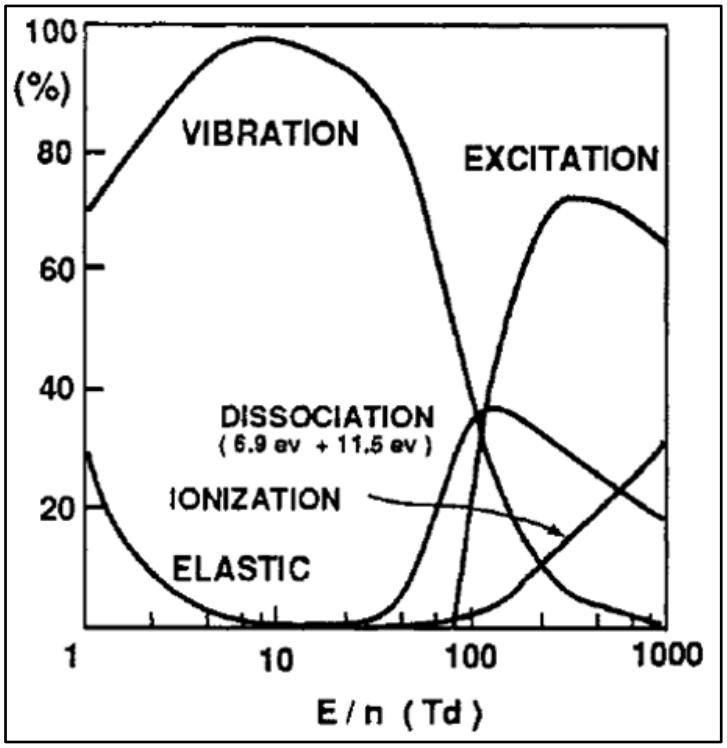

Figure 4- 7. Fractional energy losses of CO_2 molecule, taken from (Eliasson, et al., 1994)

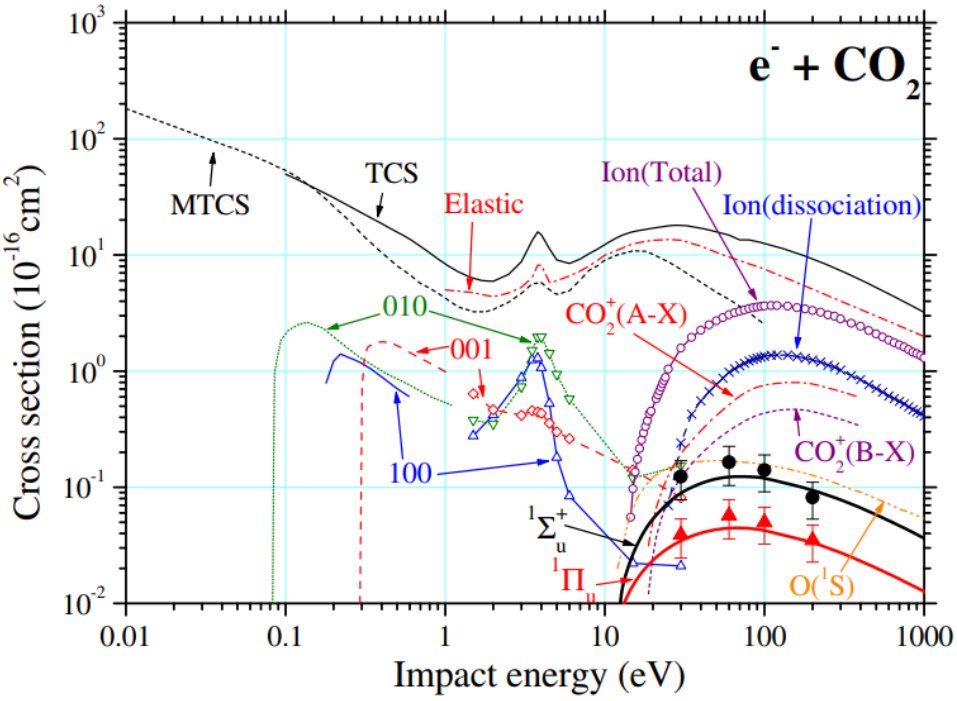

Figure 4- 8. Cross-sections of electron / CO_2 molecule collision, taken from (Anzai et al., 2012)

4.6 The behaviour of species concentration with time

The concentration of carbon dioxide and their related species as a function of time was simulated by Comsol Multiphysics® Reaction Engineering Laboratory (Zimmerman, 2006) with the electron temperatures (T_e = 3 eV). The duration of a single DBD streamer is of the order of a few nanoseconds (Fridman, 2008). The model was run in two periods, the first was the pulse from (0 to 40 ns) and the second one after the pulse (40 ns to 1 s) using piecewise function for electron temperature to calculate the rate coefficient of reactions and then rate of reaction. CO_2 molecule has three modes of vibrational levels; symmetric stretch (100); doubly degenerate bending mode (010), (020) and asymmetric (001). The dissociation of the molecule with each mode is assumed independent from each other. That is due to the low value of the characteristic vibrational energy as shown in table 4.3.

Table 4- 3. The vibrational levels considered in this model with their notations and energy.

Notation	Vibrational levels and modes	Vibrational state	Energy [eV]
CO_2	Ground state	0 0 0	0.000
CO_2v1	1st bending mode	0 1 0	0.083 eV
CO_2v2	Second bending + 1st symmetric stretch	020 + 100	0.17 eV
CO_2v3	1st asymmetric	001	0.29 eV
CO_2v4	Sum of higher bending and symmetric stretch	0n0 + n00	2.50 eV

This study focuses on excited state of CO_2 and not on the dissociation state (Fridman, 2008; Kozák and Bogaerts, 2015). Carbon dioxide is a linear tri-atomic molecule as was mentioned before, with no dipole moment appearing in the ground state, but one is induced when either the bending or asymmetric stretching modes are excited (Kitajima *et al.*, 2001).

4.6.1 Rate coefficient computation

The rate coefficient of these vibrational level calculatetd using Boltzmann equation for electron impact reactions, based on electron energy and cross sections as mentioned in model discription in section 4.5. It could be determined by the electron energy distribution function (EEDF) f (ε),which depends on gas composition and electric field. EEDF can be calculated depending on the electron temperature (T_e) according to Maxwell-Boltzmann distribution function:

$$f(\epsilon) = 2\sqrt{\epsilon/\pi(kT_e)}\, e^{-(\epsilon/kT_e)} \quad ---- \ (4.8)$$

Where k is a Boltzmann constant (k =1 if the temperature is given in energy units eV). The unknown rate coefficients (k) are determined using published cross section database and using the *BOLSIG plus* solver (Hagelaar, 2019). The rate coefficients were plotted against the mean elecron energy (Maxwellian EEDF) ‹ε› as illustrated in figure 4.9. Through using equation (4.9) to convert the relation as a guide for the electron temperature (T_e) in order to use these coefficients in the model:

$$\text{‹}\varepsilon\text{›} = \int_0^\infty \epsilon\, f(\epsilon) d\epsilon = \frac{3}{2} T_e \qquad ---------- (4.9)$$

The results show that the concentration of vibrational excited species is varied with time for each level in the discharge region (see section 4.5.2). The concentration change is usually related to reaction rate coefficients (k_i), for instance, reaction 12 with k_{12} in figure 4.9 shows very limited change with time so this behaviour appears clearly identically as in figure 4.7

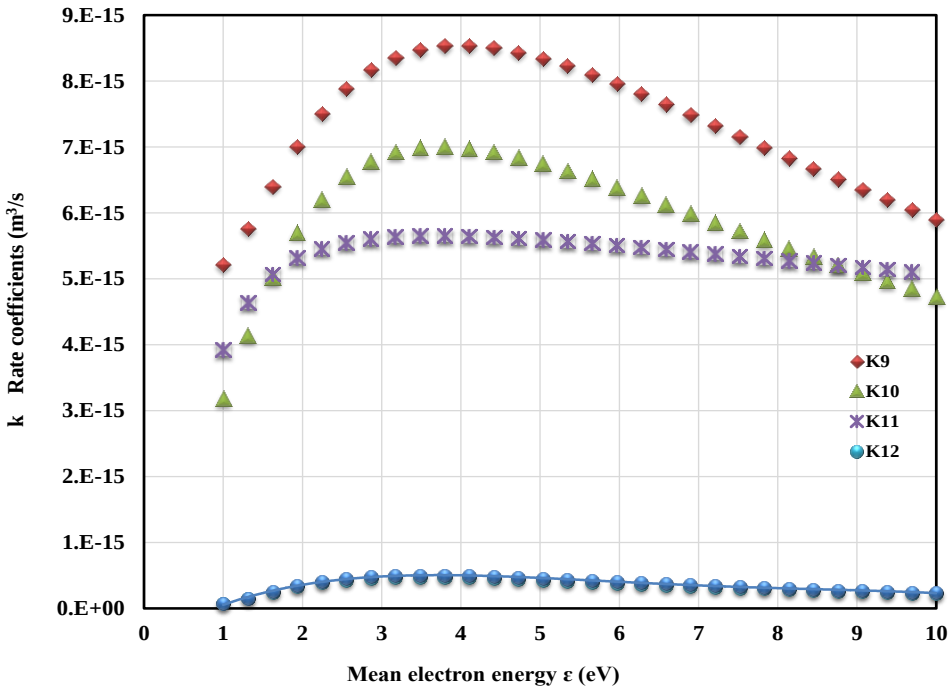

Figure 4- 9. The relation of rate coefficients of vibrational excited levels of CO_2 as a function of the mean electron energy, where; k9, k10, k11, k12 are related to the reactions 9, 10, 11and 12 as shown in table B2 appendix B

$e^- + CO_2 \rightarrow e^- + CO_2v_1$	reaction 9
$e^- + CO_2 \rightarrow e^- + CO_2v_2$	reaction 10
$e^- + CO_2 \rightarrow e^- + CO_2v_3$	reaction 11
$e^- + CO_2 \rightarrow e^- + CO_2v_4$	reaction 12

4.6.2 Vibrational excited levels of CO_2 behaviour

Figure 4.10 shows a simple comparison for the concentration of the vibrational levels as function of time for a discharge pulse of 40 ns and its afterglow. It is clear that the vibrational state (CO_2v_4) has the lowest concentration value, followed by CO_2v_3 while the 1st bending mode (CO_2v_1) and (CO_2v_2) have higher value than other levels. This behaviour of vibrationally excited species could be elucidated according to their threshold energy of excitation (see table 4.3). The lowest threshold energy for the first vibrational state (CO_2v_1) and by relaxation of the higher vibrational states to lower levels, controlled by vibration-vibration transfers (Fridman, 2008). The transfer process leads to an increase in concentrations of lowest vibrational levels, (reactions 169-188) table (B2) in Appendix B, so, at 100 µs, the concentrations of the lowest vibrational state start decrease. This does not seem to be a negative point because it has been recommended by Aerts et al. (2012) that the DBD has a series of continuous pulses spread out across volume of discharge and the time. Accumulation effects in the concentrations of some plasma species could have eventually occurred if the inter-pulse time is shorter than the relaxation time of these species. The vibrationally excited species which are diffused in-between the filament of micro discharges, which are usually free of charge could be stimulated to participate in a chemical reaction before the next discharge hits at the same point.

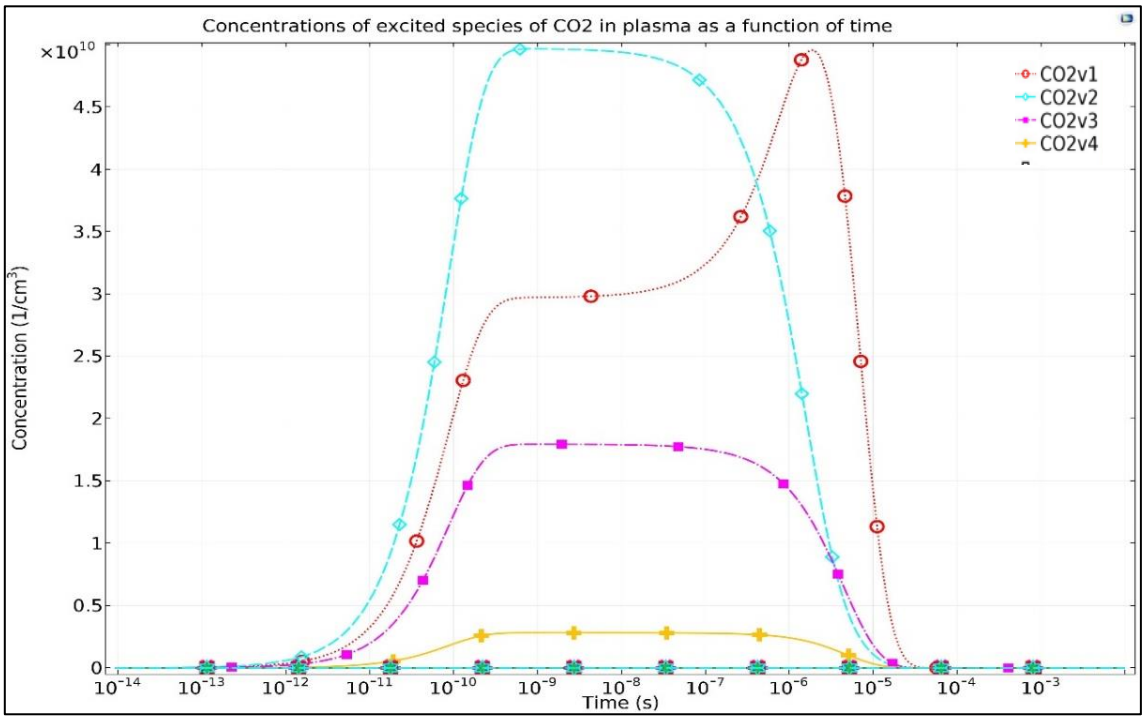

Figure 4- 10. Concentration-time variations of vibrationally excited species of CO_2 with a pulses of discharge.

4.6.3 The behaviour of charged and neutral species

The behaviour of concentrations of selected charged and neutral species as a function of time during a pulse of discharge are presented in figure 4.11. Fridman and co-workers stated the further increase of the CO_2 gas pressure and, with decrease of reduced electric field results in a more intensive excitation of the symmetric CO_2 vibrational modes. As consequence, these changes lead to a higher VT-relaxation rate, faster gas heating, and a decrease in the degree of VT non-equilibrium. It is obviously there are ions such as $C_2O_2^+$, $C_2O_3^+$, CO^+, CO_2^+, O^+, O_4^- re-combined instantly after discharge pulse, so their concentration effect have not significant,. However, according to our hypothesis, we do not need to go deeply in details about the positive ions reactions. These ions do not play a significant role in the CO_2 reaction mechanism in next part of the study, so can be neglected. The CO_2 molecules dissociate into different ions in plasma media, but in this model the main species observed with high concentrations and more stability are CO_3^-, CO_4^-. These ions form as a result of third body reactions of negative oxygen ions (O^-, O_2^-) respectively with carbon dioxide:

$$O^- + CO_2 + M \rightarrow CO_3^- + M \quad ------(\text{reaction 83 table B2 in Appendix B})$$

$$O_2^- + CO_2 + M \rightarrow CO_4^- + M \quad ------(\text{reaction 84 table B2 in Appendix B})$$

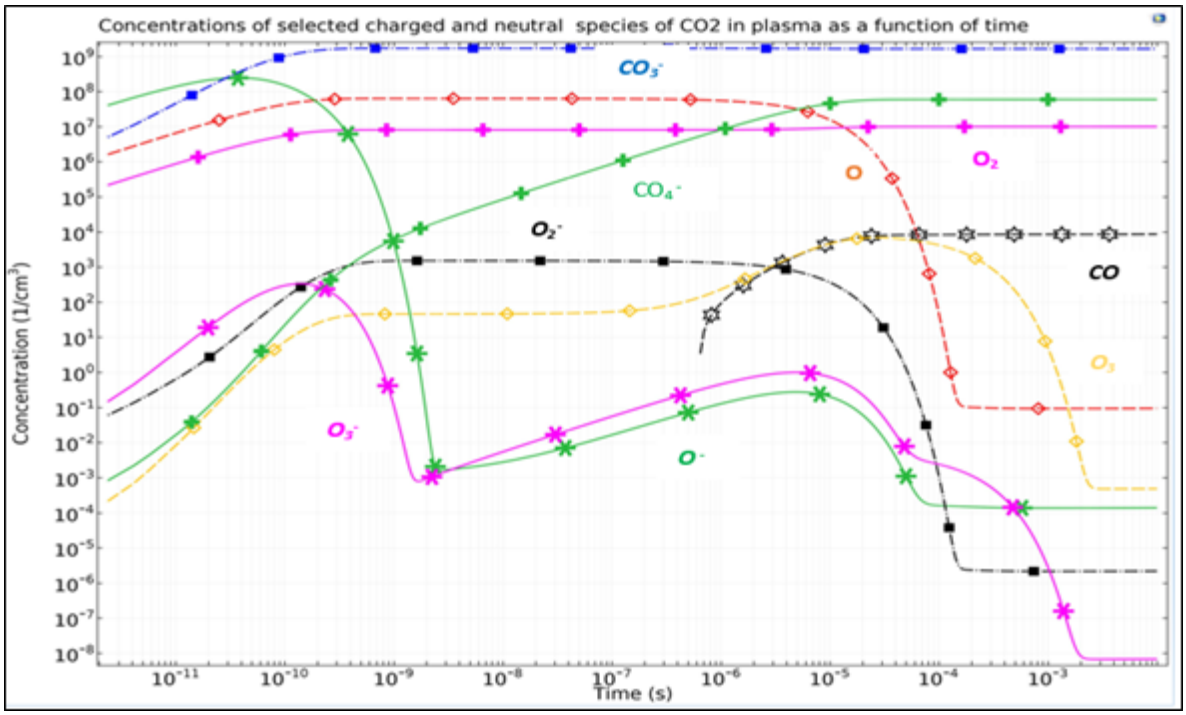

Figure 4- 11. Concentrations of a selected charged and neutral species as a function of time with a pulse of discharge.

Generally, these ions could be considered as along lived ions. But again this is not common and their loss mechanisms do not play a significant role in CO_2 plasma reactions in the current study. The CO and O_2 are the main products of CO_2 dissociation with high concentrations. The explanation for this result is the contribution of various plasma species in CO_2 splitting under the influence of high electric field discharge to O_2 and CO. Plasma generate many reactive species which are recombined with each other to produce O_2 and CO. See for instance the reactions (50, 51), and (53, 54) respectively as discussed in section 4.2 and as shown table B2 in Appendix B.

4.6.4 The behaviour of oxygen species

Oxygen has a concentration two orders of magnitude higher than carbon mono oxide as shown in figure 4.12. The figure presents the concentrations of O_2, O_3, and their excited levels, positive and negative ions as a function time with pulse discharge. However, the other branch in plasma chemistry of CO_2 is the related behaviour of oxygen species (O^-, O^+, O_2^-, O_2^+, O_3^-, O_3, O_4^+ and O_4^-) as well as the vibrational and electronic excited species of oxygen. The attachment of the electrons with neutral species drives to formation of negative ions with charge 1.6×10^{-19} C. Electric repulsion prevents the formation of multi-charge negative ions in the gas phase with repeated electron attachment. Indeed, the negative ions are considered heavy particles. They gain their energy from the collisional processes, not from the electric field (Fridman, 2008).

Atomic oxygen, molecular oxygen and ozone are the main reaction product in long time scale. The selection of these species as separate group relates to differences in concentrations with time compared to the overall model behaviour shown in figure 4.10. It is clear the concentration of ozone, for instance more stable relative to its behaviour in figure 4.12, is dramatically reduced at the 100 μs region. The same occurs with atomic oxygen.

However, the vibrational and electronic excited levels of the oxygen do not respond to the pulse as shown in figures 4.12 and 4.13. This may be because the energy requirement to dissociate or vibrationally excited the molecule is insufficient to activate these levels, therefore does not reduce contribute to reactions. The concentrations of ions O^-, O^+, O_2^-, O_3^- and O_4^- reduce directly after the pulse time (10^{-5} s) to negligible values as these species may be converted to O_2 and ozone according to reactions 77 and 78 in table B2 in Appendix B. Although the O^+ and O_2^+ concentrations also drop but not with the same behaviour, their reduction is less abrupt, with the O^+ concentrations higher than the O_2^+. The overall simulation of species as function of time is plotted in figure 4.13. Comparing the figures 4.10, 4.11 with 4.12 of the results, it

can be seen that there are some species that do not appear in previous figures profiling simulations, for instance CO_2^+, CO_{v1}. On the other hand, some neutrals are not observed such as C_2O. Excited electronic states of CO_2 also are not noticed in the model due to their requisite high energy (more than 5 eV) from the ground state. Vibrational and electronical excited species of oxygen are slightly increased for nanoseconds, then subsequently invariant. This may be due to their rate coefficient independence of electron temperature (calculated as a fixed value at 3eV by using Boltzmann equation module). Other ions and neutrals appear in model, but with a low concentration such as; $C_2O_2^+$, CO^+, $C_2O_3^+$, $C_2O_4^+$, O_4. It is clear that the main reactions occur with ground state of CO_2 to ionization and dissociation to CO and O.

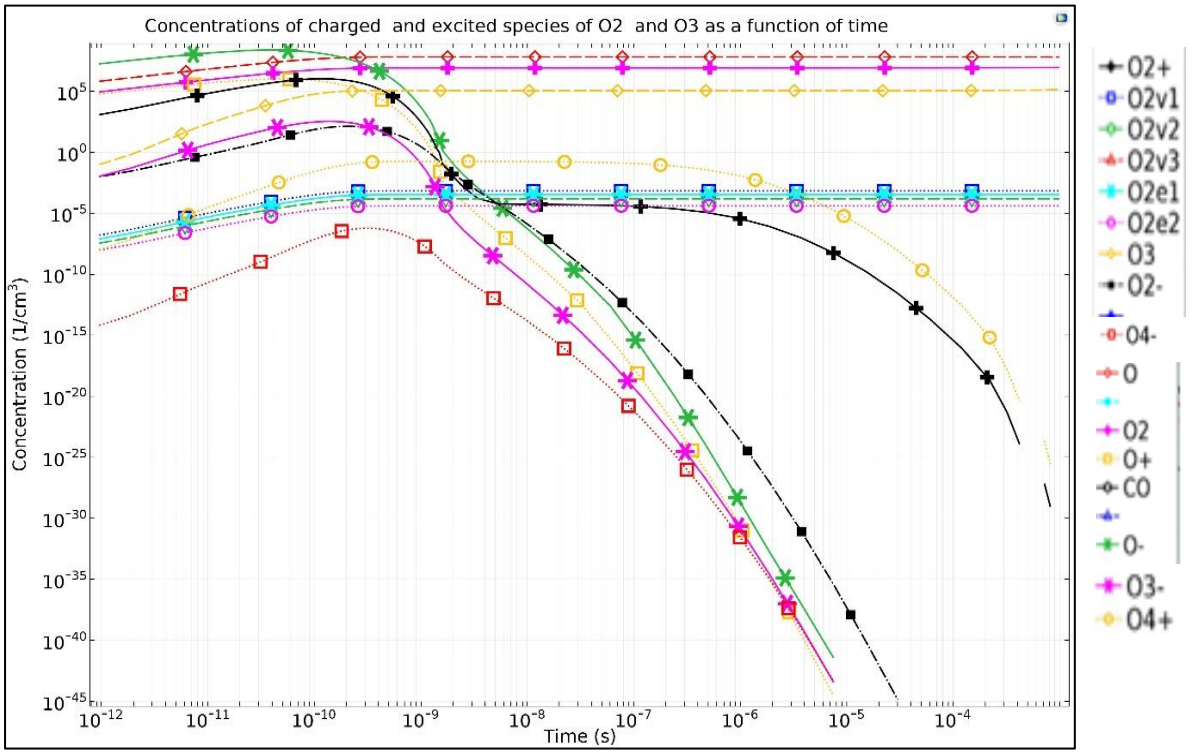

Figure 4- 12. Concentrations of O_2, O_3, and their excited levels, positive and negative ions as a function of time with a pulse discharge.

The excited levels of CO_2 concentrations decrease in an interval of milliseconds from 10^3-10^4 to 10^{-8} ($1/cm^3$) that coincides with increasing in CO_4^- and CO concentrations in same period of time (figure 4.13). In general, electrons colliding with a CO_2 molecule produce many different kinds of positive ions, and each channel of respective ion possess their own energy (Itikawa, 2002) as shown in table (4.5).

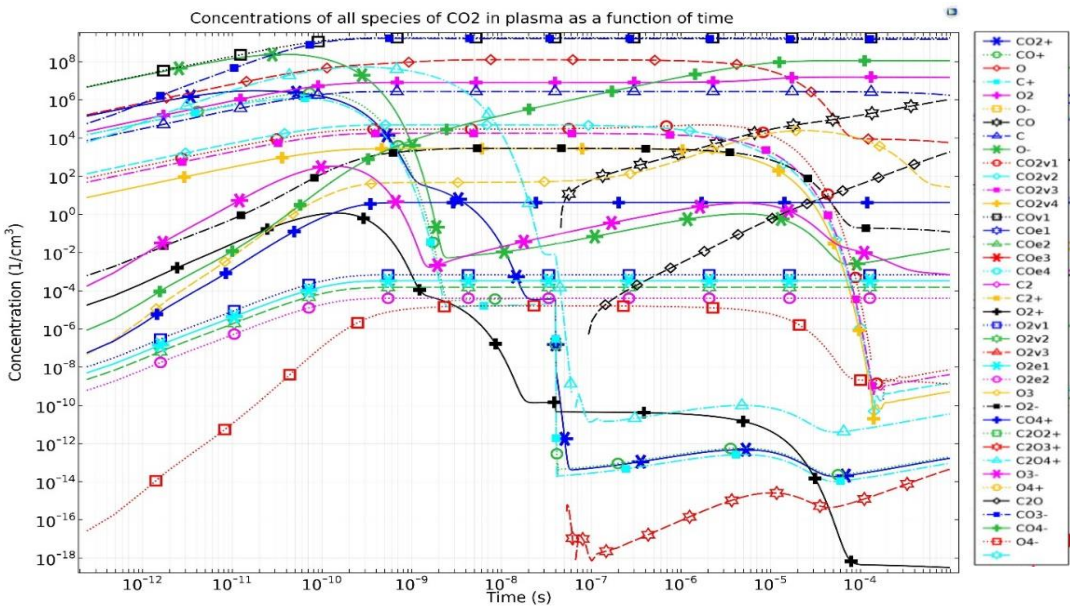

Figure 4- 13. Concentrations of all ions, neutral and excited species of CO_2 in plasma as a function of time with a pulse discharge in a single microdischarge streamer.

The majority of positive ions can be neglected from this model because their ionization energy (see table 4.4) is considerably higher than that of our assumption which is 3 eV. Some neutrals are of interest such as atomic oxygen O which is produced by the electron impact dissociation of CO_2:

$$e^- + CO_2 => CO + O + e^- \qquad see\ reaction\ (8) in\ table\ (B2)$$

Table 4- 4. illustrates the energy of some positive ions of carbon dioxide. Adapted from (Itikawa, 2002).

NO.	Reaction	Ion produced	Energy of ionisation
1	e+CO_2 =>	CO^+_2	13.8 eV
2	e+CO_2 =>	CO^+	19.5 eV
3	e+CO_2 =>	O^+	19.1 eV
4	e+CO_2 =>	C^+	27.8 eV
6	e+CO_2 =>	C^{++}	51.2 eV

The peak concentration of O is (10^8 cm^{-3}) as shown in figure 4.9, which has a significant concentration even in the millisecond range, O is quickly consumed by O_2 to form ozone:

$$O + O_2 + M => O_3 + M \qquad see\ reaction\ (76)\ in\ table\ (2)$$

The results show that the concentration of vibrationally excited levels of carbon dioxide is higher than the other vibrationally excited species of oxygen.

4.7 The influence temperatures on species concentration

4.7.1 Electron temperature (T_e)

The electron temperature is initially higher energy than the other heavy particles in plasma media. Thereby, the electrons gain their energy from the electric field within their mean free path. As electron is much lighter than a heavy particle, it loses a limited portion of energy by collision with a heavy particle. Thus, repeated collisions of the electrons with heavy species could equilibrate the temperatures if there are enough time and energy.

In plasma modelling, there are important input factors such as the electron density, electron temperature, and the gas temperature and pressure. The first two factors are related to the plasma conditions and are determined by solving the electron dynamics of the plasma. While the gas temperature and pressure are considered as the process conditions and could be set by the conservation equations of heavy species. Electron temperature in plasma is initially higher than that of heavy particles because electrons receive energy from the electric field (electrons are much lighter than the heavy particles) and lose only a small portion of that energy during the subsequent collisions. In low ionized plasma, the collisions between electrons and heavy particles lead to generating temperature difference due to Joule heating. This temperature difference is proportional to the square of the ratio of the electric field to the pressure (Fridman, 2008).

In general, the plasma temperature is considered as the starting platform for the ionization because electron temperature is about 1 eV (≈ 10,000 K), which is 10% of the total energy required for ionization process (the Arrhenius activation energy). Furthermore, increasing T_e produces high ionization rates due to the increasing electron density. It could also be said that the increase in the electron density will yield an increase in the electron impact reaction rate. Another significant factor is gained from this increasing, which is the multiples the concentration of excited particles, consequently, increasing the rates of all reactions.

The simulation results show that the vibrationally excited levels of the CO_2 have different responses to increasing the electron temperature as illustrated in figure 4.14. The gas temperature is fixed at 300 °K during the computation of the concentration for a duration time of 1 second and at electron density 1.65×10^{15} cm^{-3}. The second bending and 1st symmetric stretch (CO_2v_2) has an interesting increase in the concentration versus the electron temperature. Nevertheless, the other levels of vibrational excitation persist with very limited changes compared to the second level. The vibrational energy levels in CO_2 begin at 0.17, 0.08, and

0.29 eV for the CO_2v_2, CO_2v_1, and CO_2v_3 respectively as shown in table 4.3. The fourth mode begins at 2.5 eV, representing the sum of higher bending and symmetric stretch does not have a significant concentration change in this model. The other neutral and charged species are also simulated under the same conditions of time pulse and gas temperature. As we mentioned before our objective is focusing on the behaviour of the vibrationally excited species and not on the dissociation process of CO_2.

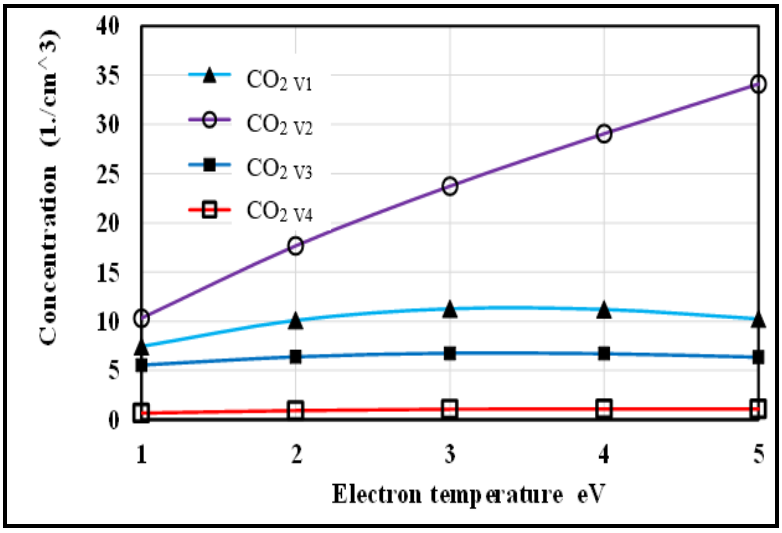

Figure 4- 14. Concentration of vibrational excited CO_2 levels as function of electron temperature

4.7.2 Gas temperature (T_g)

Generally, at a steady concentration of species, the electric field will be constant. But if there are driving forces to change the density of the species in plasma media, e.g., chemical reactions, then a high current flow could cause a gas temperature increase. Whenever the gas temperature increases, then the desired discharge voltage will decrease and eventually the total voltage of plasma will decrease. Temperature differences in various non-equilibrium discharge systems allow a specific selection of organization of the CO_2 decomposition in the plasma region. Accordingly, the energy will be directed to the relevant channels of the process.

The concentration of vibrationally excited CO_2 levels as function of gas temperature are shown in figure 4.15. The electron temperature is fixed at 1 eV during the computation of the concentration for a duration time of 1 second and at electron density 1.65×10^{15} cm^{-3}. What is surprising is the concentration decrease of the first three modes of CO_2v_1, CO_2 v_2, and CO_2 v_3 while increasing the gas temperature. So that the concentrations was 7.43, 10.36 and 5.5 cm^{-3} for the previous modes respectively at 300 °K. Another finding is related to the concentration of the fourth mode CO_2 v_4. There is a sharply change with gas temperature. The increase begins

from 200 to 270 °K, but then gradually dropped in the higher range of temperature. On the other hand, the relation of rate coefficients of vibrational excited levels of CO_2 as a function of the mean electron energy are plotted as shown in appendix B. The plots of rate coefficients are given in appendix B1.

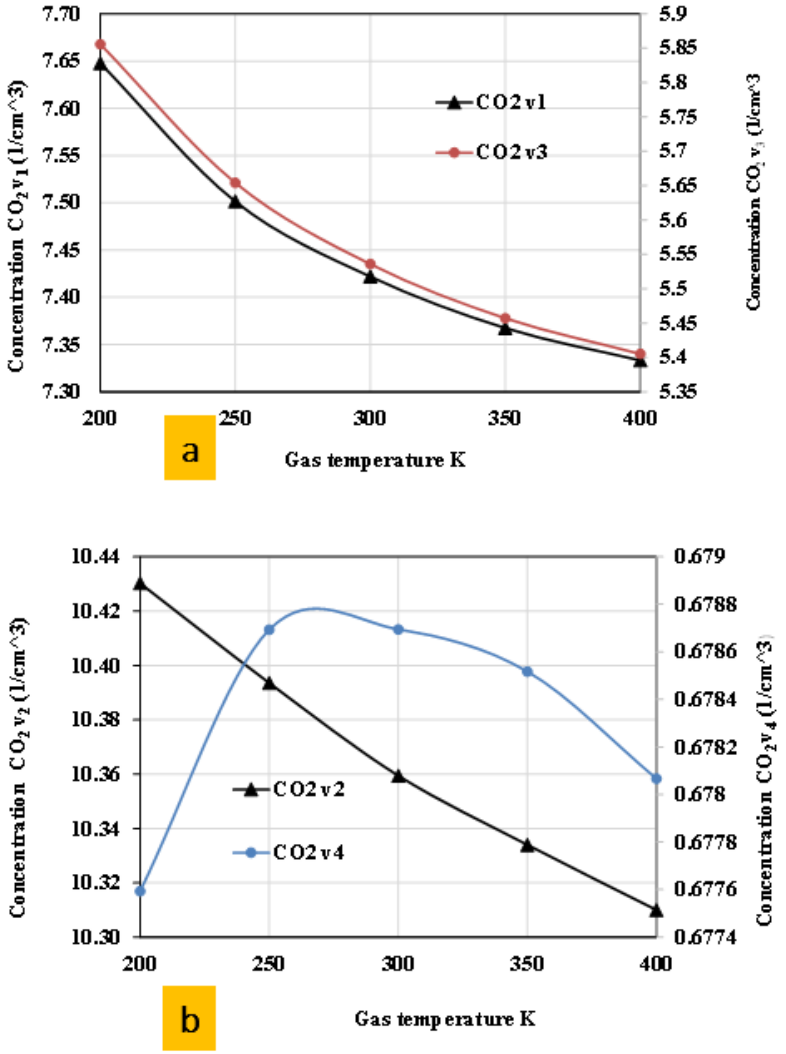

Figure 4- 15. Concentration of the vibrational excited CO_2 levels as function of gas temperature, (a) illustrates the vibrational excitation modes CO_2 v_1 and CO_2 v_3 while (b) shows the vibrational excitation modes CO_2 v_2 and CO_2 v_4

4.8 Model validation

The concentration measurement of the excited species of carbon dioxide directly is usually a matter of considerable difficulty. Therefore, the validation of the model can be achieved by comparing predicted effects with the results of our experimental study of the reaction CO_2 gas with aqueous ammonia solution. Chapter six of this study is associated with the reaction of the pure carbon dioxide gas activated using non-thermal plasma before inserted to a reaction column with aqueous ammonia solution. The influence of input high voltage on the productivity of the chemical reaction is shown in the figure 4.16.

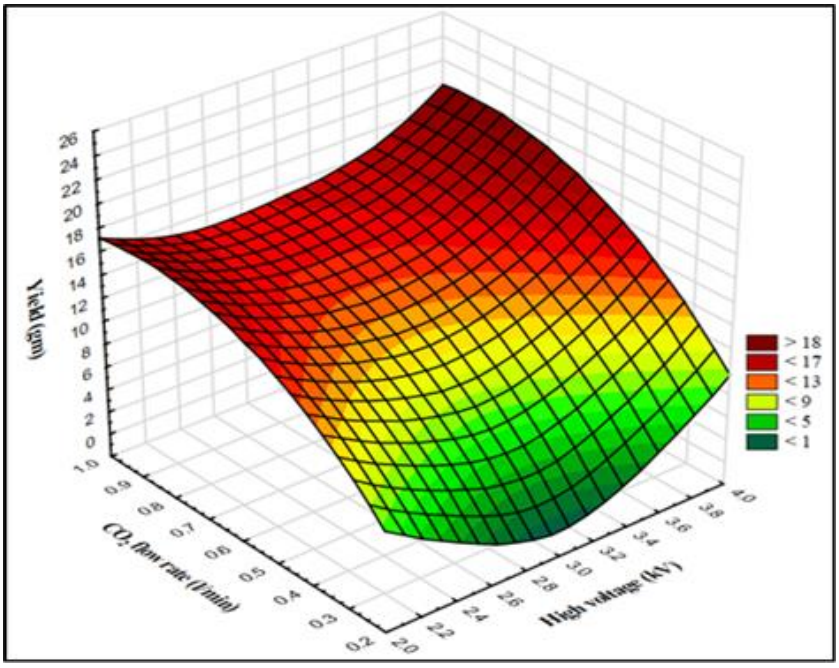

Figure 4- 16. The effect of the input high voltage of the non-thermal plasma on exciting CO_2 molecules to react with aqueous ammonia. The yield of reaction process studied at interaction of parameters; high voltage with CO_2 flowrate.

The results show that increasing the high voltage to more than 3kV increases the yield of the process. The precipitated solid is mainly ammonium bicarbonate. It is formed as evidenced by the analysis using NMR spectrum. The CO_2 flow rate used is 0.8 L/min. that means the gas velocity inside the reactor of an inside diameter (4.5 cm which gives cross area of 15.9 cm^2) was 0.8 cm/s. The solution volume was 150 cm^3, the height of the solution is 9.43 cm. So, the retention time could be calculated of the gas inside the reactor (the liquid height divided by the gas velocity) to be approximately 11 seconds. As we predicted in our hypothesis the non-thermal plasma can play an effective role to activate CO_2 molecules to participate in chemical reactions (for more details see chapter six).

4.9 Conclusion

Low-temperature plasmas represent the combination of fluid mechanics, reaction engineering, physical kinetics, heat transfer, mass transfer, and electromagnetics. The Comsol Multiphysics Plasma Module is a specialized tool for modeling non-equilibrium discharges which occur in a wide range of engineering disciplines. The overall conclusion is that this model provides a basic framework for investigating the non-thermal plasma effects on carbon dioxide chemical behaviour in a dielectric barrier discharge. Although the quality of currently available data necessary for quantification is generally poor, nevertheless, a theoretical model that assumes a stable excitation discharge and homogeneous plasma is developed. This model could be used

to predict and explore chemical reactions in the discharge plasma region. Furthermore, the effect of non-thermal plasma on CO_2 molecules and their chemical species which are produced and their chemical concentrations as function of very short time are modelled.

- The results of the carbon dioxide model show that the main species with high concentrations and more stability are charged ions and neutrals, whilst the excited levels occurred at low concentrations in milliseconds region varies from 10^3-10^4 to 10^{-8} ($1/cm^3$) that coincide with increasing in O_2 and CO concentrations in same period of time. The excited molecules are energized and have a high ability to react more than the ground-state molecules.
- The simulation results show that the vibrationally excited levels of the CO_2 have different responses to increasing the electron temperature at a constant gas temperature. The second bending and 1st symmetric stretch (CO_{2v2}) has an interesting increase in the concentration versus the electron temperature compare to the other levels.
- The concentration of vibrationally excited CO_2 levels as a function of gas temperature show the concentration decrease of the first three modes of CO_{2v1}, $CO_{2\ v2}$, and $CO_{2\ v3}$ while increasing the gas temperature. So that the concentrations are 7.43, 10.36 and 5.5 cm^{-3} for the previous modes respectively at 300 °K and 1 eV. While the fourth mode $CO_{2\ v4}$. There is a sharply change with gas temperature. The increase begins from 200 to 270 °K, but then gradually dropped in the higher range of temperature.

- The exciting molecules importance in reaction process may stem from the shift of the threshold to a lower energy level and the increased cross-section (Kim *et al.*, 2016). Although the concentrations of vibrationally excited species decreases with time, that could be overcome using DBD characteristics of continuous pulses. This feature could enhance the vibrationally excited species across the volume of discharge and the time. So the short path between the plasma source and reaction place (liquid medium) is necessary.
- The influence of input high voltage on the productivity of $CO_2/NH_{3\ (aq.)}$ reaction is tested. The design parameters are: the CO_2 flow rate used is 0.8 L/min. i.e. the gas velocity inside the reactor is 0.8 cm/s. The aqueous ammonia solution volume is 150 cm^3, the reactor cross-section area is 15.9 cm^2, gives a solution height of 9.43 cm. Thus the retention time of the gas inside the reactor is 11 seconds. The outcome shows that increasing the high voltage to more than 3kV increases the yield of the process.

It is concluded that there may be additional factors that are difficult to include within 0D model such as reduced field E/n, effect of high pressure in reactor and the energy efficiency, which may be possible with 1D, 2D or 3D to get a clear idea about the kinetic reactions in plasma. This will be a future work and will solidify understanding of the important non-thermal plasma processes which are the key to applications in the industrial field. Finally, by the integration of experimental work with simulations we can acquire more precise information on the process efficiency, in terms of conversion or yields of the reaction products.

Department of Chemical and Biological Engineering

Chapter Five

Thermogravimetric analysis of ammonium salts: development of a chemometric model

Chapter Five

Thermogravimetric analysis of ammonium salts: development of a chemometrics model

5.1 Introduction

Kinetic models and mathematical analysis for solid state reactions have received a wide range attention in different fields of chemical engineering applications. The main aims of studying the kinetics of solid-state reactions are to optimize the effective conditions of storing, in addition having a control over the decomposition behaviour for chemical compounds during the synthesis processes (Ravikiran *et al.*, 2013), (Mamleev *et al.*, 2000). Concerning the above approach, many studies have been conducted on CO_2 /NH_3 reactions in the aqueous solution and their products. Chiefly, that is due to environmental pollution, pollutants and the effects of the greenhouse gasses. This chapter focuses on the properties of the salts which are produced from CO_2 /NH_3 reaction. The major issue with the commonly used approach for "endpoint yields" such as ^{13}C NMR, is that dissolution in deuterated water of ammonium salts is invasive as the salts can interchange. The objective is to develop models which can be used to predict interesting properties based on measured properties of the chemical system. For kinetics models, that interchange could lead mechanism confusion and poor estimates of rate coefficients. One of the objectives of this study is to analyse the use of chemometric modelling of thermogravimetric analysis (TGA) data as an approach to estimating the chemical composition of a binary system of ammonium salts. However, there are three compounds are reported in this study; ammonium carbonate (A), ammonium bicarbonate (B), and ammonium carbamate (C). Since the chemical composition effects on the conversion, processing costs, yield and/or quality of products, the ability to (on-line) determine these characteristics entering the process stream will be useful, and so that the approach is a novel technology. House Jr. (1980) studied the decomposition enthalpies of ammonium carbonate and bicarbonate using differential scanning calorimetry. The mean values of decomposition enthalpies, ΔH_{dec}, were determined according to the reactions as illustrated in reactions (1) and (2), but the values cannot be considered as highly accurate due to the uncertainties in lattice energies:

$$(NH_4)_2CO_3 \xrightarrow{\Delta H\ dec.} 2NH_{3\,gas} + CO_{2\,gas} + H_2O_{gas} \quad 205 \pm 19\ \text{kJ/mole} \qquad (1)$$

$$NH_4HCO_3 \xrightarrow{\Delta Hdec.} NH_{3\,gas} + CO_{2\,gas} + H_2O_{gas} \quad 163 \pm 7\ \text{kJ/mole} \qquad (2)$$

Furthermore, the solid ammonium carbamate decomposes through an endothermic reaction to yield a gaseous mixture of carbon dioxide and ammonia (Johnson et al. 2015). The value of the heat dissociation at constant pressure is 153 kJ/mol (36.6kcal/mol) as according to Bennett et al. (1953), while Schmidt et al., (2012) found that heat of decomposition reaction is 157 kJ/mole, according to the reaction (3). Additionally, the dissolution of solid ammonium carbamate to liquid phase consumed about 10 kJ/mole and 147 kJ/mole to convert from liquid phase to gaseous phase:

$$NH_2COONH_{2\ solid} \rightleftharpoons 2NH_{3\ gas} + CO_{2\ gas} \qquad 157\ \text{kJ/mol} \qquad (3)$$

In the current work the kinetics of decomposition of the above three salts is studied under non-isothermal condition (i.e. heating the sample with a constant heating rate whereas isothermal techniques involve introducing the sample into the heated area at a constant temperature (Hillier et al., 2010)) . Ammonium salts A, B, and C (carbonate, bicarbonate, and carbamate) were heated from 20 to 200° with a different heating rate (2, 5, 10, 15, and 20 °C / min) under nitrogen gas atmosphere and mass loss data were collected.

The Pseudo-inverse method methodology developed in this study enabled the simultaneous prediction of the chemical composition of the initial solid-state mixture from the TG data. To get a better understanding of the decomposition reaction many experiments are conducted by thermogravimetric analysis. The major purpose of this study is to infer the composition (mass fraction) of a sample which might contain one or more of three components using a model of TGA mass loss evolution that can be inverted (calibrated) via linear least-squares pseudo-inversion. In this study, the model uses any two-component system w_1-w_2, w_1-w_3, and w_2-w_3 for the weight fractions of the three ammonium salts, (carbonate w_1, bicarbonate w_2, and carbamate w_3).

5.2 Kinetics modelling

Thermal profile studies using TGA are an excellent tool to promote the kinetics knowledge for the thermal decomposition process. The data collected from TGA experiments are utilized to determine kinetic parameters, starting with an assumption of the reaction order of ammonium salts decomposition (carbonate, bicarbonate, and carbamate). Analysing the derivative of the thermogravimetric curve is another approach, showing peaks corresponding to inflection points of the original TG curve. Taking this into consideration, the general form of reactions for the solid salts dissociation to carbon dioxide and ammonia (Frasco, 1964):

$$a\ NH_{4_S} \triangleq b\ CO_2 + c\ NH_3 \qquad (4)$$

Where NH_{4_S} represents the three ammonium salts (carbonate, bicarbonate, and carbamate). Assuming the rate of decomposition of each salt (S) to be described as in following equation (Coats and Redfern, 1964):

$$\frac{dW}{dt} = k\,(1-W)^{n_i} \qquad (5)$$

Where the n_i is order of the reaction; ***W*** is mass fraction decomposed at a time ***t***. *W* can be expressed as following:

$$W = \frac{w_i - w}{w_i - w_f} \qquad (6)$$

The w_i and ***w*** are the initial and present amount of sample at a specific temperature. All the products of the reaction are gases, so there is no final mass ($w_f = 0$), also the k in equation (5) is the rate constant of reaction, subjected to the Arrhenius equation:

$$k = A\,e^{\frac{-E}{RT}} \qquad (7)$$

Where ***R*** is the universal gas constant (J/mol K); ***A*** is the Arrhenius factor or it may be called a pre-exponential factor (min^{-1}); ***E*** is the activation energy of the thermal decomposition reaction (J/mol).

Through presuming β represents the rate of change of temperature with time ($^{dT}/_{dt}$) or in other words, the linear heating rate (β) with units °C/min., by combining the above equations (5-7) and re-arranging with integration yields:

$$\int_0^W \frac{dW}{(1-W)^n} = \frac{A}{\beta}\int_0^T e^{-E/RT}\,dT \qquad (8)$$

To simplify, let the left hand side in equation 8 be as in equation 9;

$$\mu(W) = \int_0^W \frac{dW}{(1-W)^n} \qquad (9)$$

According to (Coats and Redfern, 1964); equation (8) becomes:

$$\mu(W) = \frac{ART^2}{\beta E}\left[1 - \frac{2RT}{E}\right]e^{-E/RT} \qquad (10)$$

Re-arranging and taking the *natural logarithm* for both side of equation (10):

$$ln\left[\frac{\mu(W)}{T^2}\right] = ln\frac{AR}{\beta E}\left[1-\frac{2RT}{E}\right] - E/RT \qquad (11)$$

There are two cases for ***n*** values in equation 9; the first one when (n=1) the integration of equation (9) will be as in equation (12). While the other case when (n≠1) the integration of right hand side of the equation (9) will be as in equation (13):

$$n = 1 \qquad \int_0^W \frac{dW}{(1-W)^n} = \mu(W) = -\ln(1-W) \qquad (12)$$

$$n \neq 1 \qquad \int_0^W \frac{dW}{(1-W)^n} = \mu(W) = \frac{1-(1-W)^{1-n}}{1-n} \qquad (13)$$

By assuming the reaction order and using mass loss data which were collected from TGA (mass loss versus temperature), the plot of the resulting ln ($\frac{\mu(W)}{T^2}$) values vs. 1/T was performed giving indeed a straight line with slope equal to the *–E/R* (activation energy can be obtained). The pre-exponential factor can be calculated from the intercept.

5.3 The thermal dissociation reactions and thermogravimetric curves:

There are two aims achievable by measuring reaction rates. The first aim is to deduce specific information related to the mechanism of a reaction. This information could be used to modify the reaction path or may be used to predict the untested behaviour of reactions. The second aim is to obtain the kinetic parameters values of specific reactions. Such values could allow reaction rates for specific reaction conditions different from that were previously measured or use a different measuring process. Thermal dissociation reactions for solids could be split into two groups (Boldyrev, 1979); (Cieslak-Golonka et al., 1995). The first includes chemical reactions that occur interfacially on the outside or inside of solids (crystals) by breaking chemical bonds. While the second group includes chemical reactions in which charge (protons, electrons, and ions) is transferable within the lattice. Typically this happens across a long distance greater than the interatomic distances. Ammonium salt decomposition reactions are classified as reactions accompanied by proton transfer between cations and anions according to Boldyrev (as cited by Galwey & Brown, 1999). The major requirements for ideal kinetics are listed by Gallagher as cited by Brown et al. (1995). These requirements are formulated as: (i) the irreversible reaction occurring in a single stage, (ii) the absolute enthalpy of the reaction

is low, so as to reduce self-cooling or self-heating effects; (iii) the reaction for the required temperature range should occur at a slow and measurable rate to avoid temperature calibration errors; (iv) the surrounding environment does not influence the reaction of the sample ; (v) the reaction does not depend on the sample preparation method, particle size, particle size, distribution, or pre-treatment ; (vi) The measurable changes in the reaction path should be sensible values so that small samples can be used, for example, enthalpy changes, mass, amounts of evolved gases.

The thermogravimetric curves of ammonium carbonate, ammonium bicarbonate, and ammonium carbamate are shown in figure (5.1). The figure illustrates that ammonium carbamate has a faster decomposition rate than other salts at a comparatively low temperature. Ammonium bicarbonate requires a higher temperature range to start dissociation by comparison to the other two salts. The other area where a significant difference among the salts is found is the final temperature of dissociation. It was 100 °C, 115 °C, and 145 °C for carbamate, carbonate, and bicarbonate respectively.

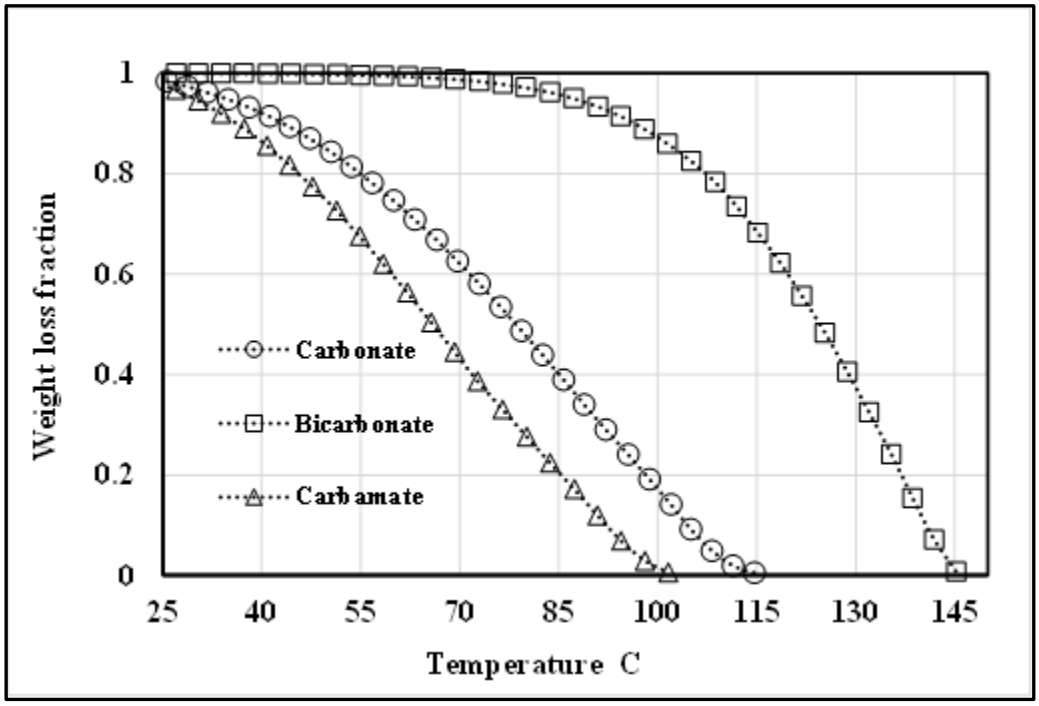

Figure 5- 1. Dissociation reaction curves of ammonium carbamate, bicarbonate, and carbonate vs. temperature

The decomposition reaction of ammonium carbonate occurs in the middle temperature range between carbamate and bicarbonate without passing by the melting step, but the solid salt is subjected to sublimation within the temperature between 20 and 100 °C (Erdey et al., 1964). With respect to ammonium bicarbonate, microscopy studies detected that the decomposition reaction coincides with a change in the physical properties of transparent crystals. These

crystals are changed to non-transparent and cavities are formed, with the growth from the interface continuing at a constant rate to the fusion stage (Galwey and Brown, 1999). Moving on to the ammonium carbamate the compound, in general, is unstable in solid state, volatilizing to form carbon dioxide and ammonia as gases. The total equilibrium pressure of the produced gases is 88.3 mm Hg at 24.9 °C (Adams and Small, 1973).

5.4 Kinetic parameters:

The most important kinetic parameters are the activation energy (***E***) and the pre-exponential factor (***A***). According to the Arrhenius equation, ***E*** is the absorbed heat or energy by inactive molecules in any transmuted process. For instance, chemical reaction becomes more productive (Vyazovkin, 2000). The reaction rate dependence on temperature is usually related to the activation energy and temperature. In general, a high E system means very temperature sensitive rates of reaction, while with low E, the system will be relatively temperature-insensitive (Levenspiel, 1999). However, the pre-exponential factor ***A*** relates to the fraction of collisions achieving transition state, i.e. the rate of the collision with the convenient orientation in order to start the reaction process. In general, to carry out any chemical reaction, the mechanism reaction pathway must be achievable before the reaction can occurs. One important condition is the kinetic energy of molecules. Halpern (1997) discusses the temperature-dependent distributions of activation energies for some applications. It is explained that the energy barriers depend on the temperature, resulting in temperature-dependent distribution of activation energies.

In this study there are significant differences in the values of activation energies of ammonium salts (carbonate, bicarbonate, and carbamate) for each heating rate (2, 5, 10, 15, and 20 °C/min.) when a particular reaction order is changed. Brown, (2001) conjectures it is impossible to determine and characterize any reaction with a complete kinetic model by a set of experiments carried out at a single heating rate. A kinetic model in interpreting experimental thermoanalytical data is analysed, thereby giving a rational explanation for the wide range of data for kinetic parameters for the three of solid-state decompositions.

5.4.1 Ammonium carbonate:

Figures 5.2 and 5.3 show a complement of the extent of activation energy and the pre-exponential factor respectively, at a heating rate ***β***: 2, 5, 10, 15, and 20 C/min for nine different reaction order models (n = 0, 1/4, 1/2, 3/4, 1.0, 5/4, 3/2, 7/4, and 2.0). The results of kinetic parameter values for thermal dissociation of ammonium carbonate are obtained according to equation (13) (or equation 12 when n=1). The ranges of *W* studied, are in the common range

(0.10-0.80) for all heating rate as illustrated in table (5.1). In general, the activation energy and the pre-exponential factor dramatically increase with increasing order of reaction. A clear trend of decreasing in *E* and *A* occurs with increasing heating rate.

From the graphs below we observe at a heating rate (β = 2 °C/min) an increase in activation energy *E* and pre-exponential factor *A* with increasing order. For example at zero order (n) the values of *E* and *A* are 52.87 kJ/mole and 1.6E+17 $min.^{-1}$ respectively. While the values became 83.28 kJ/mole and 3.9E+22 min^{-1} at n = 2 with a standard deviation of ±12.78 kJ/mole for *E* as shown in table (5.1). However, the reaction order tend to be very close to (7/4) according the values of correlation coefficient (R^2 = 0.9978). The values of activation energy at a heating rate of 2 C/min. are highest relative to all the other heating rates. The second heating rate is 5 °C/minutes. It is apparent from the results that the activation energy had the same behaviour as the previous heating rate. Thus the values of activation energy at zero reaction order was 48.69 kJ/mole with pre-exponential factor 5.1×10^{16} min^{-1}.

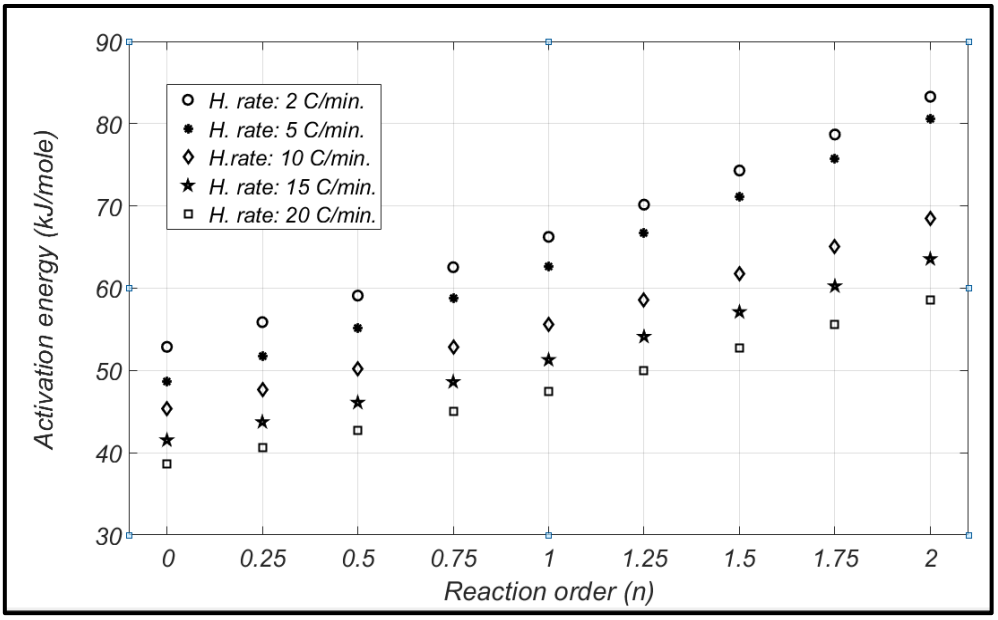

Figure 5- 2. Activation energy of ammonium carbonate decomposition reaction versus the reaction order at different heating rates.

As can be seen from figure (5.2), the change in reaction order from 0 to 2 in the heating rate of 5 °C/minute leads to an increase in the activation energy by (2-5 kJ/mole) for each increment of n. As an overview of β (10, 15, and 20 C/min) the activation energy continues to increase against reaction order as presented in figure (5.2). What is interesting about the data in the above heating rates, there are slightly limited decreases (2-4 kJ/mol) in values of activation energy for decremented order of reaction.

In summary, these results show that there is a dramatic increase in activation energy at each heating rate with increasing reaction order. Furthermore, another important indicator is that the activation energy decreases with an increased heating rate during a fixed reaction order as illustrated in figure (5.1). From the results of ammonium carbonate decomposition, a reaction could be characterized as a rational-order reaction (3/4) due to it best-fit according to correlation coefficients which are summarised in table 5.2.

Table 5- 1 illustrates the heating rate of ammonium carbonate decomposition reaction, conversion percentage, against temperature range with standard deviation.

Heating rate (C/min)	Range of W studied	Temp. range (C)	St. dev
2	8.2–79.7	30–70	±11.3
5	11.8–81.2	40–80	±11.0
10	8.1–79.2	50_100	±8.0
15	9.4–79.3	60–125	±8.6
20	9.8–78	70–145	±6.7

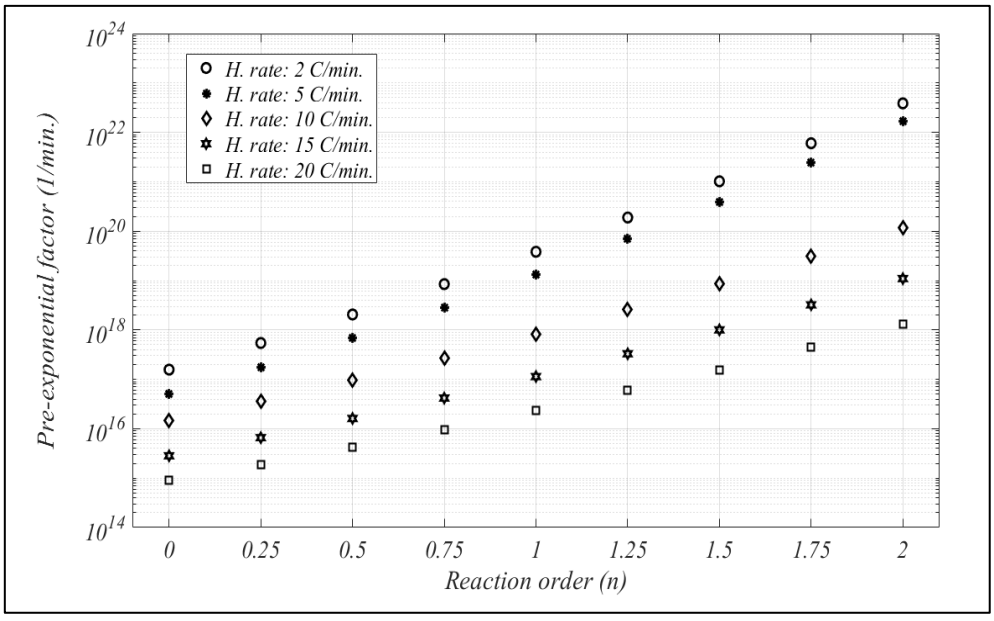

Figure 5- 3. Pre-exponential factor of ammonium carbonate decomposition reaction with different heating rates and reaction orders assumed.

The range of *E* agrees well with the literature. The average value obtained by House, (1980) for the activation energy, is (85.69 ± 6.02 kJ /mole for $(NH_4)_2CO_3$. The data of the pre-exponential factor as presented in tables 5.2 is plotted in figure 5.3, which shows the value of

A as a function of reaction order at different heating rates. The *A* values are computed from the intercepts of the regression equations achieved using the Coats and Redfern method. The *A* values monotonically increases with the increasing the presumed reaction order from n = 0 to n = 2 for each heating rate. On the other hand, one can clearly note in any specific reaction order, the values of the pre-exponential factor decrease with increasing the rate of heating.

Table 5- 2. Kinetic parameters of ammonium carbonate decomposition reaction data: heating rate β °C/min, activation energy E (kJ/mole), pre-exponential factor (A 1/min) and correlation coefficient R^2.

β		***Reaction order(Ammonium carbonate dissociation)***								
		0	0.25	0.5	0.75	1	1.25	1.5	1.75	2
2	E	52.87	55.88	59.10	62.56	66.24	70.16	74.31	78.68	83.28
	A	1.6E+17	5.4E+17	2.1E+18	8.5E+18	3.8E+19	1.9E+20	1.0E+21	6.0E+21	3.9E+22
	R_2	0.9756	0.9816	0.9867	0.9910	0.9942	0.9964	0.9976	0.9978	0.9971
5	E	48.69	51.79	55.14	58.74	62.60	66.72	71.11	75.75	80.63
	A	5.1E+16	1.8E+17	6.8E+17	2.9E+18	1.3E+19	6.9E+19	3.9E+20	2.4E+21	1.7E+22
	R_2	0.9907	0.9941	0.9964	0.9975	0.9977	0.9959	0.9934	0.9898	0.9853
10	E	45.35	47.67	50.16	52.80	55.61	58.59	61.73	65.03	68.48
	A	1.4E+16	3.6E+16	9.6E+16	2.7E+17	8.1E+17	2.6E+18	8.8E+18	3.1E+19	1.2E+20
	R_2	0.9940	0.9963	0.9978	0.9984	0.9981	0.9968	0.9947	0.9916	0.9879
15	E	41.53	43.74	46.10	48.61	51.29	54.12	57.11	60.25	63.55
	A	2.8E+15	6.6E+15	1.6E+16	4.2E+16	1.1E+17	3.3E+17	1.0E+18	3.2E+18	1.1E+19
	R_2	0.9948	0.9970	0.9984	0.9990	0.9987	0.9976	0.9956	0.9929	0.9895
20	E	38.59	40.60	42.75	45.03	47.46	50.02	52.72	55.56	58.53
	A	8.9E+14	1.9E+15	4.2E+15	9.7E+15	2.4E+16	6.0E+16	1.6E+17	4.5E+17	1.3E+18
	R_2	0.9952	0.9972	0.9985	0.9991	0.9990	0.9981	0.9965	0.9942	0.9912

5.4.2 Ammonium bicarbonate

The effect of varying heating rates and reaction order on the behaviour of kinetic parameters of ammonium bicarbonate can be seen from the data in figures 5.4 and 5.5. The studied range of conversion ***(W)***, is within common range (7.7 - 80 %) of sample mass for all heating rates

as reported in table (5.3). In the same way, there is a minimum amount of energy needed to activate the molecules to break existing bonds during a chemical reaction, i.e. the activation energy. In general, the activation energy and the pre-exponential factor increase with the increasing reaction order. Whereas there is a tendency for decreasing ***A*** and ***E*** with increasing heating rate. From the data in figures (5.4 and 5.5), we can see that the kinetic parameters of ammonium bicarbonate are distinguished with the high values relative to those of ammonium carbonate (see section 5.3.1).

Table 5- 3. Heating rates of ammonium bicarbonate decomposition reaction, conversion percentage, against temperature range with standard deviation.

Heating rate (°C/min)	Range of W studied (%)	Temp. range (°C)	St. dev
2	8.8–80	80–115	± 4.4
5	8.9–75.5	95–135	± 3.8
10	10.7–76.8	110–155	± 3.8
15	9.5–79	115–165	± 3.8
20	7.7–81.4	115–175	± 3.5

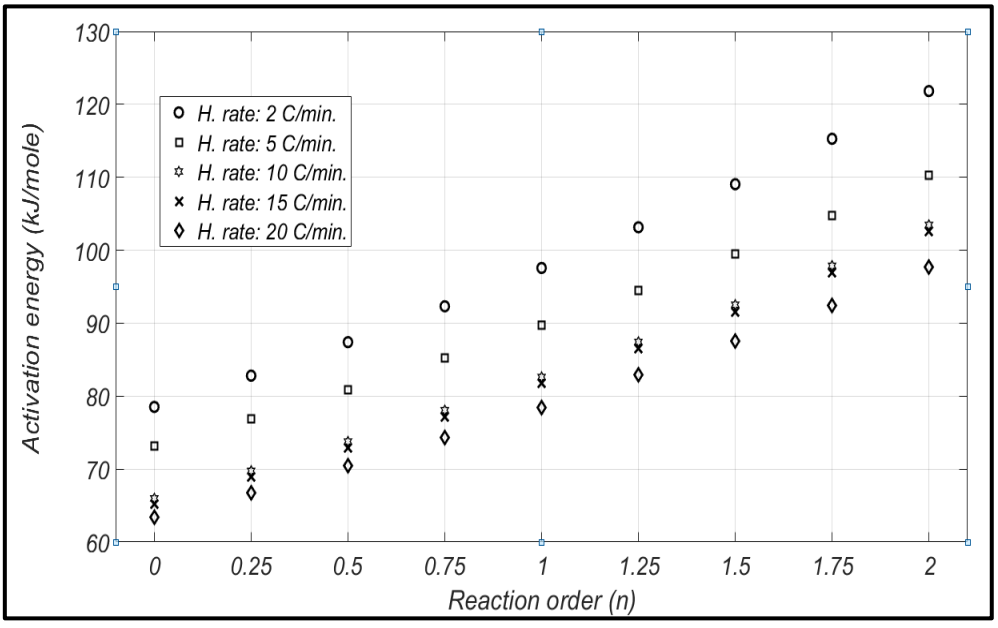

Figure 5- 4. Activation energies of ammonium bicarbonate decomposition reaction versus the reaction order at different heating rates.

According to the model equation (10), the relationship between E and β is inversely proportional. Turning now to the experimental evidence, with successively increasing heating rates, lower the activation energy and pre-exponential factor are observed. For example in

reaction order n=1 the activation energy 97.57 kJ/mole at a heating rate 2 C/min., if the heating rate is increased by factor of 10, then the activation energy is reduced about 19 kJ/min. i.e. saving approximately 20% of energy.

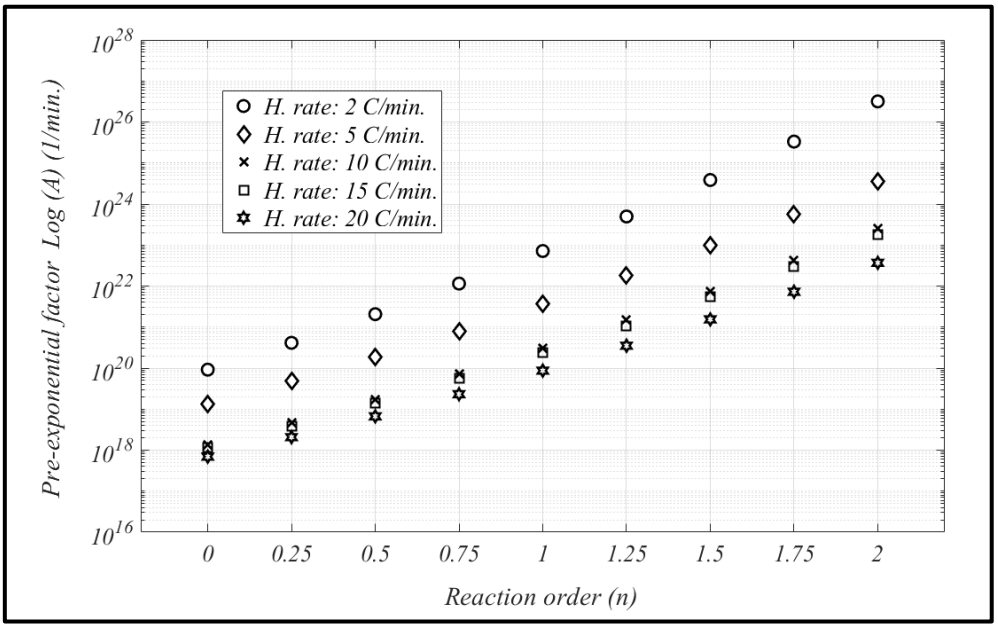

Figure 5- 5. Pre-exponential factor of ammonium bicarbonate decomposition versus reaction orders with different heating rates.

What stands out in table 5.3 is the values of the standard deviation of ***E*** were very close to each other: (±4.43, ±3.80, ±3.83, ±3.82, and ±3.50) for heating rate (2, 5. 10, 15, and 20 °C/min.) respectively. The results from the modelling for TGA made in the ammonium bicarbonate decomposition reaction and the conditions which practically was met, can be summarized in the following points; Firstly, the reaction rate is low at the low temperatures practically obtainable. Secondly, the reaction occurs and goes essentially to completion at the high temperatures within the domain.

The results of the pre-exponential factor of NH_4HCO_3 are presented in Table 5.4 and figure 5.4. It is observed that *A* values for the five heating rates present a correlation coefficient higher than 0.98. The reaction order in the range from 3/4 to 1.0 display the highest value of the correlation coefficient (R^2 = 0.999 - 0.997). R^2 was used in this study, as a criterion for the most acceptable reaction order and kinetic parameters E and A. Many researchers have utilized the linear correlation coefficient (R^2) as an indicator for the estimation of kinetic parameters such as reaction order (n), activation energy (E), and pre-exponential factor (A) from thermogravimetric analysis data. (Reich and Stivala, 1979). The minimum standard deviation obtained from the least squares fit of the best straight line. Generally, the activation energy

values obtained in this study for ammonium bicarbonate lie within the range published: 86.19 ± 7.70 kJ /mole (House Jr., 1980).

Table 5- 4 Kinetic parameters of ammonium bicarbonate decomposition reaction data: where heating rate β °C/min, activation energy E (kJ/mole), pre-exponential factor (A 1/min.) and correlation coefficient R^2.

β		***Reaction order (Ammonium bicarbonate dissociation)***								
		0	0.25	0.5	0.75	1	1.25	1.5	1.75	2
2	E	78.52	82.81	87.41	92.32	97.57	103.15	109.05	115.28	121.83
	A	9.2E+19	4.1E+20	2.1E+21	1.2E+22	7.2E+22	5.0E+23	3.8E+24	3.3E+25	3.2E+26
	R^2	0.9960	0.9984	0.9997	0.9998	0.9986	0.9963	0.9927	0.9881	0.9825
5	E	73.11	76.90	80.93	85.210	89.73	94.51	99.527	104.79	110.309
	A	1.4E+19	4.9E+19	1.9E+20	8.1E+20	3.7E+21	1.8E+22	9.8E+22	5.6E+23	3.5E+24
	R^2	0.9957	0.9978	0.9992	0.9999	0.9997	0.9989	0.9973	0.9951	0.9922
10	E	65.99	69.76	73.79	78.08	82.63	87.45	92.53	97.88	103.48
	A	1.4E+18	4.7E+18	1.7E+19	7.1E+19	3.1E+20	1.5E+21	7.6E+21	4.2E+22	2.6E+23
	R^2	0.9933	0.9960	0.9980	0.9991	0.9994	0.9989	0.9976	0.9955	0.9928
15	E	65.23	68.95	72.94	77.19	81.71	86.52	91.60	96.94	102.54
	A	1.2E+18	3.9E+18	1.4E+19	5.5E+19	2.4E+20	1.1E+21	5.5E+21	3.0E+22	1.8E+23
	R^2	0.9902	0.9937	0.9963	0.9980	0.9987	0.9985	0.9973	0.9953	0.9925
20	E	63.40	66.80	70.44	74.34	78.49	82.90	87.56	92.48	97.65
	A	6.9E+17	2.1E+18	6.7E+18	2.3E+19	8.7E+19	3.5E+20	1.5E+21	7.3E+21	3.7E+22
	R^2	0.9880	0.9919	0.9970	0.9979	0.9979	0.9978	0.9966	0.9945	0.9914

5.4.3 Ammonium carbamate

Ammonium carbamate is an unstable compound. Its solid state starts to volatilize at 24.9 °C. Gaseous products include ammonia and carbon dioxide. The dissociation of solid ammonium carbamate is studied by several investigators (Egan, Potts and Potts, 1946). In this section, the kinetic parameters estimated to find the effect of heating rate. Figures (5.6) and (5.7) show that the increasing in activation energy and pre-exponential factors are linear with the increase in reaction order for all five heating rate over the conversion range (***W***). As previously was mentioned in section (5.3), ammonium carbamate has a faster decomposition rate than other salts particularly at a relatively low temperature as compared with the ammonium carbonate/bicarbonate as clearly illustrated in figure (5.1).

The results, as shown in table 5.5, indicate that the range of mass losses studied is between (9% and 78 %), whereas a non-linear tendency occurs outside this range. According to the data in the table (5.5), the heating rates of ammonium carbamate decomposition are related to mass loss percentage and the temperature range. It is clear that increase in lower and upper limits of the temperature approximately lie between 10 to 20 °C respectively to achieve a fixed mass loss percentage for all heating rate. The precise decomposition mechanism of ammonium carbamate is not well understood, but there are many studies showing that the rate of reaction highly depends on the temperature and pressure (Claudel and Boulamri 1988; Ramachandran et al. 1998). However, (Lishnevskii and Madzievskaya 1982, cited by Ramachandran et al. 1998) claims that the kinetic analysis is only restricted to the dependency on temperature, for both the forward and back reactions of the initial rates. Nevertheless, they could not suggest any mechanism consistent with the rate equation of the decomposition reaction.

Generally, the decomposition reaction of ammonium carbamate according to the results in a table (5.6) does not have clear stability in reaction order. The higher heating rates, 15 and 20 °C/min. tend to be with reaction orders 3/2 to 2 respectively. Meanwhile, at the lower heating rates (2, 5, 10 °C/minute), the order of reaction tends to lower values of n; (1/2, 3/4, and 1) respectively. In particular, the decomposition reaction of ammonium carbamate possesses more than one mechanism of decomposition. One of these mechanisms as mentioned by Funke et al. (2004) which occurs in the presence of moisture in the carbamate sample. The side decomposition reaction is carbonate formation as in the reaction (14) which is occurring at a temperature above 60°C:

$$NH_2COONH_4 \overset{H_2O}{\longleftrightarrow} (NH_4)_2CO_3 \qquad (14)$$

The second mechanism presumes formation of carbamic acid resulting from re-arrangement and transport of a proton from ammonium ion to carbamate ion, while the ammonia is released to the gas phase. Subsequently, carbamic acid is subjected to unimolecular isomerization (a loose Van der Waals complex). The complex of NH_3-CO_2 then dissociates into ammonia and carbon dioxide as represented in reactions 15-17 (Ramachandran, et al., 1998;Wen, and Brooker 1995).

$$NH_2COONH_{4\,solid} \triangleq NH_2COOH_{gas} + NH_{3\,gas} \qquad (15)$$

$$NH_2COOH = COO--NH_3\ (Van\ der\ Waals\ complex) \qquad (16)$$

$$COO--NH_3 \overset{dissociate}{\Longleftrightarrow} CO_{2\,gas} + NH_{3\ gas} \qquad (17)$$

The third mechanism of ammonium carbamate dissociation is posed by Ramachandran et al., (1998) based on kinetics and stability of carbamic acid. Furthermore this acid does not give products directly as shown in equations (16) and (17). A bimolecular ammonia-assisted process is mooted. This mechanism involves an appearance of sequentially generated species: carbamic acid and ammonia, then Van der Waal complex with ammonia again, then decomposition of the complex to ammonia and carbon dioxide. The last two mechanisms require the presence of carbamic acid in the gas phase. On the other hand, Ramachandran et al. investigated and rejected these two mechanisms supported IR spectroscopy due to lack of evidence for the existence of these species in the gas phase. Not only Ramachandran but also Wen and Brook (1995) concluded the same results in their Raman study of ammonium carbamate, bicarbonate, and carbonate equilibria. They deduced there is no evidence for carbamic acid as well as a complexed chemical intermediate in aqueous solutions equilibria among these species. Nonetheless, another similar viewpoint should be taken into consideration the conversion of solid ammonium carbamate to carbamic acid in the solid state.

Table 5- 5 illustrate the heating rate of ammonium carbamate decomposition reaction, conversion percentage, against temperature range with standard deviation.

Heating rate (°C/min)	Range of W studied (%)	Temp. range (°C)	St. dev
2	9.3–78.4	30–75	8.5
5	10.4–77.3	40–90	7.9
10	10.1–78.8	45–100	7.8
15	10.4–76.9	60–125	7.8
20	10.0–75.1	70–145	5.9

Adams & Small (1973) posited an exceptional structure of the ammonium carbamate crystal – planer sheets of carbamate ions. Carbamate ions are formed in two-adjacent layers parallel to each other, subtended above and below by two layers of ammonium cations with some interpenetration. The ammonium ions play an important coordination role in between the layers. The NH_4^+ ion interacts with four oxygen atoms of different NH_2COO^- ions via its hydrogen atoms, three of carbamate ions in the first layer while the fourth one is located in the second layer.

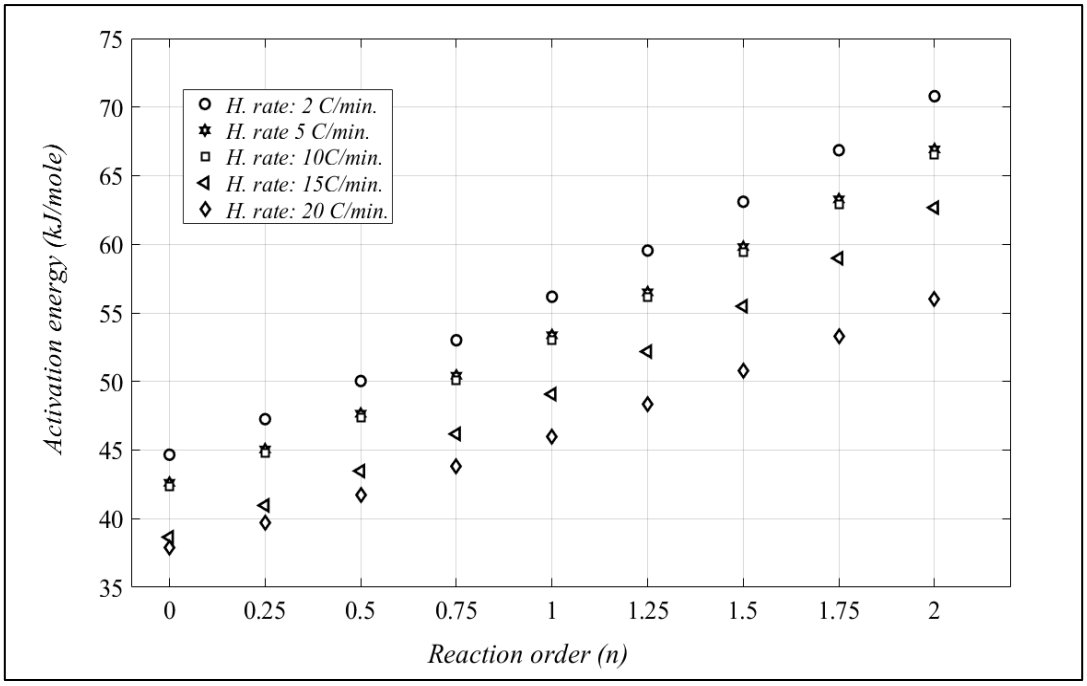

Figure 5- 6. Activation energies of ammonium carbamate decomposition reaction versus the reaction order at different heating rates.

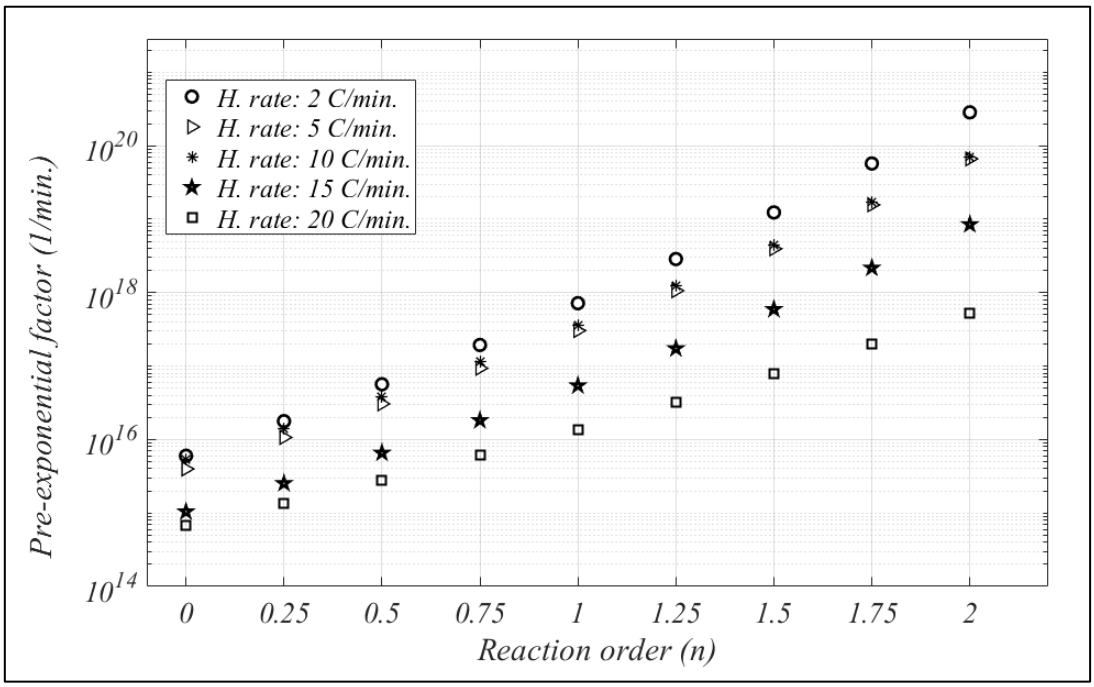

Figure 5- 7. Pre-exponential factor of ammonium carbamate decomposition versus reaction orders with different heating rate.

Table 5- 6. Kinetic parameters of ammonium carbamate decomposition reaction data: where heating rate β °C/min, activation energy E (kJ/mole), pre-exponential factor (A 1/min) and correlation coefficient R^2.

β		*Reaction order(Ammonium carbamate dissociation)*								
		0	0.25	0.5	0.75	1	1.25	1.5	1.75	2
2	E	44.66	47.25	50.03	53.01	56.18	59.54	63.10	66.86	70.80
	A	6.01E+15	1.78E+16	5.65E+16	1.94E+17	7.18E+17	2.87E+18	1.23E+19	5.72E+19	2.85E+20
	R^2	0.9681	0.9746	0.9804	0.9853	0.9893	0.9924	0.9945	0.9957	0.9961
5	E	42.62	45.05	47.65	50.42	53.37	56.50	59.80	63.28	66.92
	A	3.98E+15	1.07E+16	3.06E+16	9.35E+16	3.05E+17	1.06E+18	3.95E+18	1.57E+19	6.62E+19
	R^2	0.9858	0.9899	0.9932	0.9958	0.9976	0.9986	0.9988	0.9983	0.9971
10	E	42.35	44.76	47.34	50.09	53.02	56.13	59.42	62.89	66.52
	A	5.3E+15	1.38E+16	3.85E+16	1.14E+17	3.62E+17	1.22E+18	4.42E+18	1.7E+19	6.97E+19
	R^2	0.9923	0.9953	0.9976	0.9991	0.9997	0.9995	0.9985	0.9967	0.9943
15	E	38.65	40.97	43.47	46.18	49.08	52.18	55.48	58.98	62.67
	A	1.04E+15	2.53E+15	6.56E+15	1.82E+16	5.42E+16	1.73E+17	5.92E+17	2.17E+18	8.47E+18
	R^2	0.9953	0.9976	0.9988	0.9989	0.9977	0.9953	0.9918	0.9872	0.9818
20	E	37.88	39.74	41.71	43.80	46.01	48.33	50.77	53.33	56.00
	A	6.72E+14	1.35E+15	2.81E+15	6.09E+15	1.37E+16	3.22E+16	7.85E+16	1.99E+17	5.24E+17
	R^2	0.9979	0.9990	0.9995	0.9994	0.9987	0.9974	0.9955	0.9930	0.9900

5.5 Pseudo-inverse method (PIM) to estimate initial solid state mixture composition

In the traditional forward model, the aim is usually to predict the values of measurable outputs under a specific operation condition. By contract, inverse methods focus on the measured values of output parameters under known operation conditions to estimate the values of the physical parameters (Zimmerman and Rees, 2009). The pseudo-inverse method (PIM) is widely applied and investigated because it permits a brief expression for *linear* mathematical systems in an n-dimensional (measurement) space (Stewart, 1977). Some authors have used the "generalized inverse" rather than term "pseudoinverse". Systems of simultaneous linear equations of any sort may be solved using the PIM (Abu-Saman, 2012). Zimmerman & Rees, (2009) proposed an approach to apply that the inverse methods to estimate kinetic parameters and other *a priori* unknown physical variables of a multiphysics model by analysing measured data of the actual system. Consequently, any experimental system with a sufficiently faithful model can act as a "sensor" for the unknown parameters of the model. Generally, this approach can provide the same parameter estimates for a system which has a unique inverse and

corresponds with the one obtained with the standard parameter estimation approaches. If the system has many solutions (ill-posed) then the PIM approach estimates the best fit solution in the "least squared error" sense. While in case the system has no solution (over determined), the PIM estimates the parameters achieving a minimum residue, (Murray-Lasso, 2008). Murray-Lasso (2008) refer to the rank of system equations for the coefficient matrix $\boldsymbol{A}$ is equal to minimum number of columns or rows, then the matrix has a full rank. However, if there are more equations than the unknowns (rectangular matrix), then the system $\boldsymbol{Aw = b}$ is called overdetermined (Golub & Van Loaan, 2013). By the least squares principle, to solve the matrix equation of A with unknown parameters of vector $\boldsymbol{w}$, and observation vector b (measurements from actual system). The mass fractions w_1, w_2, and w_3 are represented as the unknown parameters of the vector $\boldsymbol{w}$. The fundamental definition of the pseudo-inverse method could be for a non-full-rank matrix $\boldsymbol{A}$, according to the following formula to calculate the pseudo inverse ($\boldsymbol{A}^{-}$) as given:

$$A^{-} = (A^{T} \times A)^{-1} \times A^{T} \qquad 18$$

Where $\boldsymbol{A}$: a matrix of **m** rows and **n** columns where m and n are any natural numbers, while the $\boldsymbol{A^T}$ is the transpose of $\boldsymbol{A}$. Golub and Van Loan (1980) show the least square solution of a system $\boldsymbol{A^* w = b}$ should satisfies:

$$A^{T} \times A \times w = A^{T} \times \mathrm{b} \qquad 19$$

So the solution of $\boldsymbol{w}$ in equation (19) will be:

$$w = (A^{T} \times A)^{-1} \times A^{T} \times \mathrm{b} \qquad 20$$

5.5.1 Computational procedure:

We presume a linear mixing relation between the pure component TGA curves and the composite curve for the solid state mixture TGA profile. $\boldsymbol{A}$ is a matrix with components representing TGA pure component, time discretized value, i.e. coefficients of w_1, w_2, and/or w_3 for pure ammonium; carbonate, bicarbonate, and carbamate (A, B, and C) respectively. The three salts decomposed at a specific heating rate (5 °C/min.) using thermogravimetric analysis. The measured data of vector b are extracted using TGA experiments which represent the remaining mass (at the same discretized times) of a mixture containing any two of the compounds. Therefore, the cases which were studied included either A + B or A + C or B + C. Also several initial mass ratios of the three compounds (0.2/0.8, 0.4/0.6, 0.5/0.5, 0.6/0.4, and

0.8/0.2) are tested for the three cases. The decomposition of mixture of samples proceeds as the same heating rate of pure salts TGA profiles. Then, to solve the system: $\boldsymbol{A * w = b}$

For $\boldsymbol{w} \in R^m$, give b $\in R^n$, $\boldsymbol{A}$ may be m $\times$ 2 with m >> 2. The general solution to find the inverse of $\boldsymbol{A}$ will be a matrix $\boldsymbol{S}$ which has dimensions m $\times$ 2 with characteristic:

$A \times S \times A = A$, then solution for w is: $w = S \times A$

The data could be organized by the following model equations for temperature at discretized times:

$$M(T_1) = w_1 M_1(T_1) + w_2 M_2(T_1)$$

$$M(T_2) = w_1 M_1(T_2) + w_2 M_2(T_2)$$

$$M(T_3) = w_1 M_1(T_3) + w_2 M_2(T_3)$$

$$M(T_n) = w_1 M_1(T_n) + w_2 M_2(T_n)$$

Where M (T_n) is the mass remaining at temperature value T_n associated with the n-th time increment. The final model could be linked between the compositions of the samples as a function with the temperature:

$$\mu_{model}(w_1, w_2, T) = \sum_{i=1}^{i=2} w_i * \mu_i (T)$$

$$\begin{vmatrix} M_1(T_1) & M_2(T_1) \\ M_1(T_2) & M_2(T_2) \\ M_1(T_3) & M_2(T_3) \\ . & . \\ . & . \\ M_1(T_n) & M_2(T_n) \end{vmatrix} \begin{vmatrix} w_1 \\ w_2 \end{vmatrix} = \begin{vmatrix} M(T_1) \\ M(T_2) \\ M(T_3) \\ . \\ . \\ M(T_n) \end{vmatrix}$$

Similarly, the matrix components are M_m (T_n) which are the pure component (m) TGA remaining mass measurements. The linear model assumes that the initial mass fractions weight the remaining mass in the solid-state mixture according to the TGA pure component profiles.

It is a "well-mixed" system model that assumes each component volatilizes/decomposes at a given heating rate/exposure time independently of the others. Such a model fails if the solid state is heterogeneously distributed or the components are chemically cooperative in either opposing or facilitating volatilization/ decomposition. The following steps are an algorithm to solve a system A*w=b with a pseudo inverse method implemented in MATLAB, which is a multi-paradigm numerical computing environment.

5.5.2 Modelling assumptions:

The following idealized assumptions are consistent with the above model for the TGA analysis

- Read matrix A which is m $\times 2$ *matrix of any two pure components.*
- Read vector b_i which is m$\times 1$ *a mixture of any two components (A, B, and C).*
- Find the transpose of matrix A => (A^T).
- Find the pseudoinverse of (A^-) = S of matrix A which is S=inv($A^T \times A$)
- Calculate $w_i = S \times A^T \times b_i$

of solid state to estimate the initial weight fractions: (***i***) the rate of reaction is very small at the lowest temperatures; (***ii***) the reaction goes mostly to completion before the highest temperature is reached; (***iii***) the temperature in the crucible is uniform; (***iv***) the heat is transferred to the sample by conduction and convection; (***v***) conversion or mass fraction loss is proportional to temperature change; (vi) the kinetics of the reaction can be described by a single rate constant depending on kinetic parameters; (vii) The activation energy and pre-exponential factor unchanged with constant heating rate.

For the assumptions ***i, ii*** and ***v***, it is actually clear from the experimental results, the reaction rate during the initial and final stages is very small especially for the ammonium bicarbonate salt so the study selected to limit the temperature range to 20-110 °C. However, since the process is a decomposition reaction, the mass loss or conversion is strongly proportional to the temperature as shown in all figures 5.7-5.22.

The third and fourth assumptions are applicable when the value of the temperature (T of the sample) is assigned for the solid inside the crucible. The condition of uniform temperature cannot be met exactly by solids. But since the mass of the sample is very small (mg), the resistance to heat transfer could be neglected by comparison to the driving force of supplied heat. Therefore, these considerations were only limited to reactions in solid-state.

The fourth assumption, related to the heat transfer nature, is as idealized as conduction is the dominant mechanism due to contact between the sample and the body of the heated crucible. So, the thermal conductivities of these compounds should take an important role in decomposition reactions, but it is currently outside of the scope of this study, simple linear model. Moreover, the heat could be transferred by gas convective flux through the surface of the sample and through interstitial spaces between the particles contacting hot gas.

Concerning the last two assumptions (*vi* & *vii)*, the main parameter is the rate constant of reaction which is a function for the activation energy and pre-exponential factor. In this part of the study, the heating rate is held at 5 C/min. so the *E, A,* and *k* should be constant. Finally the furnace temperature was calibrated with a 100 mg mass, using four reference materials; Alumel (152.6 °C), Nickel (358.2 °C), Perkalloy (596 °C) and Iron (770 °C).

5.5.3 Ammonium carbonate / bicarbonate system (A/B)

The experimental and modelling data for the decomposition reaction of mixed salts containing ammonium carbonate (A) and ammonium bicarbonate(B) are shown in figures (5.8- 5.12). Experimental data are gathered using TGA for a binary system samples as well as each pure compound at a constant heating rate (5 °C/min.). The data are listed in tables (C1) in appendix C. The data of the forward model which are calculated as illustrated in section 5.5.1 are listed in the table (C2) in appendix C.

The mass loss with different ratios of ammonium carbonate/ammonium bicarbonate A/B (0.2/0.8, 0.4/0.6, 0.5/0.5, 0.6/0.4, and 0.8/0.2) over the temperature range from 20 to 100 ˚C is tested. *MATLAB* is used to solve the matrix equations as shown in (5.18-5.20) using the pseudo inverse method as illustrated in the algorithm (section 5.5.1). The results show a restricted agreement between the experimentally measured TGA profiles and modelled weighted profiles. As can be seen, the two curves of experiments and model are only close to each other at starting and ending points, supporting the hypothesis of the linear, mass fraction weighted TGA mixture model. Nevertheless, there are noticeable discrepancies. The uncertainty comes from more than one sources, for instance, systematic error, measurement precision, measurement error, intrinsic fluctuation, and conceptional errors. The equipment for TGA is a Perkin Elmer TGA-7, which has a balance sensitivity of (±0.0001 mg) and weighing precision up to 10 ppm, temperature precision is ± 2 °C. So the systematic fluctuations errors could occur during the presence of the sample inside the furnace as a result of any vibrational noise in the surroundings interpreted as a mass fluctuation. The second source of fluctuation error is

variability of temperature in the lab. Another source of systematic errors may be related to the process, it is not exactly followed as sublimation process because of the mixed samples (w1, w2, and w3) could interact with each other in different ways. These possible sources of error could have an effect on some results in this study but could be reduced by repletion of experiments. The average of the errors percentage is (3.4, 1.6, 9.7, 9.1 and 21.0) for the 0.2/0.8, 0.4/0.6, 0.5/0.5, 0.6/0.4, and 0.8/0.2 TGA profiles and forward model. No significant relationship is indicated to use PIM in characterizing the binary mixture of the ammonium carbonate and the ammonium bicarbonate. As mentioned in the literatures, both compounds ammonium carbonate and bicarbonate are decomposed to the same products; CO_2, NH_3, and H_2O (Erdey et al., 1964; House Jr., 1980).

The results show the mass loss "conversion" is significantly related to mixing ratio and the temperature in the binary system decomposition. Accordingly, as the ratio of A to B increased the decomposition fraction is increased at constant temperature and vice versa. This is an expected result since the process is coupled by the TGA response of pure compounds. The logical reason is based on the fact that the ammonium bicarbonate decomposes at temperatures higher than that of ammonium carbonate. For instance, at 90.8 °C the mass loss fraction is dramatically increase (0.784, 0.7159, 0.592, 0.537, and 0.3304) with the rising ratio of ammonium carbonate to ammonium bicarbonate (0.2/0.8, 0.4/0.6, 0.5/0.5, 0.6/0.4, and 0.8/0.2) respectively in TGA data. While the forward model gives estimation data for the same ratios as following (0.835, 0.736, 0.686, 0.637, and 0.538). The difference between the values of the TGA profiles and forward model is clear in particular in figures (5.10) to (5.12) for the ratios (0.5/0.5, 0.6/0.4, and 0.8/0.2). So the results of PIM are poor as shown in calibration data in figure (5.13). The results of these two components did not show a significant correlation in the experimental and PIM estimation, maybe due to interaction during the decomposition process. The behaviours of the two components with the different ratios as shown in figure (5.14) support the last idea through the converging “interacting” of the curves. The curve of 0.4/0.6 with the curve 0.5/0.5 have interacted as well as the 0.6/0.4 with 0.8/0.2, so the inversion does not work well due to lack of sensitivity. Notwithstanding the increasing of ammonium bicarbonate fraction in samples lead to an increase in the temperature of decomposition as it is seen in the figure (5.14), but the inversion results apparently weak when using the entire TGA profile. Future work could explore inversion with narrower heating rates and ranges, particularly the choice of initial temperature.

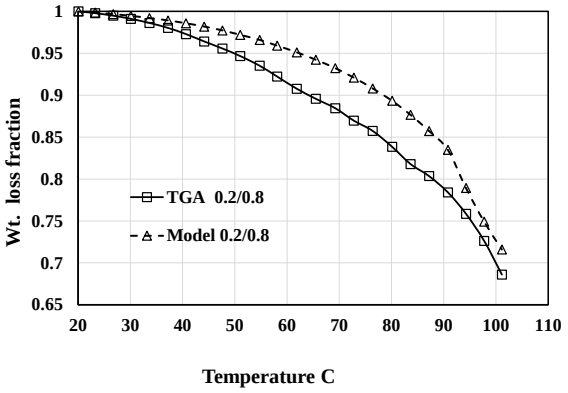

Figure 5- 8 shows the mass loss fraction of A/B salts versus the temperature, the ratio: 0.2/0.8

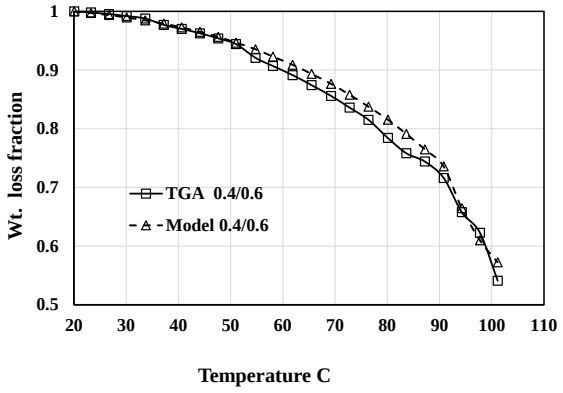

Figure 5- 9 shows the mass loss fraction of A/B salts versus the temperature, the ratio: 0.4/0.6

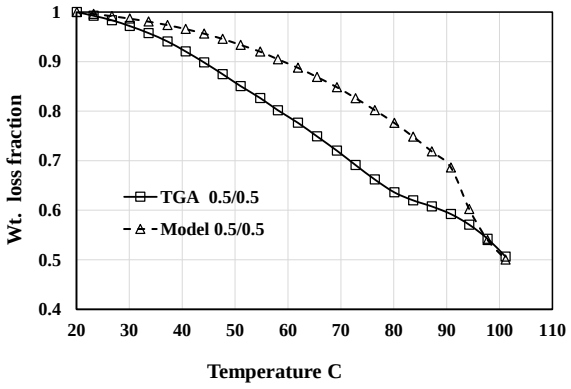

Figure 5- 10 shows the mass loss fraction of A/B salts versus the temperature, the ratio: 0.5/0.5

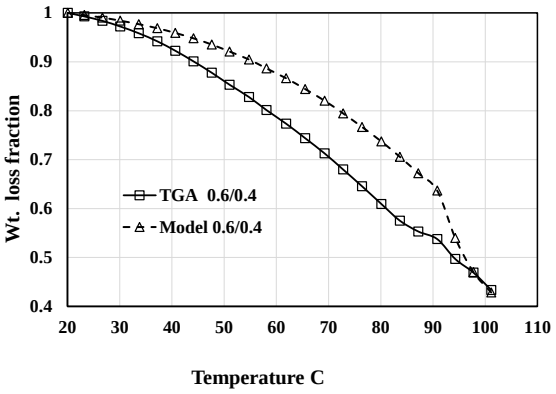

Figure 5- 11 shows the mass loss fraction of A/B salts versus the temperature, the ratio: 0.6/0.4

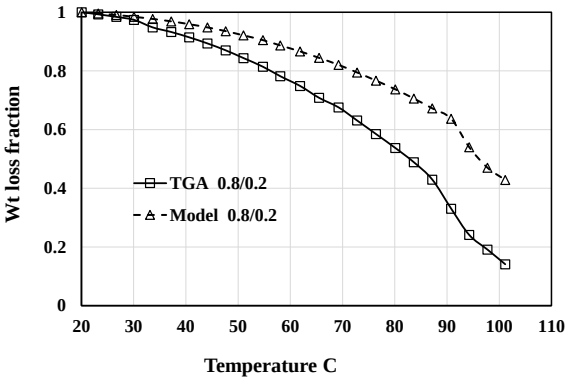

Figure 5- 12 shows the mass loss fraction of A/B salts versus the temperature, the ratio: 0.8/0.2

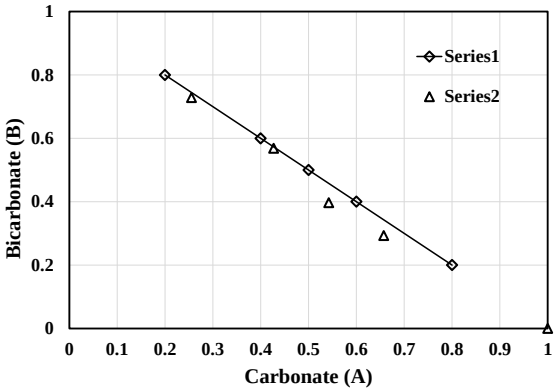

Figure 5- 13 shows TGA and PIM calibration results for the mass loss fraction (A/B)

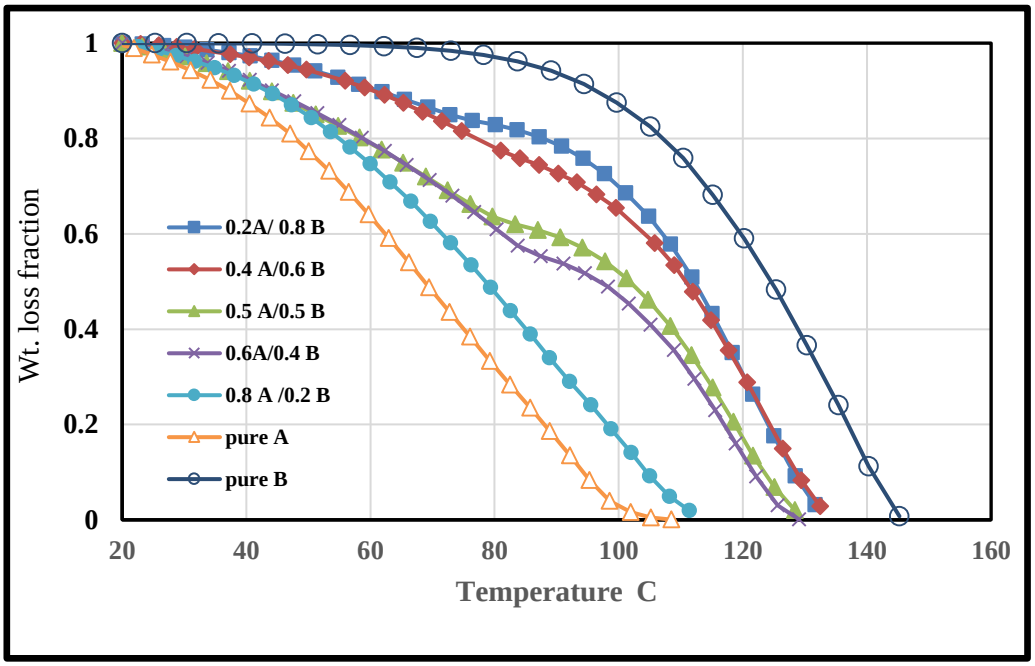

Figure 5- 14. Weight loss fraction versus temperature at heating rate 5 C/min. for a different mixtures of ammonium carbonate (A) and ammonium bicarbonate (B), as well as the pure salt.

5.5.4 Carbonate / Carbamate System (A/C)

The mass losses (decomposition) of a mixture containing ammonium carbonate and ammonium carbamate are studied as shown in figures (5.16 to 5.20) by thermogravimetric analysis. A constant heating rate (5 °C/min.) is used for gathering experimental data using TGA for binary system samples as well for each pure compound. The data are listed in tables (C3and C4) in appendix C. Different ratios (0.2/0.8, 0.4/0.6, 0.5/0.5, 0.6/0.4, and 0.8/0.2) of the above compounds were tested to show the accuracy of the PIM over the temperature range 20–95◦C. Ammonium carbamate solid decomposes at temperature 59°C and standard atmospheric pressure (Ramachandran, Halpern and Glendening, 1998), while the decomposition temperature of the ammonium carbonate begins at 60 °C (House 1980). The decomposition curves for a mixture of both compounds have approximately an identical behaviour, which could be explained to two main factors. The first factor is the compounds roughly possess a matching dissociation temperatures limit as shown above. Secondly, both compounds give two moles of ammonia and one mole of carbon dioxide during the decomposition process according to reactions 1 and 3, i.e. a high similarity in products in the gaseous state. The main difference between the compounds is the chemical bonds in carbamate molecules there is a covalent bond C-N yet in carbonates there are only ionic bonds. On the whole, the results of this study and according to the above explanation, the calibration is unsuccessful due to interference of initial composition of unknown solid mixture (figure 5.21), due to the occurrence of the interaction

of the two components. However, this fact is supported by Fulks et al. (2009) as mentioned in their review about the solid materials as alternative ammonia sources for lean NO_x with selective catalysts, that the decomposition of the carbamate and carbonate ammonium salts generate very similar pressures as shown in figure (5.15).

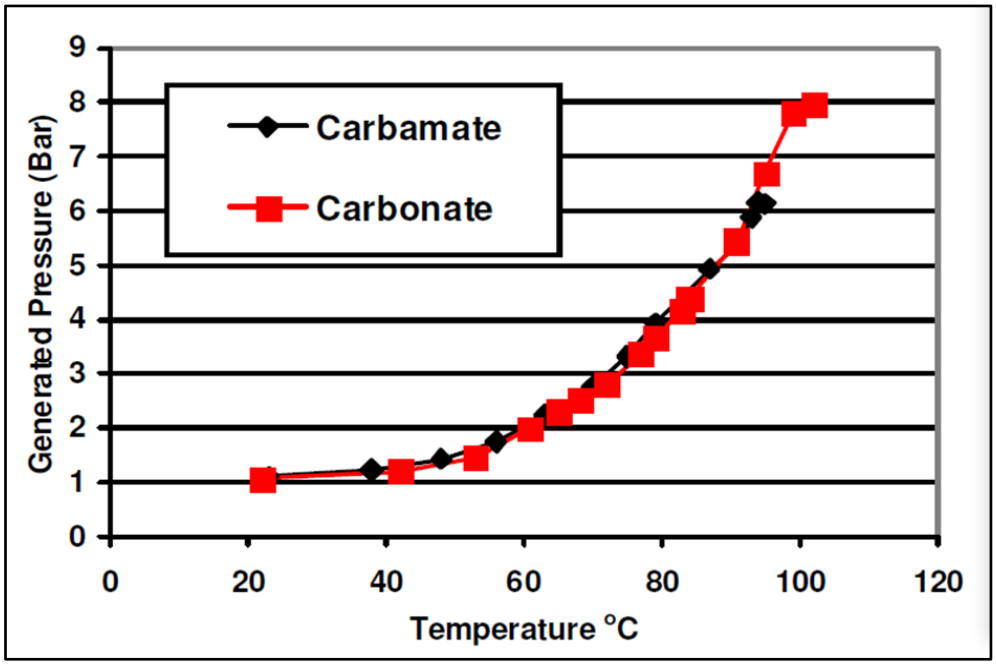

Figure 5- 15. Total gas pressure as a function of temperature for ammonium carbonate and ammonium carbamate, (Fulks et al., 2009).

In similar sense Garner (1955) explained the effect of equilibrium at the interface. There are three consecutive stages that may arise in carbonate decomposition (Garner, 1955); (i) desorption of CO_2 (ii) the production of nuclei of new phases and (iii) the occurrence of an interfacial reaction. On the other hand, he discusses the effect of the reaction kinetics at the interface by the pressure equilibrium. The arising difficulties at lower temperatures might lead to false equilibria due to the generation of small nuclei. These small nuclei usually have a high dissociation pressure at initial stages of growth. He concluded the rate of reaction in solid-state is proportional to surface area and the pressure of the gas at the interface.

As shown in figure (5.22) the weight loss fraction versus temperature at a heating rate 5 C/min. for five different mixtures of ammonium carbonate (A) and ammonium carbamate (C), as well as the pure salts, the inversion process is not possible because of the TGA profiles are very closes to each other. So the results of PIM are insufficiently accurate to infer initial composition of the unknown samples, when using the entire TGA profile. Future work could explore inversion with narrower heating rates and ranges, particularly the choice of initial temperature.

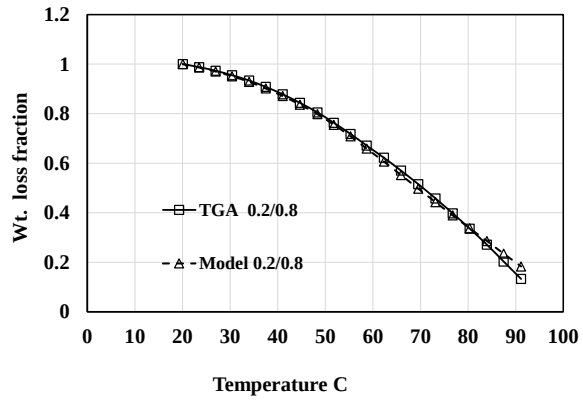

Figure 5- 16 shows the mass loss fraction of A/C salts versus the temperature, the ratio: 0.2/0.8

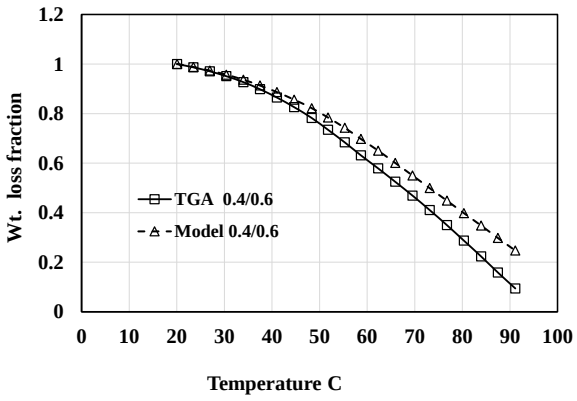

Figure 5- 17 shows the mass loss fraction of A/C salts versus the temperature, the ratio: 0.4/0.6

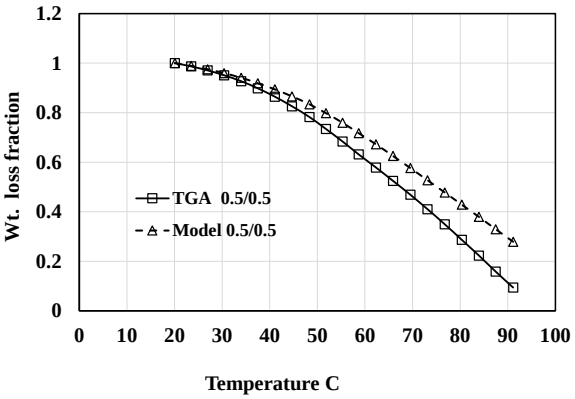

Figure 5- 18 shows the mass loss fraction of A/C s alts versus the temperature, the ratio: 0.5/0.5

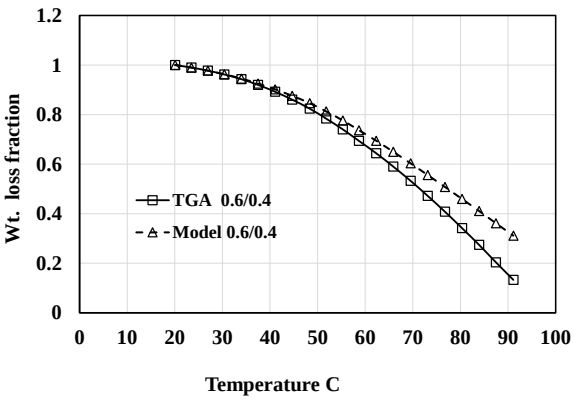

Figure 5- 19 shows the mass loss fraction of A/C salts versus the temperature, the ratio: 0.6/0.4

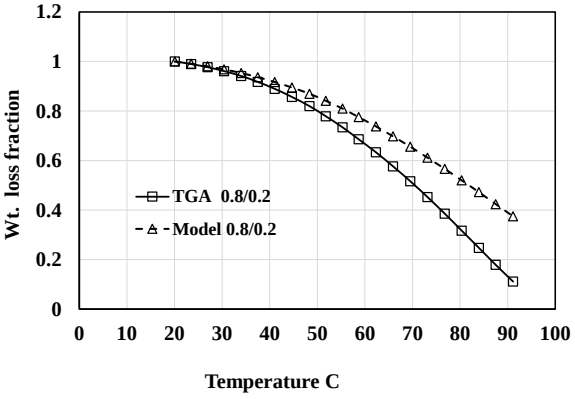

Figure 5- 20 shows the mass loss fraction of A/C salts versus the temperature, the ratio: 0.8/0.2

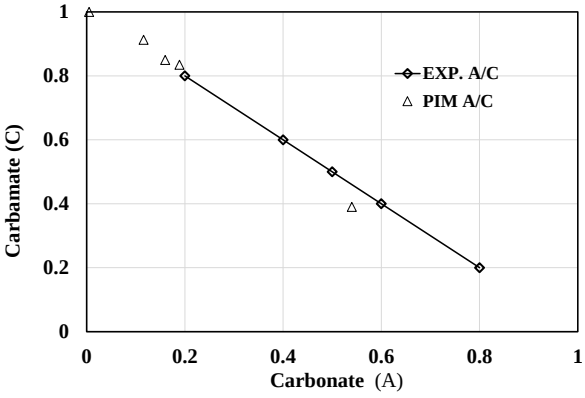

Figure 5- 21 shows TGA and PIM calibration results for the mass loss fraction (A/C)

According to the above data, we can deduce why the conversion or the fraction of mass loss for A/C mixture is very high relative to the other two mixtures. The results show that for the five cases, at temperatures ~ 90 °C the conversion exceeded 90% of sample mass. The average error percentage is high (7.1, 25.4, 44.5, 38.2, 41.7) for the carbonate/carbamate ratios (0.2/0.8, 0.4/0.6, 0.5/0.5, 0.6/0.4, and 0.8/0.2) respectively. However, the results cannot support the acceptance of this modelling approach for the characterizing the process for these two components.

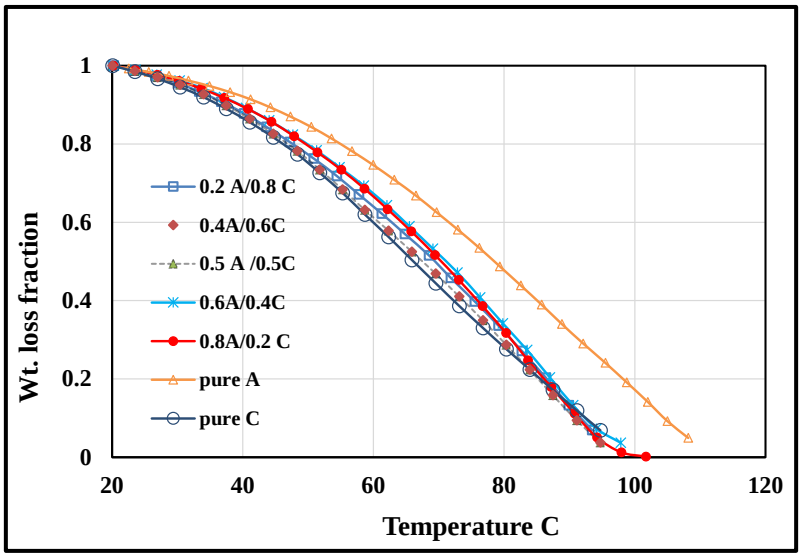

Figure 5- 22. Weight loss fraction versus temperature at heating rate 5 C/min. for a different mixtures of ammonium carbonate (A) and ammonium carbamate (C), as well as the pure salt

5.5.5 Bicarbonate / Carbamate System (B/C)

The figures (5.23 to 5.27) illustrate the fraction mass loss versus the temperature for a mixture of ammonium bicarbonate (B) and ammonium carbamate (C). The effect of component ratios (0.2/0.8, 0.4/0.6, 0.5/0.5, 0.6/0.4, and 0.8/0.2) of the B/C compounds are studied within the temperature between 20 and 102°C, the data are listed in tables C5 and C6 in appendix C. An analogous protocol is performed as shown in previous sections (5.5.3 and 5.5.4) to test the fidelity of the weighted pure component model to predict the composition of a binary mixture. The results show that an acceptable agreement between the experimental and TGA profiles and the model. In figure 5.23 the mass loss was approximately less than 0.2 at 102°C since the sample contained 80% ammonium carbamate and only 20% ammonium bicarbonate. While in figure 5.27 the fraction of mass loss, not more than 0.6 at 102 °C, as a result, the sample composed mainly from ammonium bicarbonate (80%). the inversion by using PIM as shown in figure 5.28.

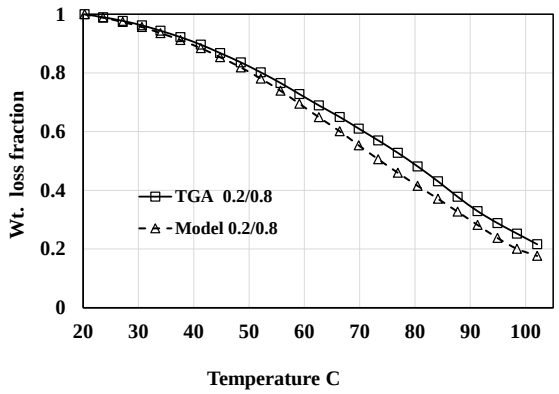

Figure 5- 23 shows the mass loss fraction of B/C salts versus the temperature, the ratio: 0.2/0.8

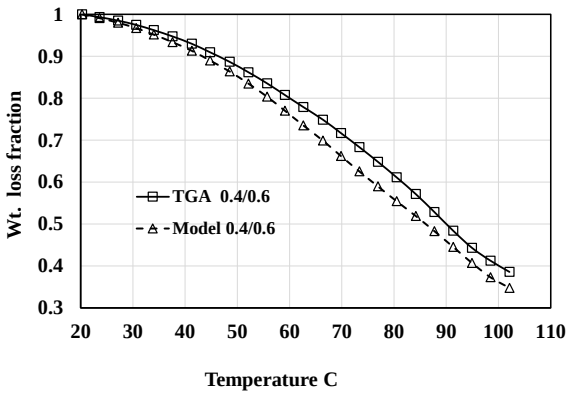

Figure 5- 24 shows the mass loss fraction of B/C salts versus the temperature, the ratio: 0.4/0.6

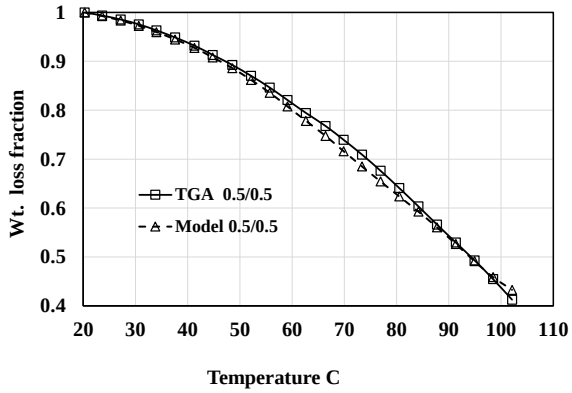

Figure 5- 25 shows the mass loss fraction of B/C salts versus the temperature, the ratio: 0.5/0.5

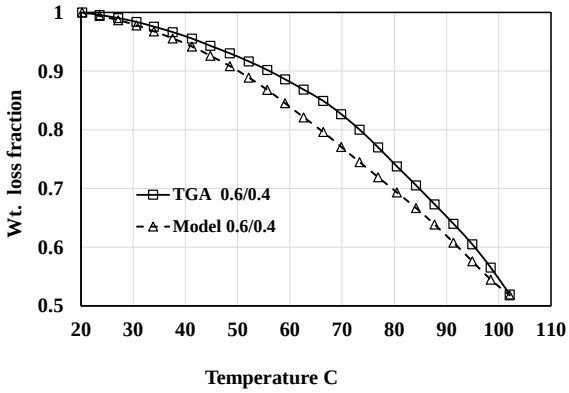

Figure 5- 26 shows the mass loss fraction of B/C salts versus the temperature, the ratio: 0.6/0.4

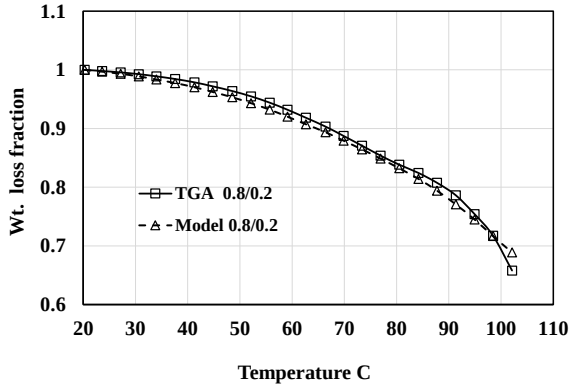

Figure 5- 27 shows the mass loss fraction of B/C salts versus the temperature, the ratio: 0.8/0.2

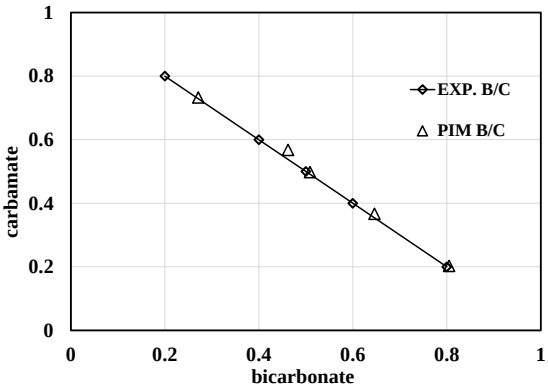

Figure 5- 28 shows TGA and PIM calibration results for the mass loss fraction (B/C)

These results seem to be consistent with that which found in section 5.3 for the dissociation reaction curves of pure single salts. The average errors percentage is (7.3, 5.1, 1.4, 3.4, 1.02) for the bicarbonate/carbamate ratios (0.2/0.8, 0.4/0.6, 0.5/0.5, 0.6/0.4, and 0.8/0.2) respectively confirming of a good agreement of this method for the characterizing by forward model and TGA experimental data. The calibration curve of binary system of the bicarbonate /carbamate

also gives a good results in the harmony between the TGA profiles and the forward model is a positive sign for potential effectiveness of the pseudo-inverse method. The other point is the TGA profiles itself appear consistent as shown in figure 5.29. There is no intercept between the curves due to the two compounds have different decomposition temperatures as shown in curves of pure salts.

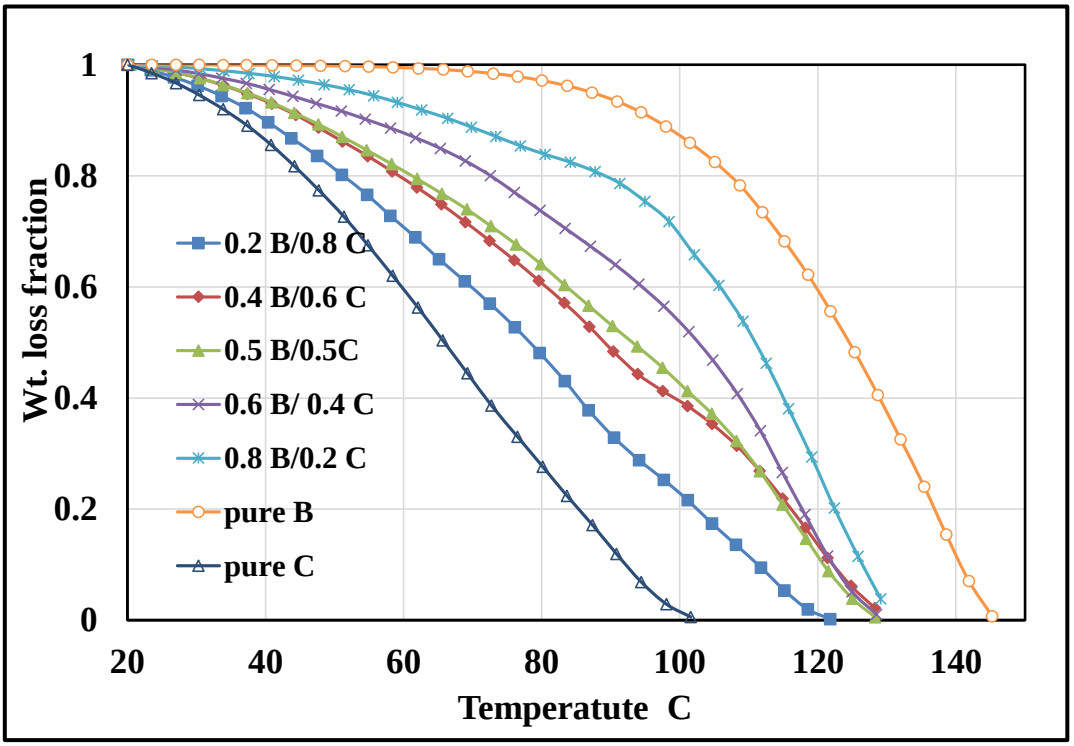

Figure 5- 29. Weight loss fraction versus temperature at heating rate 5 C/min. for a different mixtures of ammonium bicarbonate (B) and ammonium carbamate (C), as well as the pure salt

The solid materials which are separated at the end of the carbon dioxide and aqueous ammonia solution reaction in the chapter six should be characterised using different analytical techniques. In order to integrate the chapters of this thesis, two samples are chosen for analysing using the TGA (we could not analyse all samples due to time limitation and cost). However, experiment 9 which yielded highest product with reaction conditions of 3.5 kV, 0.8 L/min. CO_2 flowrate, 3.4 mol/L aqueous ammonia concentration, and reaction time 40 minutes is selected.

While the other experiment was 17 which produced a unlike solid form with different reaction conditions; 4.0 kV, 0.6 L/min. CO_2 flowrate, 2.8 mol/L aqueous ammonia concentration, and reaction time 30 minutes. The crystals of this experiment have a different shape (most experiments yielded crystals needle like morphology), it was a rectangular columns shape.

Figure 5.30 illustrates TGA profiles of the two samples, the curve of the experiment 9 is clearly looks very close to pure ammonium bicarbonate according to figure 5.14. While the result of experiment 17 is to shift apart from the pure curve. In purpose for interpreting the change in composition of samples, the reason can be mostly attributed to the reaction conditions. The main parameter influencing the conversion of carbonate to bicarbonate is the reaction time which is less than in experiment 9 by ten minutes. The other point which support this conclusion is the weight of the separated solid produced is also less, in addition the flow rate and concentration of the reactant are less too. So one can predicted the sample contains about 80 % ammonium bicarbonate and the other component is the carbonate salt according to figure 5.14. Crystallization unlikely occurs for the carbamate salts due to its high solubility.

Through the calculations using PIM, the results show that the composition consists of more than 93% ammonium bicarbonate. These results confirming the analysis that is done using NMR spectroscopy and FTIR spectroscopy in chapter six.

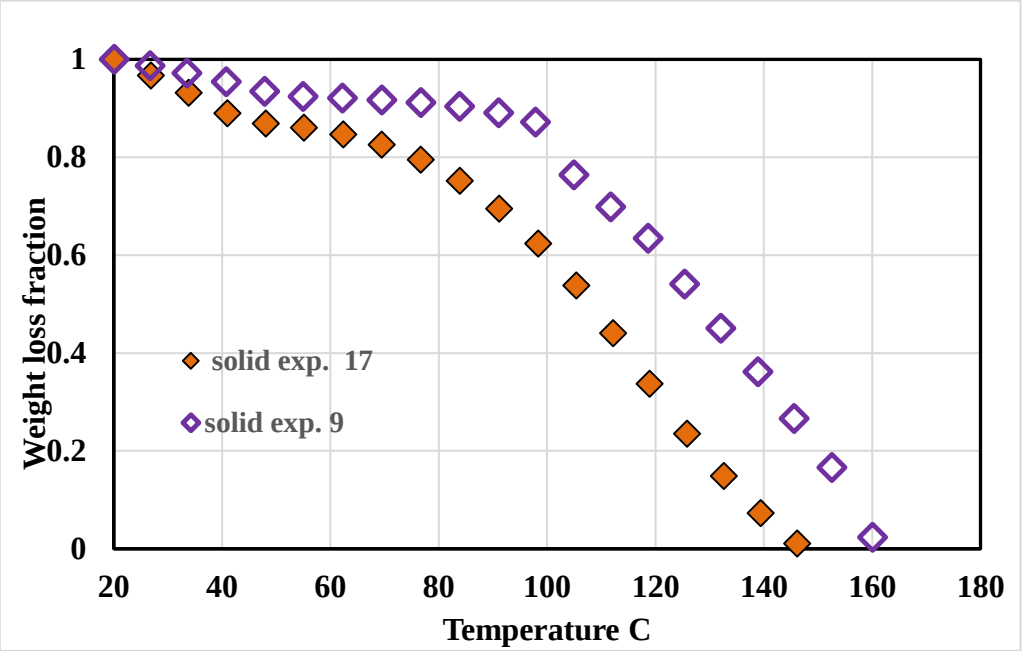

Figure 5- 30 represents TGA profiles of two samples. The weight loss fraction versus temperature at heating rate 5 C/min. for solid separated from reaction of the carbon dioxide and aqueous ammonia (the deposits produced from experiments number 9 and 17 in chapter six).

5.6 Conclusions:

The massive quantities of carbon dioxide emission and ammonia in nature have galvanized many studies to explore the reaction conditions of these two chemical compounds. The focus of this study is the analysis of the predictable salt mixture produced from CO_2 /NH_3 reaction such as ammonium carbonate (A), bicarbonate (B), and carbamate(C). The purpose of the study is subdivided into two main objectives. The first objective is to investigate the effect of changing the heating rates on the kinetics decomposition parameters of three ammonium salts in the non-isothermal condition using thermogravimetric analysis data. The data of a set of experiments which are performed on the three salts (A, B, and C) under five different heating rates are analysed using Coats and Redfern approximation method. The experimental results suggest that the values of activation energy *E* and pre-exponential factor (*A*) are decrease with increasing heating rate for the three salts. One of the more significant findings to emerge from this study is that the values of kinetic parameters are not fixed, but altered under non-isothermal conditions, theoretical conversion, and temperature. However, the results of the current study do not support the previous assumption done by (Popescu and Segal, 1994) about the kinetic parameters of the reaction in non-isothermal kinetics. They have claimed in their assumption that “there are no change" kinetic parameters of the reaction during the non-isothermal experiments. Moreover, the results of this study have supported the conclusions of Vyazovkin, (2000) of acceptance of the concept of variable activation energy which is more consistent with the concept of the multiple-step nature of the solid-state reactions.

The second purpose of this chemometrics study has been to an analytical relationship, between the pure components and an unknown mixture of two species depending on the temperature using the pseudoinverse method (PIM) to find the composition of that mixture. The study focused on mixtures: A + B or A + C or B + C. Up to the best of our knowledge, before this study, there are no estimations for unknown quantities of components in the solid-state samples using PIM. The major limitation of this study is as we expect there are side interactions between the salts lead to small incorrect prediction through the modelling of data using the PIM. The average errors percentage between the TGA profiles and the forward model is (3.4, 1.6, 9.7, 9.1 and 21.0) % for (0.2/0.8, 0.4/0.6, 0.5/0.5, 0.6/0.4, and 0.8/0.2) respectively of the ammonium carbonate/ammonium bicarbonate binary system. In addition, the average errors for the carbonate/carbamate ratios was (7.1, 25.4, 44.5, 38.2, 41.7) % for the same above ratios. So from the results, the PIM is not suitable for the above two binary mixtures

Finally, the average errors percentages were (7.3, 5.1, 1.4, 3.4, 1.02) for the bicarbonate/carbamate ratios (0.2/0.8, 0.4/0.6, 0.5/0.5, 0.6/0.4, and 0.8/0.2) respectively. The results of the PIM method for the bicarbonate/carbamate characterization show a good agreement between the modelling and experimental data. Therefore, it can be inferred that a new procedure with the algorithm is developed and tested to estimation for unknown quantities of components in the solid-state samples using PIM depending on the TGA data. The testing of a samples for solid separated from reaction of the carbon dioxide and aqueous ammonia using TGA profiles show a good agreement for characterization of solids. So one could be recommended to explore TGA operating conditions for future work, potentially those that mute interaction dynamics.

Department of Chemical and Biological Engineering

Chapter Six

Response surface method for modelling the aqueous NH_3 reaction mediated by submerged, CO_2 bubbles injected with non-thermal plasma

Chapter Six

Response surface method for modelling the aqueous NH_3 reaction mediated by submerged, CO_2 small bubbles injected with non-thermal plasma

6.1 Introduction

The increasing greenhouse gases levels in the atmosphere are a topical concern (Halstensen *et al.*, 2017) . The largest contribution comes from CO_2 emissions (Qi *et al.*, 2013). Global carbon dioxide emissions are at the highest levels with published concentration as 414.83 ppm at Mauna Loa Observatory in May 2019 (McGee, 2019). There are many driving forces that influence greenhouse gas (GHG) emissions such as socio-economic development and technological changes which are linked in very complex dynamic systems. Substantial reductions of emissions, however, hinge on minimizing the capital costs and the energy demand in carbon dioxide capture and utilization processes. One of the most common methods to capture carbon dioxide is chemical reaction to produce valuable chemicals. The experiments of the present work are conducted according to central composite rotatable design to perform a chemical reaction between CO_2 and aqueous ammonia (NH_4OH). The data obtained from the reaction is used to generate a mathematical second-order response model.

The responses (results) of experiments selected in this study are two variables. The first response is the electrical conductivity of the solution at the end of the reaction. The second response is the yield of the process as precipitated solid of ammonium bicarbonate. The responses depend on (at least) four control parameters; high voltage (X_1), carbon dioxide gas flow rate (X_2), aqueous ammonia concentration (X_3) and time of reaction (X_4). Five levels for each variable (X_1, X_2, X_3, and X_4) are selected for conducting the experiments. The levels of the variables together with their coded values are illustrated in tables 3.2 to 3.5 in chapter three. The present study is significant and novel in at least two major respects. Firstly, this carbon dioxide capturing proceeds via combining non-thermal plasma and CO_2 very fine bubbles technologies in a stagnant aqueous ammonia column. To our knowledge, the combining of these technologies is wholly novel within our research group. Secondly, it links the major operating conditions using a mathematical model with two responses. These responses are the electrical conductivity of the solution and the yield of the process (precipitated ammonium bicarbonate).

6.2 The hypotheses of the effects of parametric variation

a- The use high voltage (input voltage) to generate the non-thermal plasma can activate the CO_2 molecules and enhance in production of extreme active species to participate in chemical reaction more effectively. On another hand, the non-thermal plasma might create a specific species of atoms or radicals such as O, OH… potentially diverting the reaction to undesired side-reactions.

b- The flow rate of CO_2 is a significant factor (solely as a small bubbles) because it enhances the rate of mass transfer and degree of mixing. The role of small-bubbles in a chemical reaction of CO_2/aqueous ammonia solution mainly is to raise the ratio of surface area to volume, then increase the residence time and finally improve reaction productivity. On the second aspect, it may be that increasing flow rate of gas through using small -bubbles will decrease or have no effect on the reaction kinetics. In particular, however, this contacting configuration leads to the possibility that the bubble gas-liquid interface is the catalytic surface for the reaction. On the gas side, the activity of CO_2 is maximal, while ammonia is in excess on the liquid side. This staging makes the interface the point where both reactants are in excess simultaneously.

c- Higher aqueous ammonia concentration enhances the reaction rate due to the excess of the reactant molecules or ions. So the reaction yield of ammonium bicarbonate as a product will be high. An opposite hypothesis, could be that there are no effect from increasing the aqueous ammonia concentration on the reaction productivity. When several reactants are involved, increasing the concentration of one of them may not affect the rate of reaction if not enough concentration of the other reactants is available.

d- Does the reaction rate change under varying conditions and how the mechanism of the reaction occurs? Chemical reactions require different periods of time for completion. That is based on the characteristics of the reactants and products and the conditions of the reaction. In gas-liquid reactions, increasing surface area to volume influences the reaction time and provides an opportunity for conversion rate depending on process conditions and reaction nature. Reaction time is a key factor to determine the optimum period of reaction, so the rate of productivity will be highest due to using small bubbles. The counter hypothesis, however, is that carbon dioxide is an acidic gas and will rapidly react with an alkaline solution of ammonia so, there no effect of the reaction time on the reaction kinetics. But if the reaction is heterogeneous, it will depend on the interfacial area. If the reaction is mass transfer limited and homogeneous, it will depend on the mass transfer area.

6.3 Mathematical Model

There are several approaches that correlate the results of the experimental data with the variables that affect them to achieve a kinetic expression that describes the desired process. A second order polynomial was employed in the range of four independent variables as represented by the following equation: -

$$Y_1 = \beta_O + \beta_1 X_1 + \beta_2 X_2 + \beta_3 X_3 + \beta_4 X_4 + \beta_5 X_1 X_2 + \beta_6 X_1 X_3 + \beta_7 X_1 X_4 + \beta_8 X_2 X_3 + \beta_9 X_2 X_4 + \beta_{10} X_3 X_4 + \beta_{11} X_1^2 + \beta_{12} X_2^2 + \beta_{13} X_3^2 + \beta_{14} X_{14}^2 \quad (6.1)$$

To postulate the best values of the coefficients in equation (6.1) the experimental data of the electrical conductivity of solution (Y_1 in mS at end of reaction) and the yield of the process (Y_2 in g precipitated solid), are fitted using nonlinear regression via the Gauss-Newton method. The significance of each term in equation (1) is estimated using the F-test analysis

6.4 Estimating the polynomial coefficients

The (F-test) analysis is used for testing the significance of each term in equation (6.1), using the coded data of central composite design. The coefficients (β_i) of equation (6.1) can be determined simply using nonlinear regression estimation. The multiple regression analysis was performed using *STATISTICA TIBCO Software* (13.5.0.17) to estimate the polynomial coefficients of the quadratic multivariable model whose values are displayed in tables 6.1 and 6.2. Fitting an equation, equivalent to equation (6.1), is conducted but expressed in a slightly different, more convenient form. The design of the coded variable data of the electrical conductivity (Y_1) as given in table (6.1) is obtained and the fitted response surface model was as follows:

$$y_1 = 158.35 + 1.25X_1 + 2.25X_2 + 4.68X_3 + 3.6X_4 + 0.38X_1X_2 + 0.093X_1X_3 + 0.23X_1X_4 - 0.98X_2X_3 - 3.47X_2X_4 + 2.42X_3X_4 + 0.7X_1^2 - 0.95X_2^2 + 0.79X_3^2 - 0.82X_4^2 \quad (6.2)$$

The correlation coefficients (R^2) between the predicted and observed values were 0.992 for the electrical conductivity (y_1) and 0.996 for the process yield of precipitated solid salt (y_2) as shown in figures (6.1 and 6.2). The high values of the correlation coefficients, indicate both models are statistically important and appropriate to predict and optimize the responses. From equation (6.2), the residuals can be obtained as the difference between observed (Y_i) and predicted values (y_i) [$e_i = (Y_i - y_i)$] as shown in table D2 in appendix D. An estimate of

experimental error variance (S_r^2), is obtained by dividing the residual sum of squares ($\sum e_i^{\,2}$) by the number of degree of freedom as in equation (6.3):

$$S_r^2 = \sum_i^N \frac{e_i^2}{\gamma} \qquad (6.3)$$

The degree of freedom (γ) can be specified from the equation (6.4).

$$\gamma = N - n \qquad (6.4)$$

Where ***N*** is the number of experiments (**28**) and ***n***; is the number of coefficient (**15**) in the equation (6.1). Thus **the experimental error variance**:

$S_r^2 = 22.3558/(28-15)$ =**1.7**

The estimated variance of coefficients (S_b) was calculated from equation (6.5) and listed in table (6.1). The calculations of $\sum X_i^2$ are shown in (appendix D1).

$$S_b = \frac{S_r^2}{\sum X_i^2} \qquad (6.5)$$

Table 6- 1 shows the F-test results for the mathematical model coefficients of the electrical conductivity of the solution at the end of the experiment. (S: significant, NS: insignificant)

	ΣXi^2		β i	Sb=Sr^2/ΣXi^2	F=(βi^2 / Sb^2)	F 0.95 (1, 13) =4.67
		β_0	158.35			
X_1	24	β_1	1.25	0.071	20.5	S
X_2	24	β_2	2.25	0.071	70.9	S
X_3	24	β_3	4.68	0.071	305.5	S
X_4	24	β_4	3.60	0.071	180.4	S
X_1X_2	16	β_5	0.38	0.107	1.3	NS
X_1X_3	16	β_6	0.093	0.107	0.08	NS
X_1X_4	16	β_7	0.23	0.107	0.4	NS
X_2X_3	16	β_8	-0.98	0.107	8.9	S
X_2X_4	16	β_9	-3.47	0.107	111.9	S
X_3X_4	16	β_{10}	2.42	0.107	54.4	S
X_1^2	48	β_{11}	0.70	0.035	13.8	S
X_2^2	48	β_{12}	-0.95	0.035	25.5	S
X_3^2	48	β_{13}	0.79	0.035	17.5	S
X_4^2	48	β_{14}	-0.82	0.035	18.7	S

Finally, comparing the determined values using the **F** values at 95 % limit of confidence, the significance of each term in equation (6.2) is examined. As seen (table 6.1) the β_5, β_6, β_7 have no significant effect, which allows the neglect of the X_1X_2, X_1X_3, and X_1X_4 interaction effects. Therefore, the optimum formula of mathematical model which correlates the response function (i.e., the electrical conductivity of the solution at the end of the experiment) to the four studied variables in terms of the coded variables is:

$$y_1 = 158.35 + 1.25X_1 + 2.25X_2 + 4.68X_3 + 3.6X_4 - 0.98X_2X_3 - 3.47X_2X_4 + 2.42X_3X_4 + 0.7X_1^2 - 0.95X_2^2 + 0.79X_3^2 - 0.82X_{14}^2 \quad ----- \quad (6.6)$$

By admitting only the analogous coefficients of equation (6.1) using the experimental data of central composite design, the dependence of the process yield of the precipitated powder (Y_2) in terms of the studied variables was determined and found equal to:

$$y_2 = 12.14 + 0.43X_1 + 3.26X_2 + 1.7X_3 + 4.7X_4 + 0.1X_1X_2 + 0.16X_1X_3 + 0.08X_1X_4 + 1.67X_2X_3 - 2.13X_2X_4 + 2.05X_3X_4 + 1.21X_1^2 - 1.07X_2^2 + 0.47X_3^2 - 0.82X_{14}^2 \quad (6.7)$$

Now from equation (6.7), it is possible to compute the predicted values (y_2) and the corresponding residuals (ei=Yi-yi) calculated in table D2 in appendix D) as listed in figure 6.2 (the correlation between the predicted and observed data). Where ***N*** is the number of experiments (**28**) and ***n***; is the number of coefficient (**15**) in the equation (6.1). Thus **the experimental error variance**:

$S_r^2 = 7.8/(28 - 15)$ = **0.6**

The significance of coefficients may be estimated by comparing values of the ratio ($\boldsymbol{\beta_i}^2/S_b^2$) and compared with the critical value of **F** at 0.05 (1, 13) = 4.67 of F-distribution at 95% level of confidence with 1 and 13 degrees of freedom. F-distribution at 95% level of confidence (listed in Appendix (Montgomery, 2001)). As shown in Table (6.2) it seems that β_5, β_6, β_7 and all interaction coefficients between X_1 and the variables (X_2,X_3, and X_4) in equation (6.7) have not significant. Accordingly, the initial model equation is truncated to give the following model:

$$y_2 = 12.14 + 0.43X_1 + 3.26X_2 + 1.7X_3 + 4.7X_4 + 1.67X_2X_3 - 2.13X_2X_4 + 2.05X_3X_4 + 1.21X_1^2 - 1.07X_2^2 + 0.47X_3^2 - 0.82X_{14}^2 \quad (6.8)$$

The equation (6.8) illustrates the best formula represented the relationship between the yields of precipitated solid produced by the non-thermal plasma process with the four studied variables.

Table 6- 2 shows the F-test results for the mathematical model coefficients of the electrical conductivity of the solution at the end of the experiment. (S: significant, NS: insignificant)

	ΣXi^2		β i	Sb=Sr^2/ΣXi^2	F=(βi^2 / Sb^2)	F 0.95 (1, 13) =4.67
		β_0	12.14			
X_1	24	β_1	0.43	0.025	7.53	S
X_2	24	β_2	3.26	0.025	424.84	S
X_3	24	β_3	1.7	0.025	115.36	S
X_4	24	β_4	4.7	0.025	884.01	S
X_1X_2	16	β_5	0.1	0.037	0.301	NS
X_1X_3	16	β_6	0.16	0.037	0.74	NS
X_1X_4	16	β_7	0.08	0.037	0.198	NS
X_2X_3	16	β_8	1.67	0.037	74.95	S
X_2X_4	16	β_9	-2.13	0.037	120.98	S
X_3X_4	16	β_{10}	2.05	0.037	111.80	S
X_1^2	48	β_{11}	1.21	0.0125	118.35	S
X_2^2	48	β_{12}	-1.07	0.0125	92.002	S
X_3^2	48	β_{13}	0.47	0.0125	17.79	S
X_4^2	48	β_{14}	-0.82	0.0125	53.71	S

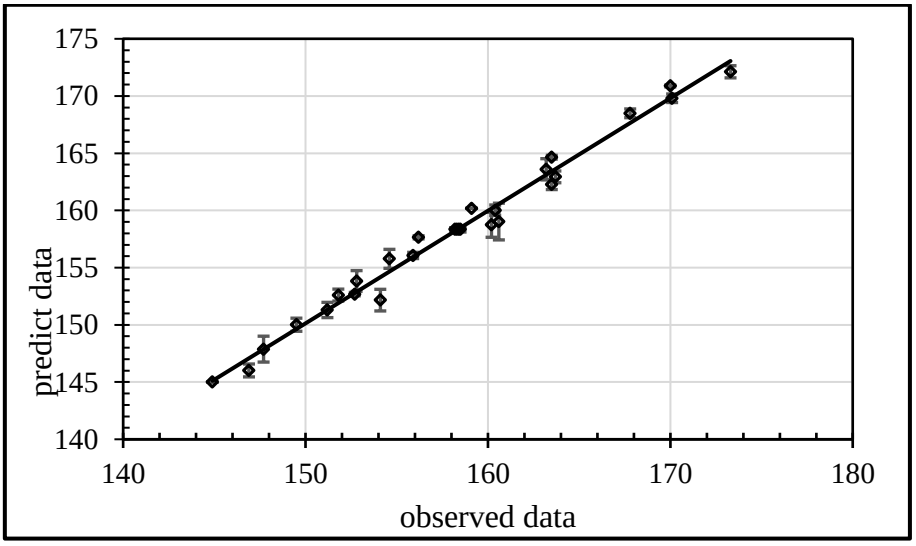

Figure 6- 1. The comparison between the predicted and observed data for electrical conductivity at the end of the experiment.

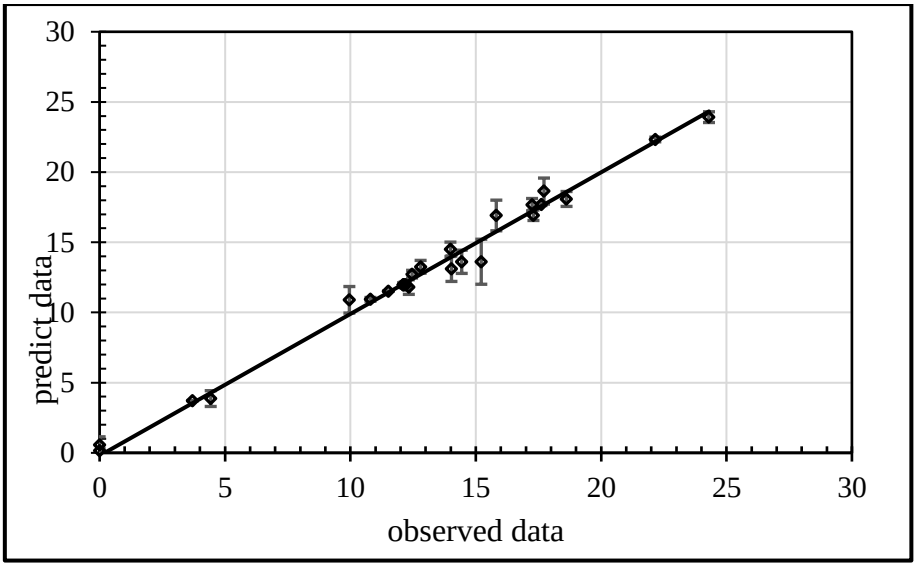

Figure 6- 2. Correlation between the predicted and observed data of the yield of the process from the separated solid substance.

6.5 Effect of the selected variables on the electrical conductivity

The electrical conductivity is defined as the ability of a solution to transmit electrical current, or in other words, it is the reciprocal of the solution's ability to resist the current (Horvath, 1985). The current is conducted by electrically charged particles called ions (current carriers), which are present in almost all solutions. Electrical conductivity data always provide a basic understanding of the behaviour of solution under specific conditions. Furthermore, it yields a convenient information required in analysing the experimental results for a variety of thermodynamic studies. Distilled water has very few ions, and therefore a low conductivity, while seawater has a large number of ions, and a high conductivity. Although a conductivity reading provides an overall measurement of the ionic strength of a solution, it is not possible to distinguish the specific amounts of individual ions. For this reason, conductivity is often used to measure the total dissolved solids (TDS) of a solution.

In general, the conductivity value of electrolytic solutions is influenced by many factors such as the temperature, the concentration, the mobility of ions, and the valences of the ions. When a voltage is applied across the electrodes, the ions in the solution conduct a current flows between the two electrodes. The conductivity of an aqueous electrolyte solution is described in terms of the ions produced by 1 mole of an electrolyte placed between two large parallel plates held a distance of 1 cm a part.

6.5.1 Effect of individual parameters on the electrical conductivity of the final solution

The effects of high voltage, carbon dioxide flow rate, aqueous ammonia concentration, and time of reaction on the electrical conductivity (E.C.) of the solution are studied and assessed. To emphasize the effect of each variable on the E.C. individually, the operating conditions of **experiment number (9)** are chosen to be the best conditions. This is because it gives high electrical conductivity of the solution and a higher yield of solid (24.3 g.) which deposited at the end of the reaction and cooling processes respectively. So all calculations of mathematical model and captions of graphs are based on these operation conditions of the high voltage, carbon dioxide flow rate, aqueous ammonia concentration, and time of reaction (3.5 kV, 0.8 LPM, 3.4 M., and 40 min.) respectively.

6.5.1.1 Effect of high voltage on the electrical conductivity

In Figure 6.3, electrical conductivity is shown over the range of voltages varied as reported in table 3.1 with all other parameters held at the fixed values as given in the caption. Generally, the dielectric barrier discharge (DBD) usually produce highly non-thermal plasma conditions under a controlled parameters at moderate temperatures of gas and atmospheric pressure. The DBD reactor has an ability to generate energetic electrons, which could induce excited species, radicals, and atoms. All previous species are considered as reactive species serving as an agent for enhancing the chemical reaction (Wagner *et al.*, 2003).

This slice of the response surface is selected as it is representative of the overall observed response that electrical conductivity apparently slightly declines then sharply increases as a function of voltage, so it shows a high sensitivity at the highest voltages. Probably, the decline in E.C. indicates that the plasma still lacks sufficient energy density, and thus would exhibit a slight potential decrease in the solution concentration at specified power levels. Under low temperature plasma conditions, the discharges channels will increase the reactivity of reactants in specific surface area per unit of time (Myshkin *et al.*, 2013). In general, with respect to the electrical conductivity, the diffuse nature of the discharges are more desirable to enhance the generation of the reactive species.

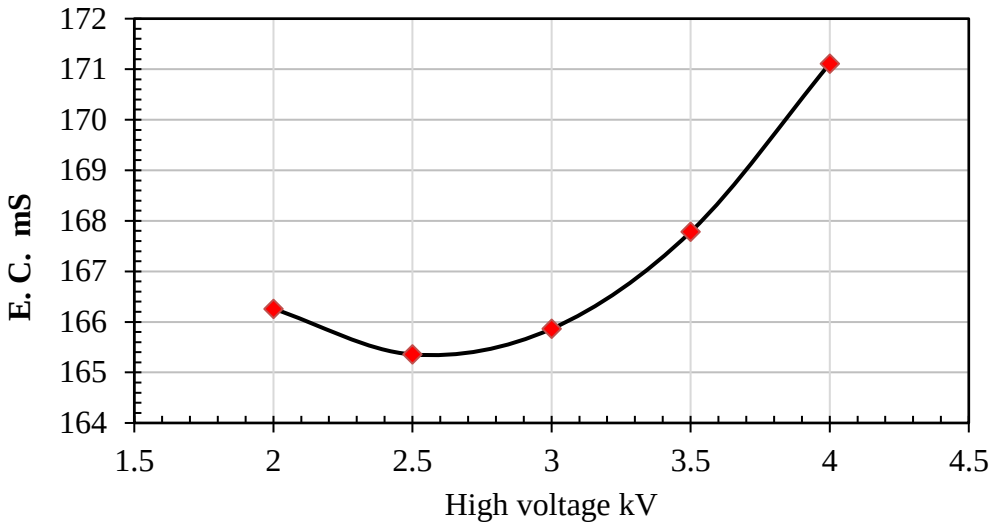

Figure 6- 3. The influence of the high voltage on the electrical conductivity of the solution at a aqueous ammonia concentration (3.4M), CO_2 flow rate (0.8 LPM), and time of the reaction (40 min.).

6.5.1.2 Effect of CO_2 flow rate on the electrical conductivity

The flow rate is varied between 0.2 to 1 LPM. The results are shown in figure 6.4. The behaviour pattern of the curve between the electrical conductivity and CO_2 flow rate could be split into two main parts. Firstly, the electrical conductivity achieves the maximum point at 0.4 L min^{-1}, thenceforward, a sharp reduction occurs at the later flow rates until it becomes less than 163 mS at 1 LPM. This observation agrees with Rehman *et al*. (2016) for ozone generation. They found an internal maximum in production of ozone for a specific flow rate, which corresponded to a residence time matching the kinetics timescale for completion of the ozone formation reaction. This is a general principle of optimum residence time for reaction in plasma microreactors was posited in the patent of Zimmerman and Lozano Parada (2009) but only experimentally validated later Rehman et al. (2016) and later supported for CO_2 transformation to CO by Liu et al. (2017).

The initial increase in the electrical conductivity of the solution with increasing gas flow rate is attributed to absorption of the limited quantity of CO_2 gas added to the solution of aqueous ammonia. The dissolved bubbles of gas in the liquid phase facilitates reactions which give specific ions such as CO_3^{-2}, HCO_3^-, NH_2COO^- OH^-, H^+, and NH_4^+ (Halstensen *et al.*, 2017) which certainly raise the electrical conductivity. Thereafter, increasing CO_2 flow rate i.e. an excess reagent relative to ammonia will enhance the formation of only one chemical compound ammonium bicarbonate so the electrical conductivity decreases (Meng, 2004).

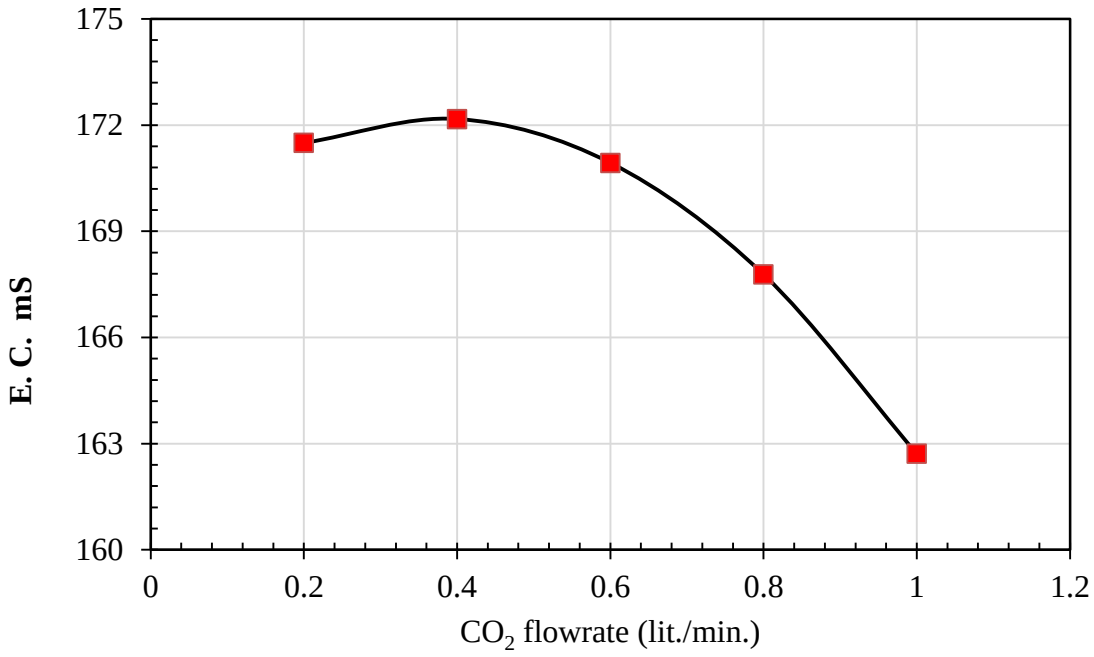

Figure 6- 4. The influence of CO_2 flow rate on the electrical conductivity of solution at constant aqueous ammonia concentration (3.4 M), high voltage (3.5kV) and time of reaction (40 min.)

6.5.1.3 Effect of the aqueous ammonia concentration on the electrical conductivity

Figure 6.5 illustrates the effect of ammonia concentration on the electrical conductivity of the solution. It can be seen that the solution conductivity is sharply increased with increasing the initial aqueous ammonia concentration. This agrees with (Kim, et al., 2009) having the ammonia concentrations range from 2 to 7 wt. % to capture CO_2 from blast furnace gas which contains high concentration CO_2. The increase in ammonia concentration results in a high CO_2 removal efficiency up to 90 percent. However, the study shows that with an increase in the concentration over 2.8 M, the curve of the electrical conductivity turns concave downward, i.e. with declining curvature. Such behaviour is consistent with an opposing mechanism to increasing the dissolution of carbon dioxide in a concentrated solution of aqueous ammonia. Appropriately, there are many intermediate reactions occurring between the two phases as well as the temperature changing (discussed in section 6.6 the behaviour of temperature and pH) during the reaction which tends to increase the reaction rate and generate various ions which leads to rising conductivity of the solution.

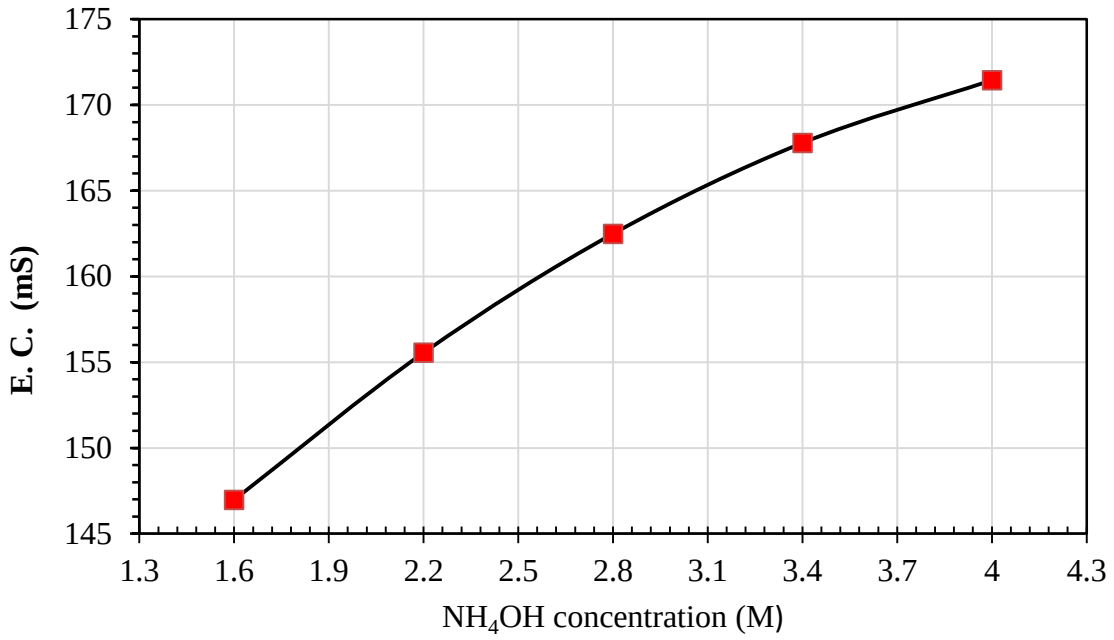

Figure 6- 5. The influence of aqueous ammonia concentration on the electrical conductivity of the solution at high voltage (3.5 kV), CO_2 flow rate (0.8 LPM)) and time of reaction (40 min.)

The CO_2 reaction in aqueous medium can be expressed by the following equation:

$$CO_{2\,(g)} \overset{at\ interface}{\Longleftrightarrow} CO_{2\,(aq.)} \qquad (6.9)$$

The reaction in equation 6.9 is the dissolution of CO_2 gas in aqueous medium. According to Pohorecki and Moniuk, (1988) the solubility is comparatively very high, the equilibrium at the interface can be assumed, described by Henry's law in equation (6.10):

$$C_{Ai} = \mathcal{H} P_{CO_2} \qquad (6.10)$$

Two reactions may be occurring after the step of absorption process (Danckwerts, 1970) by aqueous solutions:

$$CO_{2\,(l)} + OH^- = HCO_3^- \qquad (6.11)$$

$$CO_3^{-2} + H_2O = \ HCO_3^- \ + OH^- \qquad (6.12)$$

The reaction 6.11 is second order according to Danckwerts i.e. rate proportional to concentrations of both carbon dioxide and hydroxide ion. The rate constant of reaction (6.11) in infinite dilution and room temperature is about 6000 L mol^{-1}. s^{-1}. While the reaction (6.12) is first order at temperature of 20 °C with rate constant of 0.02 s^{-1}. So at the solutions of pH value greater than 10, the reaction (6.11) is faster than reaction (6.12) by 30 times in interval

of time 0.6 s^{-1}. Therefore, in this study, the OH^- ions will be enhanced by the non-thermal plasma and will play a significant role in reactions.

6.5.1.4 Effect of the reaction time on the electrical conductivity

The effect of the chemical reaction time on the electrical conductivity is studied as shown in figure 6.6. The conductivity linearly increases with time of chemical reaction. The electrical conductivity usually increases due to the formation of many current carriers which possess different valence such as CO_3^{-2}, HCO_3^{-1}, and NH_2COO^{-1}. Most ions have the tendency to associate at specific temperatures and concentrations. The electrical conductivity measurements provide a proper means for determining the degree of the association at particular conditions of the temperatures and concentrations.

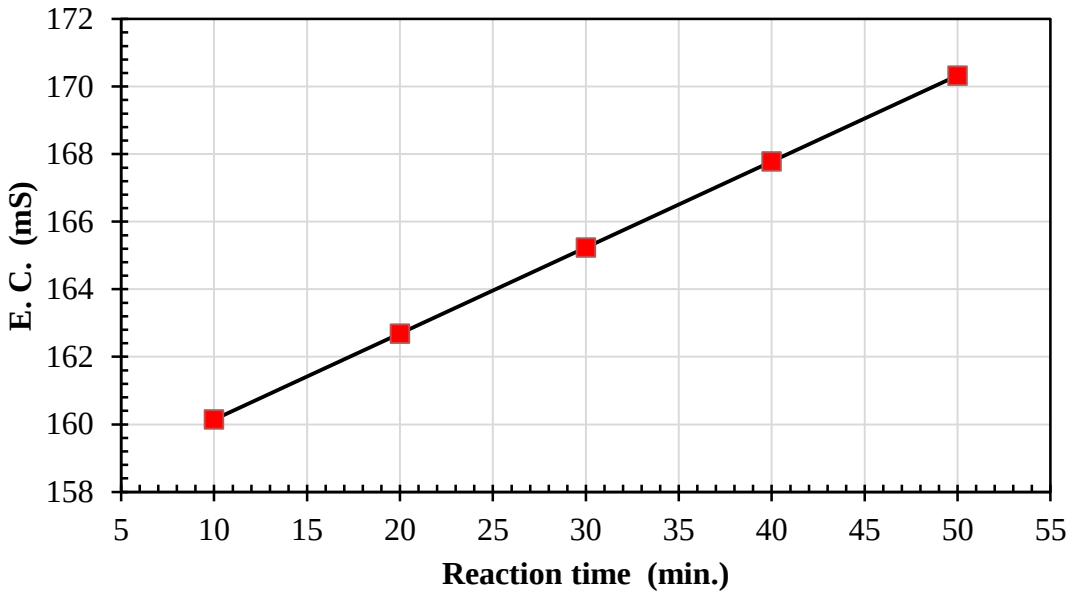

Figure 6- 6.Influence of reaction time on the electrical conductivity of solution at at high voltage (3.5 kV), CO_2 flow rate (0.8 LPM)) and NH_4OH concentration (3.4 M).

It can also be seen that using a long reaction time has increased production of ions. Using reaction time of 10 min. provides an E.C. only of 160 mS while 50 min. yields the electrical conductivity about (170 mS.). This behaviour may be due to completion of the intermediate reactions between the ions and that will enhance the yield of the process as will show in the next section (6.5) of process yield study. Sparging with micro-bubbles recently is shown a significant features to provide high mass transfer rates applicable in many industrial fields. High surface area-to-volume ratios give the pioneering role in gas-to-liquid mass transfer and solve the rate limiting step. Also, it introduces the gas as a nearly uniform cloud of very small bubbles with properties of low coalescence and nearly monodisperse size, according to

(Zimmerman *et al.*, 2008; Zimmerman, Tesař and Bandulasena, 2011) (Worden and Bredwell, 1998). Generally, as proposed in the hypothesis of the dissolved CO_2 in the liquid phase, the reaction with ammonia likely occurs at the bubble interface. There are two transfer processes are happening, in $CO_2/NH_{3\,(aq.)}$ reactions: a physical process, for dissolving which demands a short interval of time, simultaneously, along with a chemical reaction occurring at longer contact times. The reaction intensifies at a gas-liquid interface, due to the small-bubbles increasing surface area dramatically and due to staging with high reactant activity (reactants enter in different phases) enhancing driving forces for the reaction. In the other hand, long residence time or the slow velocity of small-bubbles rise will permit an efficient mass transfer to be achieved during the chemical reaction. So proportionately, if the surface area is doubled then the reaction rate will be doubled which excludes the equilibrium state.

6.5.2 The interaction effects of the variables on the electrical conductivity

The response surface methodology (RSM), using the Box–Wilson experimental design method, provides an evaluation of the relationship of the individual independent variables with their interactions on the dependent variables (response) (Çatalkaya and Şengül, 2006). The effects of parameters and their interactions on the electrical conductivity of the final solution are presented in the form of a three-dimensional response surface as shown in figures 5-10. If there are strong interactions between any two variables on the response then the lines will be curved rather than straight. On the other hand, with the case of a weak or no interaction between the process variables and response variable will be straight lines the plot of the surface will be a plane.

6.5.2.1 The effects of the high voltage and flow rate of CO_2

Figure 6.7 shows the effects of the high voltage and flow rate of CO_2 on the electrical conductivity of the solution. A maximum electrical conductivity of 166 mS is achieved at the high voltage (3.5 kV) and CO_2 flowrate (0.8-1.0 L/ min^{-1}). The E.C. increases with increase high voltage from 3kV to 3.5kV then it slightly decrease, regardless of the changes in CO_2 flow rate, which can be indicated by a nearly constant slight increase of the electrical conductivity with respect to the high voltage. So the effect of interaction is considered weak between high voltage and CO_2 flow rate as shown in the F test in table 6.1.

For all that, the trend indicates that plasma is an efficient tool as predicted in chemical kinetic simulation in chapter 4 for the formation of active species from CO_2 excitation which enhanced the reaction process. The electric field effect in electrochemical systems was reported

(Zimmerman, 2011) and discussed with their characteristics. One of these effects of the applied electric field is the flow inside micro channels and the formation of an electric double-layer when a fluid contains free ions in contact with a charging surface. This induces a driving force resulting in electro-osmotic flow. Increasing the high voltage in the plasma generator will certainly lead to an increase in the formation of the filament in a dielectric barrier glow discharge plasma (Brauer *et al.*, 1999). The energy of electrons increases due to the increase of the applied voltage. The ionization rate of gas will be enhanced, resulting in excess in the number density of ions and electrons, leading to an improvement in the reaction process. This is different from the previous results by Wang *et al.*, (1999) where the variation of the minimum voltage required to generate plasma was found to be independent of the flow rate of the gas stream on CO_2 conversion. However, the results of Wang *et al*. could be explained for a gas-gas reaction in plasma generators, while the current study is a gas-liquid. It also likely depends on the plasma generator design and its efficiency.

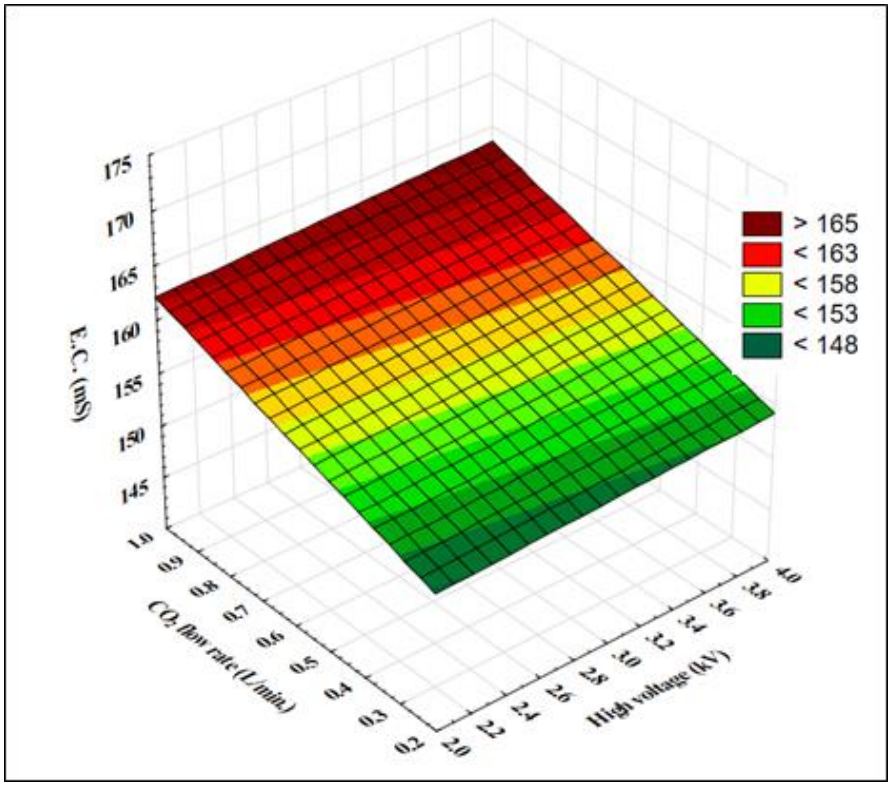

Figure 6- 7. The combined effects of the high voltage and flow rate of CO_2 on the electrical conductivity of the solution.

6.5.2.2 The effect of the high voltage and aqueous ammonia concentration

Figure 6.8 illustrates the combined effect of the high voltage and aqueous ammonia concentration on the electrical conductivity. The maximum electrical conductivity of 169 mS is achieved at the highest high voltage of 4 kV with highest concentration 4M of aqueous

ammonia solution. The concentration of ammonia plays an important role in the reaction process. Increasing the concentrations of ammonia, particularly over 3.4M, significantly enhances the electrical conductivity of the solution regardless of the high voltage. The effect of the ammonia concentrations on electrical conductivity is the result of the competing effects. Plasma activation of CO_2 molecules is not to produce ammonium carbamate or bicarbonate directly. Rather, it is a competition between the covalent bond formation and ionic bond formation. The result of this study shows that increasing the aqueous ammonia concentration from 1.6 M to 4.0 M at a fixed high voltage 3.5 kV which contributes to enhancing the electrical conductivity about 20 mS.

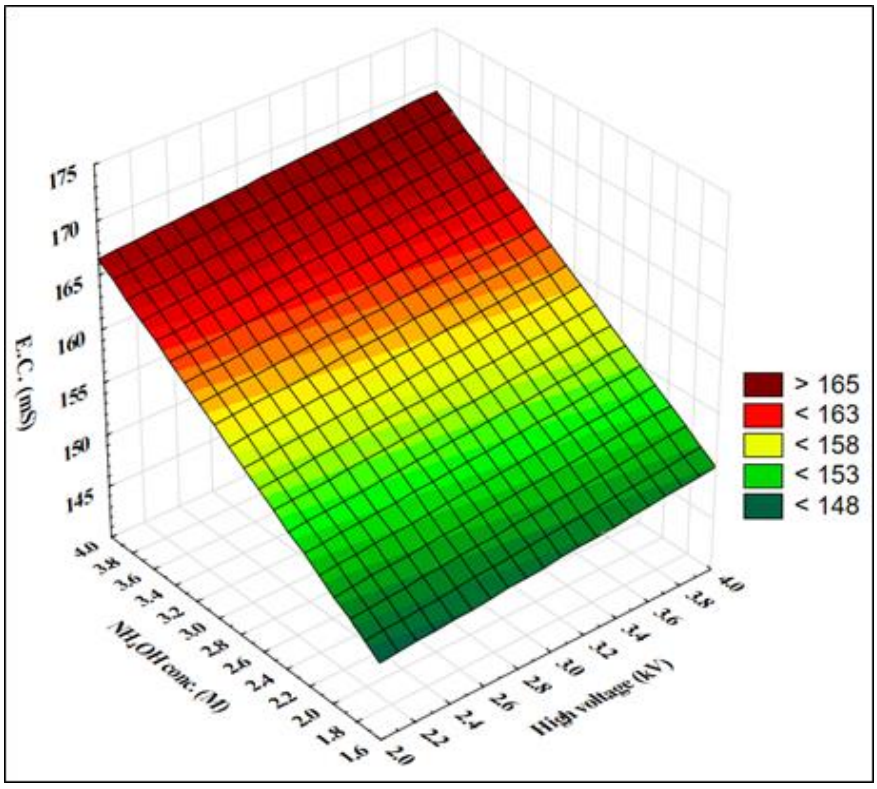

Figure 6- 8. The combined effects of the high voltage and aqueous ammonia concentration on the electrical conductivity of the solution.

The weak effect of high voltage change with concentration is seen, e.g. at a concentration of 3.4 M the electrical conductivity does not change more than 5 mS by increasing the high voltage from 2 to 4 kV. This confirms the weak interaction between the two variables as observed from the F-test (table 6.1).

6.5.2.3 The effects of the high voltage and reaction time

Figure 6.9 shows the combined effects of the high voltage and reaction time on the electrical conductivity in non-thermal plasma of CO_2 / aqueous NH_3 reaction process. At the shortest

reaction time 10 minutes, the electrical conductivity of the solution increases from less 150 to 155 mS when the high voltage rises from 2 to 4 kV. Whereas the electrical conductivity is enhanced by over 10% (from 150 to 165 mS) with the increase reaction time from 10 to 50 minutes at the highest voltage of 4 kV. In brief, the effect of high voltage on the electrical conductivity being more significant than the reaction time is observed in this study. These results indicate there is an insignificant interaction between the effect of voltage and the reaction time of CO_2 with aqueous ammonia.

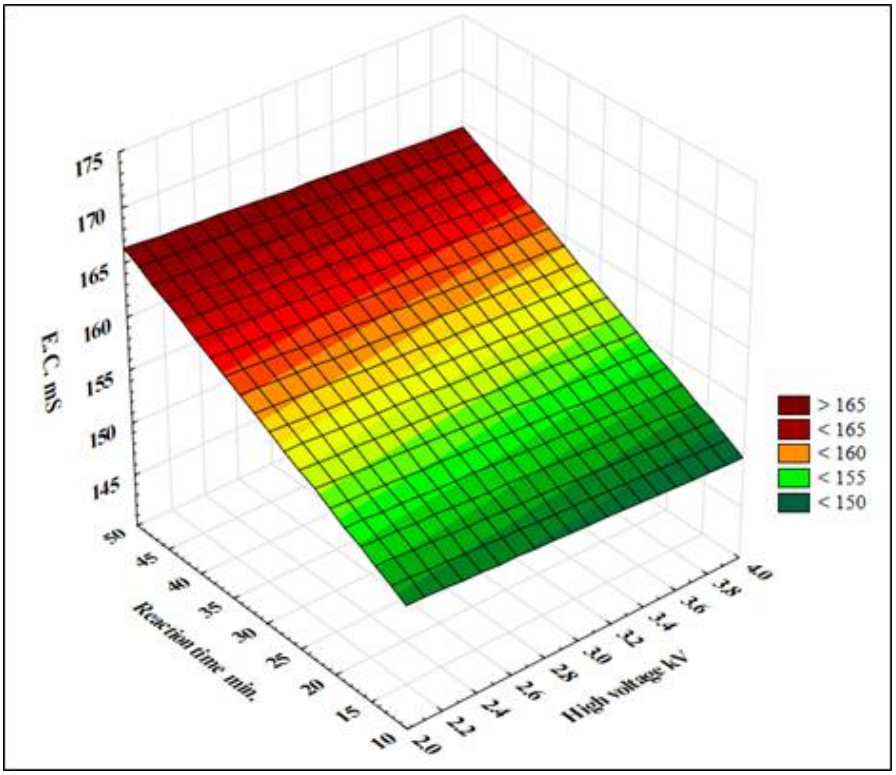

Figure 6- 9 .The combined effects of the high voltage and reaction time on the electrical conductivity of the solution

Analogous results are reported about the effect of voltage in the chemical kinetics of ozone generation (Rehman, et al., 2016) recently. The ozone production is enhanced by the increasing applied voltage in the range of 3.4-4.8 kV. However, this could also be interpreted on the basis of residence time for which the CO_2 bubble is exposed inside the reaction column and the velocity of a small bubble. Due to the small bubble size, the rise velocity at the bubble generating point on the diffuser surface with the liquid surface, actuates that the small bubble spends a longer residence time than the large bubble and provides large area to volume ratio which enhances dissolution (Kuvshinov *et al.*, 2014).

6.5.2.4 The effects of the CO_2 flow rate and aqueous ammonia concentration

The interaction of the CO_2 flow rate and aqueous ammonia concentration on the electrical conductivity of the final solution is shown in figure 6.10. At a constant CO_2 flow rate and with different concentrations of aqueous ammonia, increasing the concentration enhances the electrical conductivity of solution due to the increase of the reaction rate, which contributes to the enhancement of the producing more ions in the solution. These results agree with the results of Zhu *et al.*, (2011) in the investigation the effect of increasing ammonia concentration to capture carbon dioxide. A semi-batch experimental study in the process is used, an increase in reaction time contributed to the CO_2 loading increase.

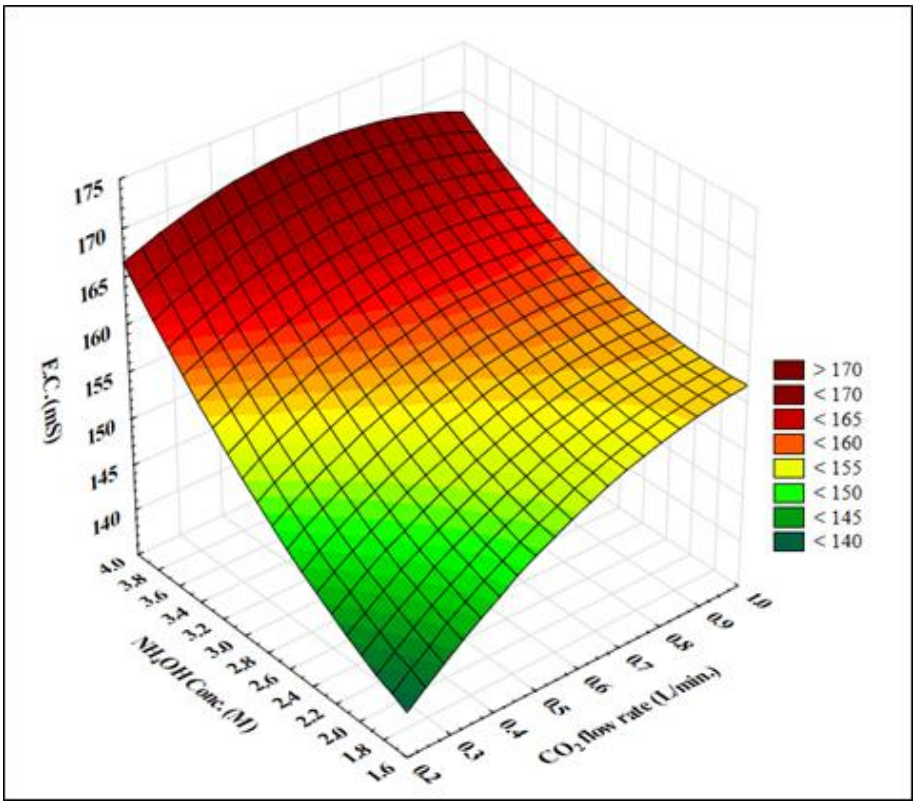

Figure 6- 10. The combined effects of the CO_2 flow rate and aqueous ammonia concentration on the electrical conductivity of the solution.

The electrical conductivity increases with the increase of the aqueous ammonia concentration from 1.6 to 4 M, regardless changes in the gas flow rate. While comparing to with effect of concentration with a CO_2 flow rate which bends down at the sides to give the upper part a rounded form such as saddle shape. This means the mid values of CO_2 flow rate are more significant in the chemical reaction process. The results in figure 6.10 give a curvature relation between the concentration of aqueous ammonia and CO_2 flow rate. In other words there a significant nonlinear coupling effect on the electrical conductivity by these two variables.

6.5.2.5 The effects of the CO_2 flow rate and reaction time

Figure 6.11 illustrates the combined effects of the CO_2 flow rate and reaction time on the electrical conductivity in CO_2 /aqueous NH_3 reaction process with the presence of non-thermal plasma. The results show that the relation between the flow rate of carbon dioxide gas and the reaction time is a significant interaction.

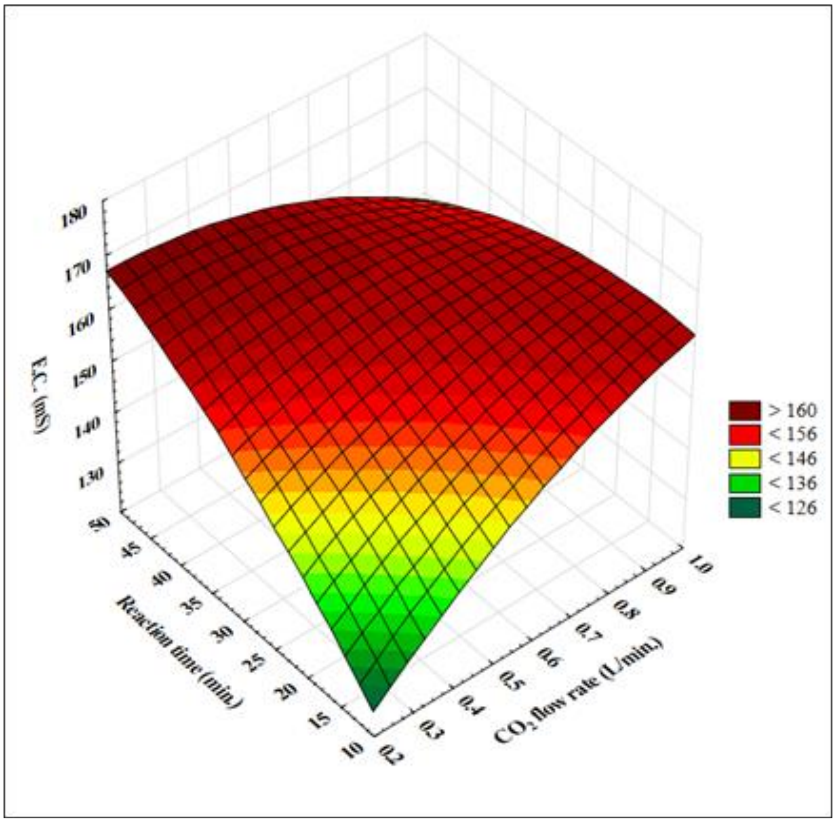

Figure 6- 11. The combined effects of the CO_2 flow rate and reaction time on the electrical conductivity of the solution.

The electrical conductivity was obtained less than 146 mS at a low CO_2 flow rate and short reaction time (0.2 to 0.6 L. min^{-1}) and 10-30 min residence time, respectively. However, the electrical conductivity of the solution gradually increases to a range of 156 to 160 mS before starting to drop again at the maximum values of both variables. The reason for electrical conductivity dropping at a high CO_2 flow rate and after a long period of reaction could be attributed to the forming a crystalline solid in the solution. The solid crystals that precipitate look like a white cloud which leads to reducing the concentration of ions in the solution (which means the ionic strength exceeded the solubility limit) eventually decreasing the values of the electrical conductivity.

6.5.2.6 The effects of aqueous ammonia concentration and reaction time

Figure 6.12 shows the combined effects of the aqueous ammonia concentration and reaction time on the electrical conductivity in non-thermal plasma of CO_2 / aqueous NH_3 reaction process. The maximum electrical conductivity of 185 mS is achieved at the highest reaction time of 50 min. and highest concentration (4M) of aqueous ammonia. As can be seen from the plot, the concentration of ammonia significantly correlates with the time of reaction. Increasing the concentrations of ammonia, in particular higher than 3.4 M, markedly enhances the electrical conductivity of the solution at a reaction time over 40 minutes.

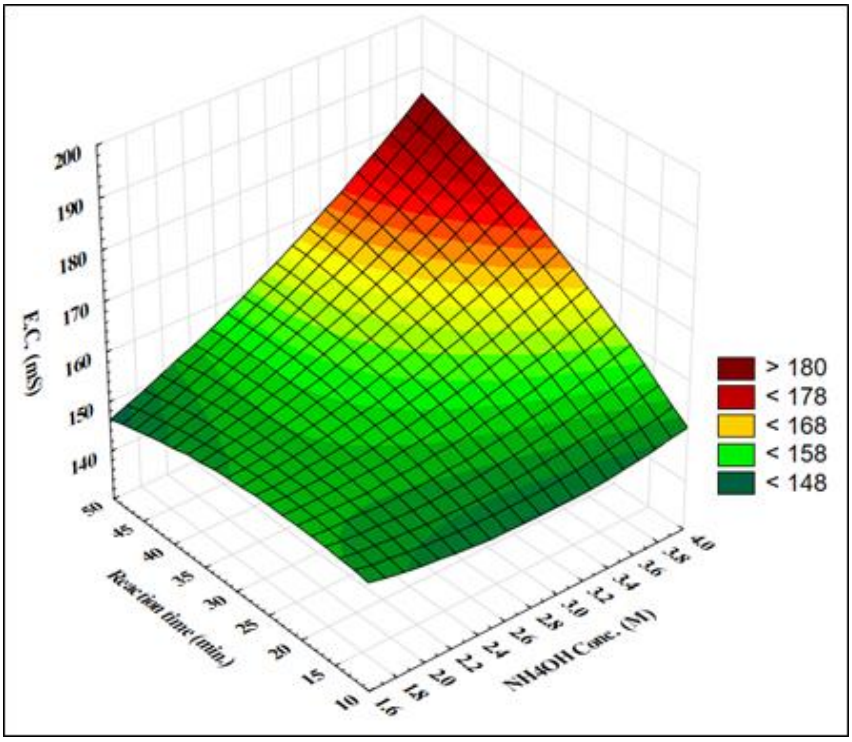

Figure 6- 12. The combined effects of the aqueous ammonia concentration and reaction time on the electrical conductivity of the solution.

In summary, the study shows that the electrical conductivity generally increases with increasing of the four studied control variables. That could be attributed to the activation process in particular, the reactive species formed by plasma are then introduced into the liquid. Therefore, the ionic concentration increases in solution, as reported in the literature (Wright *et al.*, 2018).

6.6 Effect of studied variables on the process yield of $CO_2/NH_{3\,(aq.)}$ reaction

The absorption of carbon dioxide by aqueous alkaline solutions is of major significance particularly in many applications. For instance, the key factor in the industry are purification of gases in the ammonia industry, manufacturing of $CaCO_3$, $MgCO_3$, NH_4HCO_3, $NaHCO_3$, etc. (Li *et al.*, 2003; Pohorecki and Moniuk, 1988; Meng, 2004). Also, it has importance research

through a potential contribution to reducing global warming and the passive effects on the ecosystem. The effect of high voltage, CO_2 flow rate, the concentration of aqueous ammonia, and time of reaction on the precipitated solid powder which considered as the process yield is studied and represented in Figures (6.13) to (6.22). The solution (150 ml) at end of each experiment is cooled to -10 °C to precipitate a solid as described previously in section (3.7.5) of the experimental procedure. The solid powder is separated and weighted so that is considered as actual weight to calculate the yield of the reaction process. Experiments number 3, 4, 22, and 24 did not yield any solid precipitate. The experiments number 3 and 4 were done at the same conditions of the CO_2 flow rate, the concentration of aqueous ammonia, and reaction time (0.4 LPM, 3.4 M, 20 minutes). However, the difference was in high voltage of 3.5 and 2.5 kV respectively. The reason could be attributed to the low flow rate of CO_2 combined with a short time of reaction in the same experiment. So, the solution was unsaturated with the reaction products to permit the crystallization process occurs. Whilst experiment 22 was at the lowest value of the CO_2 flow rate (0.2 LPM), thus the reaction products did not reach a saturation state. Also, the same result occurred in experiment number 24 but, the reason was the short exposure time (10 min). The second reason probably, except the low quantity of CO_2 that is provided, the reaction product might not be ammonium bicarbonate. As reported in the literature (Mani et al., 2006), the amounts of CO_2 and NH_3 are equivalent or even an excess CO_2, then the dominant product will be ammonium bicarbonate in the solution (see equations 6.13-6.15). While if an excess of NH_3 is used, in comparison to the quantity of the CO_2 absorbed, the ammonium carbamate amount will be increased and with less extent of carbonate as shown in equations 6.16 and 6.17 (see the section 6.7.2 for more details). The ammonium carbamate product possesses a solubility about three times (790 $g.L^{-1}$) as much as the ammonium carbonate/bicarbonate (320/ 220 g L^{-1}) in water respectively, so there are no crystals are seen after the cooling process.

$$NH_3 + CO_2 + H_2O = NH_4^+ + HCO_3^- \qquad (6.13)$$

$$NH_3 + HCO_3^- = NH_2CO_2^- + H_2O \qquad (6.14)$$

$$NH_3 + HCO_3^- = CO_3^{-2} + NH_4^+ \qquad (6.15)$$

$$2\,NH_3 + CO_2 = NH_2CO_2^{-2} + NH_4^+ \qquad (6.16)$$

$$2NH_3 + CO_2 + H_2O = CO_3^{-2} + 2NH_4^+ \qquad (6.17)$$

6.6.1 Effect of individual parameters on the yield of the process

As discussed in section (6.3)**,** equation (6.8) is considered the optimum mathematical formula which correlate the response function to the four variables studied in terms of the coded values. The separated solid mass of ammonium bicarbonate produced per gram of the aqueous ammonia solution (the limiting reactant) will be consider as the response variable for the non-thermal CO_2 plasma introduced as small-bubbles to the reactor.

In general, the extent of reaction can be determined through the yield, which is represented by the ratio of a specified product and reactant (mole of the limiting reactant converted to product divided by the initial amount of moles for that reactant) according to the definition of Missen et al. (1999) as shown in following:

$$Yield\ = moles\ of\ NH_4OH\ reacteed\ to\ form\ NH_4HCO_3 / moles\ of NH_4OH\ initially$$

Equation (6.8) used to predict the precipitated mass of the produced ammonium bicarbonate. The data are utilized for displaying the single and combined effect of parameters studied versus the process yield.

6.6.1.1 Effect of High voltage on the yield of the process

The relationship between the yield of the process (moles of the ammonium bicarbonate / moles of aqueous ammonia) and the high voltage, with all other variables held at constant is given in the caption. CO_2 flow rate, aqueous ammonia concentration, and reaction time are shown in Figure 6.13. As predicted in the simulation of chapter four, the role of non-thermal plasma to activate the inert molecules of CO_2 gas. The species produced from plasma generation could be free radicals, excited atoms, ions, and molecules. These reactive species have a high ability to participate in reactions compared to the conventional chemical reactions. The excited species of CO_2 gas such as CO_2*, CO*, and possibly other relatively long-lived species would react and dissolve in the liquid phase. The dissolved species could react in the solution of ammonia to form some ammonium compounds such as carbamate, carbonate and bicarbonate.

The hypothesis in this study is that the dissolved and excited CO_2 species will interact with ammonium ions to form ionic salts like the ammonium carbonate/bicarbonate compounds. Then one could expect competition between the dissolving process and reaction with CO_2 will occur. It is somewhat surprising that the yield of the reaction process intensively declines in the range of voltage 2 to 3 kV, so the minimum yield (56 %.) at these conditions is achieved. The most interesting aspect of this graph is that the trend completely changes above 3kV so that the yield of the process passes over the (70 %) near the highest value of voltage (4kV).

Mie and Tu, (2017) elucidated the effect of changing applied voltage at a constant frequency on the CO_2 conversion. Increasing the plasma power from 10 to 50 W, enhances the rise of both the number and magnitude pulses of the current, resulting in the conversion increasing from 17.4% to 22.4%. One of the exceptional features of non-thermal plasma is associated with the electron and gas temperatures. The electron temperature (T_e >> 1 eV, 1eV=11605 °K) (Bellan, 2006) is tenfold the gas temperature (T_g), so the process is called the energetic electron. Molecule excitation, ionization, and dissociation are induced by highly energetic electrons. Furthermore, the low energy electrons form negative ions by their attachment at the area of discharge (Urashima and Chang, 2000; Harling *et al.*, 2008; Tu and Whitehead, 2012; Mei and Tu, 2017). The interpretation of the reduction in the yield of the process could be attributed to the ionization degree of the carbon dioxide dissociation process. According to literature, CO_2 is converted to CO and O_2 with high percentage at sufficient specific energy (Fridmam, 2008). The same has been reported in Liu et al., (2017) in their study of carbon monoxide generation using low power CO_2 DBD plasma. The CO concentration went down at a specific condition of frequencies and then increased again. The dissociation process of CO_2 to the undesired products could be the main reason for the yield reduction.

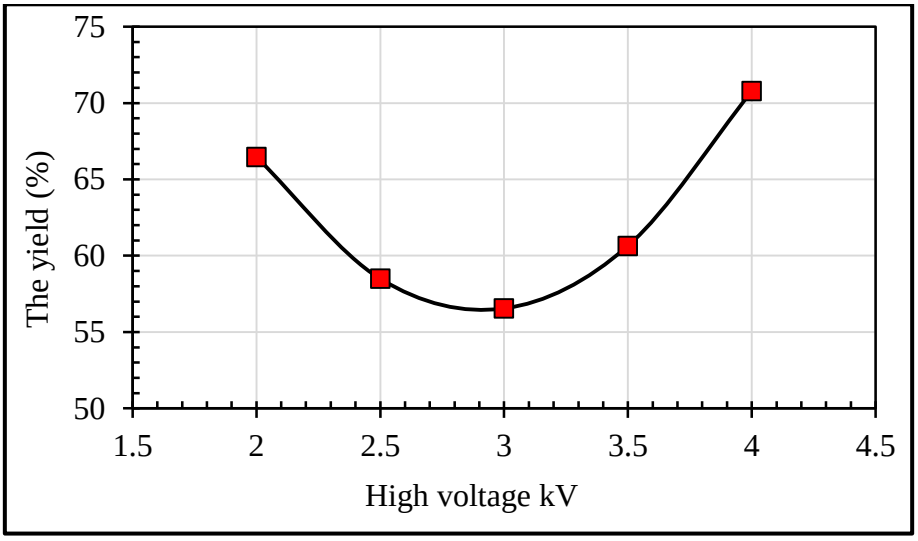

Figure 6- 13. The influence of high voltage on the yield of the process (gram of the ammonium bicarbonate / gram of aqueous ammonia) at a aqueous ammonia concentration (3.4 M), CO_2 flow rate (0.8 l/min) and time of reaction (40 min)

6.6.1.2 Effect of CO_2 flow rate on the yield of the process

Figure 6.14 presents the relationship between the yield of the process (moles of the ammonium bicarbonate / moles of aqueous ammonia) versus the CO_2 flow rate, all other variables are hold at constant as given in the caption (high voltage, aqueous ammonia concentration, and reaction time). The results obtained from the initial analysis of the CO_2 flow rate and its influence on

the yield of the process are as expected. Increasing the flow rate of gas will generally lead to enhance the products of the reaction. Therefore the highest yield (68 %) occurs at the highest flow rate of 1 LPM. So the results support the hypothesis of the study, the role of small bubbles and non-thermal plasma are essential to increase the productivity of the process.

From a simple comparison between Figures 6.4 and 6.14, completely different behaviour of the two curves is observed. However both represent the CO_2 flow rate effect on the responses, i.e. the electrical conductivity of the solution and the yield of the process. But the common linkage likely is when the conductivity is reduced, i.e. the ions (current carriers) are converted to molecules (have no charges). And that obviously appears in figure 6.14 as an increase of the reaction yield (ammonium bicarbonate).

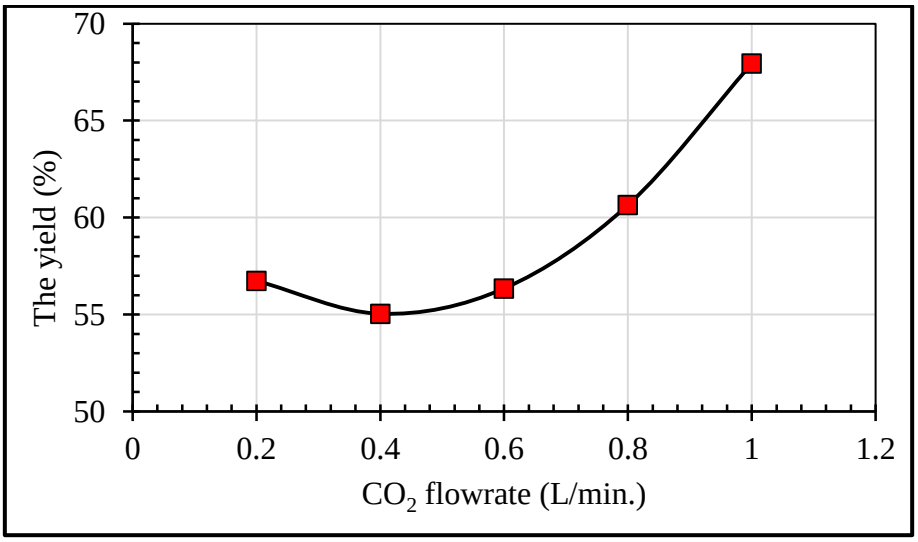

Figure 6- 14. The influence of CO_2 flow rate on the yield of the process (gram of the ammonium bicarbonate / gram of aqueous ammonia) at high voltage (3.5kV), NH_4OH concentration (3.4M), and time of reaction (40 min.).

6.6.1.3 Effect of the aqueous ammonia concentration on the yield of the process

Figure 6.15 demonstrates the relationship between the yield of the process and the aqueous ammonia concentration, with variables held at high voltage (3.5 kV), CO_2 flow rate (0.8 LPM) and time of reaction (40 min.). The reaction mechanism of CO_2 molecules and ammonium ions can create a transition state that rearranges itself as NH_3-COO^- with H^+ solvated. The transition state might rearrange itself again with another ammonium ion to form NH_2-COO-NH_4 which is the ammonium carbamate molecule. Ammonium carbamate has a covalent bond between C-NH_2, so it is a sensitive and unstable compound especially in the presence of moisture. The aqueous ammonia procedure for generating ammonium carbamate produces a hydrated carbamate. The main disadvantage with hydrated carbamates is the difficulty of drying completely due to its volatility exceeding the water (Dressel at al., 1986). The result of the

analysis using ^{13}C NMR shows that the composite of precipitated solid senses only ammonium bicarbonate as shown in appendix F. Most carbamate and carbonate are converted to bicarbonate in case of the diluted concentrations of ammonia solution with an excess of carbon dioxide gas (Li *et al.*, 2003) according to the following equilibrium reactions:

$$(NH_4)_2CO_3 + CO_2 + H_2O = 2NH_4HCO_3 \quad (6.18)$$

$$NH_2COONH_4 + CO_2 + 2H_2O = 2\,NH_4HCO_3 \quad (6.19)$$

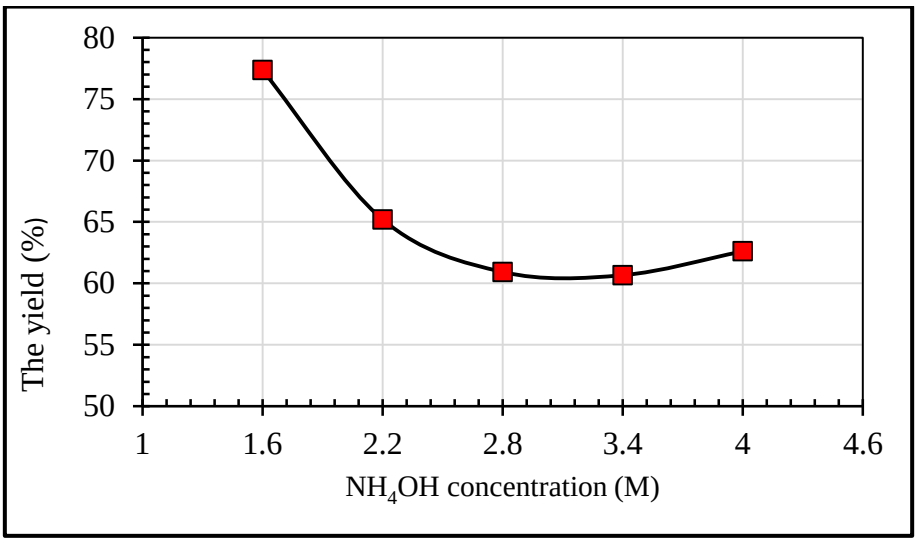

Figure 6- 15. The influence of NH_4OH concentration on the yield of the process at high voltage (3.5 kV), CO_2 flow rate (0.8 LPM) and time of reaction (40 min.)

The maximum yield of the process is close to 77 % at the concentration at 1.6 M as shown in Figure 6.15. The yield of the process is linearly decreased from the concentration of 1.6 to 2.8 M, then, it slightly increases at the high concentrations of 3.4 to 4 M. The process yield decreased interpretation may be due to the formation of the dissolved carbamate and carbonate ions in the solution. The potential for carbon dioxide reaction to produce ammonium carbamate at high concentrations of ammonia solution is one of the study findings highlighted by Mani, et al. (2005). They concluded that the main species in solution is carbamate ions in the presence of excess ammonia. While the formation of bicarbonate ions prevail when diluted ammonia concentration is used, also the carbonate anion is present in solution with lower concentrations than carbamate. In this stage of the study, the solution content is not tested or analysed, which may occur in separated future work.

6.6.1.4 Effect of the reaction time on the yield of the process

In general, for the chemical reaction system, two crucial matters should be discussed. The first is the nature of thermodynamic changes which must be assessed as the reactants combine to

produce new substances. The second issue is related to duration of those changes or in other words, the rate of change during process operation. The relationship between the process yield and the reaction time, is shown in Figure 6.16, with all other variables held constant (high voltage, CO_2 flow rate, and aqueous ammonia concentration). The results demonstrate that the yield of the reaction process is linearly increasing with time as we expected in section 6.2 for the positive hypothesis. For the longer processing time (50 minutes), according to the mathematical model, the yield of the process increases to the maximum value of approximately 72%. While the minimum process yield at minimum reaction time 10 minutes was about 27%.

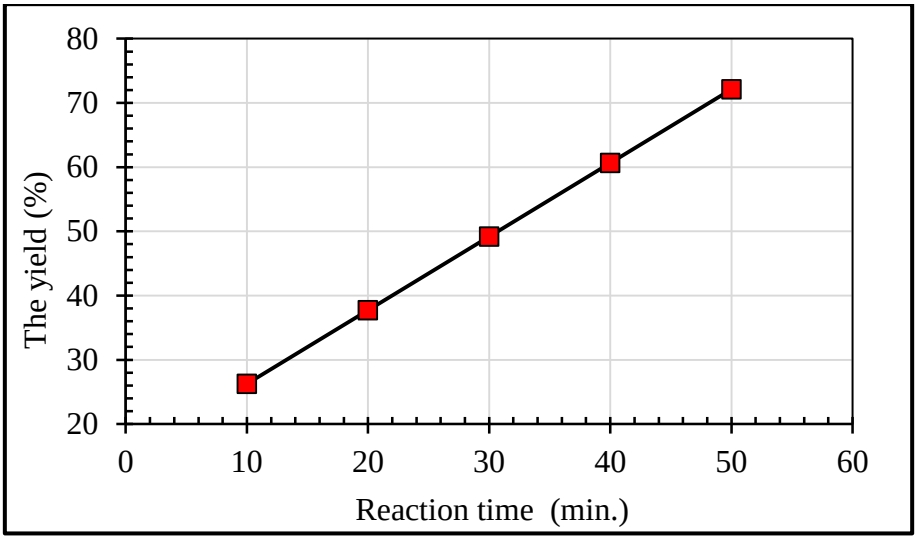

Figure 6- 16 . The influence of reaction time on the yield of the process at constant high voltage (3.5 kV), CO_2 flow rate (0.8 LPM), and NH_4OH concentration (3.4 M)

The CO_2/aqueous NH_3 reaction may occur during the following steps after the absorption of carbon dioxide gas into aqueous ammonia as previously mentioned in the equations (6.9 and 6.10) section (6.4.1.2). Danckwerts, (1970) adds another possible pathway:

$$CO_{2\,(l)} + H_2O = HCO_3^- + H^+ \qquad 6.20$$

The reaction (6.20) is first order with rate constant of 0.02 sec^{-1}, while the reaction (6.10) is considered as a second-order due to the rate proportional to concentrations of both carbon dioxide gas and hydroxyl ions with rate constant of 6000 L $mol^{-1}.s^{-1}$. Also, Danckwerts considers the effect of pH on the reaction of the CO_2. So that if the pH value is greater than 10, then the reaction rate of the CO_2 with hydroxyl ions is more than 30 times as fast as the reaction (6.20).

6.6.2 The interaction influences of the variables on the process yield

The first-order interaction terms for each paired combination X_1X_2, X_1X_3, and X_1X_4 as shown in statistical analysis are not significant (see table 6.2). While the linear terms of the variables X_1, X_2, X_3, and X_4, as well as the squared terms of the variables X_1^2, X_2^2, X_3^2, and X_4^2, are significant and appear in the mathematical model equation (6.7). The effects of parameters interaction on the yield of the process are shown as in figures (6.17-6.22).

6.6.2.1 The combined influence of high voltage and CO_2 flow rate

Figure 6.17 depicts the variation of the yield of the process with high voltage at constant aqueous ammonia concentration of 3.4 M and reaction time of 40 minutes (in a typical experiment); while varying the CO_2 flow rate. The maximum yield is obtained as slightly more than 78% in 4 kV at CO_2 flow rate 1 LPM. However, the range of high voltage between 2.0 to 3.0 kV depresses yield, probably because of production of intermediate species. The yield decreases at low CO_2 flow rates. Data for the CO_2 flow rate of 0.2, 0.4, and 0.6 LPM were close to each other as illustrated in figure 6.17, because the reaction is not directed toward ammonium bicarbonate production.

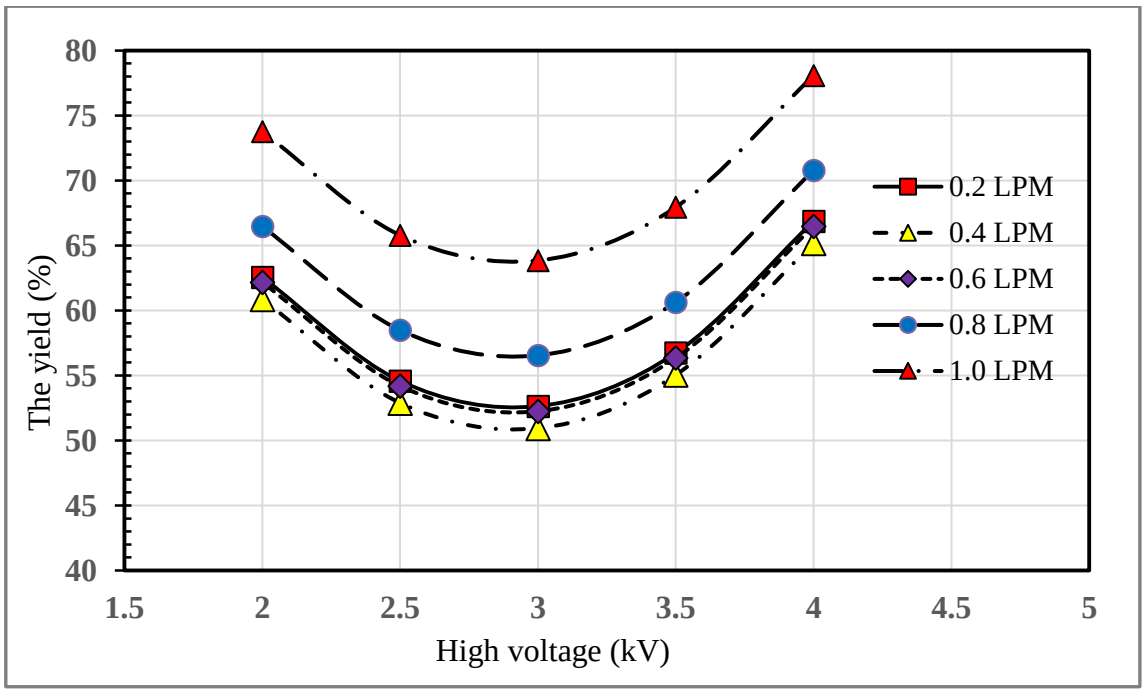

Figure 6- 17. The influence of high voltage and CO_2 flow rate on the yield of the process at constant NH_4OH concentration (3.4 M) and time of reaction (40 min.).

In other hand, electro-kinetic systems in presence of counter-ions released in solution opens the possibility of controlling the bubble charges at limited conditions through the applied electric field. Charging the fluids can generate flow on the diffuse layer because of the

superposition of the electroosmotic flow contribution and the electrophoretic mobility. Practically, the electrophoresis and electroosmosis usually appear synchronously, these phenomena may lead to suppress the intermediate reactions and eventually reduces process yield. The observed decrease also is probably due to the fast decomposition of produced compounds through attacked by some active plasma species such as free radicals, excited atoms and molecules, which may be generated or activated at such limits of the process conditions (Kim *et al.*, 2016).

6.6.2.2 The common influence of high voltage and aqueous ammonia concentration

Figure 6.18 describes the variation of the yield of the process with high voltage at a constant CO_2 flow rate (0.8 L/min.) and time of reaction (40 min.) while, the aqueous ammonia concentration varied between 1.6 and 4.0 M. The process yield (precipitate solid mass) with these conditions is higher than that of the previous in figure 6.17. The mathematical model shows a maximum yield (94 %) is achieved within the 1.6 M concentration of aqueous ammonia at 2.0 kV and 0.8 LPM CO_2 flow rate and 40 min of reaction time. In general, the low initial aqueous ammonia concentration enhances the production of ammonium bicarbonate as discussed in section 6.6.1.3. The effect of high voltage up to a certain points (2.5-3.5 kV) at which a drop in yield occurs, then return to increase in all runs of the concentration.

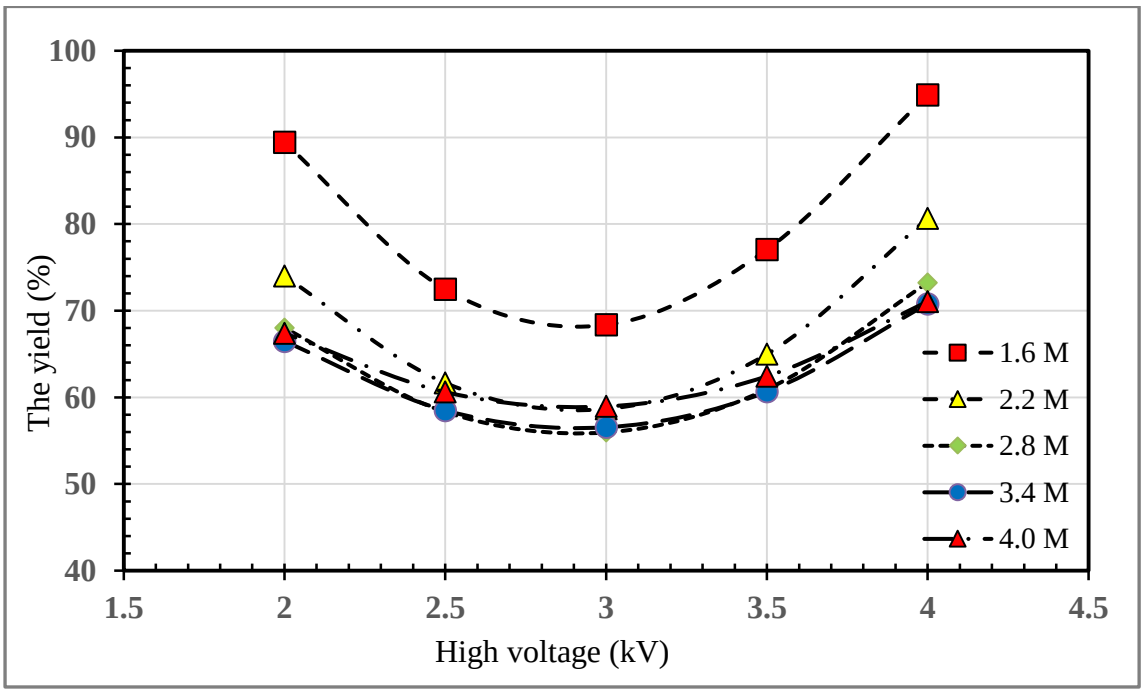

Figure 6- 18. The influence of High voltage and NH_4OH concentration on the yield of the process at constant CO_2 flow rate (0.8 L/min.) and time of reaction (40 min.).

Evaluation of the results by means of productivity efficiency, for the 4 kV at an aqueous ammonia concentration of 1.6 M to 4.0 M, the Figure 6.18 shows that the yield was increased from 71% to slightly less 95%, i.e. the yield increased 26%. It seems, low aqueous NH_3 concentration integrated with the generation rate of species produced via plasma mainly from the excitation of CO_2 molecules is responsible for enhancing the yield. That also probably is attributable to the consumption of the radicals by side reactions before they reduce the overall product, compared with results of figure 6.17. Another observation from the two figures (6.17 and 6.18) is the effect of NH_3 solution concentration grows the yield is more than the CO_2 flow rate.

6.6.2.3 The combined influence of high voltage and time of reaction

A maximum yield of the process (≈ 84%) is achieved at 4.0 kV and reaction time 50 minutes, at the interaction of a variant voltage and reaction time. While the CO_2 flow rate and concentration of aqueous ammonia were constant (0.8 LPM. and 3.4 M) respectively.

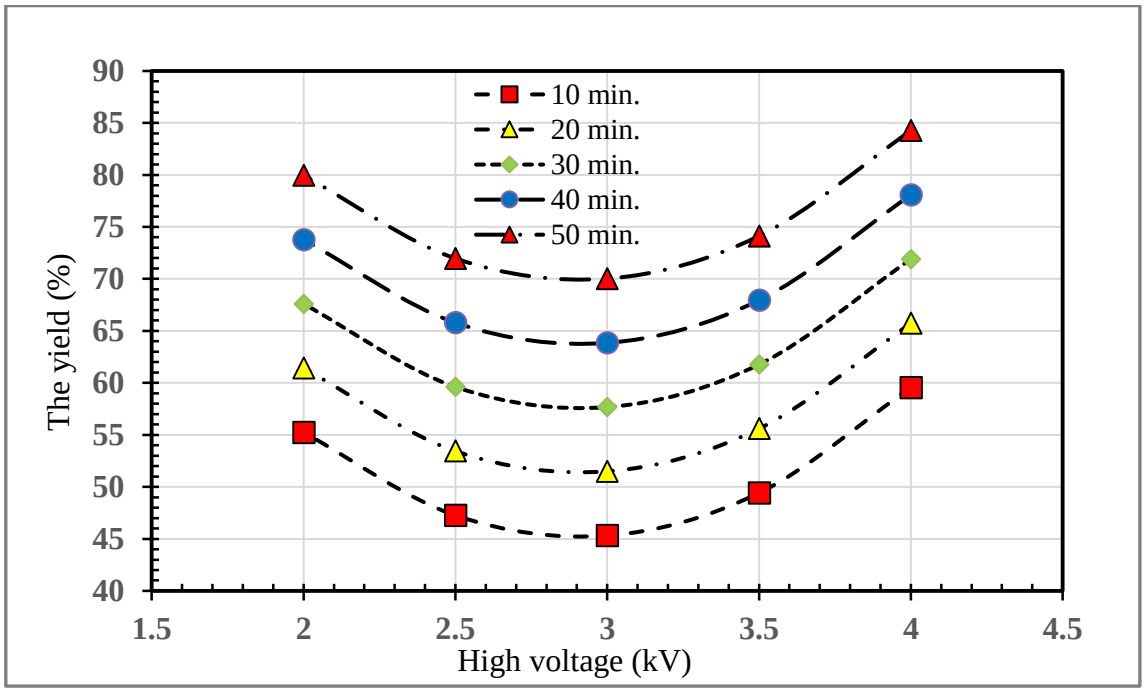

Figure 6- 19. The influence of high voltage and time of reaction on the yield of the process at constant CO_2 flow rate (0.8 L/min.) and NH_4OH concentration (3.4 M).

The strong effect of high voltage continues by reducing the precipitated solids range of 2.5 to 3.5 kV as presented in Figure 6.19. At the 3 kV, the minimum point occurs for all the experiments of the reaction time. The most probable reason for the non-monotonicity is due to CO_2 decomposing to some reactive species leading to side reactions occurring at this value of the voltage. However, after 3.0 kV the increase in the yield is achieved for all the reaction time

curves of 10 to 50 minutes. Another important finding was that the process yield is improved for example at 4 kV from 60 to 84 %., as the reaction time varies within 10 to 50 minutes.

6.6.2.4 The combined influence of CO_2 flow rate and NH_4OH concentration

Figure 6.20 shows the combined influence of CO_2 flow rate and aqueous ammonia concentration on the yield of the process at 3.5 kV (high voltage) and 40 minutes (time of reaction) as calculated using regression. As shown in results, the yield of the process increased from (68 %.) to (92 %.) as the CO_2 flow rate increased from (0.2 to 1 LPM) at concentration 1.6 M of ammonia solution. The total increase of the process yield at 1.6 M of aqueous NH_3 concentration is 24% at changing the flow of gas from minimum value (0.2 LPM) to high value (1 LPM).

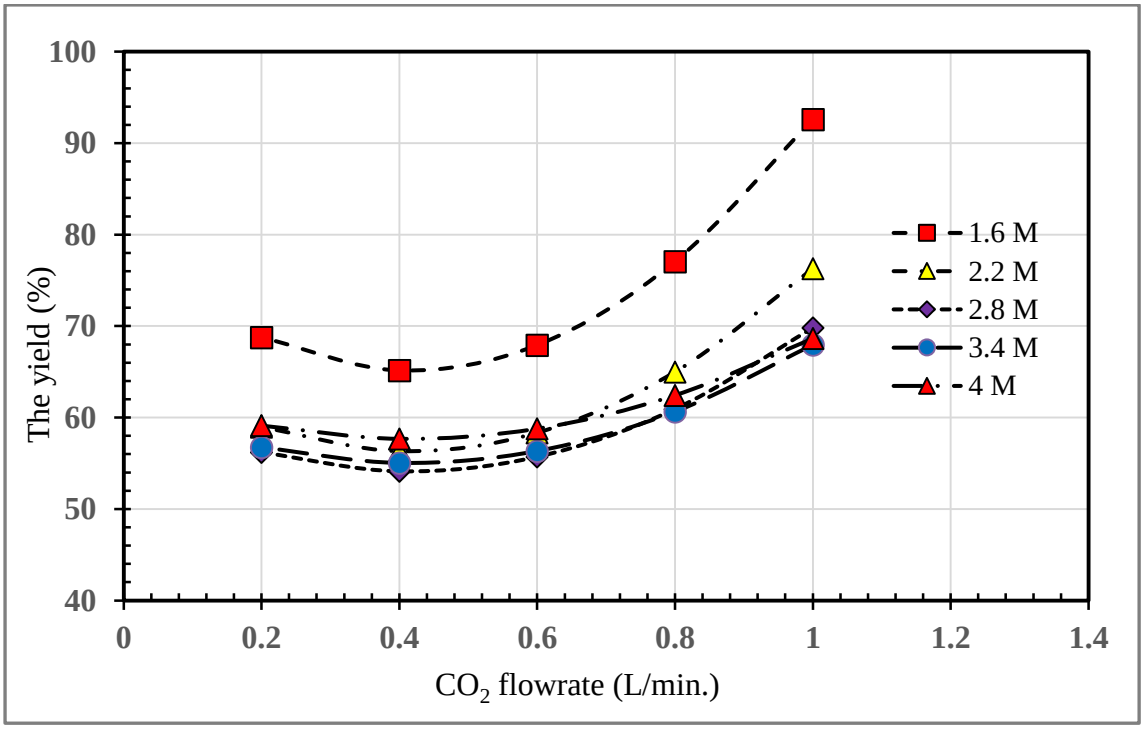

Figure 6- 20. The influence of CO_2 flow rate and NH_4OH concentration on the yield of the process at constant high voltage (3.5 kV) and time of reaction (40 min.).

Figure 6.20 illustrates the same increase could nearly be obtained at a constant (1 LPM) CO_2 flow rate when changing the concentration of aqueous ammonia from 1.6 to 4.0 M. However, concentrations curves (2.8, 3.4, and 4 M) do not show a significant change in the yield of the process and their values are very adjacent to each other. The maximum yield is obtained at 1.0 LPM of the CO_2 flow rate and of 1.6 M aqueous ammonia concentration according to mathematical regression model calculations. In general one can conclude the yield of the

ammonium bicarbonate production could be enhanced through increasing CO_2 flow rate in a dilute concentrations of ammonia solution.

6.6.2.5 The combined influence of CO_2 flow rate and reaction time

The influence of the CO_2 flow rate and reaction time on the yield of the process is shown in figure 6.21 at fixed high voltage (3.5 kV) and aqueous NH_3 concentration (3.4 M). Generally, increasing the period of reaction from 10 to 50 min enhances the yield of ammonium bicarbonate production at any constant CO_2 flow rate. But the status will be different for constant reaction time with changed flow rate of carbon dioxide. This could be attributed to the increase in the conversion rate of reactants into products, which contributes to the enhancement of product ratio in the solution. The most relevant finding is that no solid precipitate is separated from the solution at a CO_2 flow rate of 0.2 and 0.4 LPM at reaction time of 10 min., also in the 0.2 LPM of the CO_2 flow rate at 20 minutes of the reaction time.

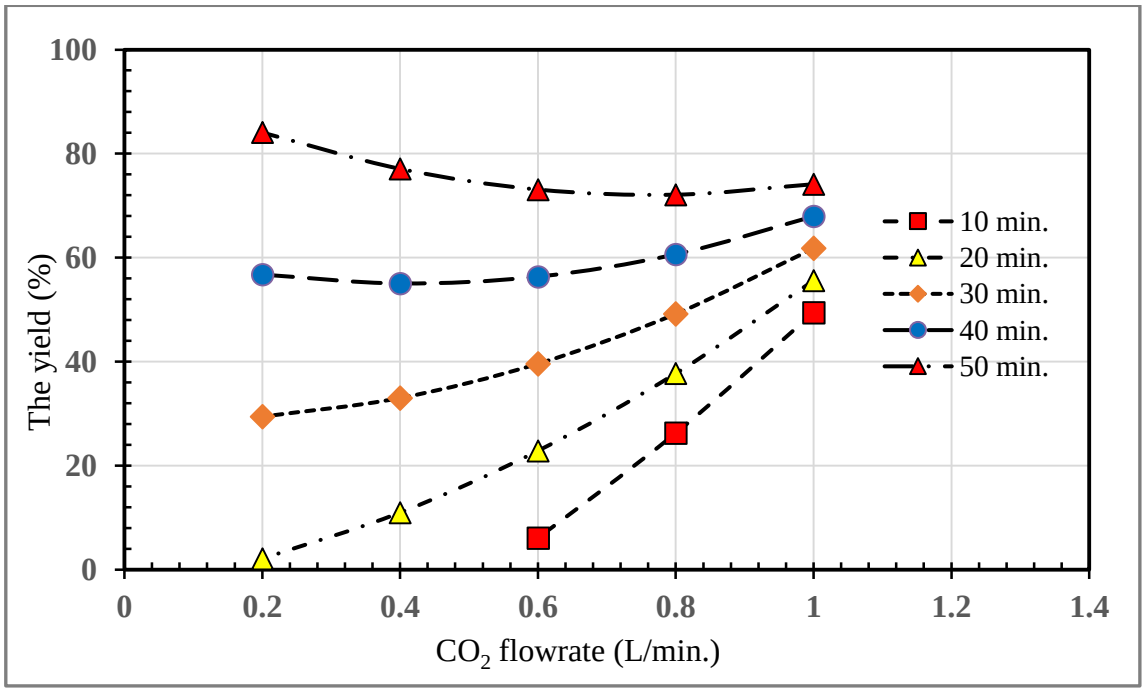

Figure 6- 21. The influence of CO_2 flow rate and time of reaction on the yield of the process at constant High voltage (3.5 kV) and NH_4OH concentration (3.4 M).

These results are consistent with the experimental findings as explained in section (6.5) and the ammonium bicarbonate formation may not have equilibrated to saturation. The maximum yield (84%) at 0.2 LPM of the CO_2 flow rate and of 50 minutes reaction time is obtained. However, the yield linearly increases with increasing flow rates of CO_2 and reaction time for the 10 to 30 minutes curves. Then the relationship changes at 40 and 50 minutes curves to be flat and descending respectively. This could be attributed to the low flow rate giving smaller

bubbles inducing a high surface area of absorption for CO_2. This factor enhances the reaction and higher yield will be obtained, and conversely for the higher flow rates.

6.6.2.6 The combined influence of NH_4OH concentration and time of reaction

The combined influence of the aqueous ammonia concentration and reaction time on the yield of the process through fixing both of high voltage (3.5kV) and the CO_2 flow rate (0.8 L/min.) is shown in figure 6.22.

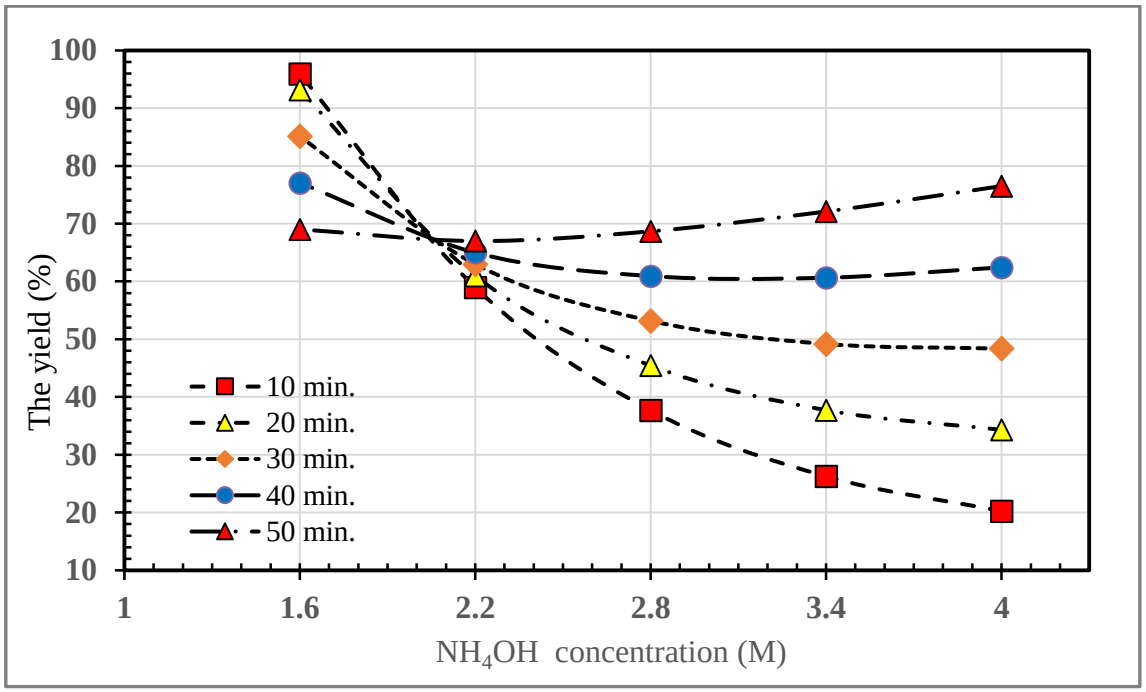

Figure 6- 22. The influence of NH_4OH concentration and time of reaction on the yield of process at constant high voltage (3.5kV) and CO_2 flow rate (0.8 L/min.).

From Figure (6.22) one can characterize two different behaviours for the yield of the process associated with the concentration and the time of the reaction. An overturning point in the process yield behaviour can be observed before and after the concentration of about 2 M. The yield increases with the declining concentration of aqueous ammonia and reaction time before the overturn point, thus the maximum yield achieved (> 93%) at 1.6 M and 10 minutes curve. Whereas after this level of concentration, the converse occurs. The process yield declines with increasing concentration for 10 to 30 minutes curves. Then the relation tends to change at 40 and 50 minutes curves to be flattened or slightly growing respectively. The reason for this behaviour may be attributed to the combined effect of the short time of reaction and the high concentration of aqueous ammonia solution. Therefore, increasing these two parameters leads to reducing the concentration of ammonium bicarbonate in solution and subsequently reducing the yield. In general, high concentration of NH_3 drives the reaction to ammonium carbamate

formation, while the short period limits the ammonium bicarbonate concentration from reaching the saturation state in solution.

6.6.3 CO_2 captured ratio:

According to the following reaction the amount of reactant carbon dioxide and the portion which is vented could be approximately estimated:

$$NH_{3\,(aq.)} + H_2O + CO_{2\,(g)} \Leftrightarrow NH_4HCO_3 \text{ ---------- (3-8)}$$

The carbon dioxide consumed quantity to produce 24 g (the best result achieved in Chapter 6) of the bicarbonate is:

$$x_{CO2} = \frac{44 * 24}{79.055} = 13.3\ g$$

The above value represent the absorbed quantity of carbon dioxide from the small bubbles.

The reaction conditions of experiment includes:

Carbon dioxide flow rate of 0.8 (l/min) at reaction time of 40 min, hence, the total CO_2 inlet to the reactor was:

Total volume = 0.8 L/min * 40 min= 32 litre

The density of CO_2 at 20 °C and 1 bar is 1.839 g/ L.

So the total mass of CO_2 input is:

The CO_2 mass = 1.839 g /L *32 L = 58.85 g

The ratio of captured CO_2 by the reaction could be estimated = mass of consumed CO_2 in reaction / total mass of gas input.

= 13.3/ 58.8 *100 = 23%

6.7 The behavior of temperature and pH value during the reaction process

6.7.1 The temperature of reaction behavior

Figures in appendices E1-E4 demonstrate the curves of pH values and temperature variations in the reactor with respect to time of the reaction (CO_2- aqueous NH_3) for the 28 experiments. As seen in figures, the CO_2/NH_3 reactions are exothermic (Yeh and Bai, 1999). The ammonium bicarbonate compound possesses a heat of formation from gaseous ammonia and CO_2, in liquid water (-126.5) kJ/mol (Grayson, 2001). While Qin *et al.* (2011) address the heat of absorption of CO_2 with 2.5 wt. % aqueous ammonia solution and determine the heat by about 70 kJ/mol at 35 to 40 °C.

In this study, the reaction is conducted without cooling control, where the temperature behaves freely depending on reaction conditions. In general, the temperature is sharply increased at the starting point of the reaction until it reaches the maximum of 60's °C during the 10 to 15 minutes. The solution temperature then decreases from the maximum degree to less than 50 °C with some exceptions of experiments. The duration of experiments from 1 to 8 is 20 minutes. The experiments group of 1, 2, 5, and 6 are shown the same thermal behavior, where the temperature increases from 25 °C to reach the maximum (60 °C) then decrease to less than 50 °C. While the experiments 3, 4, 7, and 8 show a linearly behavior so that an increase from the initial temperature to the end of the experiment is occurred.

The interesting theme noticed in the experimental group 3 and 4, there is no precipitate, while the group of 7 and 8 yield precipitate even though the concentration of aqueous ammonia is higher in the first group. But it seems the CO_2 is another influential factor, since it converts all ammonium ions to bicarbonate in the case of low concentration relative to the higher concentration (still unsaturated). Also, from the results as shown in experiments 3 and 4, the temperature curves do not tend to be flattened at the end of reaction time. However, the opposite occurs in the experiments 7 and 8, where the curves have a tendency to flatten, and the solid substance precipitates from the solutions (see appendix E1).

In appendix E2, the reaction time for the experiments 9 to 16 is 40 minutes. The most interesting aspect of this group of graphs is related to experiments 9 and 10. They have the same conditions except the high voltage are 3.5 and 2.5 kV respectively. The results show experiment 9 yielded higher productivity than, not only experiment 10 but, all other experiments. This is a piece of excellent evidence on the influence of the non-thermal plasma to promote the CO_2 reaction with aqueous ammonia. The second observation could be summarized from the figures, is the extent of effect changing the gas flow rate and the ammonia concentration on the reaction time to arrive at the maximum temperature. For instance, at a constant ammonia concentration of 3.4 M, using a CO_2 flow rate of 0.8 instead of 0.4 LPM. The results show that the reaction time required to reach the highest temperature is decreased by 50%.

The reaction temperature of the high and low values for the studied variables are clarified in Appendix E3. High values for the high voltage, CO_2 flow rate, the concentration of ammonia solution, and reaction time are represented in the experiments 17 to 20. While the low values are illustrated in experiments 21to 24. The maximum temperature ($T_{max.}$) which is recorded

according to the reaction time for the high values of the studied variables as follows; with the high voltage (4kV) = 15 minutes, the $T_{max.}$ = 62 °C, the gas flow rate (1.0 LPM) = 10 minutes, the $T_{max.}$ = 63 °C, ammonia concentration (4 M) = 20 minutes the $T_{max.}$ = 66 °C, and with reaction time (50 min) = 17.5 min. the $T_{max.}$ = 60 °C. On the other hand, the maximum temperature ($T_{max.}$) which is recorded according to the reaction time for the low values of the studied variables as follows; with the high voltage (2 kV) = 15 minutes, the $T_{max.}$ = 60 °C, the gas flow rate (0.2 LPM) = 30 minutes, the $T_{max.}$ = 52 °C, ammonia concentration (1.6 M) = 11 minutes the $T_{max.}$ = 51 °C, and with reaction time (10 min) = 10 minutes the $T_{max.}$ = 52 °C. Finally, the maximum temperature ($T_{max.)}$ which is recorded according to the reaction time for the central values of the studied variables the high voltage (3 kV), the gas flow rate (0.6 LPM), ammonia concentration (2.8 M), and with reaction time (30 min) the maximum temperature of 52 °C, at reaction time of 16 minutes. Curves of temperature and pH versus time of the experiments (25 to 28) are shown in appendix E4. All these four experiments performed at the same conditions to demonstrate the experimental error value. The temperature curves approximately have the same behaviour, i.e. reach 60 °C at first 15 min then dropped to less than 50 °C. The amount of evaporating ammonia as a result of temperature increases, is a worthwhile factor but it is out of our scope in this study. Notwithstanding, to overcome this problem, the elevated vapour is collected by fixing a condenser over the reactor as shown in Figure (3.17). However Mani, et al., (2006) reports that the loss of ammonia from the 2.5 M ammonia solution never exceeded 1.3% at lab conditions.

6.7.2 The pH value of the reaction behaviour

The pH values in most experiments take the same behaviour. Generally, the starting concentrations hold a pH range of 11.5 to 12.0, depending on the desired aqueous ammonia concentration. As can be seen from the figures in Appendices E1 to E4, the pH value is linear decreases from the initial values to 8.5 during the first one-third of reaction time. While in the remaining time of reaction continue a steady state with simple fluctuation of ± 0.25 unit far off from a pH value of 8.5. The standard pH values of the bicarbonate, carbonate, and carbamate solutions are 7.9-8.0, 9.1, and 9.2 respectively. Therefore, the pH value is another indicator of bicarbonate formation as the main product of the carbon dioxide -aqueous ammonia reaction in our study. Changes in pH values agree with those investigated by Mani et al. (2006). They reported the values steadily decrease from 10.5 to 8.5 for initial ammonia solution concentration of 2.5 M (4.3 % w/w). The reaction of the CO_2 (a weak acid, $K_a = 4.08*10^{-7}$ at 20 °C) with the ammonia solution (a weak base, $K_b = 1.71\times10^{-5}$ at 20 °C) undergoes a complex

thermodynamic behaviour, conjunct with many reaction equilibria. However, Mani et al. (2006) and Edwards, et al. (1978) studied the NH_3 - CO_2 – H_2O system and determine the equilibrium constants for the main reactions when CO_2 reacts with aqueous ammonia:

$NH_{3\,(aq.)} with\ CO_2 \leftrightarrow ammon.\ bicarbonate$ (6.21) K_{eq} (20 °C) = 1.02×10^3

$ammon.\ bicarbonate \leftrightarrow ammon.carbamate$ (6.22) K_{eq} (20 °C) = 3.61

$ammon.\ bicarbonate \leftrightarrow ammon.carbonate$ (6.23) K_{eq} (20 °C) = 10.4

The pH of the system could be controlled through the NH_3/NH_4^+ and CO_3^{-2}/HCO_3^- buffers

$$NH_3 + H_2O \leftrightarrow NH_4^+ + OH^- \quad (6.24)$$

$$CO_3^{-2} + H_2O \leftrightarrow HCO_3^- + OH^- \quad (6.25)$$

The equilibrium reaction (6.21) dominates i.e. HCO_3^- are the main ions in the solution, if the reaction occurs between analogous quantities or an excess of carbon dioxide reacts with ammonia. Whereas, the excess of ammonia, compared to the absorbed CO_2, enhances the ammonium carbamate formation as well as, but a less extent, of carbonate as shown in the reactions (6.22) and (6.23), respectively (Mani et al., 2006).

6.7.3 Thermal Calculations:

A primary thermal calculation for the heat which is released due to reactions is conducted. The main purpose of these calculations is to determine the quantity of heat that originating from the applied high voltage of the non-thermal plasma generation as result the joule heating. Qin et al. (2011) report the heat of absorption of CO_2 with 2.5 wt. % aqueous ammonia solution is found to be about 70 kJ/mol. They assert that is not as low a value as expected by the carbonate–bicarbonate reaction (26.88 kJ/mol) which mentioned by Diao et al. (2004). The approximate value of the heat due to the reaction CO_2/aqueous ammonia can be estimated, by assuming the thermal properties of the solution are close as the properties of water i.e. the heat capacity is 4.18 J/g. °C).

The volume of used solution is **150 ml** in the experiments (without or with plasma) conducted under the same conditions of experiment number 9 at 3.5 kV high voltage, 0.8 l/min CO_2 flowrate, 40 min. reaction time and 3.4 M of the aqueous ammonia concentration, which gives the highest yield of ammonium bicarbonate. The density of solution can be roughly estimated from the molarity (M) and percentage (%) relationship depend on the molecular weight (M wt.) of the dissolved substance. The equation outlining the interconversion of these parameters is:

$$M = \left(\frac{\%*d}{M\,wt.}\right) * 10 \qquad (6.26)$$

$$3.4 = \left(\frac{13.2 * d}{35.05}\right) * 10$$

Density or specific weight of the solution will be 0.9

$$heat = m \int_{T1}^{T2} cp\, dT \quad ---------- (6.27)$$

The temperature range is determined according figures in appendices E to be about 40 °C

= ((150) ml × 0.9 (g/ ml) × 4.18 J/ (g. °C) ×(40) °C =22600 J

=22.6 kJ

This liberated quantity of the reaction heat which gives 24 g of the ammonium bicarbonate (molecular weight 79.05 g/mol), that equal 0.3 mole of the NH_4HCO_3:
As Qin mentioned the heat of the reaction value is 70 kJ /mol. Since in our study the produced amount is 0.3 mol., the liberated heat should be 21 kJ.

The difference between the theoretical value of liberated heat during the reaction and the experimental value in this study is about 1.6 kJ that can represent a temperature range of 2-3 °C.
The temperature difference is relatively not very high because the gas in the cylinder is under high pressure then expanded (cooled) during the flow to plasma zone, i.e. therefore the gas temperature is nearly equal the room temperature at the entrance of the reaction zone.
Figure 6.23 illustrates the data of the reaction temperature against the reaction time, in presence of the plasma, and in the absence of it. The results show the curves are close to each other or have slightly higher temperature in presence of plasma at the first ten minutes of the reaction. This completely agrees with the above theoretical calculations.

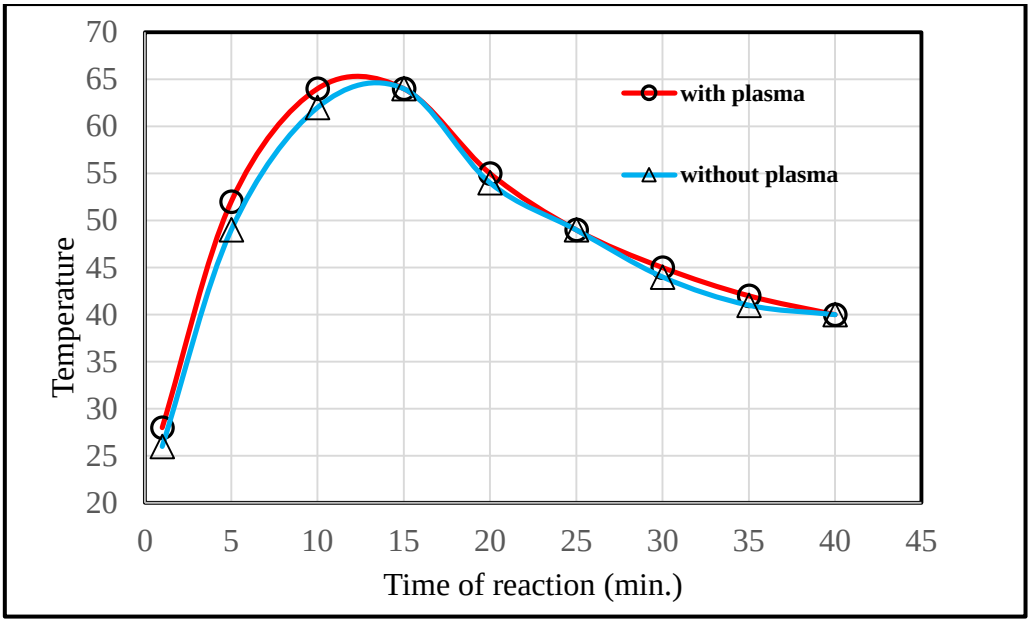

Figure 0-1 represents a comparison of the reaction temperatures of CO_2 with aqueous ammonia in the presence plasma (3.5 kV) and absence of it at (0.8 l/min CO_2 flowrate, 40 min. reaction time, and 3.4 M of the aqueous ammonia concentration)

6.8 Absorption calculation

The absorption rate of carbon dioxide can be determined by using the material balance under steady-state operation. Details of two streams with a counter-current contacting within the bubbling column are reported by Chen, (2012). By supposition, the plug flow for the gas phase through the column contains many tubes. The material balance for carbon dioxide in the ith tube at steady state is:

$$[(u_i C_{Ai})_z - (u_i C_{Ai})_{z+\Delta z}]\, S_i - r_{Ai}\, \pi d_i \Delta z = 0 \qquad (6.28)$$

Where S_i the cross-section of ith tube, u_i is the linear velocity, r_{Ai} the absorption rate per unit area of the *ith* tube, and d_i the diameter of *ith* tube.

The overall molar flow rate of the gas phase is F_{Ai}, which is equal to $u_i\, S_i\, C_{Ai.,}$ The equations can be rewritten as:

$$(F_{A1} - F_{A2}) - r_A A = 0 \qquad (6.29)$$

Where r_A is the mean absorption rate, and A is the total surface area of the gas phase in the column, which cannot be obtained directly. The absorption rate value can be determined by measuring the concentration of carbon dioxide and the gas-flow rate. Determination of absorption rate and mass-transfer coefficients are not addressed in this study and may be performed in a separate paper in the future. To determine the retention time of the gas inside the liquid phase, we selected the experiment no. 9 conditions to perform with some design calculations:

CO_2 flow rate is 0.8 L.min.$^{-1}$ = 13.3 cm^3.s^{-1}

The CO_2 velocity inside the column will be: volumetric mass flow rate / cross section area of the column: $A = \pi.d^2/4$ (where d is the inside diameter of column =4.5 cm)

Thus the cross section area = 15.9 cm^2

The linear velocity = 13.3 cm^3.s^{-1}/ 15.9 cm^2 = 0.83 cm.s^{-1}

150 cm^3, is the solution volume, gives liquid column height in the reactor of 9.43 cm. So, the holding time could be calculated from the liquid height divided by the linear gas velocity to be approximately 11 seconds.

As discussed in section 3.8.3 in Chapter 3, the carbon dioxide capture ratio can be estimated as following:

The flow rate of 0.8 (l/min) at reaction time of 40 min, used to calculate the total volume of CO_2 inlet to the reactor:

Total volume = 0.8 l/min × 40 min= 32 L. The density of carbon dioxide at 20 ℃ and 1 bar is 1.839 g/ L, so the total mass of CO_2 input is:

The CO_2 mass = 1.839 g /L ×32 L = 58.85 g

While the precipitated mass of solid ammonium bicarbonate is 24.3 g from chemical equation and as a stoichiometric amount of this quantity is required for the removals of the CO_2:

(24.3/79.05) × 44 = 13.3 g of CO_2

The ratio of captured CO_2 by the reaction could be estimated = mass of consumed CO_2 in reaction / total mass of gas input.

= 13.3/ 58 ×100 = 23%

The capture ratio of carbon dioxide in this study is slightly better than that mentioned (15-20 %) by Mani et al. (2006). However, the ratio of captured CO_2 may be greater than this because the filtrate solution certainly still has an important amounts from other carbon compounds. The compounds do not crystallize from the solution due to their high solubility.

6.9 The effect of absence of non-thermal plasma (the control experiment)

The effect of absence non-thermal plasma on the reaction is tested in a separate experiment. The conditions of the experiment are chosen to be same as the experimental conditions number (9), which yielded the highest process yield of 60% (24.3 g of the ammonium bicarbonate). Therefore no plasma applied, while concentration of the aqueous ammonia, the CO_2 flow rate, and time of the reaction are; 3.4 M, 0.8 LPM, and 40 minutes respectively.

The experiment yielded mass of precipitate only about 18 g of ammonium bicarbonate after cooling and separation processes (process yield ≈ 44%). Therefore, the presence of non-thermal plasma enhances the process yield by **36%**. Mani et al. (2005) simulated a flue gas of 10%

(v/v) CO_2 diluted with N_2. The mixture of gases CO_2/N_2 continuously flow through a glass diffuser at the bottom of 2.5 M NH_3 absorbing solution. They used a constant flow of the gas mixture at the rate of 15 l/hr. Their results show there is no more than 15–20% of CO_2 is absorbed by the ammonia solution. Also, they indicate that the carbamate ions in the NH_3/CO_2 system decrease at high CO_2 loading or at low pH of the solution. They mentioned there is no observed formation of any solid compounds during the CO_2 absorption tests. In other hand, Campbell (2016) studied the conversion of CO_2 in a saturated NH_3 aqueous solution. Campbell's study used a 25% saturated (13.2 M) solution of NH_3 to react with microbubbles of the order of 10 μm of CO_2, using fluidic oscillation flow of 0.2 L/min, He reported an increase in the conversion and precipitate mass yields of carbamate using a fluidic oscillator. In another hand, the study refer to the conversion of the process is diminished when a plasma reactor is used in reaction process. Campbell's study had demonstrably smaller bubbles than the present work due to fluidic oscillation, so is not a direct scientific control.

6.10 Analysis of the precipitated solid

6.10.1 Analysis using C^{13} nuclear magnetic resonance (NMR):

The composition of specific ammonium salts which are produced by a CO_2 reaction with varied aqueous ammonia concentrations is analysed by using a C^{13} nuclear magnetic resonance (NMR) by Mani et al. (2006). The study identifies the capability for interconversion between the various ammonium anions and consequences of the pH value of the solution during the conversion process. NMR analysis provides an accurate estimation for the reaction products of CO_2/aqueous ammonia. The signal in the range from 161.50 to 165.23, ppm refers to the carbon atoms of the bicarbonate and carbonate ions which are fast exchanging on the NMR time scale by proton scrambling.

In this study, several samples are analysed using C^{13} NMR. The analysis shows that the sample compositions comprise solely ammonium bicarbonate and no other compounds according to signal peaks. For each of the samples, a saturated solution was made by adding ~1mL D_2O to the 250 mg samples provided. This was agitated with a pipette for 1 min, before filtering into an NMR tube.

C^{13} NMR spectra were recorded at 100.63MHz, using a thirty-degree flip angle and an inverse gated decoupling scheme with 64 transients on a Bruker AVANCE III spectrometer. The acquisition window was 25.2 kHz and the recycle delay was the 30 seconds. The analysis data and figures are shown in **Appendix F** for a selected experiments (exp.no. 17 to 20).

6.10.2 Analysis using infrared spectrum:

The aqueous solution of reaction is cooled and separated by filter papers, then the samples are withdrawn from the precipitated solid. The samples of the liquids and solids of all experiments are analysed using the Fourier transform infrared spectroscopy (FTIR). After proceeding FTIR analyses of samples crystalline solids, and the solutions. The FTIR pattern compares to the standards of ammonium compounds (carbonate, bicarbonate, and carbamate) FTIR pattern. It is apparent that NH_4HCO_3 is the lone product of the chemical reaction.

(Meng *et al.*, 2005) studied the spectrum of ammonium bicarbonate. The symmetric C=O stretch appears at the peak near 1600 cm^{-1}, and the asymmetric C=O stretch of the bicarbonate ion is shown the peaks in the region of 1200- 1450 cm^{-1}. While the ammonium carbonate spectrum has peaks of 1300-1600 cm^{-1}, which represents the asymmetric C=O stretch of the carbonate ion. The results show that the carbonate and bicarbonate spectra are identically and difficult to identify. The similar peaks lie in the region between 1200 and 1700 cm^{-1}, also the second one is the peak of ammonium ion at a region at 3098 cm^{-1}. The analysis data using FTIR is shown in figures in **Appendix G** for all solid samples achieved from the experiments.

6.11 Conclusion

The chemical reaction as a sequestration / utilisation process is a promising method for CO_2 reduction in the atmosphere. In this thesis, the non-thermal plasma is combined with the very small bubbles currently utilized to enhance the carbon dioxide / an aqueous ammonia solution reaction at ambient conditions. The study findings highlight the potential for sustainable carbon capture to produce in a value-added chemical commodity such as ammonium bicarbonate. However, it is important to understand the role of control variables of any chemical process and their combined influences. To our knowledge, the use of the non-thermal plasma of CO_2 reaction with aqueous ammonia combined with small-bubbles technology is novel and original to our research group. Furthermore, a *priori* it is possible to predict the effects of operating variables, for instance, the optimum or maximum responses of the plasma process.

In this study, the effect of variables including a plasma processing parameters e.g. high applied voltage, CO_2 flow rate, initial aqueous ammonia concentrations, and reaction time on the conversion of CO_2 to ammonium bicarbonate are explored. Empirical models based on the process operating parameters are developed to show the significance of these parameters through the response surface methodology aimed at multi objective optimization. At an applied voltage of 3.5 kV, the maximum electrical conductivity of 167 mS is achieved at the CO_2 flow rate of 0.8 LPM and 3.4 M of aqueous ammonia solution, and reaction time of 40 minutes. Due

to the individual effects observed from the applied voltage variation, it is an important parameter driving the reaction of CO_2. Since the DBD can generate energetic electrons, high voltage induces reactive species that serves as agents for enhancing the chemical reaction.

The interactions of applied high voltage with other parameters show a weak effect on the reaction responses. In contrast, there are significant interactions of the CO_2 flow rate with either concentration of aqueous ammonia or reaction time, as well as the concentration with reaction time on the electrical conductivity of the solution and the yield of the process. The optimal yield of the process as a solid precipitate for the plasma CO_2 reaction process is 36% achieved experimentally at an applied high voltage of 3.5 kV, a feed CO_2 flow rate of 0.8 L/min, concentration of 3.4 M ammonia solution and a reaction time of 40 min. A correlation factor of 0.992 for the electrical conductivity and of 0.996 for the process yield of precipitated salt are computed for the empirically fitted polynomial models representing the data.

The maximum process yield according the mathematical regression model achieved is 78% with the combined influence of high voltage and CO_2 flow rate. A decline in yield at 2 to 3 kV is observed, that could be attributed to electroosmosis and electrophoresis phenomenon which occurs in the electro-kinetic systems, as well as may be due to the activated species such as free radicals and activated atoms and molecules. While the common influence of high voltage and aqueous ammonia concentration shows the low concentrations can enhances process yield more than the high concentrations. Therefore the maximum yields (>> 94 %) achieved at the 1.6 M curve and 4.0 kV at constant CO_2 flow rate (0.8 LPM) and period of reaction of 40 min.

Meanwhile, 84% yield is achieved by the combined effect of the high voltage and reaction time at fixed CO_2 flow rate (0.8 LPM) and aqueous ammonia concentration (3.4 M). The combined influence of the CO_2 flow rate and aqueous ammonia (at 3.5 kV and 40 minutes) displays an increase in process yield from 68 % to 92% at diluted concentration of aqueous ammonia solutions (1.6 M) and higher than the other high concentrations. At 3.5 kV and 3.4 M., the yield of the process increases with increasing CO_2 flow rate and reaction time (from 10 to 40 minutes curves) but the state is reversed at the curve of 50 min. The low flow rate provides very small bubbles and that means a high surface area for increasing the absorption of the CO_2.

The non-thermal plasma activate bubble charge distribution that mediate in the reaction process, giving rise to some unexpected results about the formation of ammonium salts. The study is an addition of knowledge and it is useful for engineering science because there is learning about the reaction mechanism. The role of plasma activation of CO_2 molecules is not

to produce a specific ammonium compound, but it to create a competition between the ionic and covalent bond to produce one of them. To achieve a specific compound, control of the two substantial factors pH value and reactant concentrations is required. There is many evidence that an excess of CO_2 produces the bicarbonate salts (Pelkie *et al.*, 1992). So one of the recommendations of this study for developing the reaction is studying the excess ammonia concentration effect to deviate the reaction products into carbamate. Another point is raising the range of the input (high) voltage more than 4 kV.

Department of Chemical and Biological Engineering

Chapter Seven

Conclusions and recommendation future work

Chapter Seven

Conclusion and recommendation future work

7.1 Introduction

Many pieces of research in the literature, are concerned with carbon dioxide reduction using several methods such as physical absorption, membrane separation, catalytic conversion, and chemical absorption. Each method above has advantages and disadvantages which may be related to chemical and physical solvent properties or to operation conditions. In this chapter, summary and conclusions are presented for the current study as well as some suggested and recommended points for the future work

7.2 Conclusions

Below the major novel and original contributions of this study are itemised, but without prioritisation.

- The study suggested a new route, based on the role of non-thermal plasma to increase the activity of the CO_2 molecules. The non-thermal plasma is combined with injecting the gas as current of bubbles to increase the surface area. These two technologies enhance the reaction between the "activated" CO_2 and aqueous ammonia to produce a valuable compound (ammonium bicarbonate).

- The experimental results show the high yield of the process (typical experiment) in presence of the non-thermal plasma, (60%) is achieved at an applied high voltage of 3.5 kV, a feed CO_2 flow rate of 0.8 L/min and 3.4 M aqueous ammonia concentration and a reaction time of 40 min. At same previous conditions and in absence the effect of non-thermal plasma (zero high voltage) the process yields 44%. Therefore, the process yield enhancement using the non-thermal plasma is about 36%.
- Although the quality of currently available property and kinetic data necessary for quantification is generally poor, nevertheless a theoretical model that assumes a stable excitation discharge and homogeneous plasma is developed. The study provide a model can used to predict and explore chemical reactions and the species concentration in the discharge plasma region.
- The results of the carbon dioxide model show that the main species with high concentrations and more stability are charged ions and neutrals, whilst the excited levels occurred at low

concentrations in milliseconds region varies from 10^3–10^4 to 10^{-8} cm^{-3} that coincide with increasing in O_2 and CO concentrations in same period of time.

- The design of the plasma generator (DBD) should be incorporated with the absorber column so that the vibrationally excited species of the CO_2 pass over a very short path between the plasma source and reaction zone (liquid medium) to overcome their decreased concentration with the time.

- The characterization of salt mixture, which could be produced from the reaction of CO_2 /NH_3 (aq.) such as ammonium carbonate (A), bicarbonate (B), and carbamate (C) is a substantial step in this study. The effect of changing the heating rate on the kinetics decomposition parameters of three ammonium salts in the non-isothermal condition using thermogravimetric analysis data is addressed in this work. The main finding is the kinetic parameters of the reaction in non-isothermal kinetics agrees with the concept of the multiple-step nature of the solid-state reactions concluded by Vyazovkin, (2000). That means the values of kinetic parameters are not fixed but altered under non-isothermal conditions, theoretical conversion, and temperature.
- The study presents the link between the pure components and an unknown mixture of two species depending on the temperature using the pseudoinverse method (PIM) to determine the composition of that mixture. New algorithms and procedure are developed and tested to generalize a model of calculation using the pseudo-inverse method have been combined into a thermogravimetric data analysis to predict the composition of the unknown solid sample.
- At an applied voltage of 3.5 kV, the maximum electrical conductivity of 167 mS is achieved at the CO_2 flow rate of 0.8 LPM, 3.4 M aqueous ammonia concentration, and reaction time of 40 minutes. Due to the individual effects observed from the applied voltage variation, it is an important parameter driving the reaction of CO_2. Since the DBD can generate energetic electrons, high voltage induces reactive species that serves as agents for enhancing the chemical reaction.
- A decrease in yield at 2 to 3 kV is noticed, that could be attributed to electroosmosis and electrophoresis phenomenon which occurs in the electro-kinetic systems, as well as may be due to the activated species such as free radicals and activated atoms and molecules.
- The yield of the process increases as the CO_2 flow rate increased with lower concentrations of the aqueous ammonia solution. While the process yield linearly increases with increasing flow rates of CO_2 and reaction time for the 10 to 30 minutes curves. Then the relationship

changes to be flat and descending at longer reaction time because the low flow rate allows smaller bubbles generated, subsequently, a high surface area of CO_2 absorption.

- Two different behaviours for the yield of the process associated with the aqueous ammonia concentration and the time of the reaction before and after the concentration of about 2 M is observed. The yield increases with the declining concentration of aqueous ammonia and reaction time before the overturn point. Whereas after this point of the concentration, the converse occurs. The high concentration of NH_3 drives the reaction to ammonium carbamate formation, while the short period limits the ammonium bicarbonate concentration from reaching the saturation state in solution.
- The behaviour of the solution temperature in presence of the non-thermal plasma, and with the absence it is determined. The results obviously show the two state are slightly different. However, the solution temperatures are higher in presence of plasma at the first few minutes of the reaction no more than 2-3 C.

7.3 Recommendations for future work

More experimental investigations are required for developing the reaction condition in the following domains:

i. Plasma generators design:
   - It is recommended to increase the surface area of discharge to get more efficient contact of gas molecules and increase the pulsing of the current to support the continuity of filament of discharge and finally increase the exciting species of vibrational modes.
   - Reducing the distance as much as possible between the discharge area and the injection of gas to the reaction zone, to ensure the excited molecule arrive into the reaction zone without loss of energy.
   - There are many fundamental components in the lab experimental system; a plasma generator, a diffuser, and absorption unite each possessing scale-up scope.
   - For plasma generator to activate the CO_2 could use the DBD plasma reactors which are already widely designed principally for ozone production in the commercial industry. The unit geometry and the size does not need many modifications, the reactors can be designed and operated in packages of small pipes.
   - In this study, we use 4 cm diameter sintered glass as a diffuser. The material of the diffuser may represent a challenge to increase in the scaling-up due to the potential of breakage during the periodic maintenance. Therefore this point should be taken into

account and seek a different diffuser material. The ceramics or metallic material maybe a better choice but the diffuser surface should not react with the reaction media.

- In this study, we have not been able to exploit fluidic oscillation for smaller bubble generation due very low flow rate. Desai (2017) introduced a fluidic oscillator suitable for very high turndown ratios, i.e. low flow rates as small as 100 L/min, but requires substantial tuning as microbubble formation strongly depends on the liquid composition. Therefore, we recommend using the fluidic oscillator in future work.

ii. Simulation study is recommended for the gas-liquid near the interface of the bubble to provide a deep understanding of the reaction kinetics with relating to the framework of heat and mass transfer phenomena.

iii. Future work must be conducted to test the feasibility of ammonia utilization with high concentrations and a continuous-flow of the reactants to simulate conditions in the industrial system. In presence suitable control system on the pH value and the reaction temperatures, we think could get ammonium carbamate, which more valuable compound than the bicarbonate.

iv. Finally, further work is required to establish the viability of the pseudo-inverse method in predict and interpret data for other interesting solid-state reactions.

References

- Abdul-Majeed, W. S., Parada, J. H. L. and Zimmerman, W. B. (2011) 'Optimization of a miniaturized DBD plasma chip for mercury detection in water samples', *Analytical and Bioanalytical Chemistry*, 401(9), pp. 2713–2722. doi: 10.1007/s00216-011-5118-9.
- Abdulrazzaq, N.N., Al-Sabbagh, B.H., Rees, J.M. and Zimmerman, W.B. (2016) 'Purification of Bioethanol Using Microbubbles Generated by Fluidic Oscillation: A Dynamical Evaporation Model', *Industrial & Engineering Chemistry Research*, 55(50), pp. 12909–12918. doi: 10.1021/acs.iecr.6b01666.
- Abu-Saman A. M. (2012) 'Solution of Linearly-Dependent Equations by Generalized Inverse of a Matrix', *International Journal of Science & Emerging Technologies*, 4(2), pp. 138–142.
- Adams, J. M. and Small, R. W. H. (1973) 'The crystal structure of ammonium carbamate', *Acta Crystallographica Section B: Structural Crystallography and Crystal Chemistry*, 29(11), pp. 2317–2319. doi: 10.1107/s056774087300662x.
- Aerts, R., Martens, T. and and Bogaerts, A. (2012) 'Influence of vibrational states on CO_2 splitting by dielectric barrier discharges', *Journal of Physical Chemistry C*, 116(44), pp. 23257–23273. doi: 10.1021/jp307525t.
- Aerts, R., Somers, W. and Bogaerts, A. (2015) 'Carbon Dioxide Splitting in a Dielectric Barrier Discharge Plasma: A Combined Experimental and Computational Study', *ChemSusChem*, 8(4), pp. 702–716. doi: 10.1002/cssc.201402818.
- Agarwal, A., Ng, W. J. and Liu, Y. (2011) 'Principle and applications of microbubble and nanobubble technology for water treatment', *Chemosphere*. Elsevier Ltd, 84(9), pp. 1175–1180. doi: 10.1016/j.chemosphere.2011.05.054.
- Aieta, E. M. and Roberts, P. V. (1986) 'Application of mass-transfer theory to the kinetics of a fast gas-liquid reaction: chlorine hydrolysis', *Environmental Science & Technology*, 20(1), pp. 44–50. doi: 10.1021/es00143a004.

  Al-Mashhadani, M. K. H., Bandulasena, H. C. H. and Zimmerman, W. B. (2012) 'CO_2 mass transfer induced through an airlift loop by a microbubble cloud generated by fluidic oscillation', *Industrial and Engineering Chemistry Research*, 51(4), pp. 1864–1877. doi: 10.1021/ie200960v.
- AL-Mashhadani, M. K. H., Wilkinson, S. J. and Zimmerman, W. B. (2015) 'Airlift bioreactor for biological applications with microbubble mediated transport processes', *Chemical Engineering Science*. Elsevier, 137, pp. 243–253. doi: 10.1016/j.ces.2015.06.032.
- Anzai, K. *Anzai, K., Kato, H., Hoshino, M., Tanaka, H., Itikawa, Y., Campbell, L., Brunger, M.J., Buckman, S.J., Cho, H., Blanco, F. and Garcia, G.*, (2012) 'Cross section data sets for electron collisions with H_2, O_2, CO, CO_2, N_2O and H_2O', *The European Physical Journal D*, 66(2), pp. 1–8. doi: 10.1140/epjd/e2011-20630-1.

- Bai, H. and Yeh, A. C. (1997) 'Removal of CO_2 greenhouse gas by ammonia scrubbing', *Industrial and Engineering Chemistry Research*, 36(6), pp. 2490–2493.
- Becker, K. H., Schoenbach, K. H. and Eden, J. G. (2006) 'Microplasmas and applications', *Journal of Physics D: Applied Physics*, 39(3). doi: 10.1088/0022-3727/39/3/R01.
- Bellan, M. P. (2006) *Fundamentals of plasma physics*. 1 st ed. New York: Cambridge University Press, Cambridge.
- Beuthe, T. and Chang, J. (1997) 'Chemical Kinetic Modelling of Non-Equilibrium Ar-CO_2 Thermal Plasmas', *Japanese Journal of Applied Physics*, 36(Part 1, No. 7B), pp. 4997–5002. doi: 10.1143/JJAP.36.4997.
- Bogaerts, A., Kozák, T., Van Laer, K. and Snoeckx, R.. (2015) 'Plasma-based conversion of CO_2 : current status and future challenges', *Faraday Discussions*, 183, pp. 217–232. doi: 10.1039/C5FD00053J.
- Boldyrev, V. V. (1979) 'Control of the Reactivity of Solids', *Annual Review of Materials Science*, 9, pp. 455–468.
- Bontozoglou, V. and Karabelas, A. J. (1993) 'Simultaneous absorption of hydrogen sulfide and carbon dioxide in sodium hydroxide solutions: experimental and numerical study of the performance of a short-time contactor', *Industrial & Engineering Chemistry Research*, 32(1), pp. 165–172. doi: 10.1021/ie00013a022.
- Boulos, M.I., 1991. Thermal plasma processing. IEEE transactions on Plasma Science, 19(6), pp.1078-1089.
- Box, G, and Wilson (1951) 'On the Experimental Attainment of Optimum Conditions', *Journal of the Royal Statistical Society*, 13(1), pp. 1– 45.
- Brauer, I., Punset, C., Purwins, H.G. and Boeuf, J.P., (1999) 'Simulations of self-organized filaments in a dielectric barrier glow discharge plasma', *Journal of Applied Physics*, 85(11), pp. 7569–7572. doi: 10.1063/1.370556.
- Brock, S.L., Marquez, M., Suib, S.L., Hayashi, Y. and Matsumoto, H., (1998) 'Plasma Decomposition of CO_2 in the Presence of Metal Catalysts', *Journal of Catalysis*, 180(2), pp. 225–233. doi: 10.1006/jcat.1998.2258.
- Brown, M.E., 2001. Introduction to thermal analysis: techniques and applications (Vol. 1). Springer Science & Business Media.
- Brown, M., Flynn, R. M. and Flynn, J. H. (1995) 'Report on the ICTAC Kinetics Committee (August 1992 to September 1994)', *Thermochimica Acta*, 256(2), pp. 477–483. doi: 10.1016/0040-6031(94)02225-D.
- Bruggeman, P. and Leys, C. (2009) 'Non-thermal plasmas in and in contact with liquids', *Journal of Physics D: Applied Physics*, 42(5), pp. 1–28. doi: 10.1088/0022-3727/42/5/053001.
- Butterworth, T., Elder, R. and Allen, R. (2016) 'Effects of particle size on CO_2 reduction and discharge characteristics in a packed bed plasma reactor', *Chemical Engineering Journal*, 293(FEBRUARY), pp.

55–67. doi: 10.1016/j.cej.2016.02.047.

- Campbell, Lawrie G. (2016). Micro-Plasma Activated Urea Synthesis from CO_2 and NH_3. MEng Dissertation as Internal report, University of Sheffield.
- Çatalkaya, E. Ç. and Şengül, F. (2006) 'Application of Box-Wilson experimental design method for the photodegradation of bakery's yeast industry with UV/H_2O_2 and UV/H_2O_2/Fe(II) process', *Journal of Hazardous Materials*, 128(2–3), pp. 201–207. doi: 10.1016/j.jhazmat.2005.07.052.
- Cavazzuti, M. (2013) *Optimization Methods From Theory to Design Scientific and Technological Aspects in Mechanics*. Springer-Verlag Berlin Heidelberg. doi: 0.1007/978-3-642-31187-1_2,.
- Cenian, A., Chernukho, A. and Borodin, V. (1995) 'Modeling of Plasma-Chemical Reactions in Gas Mixture of CO_2 lasers. II. Theoretical Model and its Verification', *Contributions to Plasma Physics*, 35(3), pp. 273–296. doi: 10.1002/ctpp.2150350309.
- Cents, A. H. G., Brilman, D. W. F. and Versteeg, G. F. (2005) 'CO_2 absorption in carbonate/bicarbonate solutions: The Danckwerts-criterion revisited', *Chemical Engineering Science*, 60(21), pp. 5830–5835. doi: 10.1016/j.ces.2005.05.020.
- Chakma, A. (1995) 'Separation of CO_2 and SO_2 from flue gas streams by liquid membranes', *Energy Conversion and Management*, 36(6–9), pp. 405–410. doi: 10.1016/0196-8904(95)00031-8.
- Chen, P. C. (2012) 'Absorption of carbon dioxide in a bubble-column scrubber', in G Liu. InTech, C. (ed.) *Greenhouse Gases-Capturing, Utilization and Reduction*. Taiwan: InTech, pp. 95– 112. doi: 10.5772/57353.
- Cieslak-Golonka, M., Ingier-Stocka, E. and Bartecki, A. (1995) 'Comparison of Ea values obtained by thermal analysis with energy of "charge-transfer" spectra for potassium and silver permanganates', *Journal of Thermal Analysis*, 43(1), pp. 157–167. doi: 10.1007/BF02635978.
- Claudel, B. and Boulamri, L. (1988) 'A new model of gas-solid kinetics: the case of ammonium carbamate formation and decomposition', *Thermochimica Acta*, 126(C), pp. 129–148. doi: 10.1016/0040-6031(88)87258-7.
- Coats, A. W. and Redfern, J. P. (1964) 'Kinetic parameters from thermogravimetric data', *Nature*, 201(4914), pp. 68–69. doi: 10.1038/201068a0.
- Coogan, J. J. and Sappey, A. D. (1996) 'Distribution of OH within silent discharge plasma reactors', *IEEE Transactions on Plasma Science*, 24(1), pp. 91–92. doi: 10.1109/27.491706.
- Cullinane, J. T. and Rochelle, G. T. (2005) 'Thermodynamics of aqueous potassium carbonate, piperazine, and carbon dioxide', *Fluid Phase Equilibria*, 227(2), pp. 197–213. doi: 10.1016/j.fluid.2004.11.011.
- Danckwerts, P. V. (1951) 'Significance of Liquid-Film Coefficients in Gas Absorption', *Industrial & Engineering Chemistry*, 43(6), pp. 1460–1467. doi: 10.1021/ie50498a055.
- Danckwerts, P. V. (1970) *Gas-Liquid Reactions*. London: McGraw-Hill.
- De Bie, C., Martens, T., van Dijk, J., Paulussen, S., Verheyde, B., Corthals, S. and Bogaerts, A.,. (2011) 'Dielectric barrier discharges used for the conversion of greenhouse gases: modeling the plasma

chemistry by fluid simulations', Plasma Sources Science and Technology, 20(2), p. 024008. doi: 10.1088/0963-0252/20/2/024008.

- Desai, Pratik (2018). A Fluidic Oscillator Based on a New Mechanism for Microbubble Generation and Developing Microbubble Stripping for Separation Phenomena. PhD thesis, University of Sheffield.
- Diao, Y.F., Zheng, X.Y., He, B.S., Chen, C.H. and Xu, X.C., (2004) 'Experimental study on capturing CO_2 greenhouse gas by ammonia scrubbing', *Energy Conversion and Management*, 45(13–14), pp. 2283–2296. doi: 10.1016/j.enconman.2003.10.011.
- Dinklage, A., Klinger, T., Marx, G. and Schweikhard, L. eds., (2005) *Plasma Physics Confinement, Transport and Collective Effects*. Edited by Andreas Dinklage et al. Berlin, Heidelberg: Springer Berlin Heidelberg (Lecture Notes in Physics). doi: 10.1007/b103882.
- Dressel, M., Eberle, H., Ripperger, W., Ruehenbeck, W. and Zwick, W., BASF SE, 1986. Preparation of ammonium carbamate. U.S. Patent 4,567,294.
- Edwards, T.J., Maurer, G., Newman, J. and Prausnitz, J.M., (1978). Vapor-liquid equilibria in multicomponent aqueous solutions of volatile weak electrolytes. AIChE Journal, 24(6), pp.966-976.
- Edzwald, J.K., 2010. Dissolved air flotation and me. Water research, 44(7), pp.2077-2106.
- Egan, E. P., Potts, J. E. and Potts, G. D. (1946) 'Dissociation Pressure of Ammonium Carbamate', *Industrial & Engineering Chemistry*, 38(4), pp. 454–456. doi: 10.1021/ie50436a027.
- Eliasson, B., Egli, W. and Kogelschatz, U. (1994) 'Modelling of dielectric barrier discharge chemistry', *Pure and Applied Chemistry*, 66(6), pp. 1275–1286. doi: 10.1351/pac199466061275.
- Eliasson, B. and Kogelschatz, U. (1991) 'Nonequilibrium volume plasma chemical processing', *IEEE Transactions on Plasma Science*, 19(6), pp. 1063–1077. doi: 10.1109/27.125031.
- Erdey, L., Gál, S. and Liptay, G. (1964) 'Thermoanalytical properties of analytical-grade reagents. Ammonium salts', *Talanta*, 11(6), pp. 913–940. doi: 10.1016/0039-9140(64)80128-4.
- FAO (2000) *FERTILIZERS AND THEIR USE*. Fourth. Rome: Food and Agriculture Organization of the United Nation international fertilizer industry association.
- Frasco, D. L. (1964) 'Infrared spectra of ammonium carbamate and deuteroammonium carbamate', *The Journal of Chemical Physics*, 41(7), pp. 2134–2140. doi: 10.1063/1.1726217.
- Fridmam, A. (2008) *Plasma Chemistry*. First eddition. Cambridge University Press, New York. doi: 10.1017/CBO9781107415324.004.
- Fridman, A., Nester, S., Kennedy, L.A., Saveliev, A. and Mutaf-Yardimci, O., (1999). Gliding arc gas discharge. Progress in energy and combustion science, 25(2), pp.211-231.
- Fridman, A., Chirokov, A. and Gutsol, A. (2005) 'Non-thermal atmospheric pressure discharges', *Journal of Physics D: Applied Physics*, 38(2), pp. R1–R24. doi: 10.1088/0022-3727/38/2/R01.
- Fridman, A. and Kennedy, L. A. (2011) *Plasma Physics and Engineering*. Second edd. Boca Raton: CRC Press Taylor & Francis Group.

Fulks, G., Fisher, G.B., Rahmoeller, K., Wu, M.C., D'Herde, E. and Tan, J., (2009) 'A Review of Solid Materials as Alternative Ammonia Sources for Lean NOx Reduction with SCR', in *SAE Technical*

Paper Series. doi: 10.4271/2009-01-0907.

- Funke, H.H., Welchhans, J., Watanabe, T., Torres, R., Houlding, V.H. and Raynor, M.W., (2004) Impurities in hydride gases part 2: Investigation of trace CO 2 in the liquid and vapor phases of ultra-pure ammonia. Journal of electronic materials, 33(8), pp.873-880.
- Gal'perin, V. A. and Finkel'shtein, A. I. (1972) 'Infrared spectra of ammonium carbamate and bicarbonate', *Journal of Applied Spectroscopy*, 17(3), pp. 1176–1178.
- Galwey, A. K. & and Brown, M. E. (1999) *Thermal decomposition of ionic solids*. First edit. Edited by ELSEVIER SCIENCE B.V. Amsterdam.
- Garner, W. E. (1955) *Chemistry of the solid state*. London: Butterworths Scientific.
- Golub, G.H. and Van Loan, C.F., 1980. SIAM Journal on Numerical Analysis, 17(6), pp.883-893.
- Golub, G. and Van Loan, C., 2013. Matrix Computations, 4th edn. Baltimore.
- Gondal, S., Asif, N., Svendsen, H.F. and Knuutila, H., (2015) 'Kinetics of the absorption of carbon dioxide into aqueous hydroxides of lithium, sodium and potassium and blends of hydroxides and carbonates', *Chemical Engineering Science*. Elsevier, 123, pp. 487– 499.
- Grayson, M. (2001) *Kirk-Othmer Encyclopedia of Chemical Technology volume 2*. 4th ed. Edited by Kirk-Othmer. New York: John Wiley & Sons Ltd.
- Hagelaar, G. (2019) *BOLSIG+ Electron Boltzmann equation solver, [online] BOLSIG+. Available at: https://www.bolsig.laplace.univ-tlse.fr/ [Accessed 1 Aug. 2019]*.
- Halpern, V. (1997) 'The significance of temperature-dependent distributions of activation energies', *Journal of Physics Condensed Matter*, 9(25), pp. 5479–5484. doi: 10.1088/0953-8984/9/25/015.
- Halstensen, M., Jilvero, H., Jinadasa, W.N. and Jens, K.J., (2017) 'Equilibrium Measurements of the NH_3-CO_2-H_2O System: Speciation Based on Raman Spectroscopy and Multivariate Modeling', *Journal of Chemistry*, 2017, pp. 1–13. doi: 10.1155/2017/7590506.
- Hanotu, J. O., Bandulasena, H. and Zimmerman, W. B. (2017) 'Aerator design for microbubble generation', *Chemical Engineering Research and Design*. Institution of Chemical Engineers, 123, pp. 367–376. doi: 10.1016/j.cherd.2017.01.034.
- Harling, A.M., Glover, D.J., Whitehead, J.C. and Zhang, K., (2008) 'Novel method for enhancing the destruction of environmental pollutants by the combination of multiple plasma discharges', *Environmental Science and Technology*, 42(12), pp. 4546–4550. doi: 10.1021/es703213p.
- Hayashi, N., Yamakawa, T. and Baba, S. (2006) 'Effect of additive gases on synthesis of organic compounds from carbon dioxide using non-thermal plasma produced by atmospheric surface discharges', *Vacuum*, 80(11–12), pp. 1299–1304. doi: 10.1016/j.vacuum.2006.01.062.
- Hessel, V., Anastasopoulou, A., Wang, Q., Kolb, G. and Lang, J., (2013) 'Energy, catalyst and reactor considerations for (near)-industrial plasma processing and learning for nitrogen-fixation reactions', *Catalysis Today*. Elsevier B.V., 211, pp. 9–28. doi: 10.1016/j.cattod.2013.04.005.
- Hessel, V. (2015) 'Special Issue: Design and Engineering of Microreactor and Smart-Scaled Flow Processes', *Processes*, 3(1). doi: 10.3390/pr3010019.

- Higbie, R. (1935) 'The rate of absorption of a pure gas into a still liquid during short periods of exposure.', *Trans. AIChE*, 31, pp. 365–389.
- Hillier, J., Bezzant, T. and Fletcher, T. H. (2010) 'Improved Method for the Determination of Kinetic Parameters from Non-isothermal Thermogravimetric Analysis (TGA) Data', *Energy & Fuels*, 24(5), pp. 2841–2847. doi: 10.1021/ef1001265.
- Hokazono, H. and Fujimoto, H. (1987) 'Theoretical analysis of the CO_2 molecule decomposition and contaminants yield in transversely excited atmospheric CO_2 laser discharge', *Journal of Applied Physics*, 62(5), pp. 1585–1594. doi: 10.1063/1.339606.
- Horvath, A. L. (1985) *Handbook of aqueous electrolyte solutions*. First. Edited by T. J. Kemp. Chichester: Ellis Horwood limited.
- House Jr., J. E. (1980) 'Decomposition of Ammonium Carbonate And Ammonium Bicarbonate And Proton Affinities of the Anions', *Inorganic and Nuclear Chemistry Letters*, 16(4), pp. 185–187. doi: 10.1016/0020-1650(80)80118-8.
- Hu, B., Guild, C. and Suib, S. L. (2013) 'Thermal, electrochemical, and photochemical conversion of CO_2 to fuels and value-added products', *Journal of CO_2 Utilization*. Elsevier Ltd., 1, pp. 18–27. doi: 10.1016/j.jcou.2013.03.004.
- Indarto, A., Yang, D.R., Choi, J.W., Lee, H. and Song, H.K., (2007) 'Gliding arc plasma processing of CO_2 conversion.', *Journal of hazardous materials*, 146(1–2), pp. 309–15. doi: 10.1016/j.jhazmat.2006.12.023.
- Itikawa, Y. (2002) 'Cross sections for electron collisions with carbon dioxide', *Journal of Physical and Chemical Reference Data*, 31(3), pp. 749–767. doi: 10.1063/1.1481879.
- Jeanmeure, L.F.C., Dyakowski, T., Zimmerman, W.B.J. and Baker, G., 2001. Use of raw capacitance tomography data for flow pattern control. In *Proceedings of 2nd World Congress on Industrial Process Tomography, Hannover, Germany* (pp. 12-19).
- Jeanmeure, L.F., Dyakowski, T., Zimmerman, W.B. and Clark, W., 2002. Direct flow-pattern identification using electrical capacitance tomography. *Experimental Thermal and Fluid Science*, *26*(6-7), pp.763-773.
- Joshi, R.P., Kolb, J.F., Xiao, S. and Schoenbach, K.H., (2009) 'Aspects of plasma in water: Streamer physics and applications', *Plasma Processes and Polymers*, 6(11), pp. 763–777. doi: 10.1002/ppap.200900022.
- Kauffman, G. B. (1996) *Kirk-Othmer encyclopedia of chemical technology*. fourth. Edited by Http://www.watcherworld.narod.ru/. American Scientist.
- Kawazuishi, K. and Prausnitz, J. M. (1987) 'Correlation of vapor-liquid equilibria for the system ammonia-carbon dioxide-water', *Industrial & Engineering Chemistry Research*, 26(7), pp. 1482–1485. doi: 10.1021/ie00067a036.
- Keeler, J. (2005) *Understanding NMR spectroscopy*. 1st edn. Cambridge: John Wiley & Sons Ltd. doi: 10.1007/SpringerReference_67582.

- Kettani, M. A. and Hoyaux, M. F. (1973) *PLASMA ENGINEERING*. 1st edn. London Butterworths: Butterworths & Co Ltd. pp. (1-10)
- Khan, W. (1990) 'An extension of Danckwerts theoretical surface renewal model to mass transfer at contaminated turbulent interfaces', *Mathematical and Computer Modelling*, 14(C), pp. 750–754. doi: 10.1016/0895-7177(90)90282-R.
- Kim, H.H., Teramoto, Y., Ogata, A., Takagi, H. and Nanba, T., (2016) 'Plasma Catalysis for Environmental Treatment and Energy Applications', *Plasma Chemistry and Plasma Processing*. Springer US, 36(1), pp. 45–72. doi: 10.1007/s11090-015-9652-7.
- Kim, J. Y., Han, K. and Chun, H. D. (2009) 'CO_2 absorption with low concentration ammonia liquor', *Energy Procedia*. Elsevier, 1(1), pp. 757–762. doi: 10.1016/j.egypro.2009.01.100.
- Kitajima, M., Watanabe, S., Tanaka, H., Takekawa, M., Kimura, M. and Itikawa, Y., (2001) 'Differential cross sections for vibrational excitation of CO_2 by 1.5-30 eV electrons', *Journal of Physics B: Atomic, Molecular and Optical Physics*, 34(10), pp. 1929–1940. doi: 10.1088/0953-4075/34/10/308.
- Kogelschatz, U. (2007) 'Twenty Years of Hakone Symposia: From Basic Plasma Chemistry to Billion Dollar Markets', *Plasma Processes and Polymers*, 4(7–8), pp. 678–681. doi: 10.1002/ppap.200700018.
- Kogelschatz, U. (2010) 'Collective phenomena in volume and surface barrier discharges', *Journal of Physics: Conference Series*, 257, p. 012015. doi: 10.1088/1742-6596/257/1/012015.
- Kogelschatz, U., Eliasson, B. and Egli, W. (1997) 'Dielectric-Barrier Discharges. Principle and Applications', *Le Journal de Physique IV*, 07(C4), pp. C4-47-C4-66. doi: 10.1051/jp4:1997405.
- Kostov, K. G. *et al.* (2009) 'Characteristics of dielectric barrier discharge reactor for material treatment', *Brazilian Journal of Physics*, 39(2), pp. 322–325. doi: 10.1590/S0103-97332009000300015.
- Kozák, T. and Bogaerts, A. (2015) 'Evaluation of the energy efficiency of CO_2 conversion in microwave discharges using a reaction kinetics model', *Plasma Sources Science and Technology*. IOP Publishing, 24(1), p. 15024. doi: 10.1088/0963-0252/24/1/015024.
- Kozák, T. and Bogaerts, A. (2014) 'Splitting of CO_2 by vibrational excitation in non-equilibrium plasmas: a reaction kinetics model', *Plasma Sources Science and Technology*, 23(4), p. 045004. doi: 10.1088/0963-0252/23/4/045004.
- Krauß, M. and Rzehak, R. (2018) 'Reactive absorption of CO_2 in NaOH: An Euler-Euler simulation study', *Chemical Engineering Science*, 181, pp. 199–214. doi: 10.1016/j.ces.2018.01.009.
- Kushner, M. J. (1988) 'A model for the discharge kinetics and plasma chemistry during plasma enhanced chemical vapor deposition of amorphous silicon', *Journal of Applied Physics*, 63, pp. 2532–2551. Available at: http://jap.aip.org/resource/1/japiau/v63/i8/p2532_s1.
- Kushner, M. J. (2005) 'Modelling of microdischarge devices: Plasma and gas dynamics', *Journal of Physics D: Applied Physics*, 38(11), pp. 1633–1643. doi: 10.1088/0022-3727/38/11/001.
- Kuvshinov, D., Siswanto, A., Lozano-Parada, J., Zimmerman, W. B. (2014) 'Efficient compact micro DBD plasma reactor for ozone generation for industrial application in liquid and gas phase systems', *World Academy of Science, Engineering and Technolog. International Journal of Chemical, Molecular,*

Nuclear, Materials and Metallurgical Engineering, 8(1), pp. 80-83.

- Levenspiel, O. (1999) *Chemical reaction engineering, Chemical Engineering Science*. John Wiley & Sons, Inc. doi: 10.1016/0009-2509(64)85017-X.
- Li-Fang, D., Xue-Chen, L., Zeng-Qian, Y., Sheng-Fa, Q., Ji-Ting, O. and Long, W., (2001) 'Self-Organized Filaments in Dielectric Barrier Discharge in Air at Atmospheric Pressure', *Chinese Physics Letters*, 18(10), pp. 1380–1382. doi: 10.1088/0256-307X/18/10/326.
- Li, X., Hagaman, E., Tsouris, C. and Lee, J.W., (2003) 'Removal of carbon dioxide from flue gas by ammonia carbonation in the gas phase', *Energy and Fuels*, 17(1), pp. 69–74. doi: 10.1021/ef020120n.
- Liao, Y. and Lucas, D. (2018) 'Evaluation of Interfacial Heat Transfer Models for Flashing Flow with Two-Fluid CFD', *Fluids*, 3(2), p. 38. doi: 10.3390/fluids3020038.
- Lin, L. and Wang, Q. (2015) 'Microplasma: A New Generation of Technology for Functional Nanomaterial Synthesis', *Plasma Chemistry and Plasma Processing*. Springer US, 35(6), pp. 925–962. doi: 10.1007/s11090-015-9640-y.
- Liu, Y., Rehman, F. and Zimmerman, W. B. (2017) 'Reaction engineering of carbon monoxide generation by treatment with atmospheric pressure, low power CO2 DBD plasma', *Fuel*. Elsevier, 209(December 2016), pp. 117–126. doi: 10.1016/j.fuel.2017.07.097.
- Locke, B.R., Sato, M., Sunka, P., Hoffmann, M.R. and Chang, J.S., (2006) 'Electrohydraulic discharge and nonthermal plasma for water treatment', *Industrial and Engineering Chemistry Research*, 45(3), pp. 882–905. doi: 10.1021/ie050981u.
- Lozano-Parada, J. H. and Zimmerman, W. B. (2010) 'The role of kinetics in the design of plasma microreactors', *Chemical Engineering Science*, 65(17), pp. 4925–4930. doi: 10.1016/j.ces.2010.03.056.
- Mamleev, V., Bourbigot, S., Le Bras, M., Duquesne, S. and Šesták, J., (2000) 'Modelling of nonisothermal kinetics in thermogravimetry', *Physical Chemistry Chemical Physics*, 2(20), pp. 4708–4716. doi: 10.1039/b004355i.
- Mani, F., Peruzzini, M. and Stoppioni, P. (2006) 'CO_2 absorption by aqueous NH3 solutions: speciation of ammonium carbamate, bicarbonate and carbonate by a ^{13}C NMR study', *Green Chemistry*, 8(11), p. 995. doi: 10.1039/b602051h.
- Mariotti, D. (2008) 'Nonequilibrium and effect of gas mixtures in an atmospheric microplasma', *Applied Physics Letters*, 92(15), pp. 3–5. doi: 10.1063/1.2912039.
- Market.Biz company (2017) *Global Ammonium Bicarbonate Market Research Report Forecast 2017 to 2022*. Available at: https://market.biz/report/global-ammonium-bicarbonate-market-sp/108301/.
- McGee, M. (2019) *CO_2.earth*. Available at: https://www.CO_2 .earth (Accessed: 21 May 2019).
- Mei, D., He, Y.L., Liu, S., Yan, J. and Tu, X., 2016. Optimization of CO_2 conversion in a cylindrical dielectric barrier discharge reactor using design of experiments. Plasma Processes and Polymers, 13(5), pp.544-556. doi: 10.1002/ppap.201500159.
- Mei, D. and Tu, X. (2017) 'Conversion of CO_2 in a cylindrical dielectric barrier discharge reactor: Effects of plasma processing parameters and reactor design', *Journal of CO_2 Utilization*. Elsevier Ltd.,

19, pp. 68–78. doi: 10.1016/j.jcou.2017.02.015.

- Meng, L. (2004) *Development of an analytical method for distinguishing ammonium bicarbonate from the products of an aqueous ammonia CO_2 scrubber and the characterization of ammonium bicarbonate, Western Kentucky University*. Masters thesis, Western Kentucky University. Available at: http://digitalcommons.wku.edu/theses/243.
- Meng, L., Burris, S., Bui, H. and Pan, W.P., (2005) 'Development of an analytical method for distinguishing ammonium bicarbonate from the products of an aqueous ammonia CO_2 scrubber', *Analytical Chemistry*, 77(18), pp. 5947–5952. doi: 10.1021/ac050422x.

Metcalfe, I.S., 1997. *Chemical reaction engineering: a first course*. Oxford, UK: Oxford University Press.

- Miller, F.A. and Wilkins, C. H. (1952) 'Infrared Spectra and Characteristic Frequencies of Inorganic Ions', *Analytical chemistry*, 24(8), pp. 1253–1294. doi: 10.1021/ac60068a007.
- Missen R., W., Mims Charles, A. and Saville Bradley, A., 1999. Introduction to chemical reaction engineering and kinetics. Estados Unidos, Editorial John Wiley & Sons, 29, pp.92.

Montgomery, D. C. (2001) *Design and Analysis of Experiments*. 5th editio. New York: JOHN WILY & SONS, INC.

- Morent, R., Leys, C., Dewulf, J., Neirynck, D., Van Durme, J. and Van Langenhove, H., (2007) 'DC-excited non-thermal plasmas for VOC abatement', *Journal of Advanced Oxidation Technologies*, 10(1), pp. 127–136.
- Murray-Lasso M. A. (2008) 'Alternative methods of calculation of the pseudo-inverse of a non full-rank matrix', *Journal of Applied Research and Technology*, 6(3), pp. 170–183.
- Myshkin, V. F. *et al.* (2013) 'Isotope effects of plasma chemical carbon oxidation in a magnetic field', *Natural Science*, 05(01), pp. 57–61. doi: 10.4236/ns.2013.51010.
- Nasser, E., 1971. Fundamentals of gaseous ionization and plasma electronics. Wiley-Interscience.
- Nishikawa, K. and Wakawtani, M. (2000) *Plasma Physics*. 3rd. Edited by G. Ecker. Springer-Verlag Berlin Heidelberg.
- Niu, Z., Guo, Y., Zeng, Q. and Lin, W., (2013) 'A novel process for capturing carbon dioxide using aqueous ammonia', *Fuel Processing Technology*. Elsevier B.V., 108, pp. 154–162. doi: 10.1016/j.fuproc.2012.05.028.
- Omae, I. (2012) 'Recent developments in carbon dioxide utilization for the production of organic chemicals', *Coordination Chemistry Reviews*. Elsevier B.V., 256(13–14), pp. 1384–1405. doi: 10.1016/j.ccr.2012.03.017.
- O'neill, B.C., Dalton, M., Fuchs, R., Jiang, L., Pachauri, S. and Zigova, K., 2010. Global demographic trends and future carbon emissions. Proceedings of the National Academy of Sciences, 107(41), pp.17521-17526.
- Pelkie, J.E., Concannon, P.J., Manley, D.B. and Poling, B.E., (1992). Product distributions in the carbon dioxide-ammonia-water system from liquid conductivity measurements. Industrial & engineering

chemistry research, 31(9), pp.2209-2215. doi: 10.1021/ie00009a018.

- Perlmutter, D. D. (1969) 'Surface -renewal models in mass transfer', *Chemical Engineering Science*, 16, pp. 287–296.
- Petitpas, G., Rollier, J.D., Darmon, A., Gonzalez-Aguilar, J., Metkemeijer, R. and Fulcheri, L., (2007) 'A comparative study of non-thermal plasma assisted reforming technologies', *International Journal of Hydrogen Energy*, 32(14), pp. 2848–2867. doi: 10.1016/j.ijhydene.2007.03.026.
- Pietsch, G. J. and Gibalov, V. I. (1998) 'Dielectric barrier discharges and ozone synthesis', *Pure and Applied Chemistry*, 70(6), pp. 1169–1174. doi: 10.1351/pac199870061169.
- Pohorecki, R. and Moniuk, W. (1988) 'Kinetics of reaction between carbon dioxide and hydroxyl ions in aqueous electrolyte solutions', *Chemical Engineering Science*, 43(7), pp. 1677–1684. doi: 10.1016/0009-2509(88)85159-5.
- Popescu, C. and Segal, E. (1994) 'Inequalities for the activation energy in non-isothermal kinetics', *Thermochimica Acta*, 237(1), pp. 159–165.
- Qi, G., Wang, S., Yu, H., Wardhaugh, L., Feron, P. and Chen, C., (2013) 'Development of a rate-based model for CO_2 absorption using aqueous NH3 in a packed column', *International Journal of Greenhouse Gas Control*. Elsevier Ltd, 17, pp. 450–461. doi: 10.1016/j.ijggc.2013.05.027.
- Ramachandran, B. R., Halpern, A. M. and Glendening, E. D. (1998) 'Kinetics and Mechanism of the Reversible Dissociation of Ammonium Carbamate : Involvement of Carbamic Acid', *The Journal of Physical Chemistry A*, 102(22), pp. 3934–3941. doi: 10.1021/jp980376n.
- Ravikiran, A., Arthanareeswari, M., Kamaraj, P. and Praveen, C., (2013) 'Nonisothermal Kinetics Analysis of the Dehydration of Ziprasidone Hydrochloride Monohydrate by Thermogravimetry.', *Indian Journal of Pharmaceutical Sciences*, 75(3), pp. 361–364. doi: 10.4103/0250-474X.117416.
- Rehman, F., Medley, G.J., Bandulasena, H. and Zimmerman, W.B., (2015) 'Fluidic oscillator-mediated microbubble generation to provide cost effective mass transfer and mixing efficiency to the wastewater treatment plants', *Environmental Research*. Elsevier, 137, pp. 32–39. doi: 10.1016/j.envres.2014.11.017.
- Rehman, F., Abdul Majeed, W. S. and Zimmerman, W. B. (2013) 'Hydrogen Production from Water Vapor Plasmolysis Using DBD-Corona Hybrid Reactor', *Energy & Fuels*, 27(5), pp. 2748–2761. doi: 10.1021/ef301981f.
- Rehman, F., Liu, Y. and Zimmerman, W. B. J. (2016) 'The role of chemical kinetics in using O_3 generation as proxy for hydrogen production from water vapour plasmolysis', *International Journal of Hydrogen Energy*. Elsevier Ltd, 41(15), pp. 6180–6192. doi: 10.1016/j.ijhydene.2016.02.071.
- Rehman, F., Lozano-Parada, J. and Zimmerman, W. B. (2012) 'A kinetic model for H_2 production by plasmolysis of water vapours at atmospheric pressure in a dielectric barrier discharge microchannel reactor', *International Journal of Hydrogen Energy*. Elsevier Ltd, 37(23), pp. 17678–17690. doi: 10.1016/j.ijhydene.2012.08.113.
- Reich, L. and Stivala, S. S. (1979) 'Correlation coefficients and mechanism using TG data',

Therrnochzmica Acta, 34, pp. 287–292.

- Roth, J. R. (1995) *INDUSTRIAL PLASMA ENGINEERING Volume 1 principles*. London: Institute of Physics Publishing ristol and Philadelphia.
- Sakiyama, Y., Graves, D.B., Chang, H.W., Shimizu, T. and Morfill, G.E., (2012) 'Plasma chemistry model of surface microdischarge in humid air and dynamics of reactive neutral species', *Journal of Physics D: Applied Physics*, 45(42). doi: 10.1088/0022-3727/45/42/425201.
- Samukawa, S., Hori, M., Rauf, S., Tachibana, K., Bruggeman, P., Kroesen, G., Whitehead, J.C., Murphy, A.B., Gutsol, A.F., Starikovskaia, S. and Kortshagen, U., (2012) 'The 2012 Plasma Roadmap', *Journal of Pysics D: Applied Physics*, 45(45), p. 253001(37). doi: 10.1088/0022-3727/45/25/253001.
- Sarkar, D., Bardhan, S., Bandyopadhyay, A., Chakraborty, M. and Bhattacharjee, C., (2012). Simulation of continuous stirred ultrafiltration process: an approach based on surface renewal theory. *Asia-Pacific Journal of Chemical Engineering*, 7(2), pp.279-294.
- Schmidt, J. E., Dudis, D. S. and Miller, D. J. (2012) 'Expendable High Energy Density Thermal Management Material: Ammonium Carbamate', *Journal of Thermophysics and Heat Transfer*, 26(2), pp. 345–351. doi: 10.2514/1.T3776.
- Shah, Y. (1979) *Gas - Liquid - Solid Reactor Design*. United States of America: McGraw-Hill.
- Simpson, T.W., Peplinski, J., Koch, P.N. and Allen, J.K., (1997), September. On the use of statistics in design and the implications for deterministic computer experiments. In ASME Design Engineering Technical Conferences (Vol. 14, p. 14).
- Shcherbakov, V.V., Artemkina, Y.M., Ponomareva, T.N. and Kirillov, A.D., 2009. Electrical conductivity of the ammonia-water system. Russian journal of inorganic chemistry, 54(2), pp.277-279.
- Stalder, K. R., McMillen, D. F. and Woloszko, J. (2005) 'Electrosurgical plasmas', *Journal of Physics D: Applied Physics*, 38(11), pp. 1728–1738. doi: 10.1088/0022-3727/38/11/014.
- Stewart, G.W., (1977). On the perturbation of pseudo-inverses, projections and linear least squares problems.', *Society for Industrial and Applied Mathematics*, 19(4), pp. 634–662.
- Tachibana, K. (2006) 'Current status of microplasma research', *IEEJ Transactions on Electrical and Electronic Engineering*, 1(2), pp. 145–155. doi: 10.1002/tee.20031.
- Takahashi, M., Kawamura, T., Yamamoto, Y., Ohnari, H., Himuro, S. and Shakutsui, H., (2003) 'Effect of shrinking microbubbles on gas hydrate formation', *Physical Chemistry B*, 107(107), pp. 2171–2173.
- Takahashi, M. (2005) 'Zeta potential of microbubbles in aqueous solutions: electrical properties of the gas-water interface.', *The journal of physical chemistry. B*, 109(46), pp. 21858–21864. doi: 10.1021/jp0445270.
- Takahashi, M., Chiba, K. and Li, P. (2007) 'Free-radical generation from collapsing microbubbles in the absence of a dynamic stimulus.', *The journal of physical chemistry. B*, 111(6), pp. 1343–7. doi: 10.1021/jp0669254.
- Takahashi, T., Miyahara, T. and Mochizuki, H. (1979) 'Fundamental Study of Bubble Formation in Dissolved Air Pressure Flotation.', *Journal of Chemical Engineering of Japan*, 12(4), pp. 275–280. doi:

10.1252/jcej.12.275.

- Tavan, Y. and Hosseini, S. H. (2017) 'A novel rate of the reaction between NaOH with CO2 at low temperature in spray dryer', *Petroleum*. Elsevier Ltd, 3(1), pp. 51–55. doi: 10.1016/j.petlm.2016.11.006.
- Taylan, O. and Berberoglu, H. (2013) 'Discharge of Carbon Dioxide Using a Non-Thermal Plasma Reactor', in *ASME 2013 Heat Transfer Summer Conference collocated with the ASME 2013 7th International Conference on Energy Sustainability and the ASME 2013 11th International Conference on Fuel Cell Science, Engineering and Technology*. Austin, pp. 1–8.
- Taylan, O. and Berberoglu, H. (2015) 'Dissociation of carbon dioxide using a microhollow cathode discharge plasma reactor: effects of applied voltage, flow rate and concentration', *Plasma Sources Science and Technology*. IOP Publishing, 24(1), p. 015006. doi: 10.1088/0963-0252/24/1/015006.
- Temesgen, T., Bui, T.T., Han, M., Kim, T.I. and Park, H.,. (2017) 'Micro and nanobubble technologies as a new horizon for water-treatment techniques: A review', *Advances in Colloid and Interface Science*. Elsevier, 246(June), pp. 40–51. doi: 10.1016/j.cis.2017.06.011.
- Toor, H. L. and Marchello, J. M. (1959) 'Film-penetration -Model for Mass and Heat Transfer', *A.I.Ch.E. Journal*, 4(1), pp. 97–101.
- Tu, X. and Whitehead, J. C. (2012) 'Plasma-catalytic dry reforming of methane in an atmospheric dielectric barrier discharge: Understanding the synergistic effect at low temperature', *Applied Catalysis B: Environmental*, 125, pp. 439–448. doi: 10.1016/j.apcatb.2012.06.006.
- Urashima, K. and Chang, J. (2000) 'Removal of volatile organic compounds from air streams and industrial flue gases by non-thermal plasma technology', *IEEE Transactions on Dielectrics and Electrical Insulation*, 7(5), pp. 602–614. doi: 10.1109/94.879356.
- Vesel, A., Mozetic, M., Drenik, A. and Balat-Pichelin, M., (2011) 'Dissociation of CO_2 molecules in microwave plasma', *Chemical Physics*. Elsevier B.V., 382(1–3), pp. 127–131. doi: 10.1016/j.chemphys.2011.03.015.
- Vyazovkin, S., (2000) 'On the phenomenon of variable activation energy for condensed phase reactions', *New Journal of Chemistry*, 24(11), pp. 913–917. doi: 10.1039/b004279j.
- Vyazovkin, S. (2000) 'Kinetic concepts of thermally stimulated reactions in solids: A view from a historical perspective', *International Reviews in Physical Chemistry*, 19(1), pp. 45–60. doi: 10.1080/014423500229855.
- Vyazovkin, S., Burnham, A.K., Criado, J.M., Pérez-Maqueda, L.A., Popescu, C. and Sbirrazzuoli, N., (2011) 'ICTAC Kinetics Committee recommendations for performing kinetic computations on thermal analysis data', *Thermochimica Acta*. Elsevier B.V., 520(1–2), pp. 1–19. doi: 10.1016/j.tca.2011.03.034.
- Wagner, H.E., Brandenburg, R., Kozlov, K.V., Sonnenfeld, A., Michel, P. and Behnke, J.F., (2003) 'The barrier discharge: Basic properties and applications to surface treatment', *User Modeling and User-Adapted Interaction*, 71(3 SPEC.), pp. 417–436. doi: 10.1016/S0042-207X(02)00765-0.
- Walas, S. M. (1989) *Reaction Kinetics for Chemical Engineerings*. New York: Butterworth.

- Wang, J.Y., Xia, G.G., Huang, A., Suib, S.L., Hayashi, Y. and Matsumoto, H., (1999) 'CO_2 Decomposition Using Glow Discharge Plasmas', *Journal of Catalysis*, 185(1), pp. 152–159. doi: 10.1006/jcat.1999.2499.
- Wen, N. and Brooker, M. . (1995) 'Ammonium carbonate, ammonium bicarbonate, and ammonium carbamate equilibria: A raman study', *Journal of Physical Chemistry®*, 99(1), pp. 359–368. doi: 10.1021/j100001a054.
- Wen, Y. and Jiang, X. (2001) 'Decomposition of CO_2 using pulsed corona discharges combined with catalyst', *Plasma Chemistry and Plasma Processing*, 21(4), pp. 665–678. doi: 10.1023/A:1012011420757.
- Worden, R. M. and Bredwell, M. D. (1998) 'Mass-transfer properties of microbubbles. 2. Analysis using a dynamic model', *Biotechnology Progress*, 14(1), pp. 39–46. doi: 10.1021/bp970131c.
- Wright, A., Bandulasena, H., Ibenegbu, C., Leak, D., Holmes, T., Zimmerman, W., Shaw, A. and Iza, F., (2018) 'Dielectric barrier discharge plasma microbubble reactor for pretreatment of lignocellulosic biomass', *AIChE Journal*, 64(11), pp. 3803–3816. doi: 10.1002/aic.16212.
- Wu, Z., Chen, H., Dong, Y., Mao, H., Sun, J., Chen, S., Craig, V.S. and Hu, J., (2008) 'Cleaning using nanobubbles: Defouling by electrochemical generation of bubbles', *Journal of Colloid and Interface Science*. Elsevier Inc., 328(1), pp. 10–14. doi: 10.1016/j.jcis.2008.08.064.
- Xiang, X., Guo, L., Wu, X., Ma, X. and Xia, Y., (2012) 'Urea formation from carbon dioxide and ammonia at atmospheric pressure', *Environmental Chemistry Letters*, 10(3), pp. 295–300. doi: 10.1007/s10311-012-0366-2.
- Xu, Q., Nakajima, M., Ichikawa, S., Nakamura, N. and Shiina, T., (2008) 'A comparative study of microbubble generation by mechanical agitation and sonication', *Innovative Food Science & Emerging Technologies*, 9(4), pp. 489–494. doi: 10.1016/j.ifset.2008.03.003.
- Yap, D., Tatibouët, J.-M. and Batiot-Dupeyrat, C. (2015) 'Carbon dioxide dissociation to carbon monoxide by non-thermal plasma', *Journal of CO_2 Utilization*. Elsevier Ltd., 12, pp. 54–61. doi: 10.1016/j.jcou.2015.07.002.
- Yeh, A. C. and Bia, H. (1999). Comparison of ammonia and monoethanolamine solvents to reduce CO_2 greenhouse gas emissions. *Science of the Total Environment*, 228(2-3), pp.121-133.
- Ying, K., Al-Mashhadani, M.K., Hanotu, J.O., Gilmour, D.J. and Zimmerman, W.B., (2013) 'Enhanced Mass Transfer in Microbubble Driven Airlift Bioreactor for Microalgal Culture', *Engineering*, 05(09), pp. 735–743. doi: 10.4236/eng.2013.59088.
- Ying, K., Gilmour, D. J. and Zimmerman, W. B. (2014) 'Effects of CO_2 and pH on growth of the microalga Dunaliella salina', *Journal of Microbial and Biochemical Technology*, 6(3), pp. 167–173. doi: 10.4172/1948-5948.1000138.
- Zhu, D., Fang, M., Zhong, L., Zhang, C. and Luo, Z., (2011) 'Semi-batch experimental study on CO_2 absorption characteristic of aqueous ammonia', *Energy Procedia*. Elsevier, 4, pp. 156–163. doi: 10.1016/j.egypro.2011.01.036.

- Zhuang, Q., Clements, B. and Li, Y. (2012) 'From ammonium bicarbonate fertilizer production process to power plant CO2 capture', *International Journal of Greenhouse Gas Control*. Elsevier Ltd, 10, pp. 56–63. doi: 10.1016/j.ijggc.2012.05.019.
- Zimmerman, W. B. (2006) Multiphysics Modelling with Finite Element Methods, series on stability, vibration and control of systems, *series A, vol. 18.* Edited by A. Guran and W. B. Zimmerman. London: World Scintiffic.
- Zimmerman, W.B., Tesar, V., Butler, S. and Bandulasena, H.C., 2008. Microbubble generation. Recent patents on engineering, 2(1), pp.1-8. doi: 10.2174/187221208783478598.
- Zimmerman, W.B., Hewakandamby, B.N., Tesař, V., Bandulasena, H.H. and Omotowa, O.A.,. (2009) 'On the design and simulation of an airlift loop bioreactor with microbubble generation by fluidic oscillation', *Food and Bioproducts Processing*, 87(3), pp. 215–227. doi: 10.1016/j.fbp.2009.03.006.
- Zimmerman, W.B., Zandi, M., Bandulasena, H.H., Tesař, V., Gilmour, D.J. and Ying, K., (2011) 'Design of an airlift loop bioreactor and pilot scales studies with fluidic oscillator induced microbubbles for growth of a microalgae Dunaliella salina', *Applied Energy*, 88(10), pp. 3357–3369. doi: 10.1016/j.apenergy.2011.02.013.
- Zimmerman, W. B. (2011) 'Electrochemical microfluidics', *Chemical Engineering Science*. Elsevier, 66(7), pp. 1412–1425. doi: 10.1016/j.ces.2010.03.057.

  Zimmerman, W. B., Al-Mashhadani, M. K. H. and Bandulasena, H. C. H. (2013) 'Evaporation dynamics of microbubbles', *Chemical Engineering Science*. Elsevier, 101, pp. 865–877. doi: 10.1016/j.ces.2013.05.026.
- Zimmerman, W. B. and Rees, J. M. (2009) 'Optimal modelling and experimentation for the improved sustainability of microfluidic chemical technology design', *Chemical Engineering Research and Design*, 87(6), pp. 798–808. doi: 10.1016/j.cherd.2008.11.010.
- Zimmerman, W. B., Tesař, V. and Bandulasena, H. C. H. (2011) 'Towards energy efficient nanobubble generation with fluidic oscillation', *Current Opinion in Colloid and Interface Science*, 16(4), pp. 350–356. doi: 10.1016/j.cocis.2011.01.010.

Appendences

Appendix A

Appendix (A1): The chemicals used in the study and their specification

1- **Carbon dioxide gas CO_2**: A compressed gas of carbon dioxide was used from a cylinder which was supplied by BOC Limited with a 99.8% carbon dioxide, formula of gas is CO2, molecular weight: 44.01 g/mol.

2- **Ammonium hydroxide**: A solution of ammonium hydroxide with concentration 28-30% was used in this work as liquid ammonia source for the reaction. Its specific gravity is 0.9, supplied from EMSURE®. The equation formula which was used to calculate molarity where the concentration is presumed in wt. % is: Molarity = [(% * d) / MW] * 10

   Where: %: Weight percentage % 28-30; d: Density or specific gravity 0.9, MW: Molecular Weight of ammonium hydroxide Mwt. =35.05 g/mol, so for instance the wt.% was taken 28 or 30the molarity will be as following:

   Molarity = (28*0.9/35.05)*10 =7.189 M or

   Molarity = (30*0.9/35.05)*10 =7.703 M

3- **Ammonium carbamate:**

Molecular formula (NH_2COONH_4 with molecular weight Mwt. (78.071 g/mol) a solid white crystals was used to characterize the properties of salt decomposition by thermogravimetric analysis and the electric conductivity. The compound supplied by Fluorochem Ltd. The purity of the salt is: 100% Ammonium carbamate, and melting point 59 C for more data see appendix (Safety Data Sheet)

4- **Ammonium bicarbonate:**

Molecular formula NH_4HCO_3 with molecular weight Mwt. (79.055 g/mol) a solid white crystals was used to characterize the properties of salt decomposition by thermogravimetric analysis and the electric conductivity. The compound supplied by Fluorochem Ltd. The purity of the salt is 95+% Ammonium bicarbonate, Mol Formula CH_5NO_3 and relative density 1.580 for more data see appendix (Safety Data Sheet)

5- **Ammonium carbonate:**

Molecular formula $(NH_4)_2CO_3$ with molecular weight (96.11 g/mol), solid substance: colourless, ammoniacal odour. It was used to characterize the properties of salt decomposition by thermogravimetric analysis and the electric conductivity. The compound supplied by Fluorochem

Ltd. The purity of the salt is Ammonium Carbonate Assay: 100%, and Melting point 58 °C for more data see appendix (Safety Data Sheet)

6- Deionized water:

It was produced by Milli-Q® Reference Water Purification System. Water is processed through Q-Gard® and Quantum® purification cartridges to reach a resistivity of 18.2 MΩ.cm (at 25°C) and a TOC value below 5 ppb.

Appendix (A2): Arduino Data interface: Arduino Code – Temperature and pH values measurement

```
#include <SPI.h>
#include "Adafruit_MAX31855.h"

// Default connection is using software SPI, but comment and uncomment one of
// the two examples below to switch between software SPI and hardware SPI:
// Example creating a thermocouple instance with software SPI on any three
// digital IO pins.
#define MAXDO   3
#define MAXCS   4
#define MAXCLK  5

// initialize the Thermocouple
Adafruit_MAX31855 thermocouple(MAXCLK, MAXCS, MAXDO);
/*
 # This sample code is used to test the pH meter V1.0.
 # Editor : YouYou
 # Ver    : 1.0
 # Product: analog pH meter
 # SKU    : SEN0161
*/
#define SensorPin A0            //pH meter Analog output to Arduino Analog Input 0
#define Offset -0.1113          //deviation compensate
#define LED 13
#define samplingInterval 20
#define printInterval 5000
#define ArrayLenth  40    //times of collection
int pHArray[ArrayLenth];   //Store the average value of the sensor feedback
int pHArrayIndex=0;

void setup() {
  pinMode(LED,OUTPUT);
  Serial.begin(9600);
  Serial.println("CLEARDATA"); //clears up any data left from previous projects
  Serial.println("pH meter experiment!");    //Test the serial monitor
  Serial.println("LABEL,    Time,    Timer,    Voltage,    pH value,       Internal Temperature,   Reactor Temperature");
  Serial.println("RESETTIMER"); //resets timer to 0
}
void loop()
{
   static unsigned long samplingTime = millis();
  static unsigned long printTime = millis();
  static float pHValue,voltage;
  if(millis()-samplingTime > samplingInterval)
  {
     pHArray[pHArrayIndex++]=analogRead(SensorPin);
     if(pHArrayIndex==ArrayLenth)pHArrayIndex=0;
     voltage = avergearray(pHArray, ArrayLenth)*5.0/1024;
     pHValue = 3.6927*voltage+Offset;
     samplingTime=millis();
  }
  if(millis() - printTime > printInterval)   //Every 5000 milliseconds, print a numerical, convert the state of the LED indicator
  {
```

```
  Serial.print("DATA,TIME,TIMER,");
  //Serial.print("Voltage:data");
        Serial.print(voltage,2);
        //Serial.print("    pH value:data ");
        Serial.print(",");
  Serial.print(pHValue,2);
        digitalWrite(LED,digitalRead(LED)^1);
        printTime=millis();
        Serial.print(",");
        Serial.print(thermocouple.readInternal());
        Serial.print(",");
        double c = thermocouple.readCelsius();
   if (isnan(c)) {
     //Serial.println("Something wrong with thermocouple!");
     Serial.println("------");
   } else {
     //Serial.print("C = ");
     Serial.println(c);
   }
  }
}
double avergearray(int* arr, int number){
  int i;
  int max,min;
  double avg;
  long amount=0;
  if(number<=0){
    Serial.println("Error number for the array to avraging!/n");
    return 0;
  }
  if(number<5){   //less than 5, calculated directly statistics
    for(i=0;i<number;i++){
      amount+=arr[i];
    }
    avg = amount/number;
    return avg;
  }else{
    if(arr[0]<arr[1]){
      min = arr[0];max=arr[1];
    }
    else{
      min=arr[1];max=arr[0];
    }
    for(i=2;i<number;i++){
      if(arr[i]<min){
        amount+=min;        //arr<min
        min=arr[i];
      }else {
        if(arr[i]>max){
          amount+=max;    //arr>max
          max=arr[i];
        }else{
          amount+=arr[i]; //min<=arr<=max
        }
      }//if
    }//for
    avg = (double)amount/(number-2);
  }//if
  return avg;

}
```

Appendix B

Appendix B1: Figures show the relation of rate coefficients of vibrational excited levels of CO_2 as a function of the mean electron energy, which is related to electron temperature as:

$< \varepsilon > = 3/2\ T_e$.

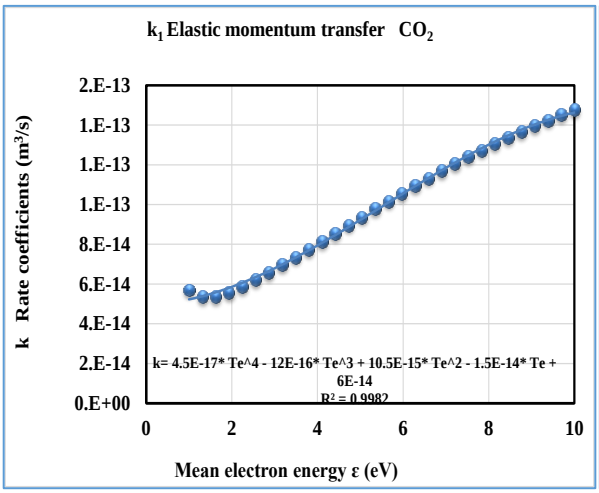

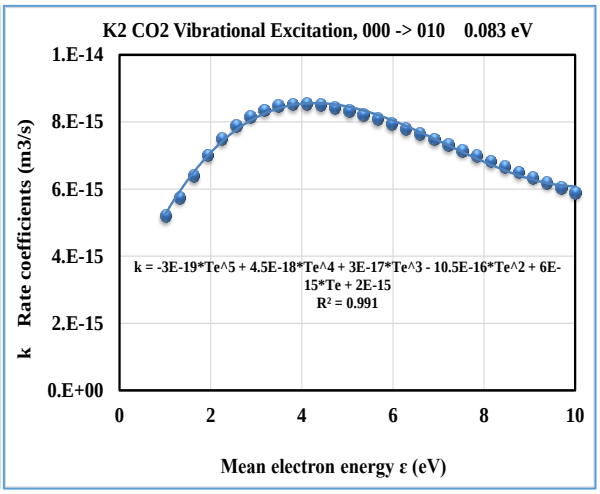

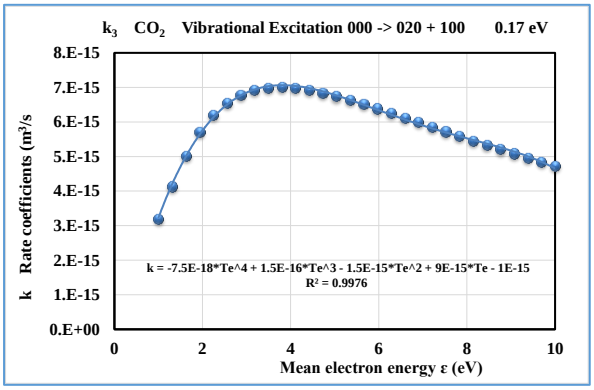

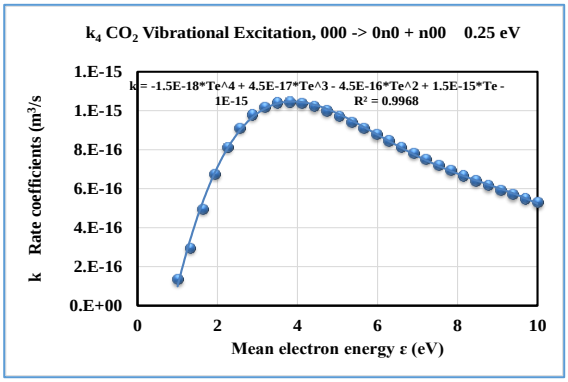

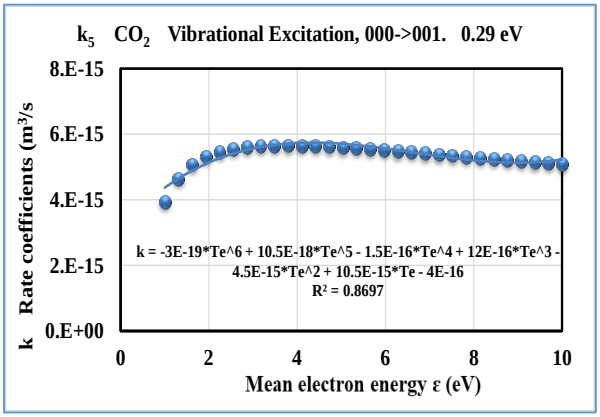

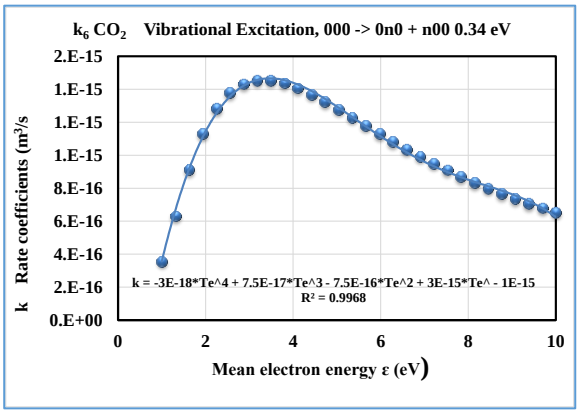

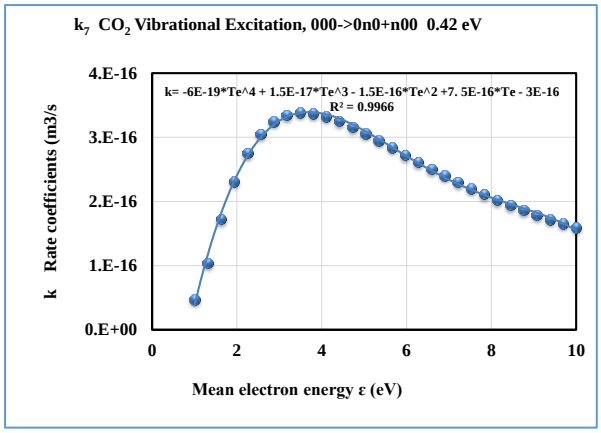
k7 CO2 Vibrational Excitation, 000->0n0+n00 0.42 eV
k= -6E-19*Te^4 + 1.5E-17*Te^3 - 1.5E-16*Te^2 +7. 5E-16*Te - 3E-16
R² = 0.9966
k Rate coefficients (m3/s
4.E-16
3.E-16
2.E-16
1.E-16
0.E+00
0
2
4
6
8
10
Mean electron energy ε (eV)

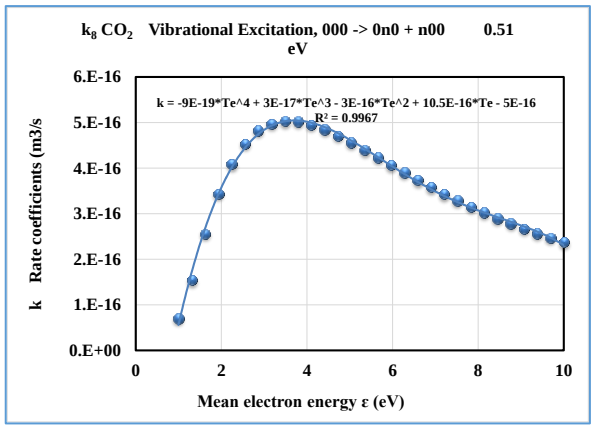
k8 CO2 Vibrational Excitation, 000 -> 0n0 + n00 0.51 eV
k = -9E-19*Te^4 + 3E-17*Te^3 - 3E-16*Te^2 + 10.5E-16*Te - 5E-16
R² = 0.9967
k Rate coefficients (m3/s
6.E-16
5.E-16
4.E-16
3.E-16
2.E-16
1.E-16
0.E+00
0
2
4
6
8
10
Mean electron energy ε (eV)

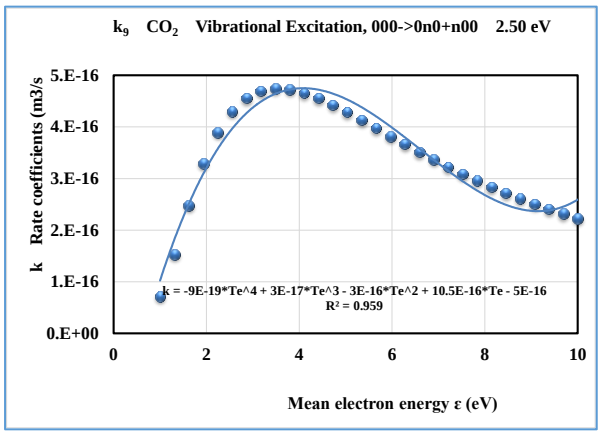
k9 CO2 Vibrational Excitation, 000->0n0+n00 2.50 eV
k = -9E-19*Te^4 + 3E-17*Te^3 - 3E-16*Te^2 + 10.5E-16*Te - 5E-16
R² = 0.959
k Rate coefficients (m3/s
5.E-16
4.E-16
3.E-16
2.E-16
1.E-16
0.E+00
0
2
4
6
8
10
Mean electron energy ε (eV)

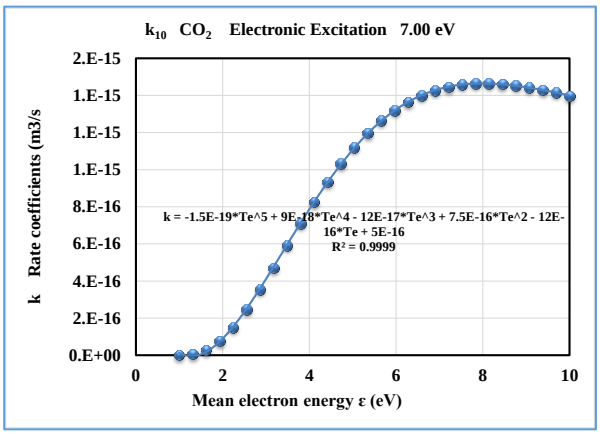
k10 CO2 Electronic Excitation 7.00 eV
k = -1.5E-19*Te^5 + 9E-18*Te^4 - 12E-17*Te^3 + 7.5E-16*Te^2 - 12E-16*Te + 5E-16
R² = 0.9999
k Rate coefficients (m3/s
2.E-15
1.E-15
1.E-15
1.E-15
8.E-16
6.E-16
4.E-16
2.E-16
0.E+00
0
2
4
6
8
10
Mean electron energy ε (eV)

Appendix B2

Table (B2) Chemical reactions in plasma reactor and the corresponding rate coefficients. The units of these coefficients are $(m^3)/s$ for two-body reactions and $(m^6)/s$ for thee-body reactions (Aerts et. al. 2015) and (Beuthe and Chang 1997)

Rea c.no.	Reaction	Rate Coefficient	units
1	$e^- + CO_2 \rightarrow e + CO_2$	4.5E-17* Te^4 - 12E-16* Te^3 + 10.5E-15* Te^2 - 1.5E-14* Te + 6E-14	cm^3/s
2	$e^- + CO_2 \rightarrow 2e + CO^+_2$	0.65*1.4*10^-11*Te^0.5*(1+1.3*10^-5*Te)*exp(-1.5*10^5/Te)	cm^3/s
3	$e^- + CO_2 \rightarrow 2e + CO^+ + O$	$0.1*K_2$	cm^3/s
4	$e^- + CO_2 \rightarrow 2e + C^+ + O_2$	$0.1*K_2$	cm^3/s
5	$e^- + CO_2 \rightarrow 2e + O^+ + CO$	$0.1*K_2$	cm^3/s
6	$e^- + CO_2 \rightarrow 2e + O_2^+ + C$	$0.1*K_2$	cm^3/s
7	$e^- + CO_2 \rightarrow O^- + CO$	5.0*10^-13*(T_g/300)^1.5*(Te/300)^-1.5	cm^3/s
8	$e^- + CO_2 \rightarrow e^- + O + CO$	1.6*10^-11	cm^3/s
9	$e^- + CO_2 \rightarrow e^- + CO_2v1$	-3E-19*Te^5 + 4.5E-18*Te^4 + 3E-17*Te^3 - 10.5E-16*Te^2 + 6E-15*Te + 2E-15	cm^3/s
10	$e^- + CO_2 \rightarrow e^- + CO_2v2$	-7.5E-18*Te^4 + 1.5E-16*Te^3 - 1.5E-15*Te^2 + 9E-15*Te - 1E-15	cm^3/s
11	$e^- + CO_2 \rightarrow e^- + CO_2v3$	-3E-19*Te^6 + 10.5E-18*Te^5 - 1.5E-16*Te^4 + 12E-16*Te^3 - 4.5E-15*Te^2 + 10.5E-15*Te - 4E-16	cm^3/s
12	$e^- + CO_2 \rightarrow e^- + CO_2v4$	-9E-19*Te^4 + 3E-17*Te^3 - 3E-16*Te^2 + 10.5E-16*Te - 5E-16	cm^3/s
13	$e^- + CO_2 \rightarrow e^- + CO_2$ e1	-1.5E-19*Te^5 + 9E-18*Te^4 - 12E-17*Te^3 + 7.5E-16*Te^2 - 12E-16*Te + 5E-16	cm^3/s
14	$e^- + CO_2 \rightarrow e^- + CO_2$ e2	3E-16*Te^2 - 10.5E-16*Te + 7E-16	cm^3/s
15	$e^- + CO \rightarrow e^- + e^- + CO^+$	0.7*1.4*10^-11*Te^0.5*(1+1.3*10^-5*Te)*exp(-1.5*10^5/Te)	cm^3/s
16	$e^- + CO \rightarrow e^- + e^- + C^+ + O$	$02*K_{16}$	cm^3/s
17	$e^- + CO \rightarrow e^- + e^- + C + O^+$	$0.1*K_{16}$	cm^3/s
18	$e^- + CO \rightarrow O^- + C$	0.18*10^-13*(Tg/300)	cm^3/s
19	e- + CO → e-+O +C	1.0*10^-12	cm^3/s
20	e- + CO → e- +COv1	1.14*10*-14	cm^3/s
21	e- + CO → e- +COe1	3.15*10^-16	cm^3/s
22	e- + CO → e- +COe2	2.75*10^-17	cm^3/s
23	e- + CO → e- +COe3	1.43*10^-17	cm^3/s
24	e- + CO → e- +COe4	6.47*10^-20	cm^3/s
25	$e^- + C \rightarrow e^- + C$	1.35*10^-13	cm^3/s
26	$e^- + C \rightarrow e^- + e^- + C^+$	5.65*10^-24	cm^3/s
27	$e^- + O_2 \rightarrow e^- + O_2$	1.04e-15*exp(-2.59/ Te)	cm^3/s
28	$e^- + O_2 \rightarrow e^- + O + O$	4.5*10^-11*Te^0.5*(1+2.9*10^-5*Te)*exp(-7.0*10^4/Te)	cm^3/s
29	$e^- + O_2 \rightarrow e^- + e^- + O^+_2$	1.1*10^-12*Te^0.5*(1+1.4*10^-5*Te)*exp(-1.4*10^5/Te)	cm^3/s
30	$e^- + O_2 \rightarrow e^- + e^- + O^+ + O$	$0.75*K_{33}$	cm^3/s
31	$e^- + O_2 \rightarrow O^- + O$	3.0*10^-12*(Tg/300)^1.5*(Te/300)^-1.5	cm^3/s
32	$e^- + O_2 \rightarrow e^- + O_2v1$	2.76*10^-15	cm^3/s
33	$e^- + O_2 \rightarrow e^- + O_2v2$	5.05*10^-16	cm^3/s
34	$e^- + O_2 \rightarrow e^- + O_2e1$	9.27*10^-16	cm^3/s
35	$e^- + O_2 \rightarrow e^- + O_2e2$	7.45*10^-16	cm^3/s
36	$e^- + O_3 \rightarrow e^- + O_3$	2.29*10^-13	cm^3/s
37	$e^- + O_3 \rightarrow e^- + O_2 + O$	9.0*10^-10	cm^3/s
38	$e^- + O_3 \rightarrow e^- + e^- + O^+_2 + O$	3.2*10^-11*Te^0.5*(1+1.3*10^-5*Te)*exp(-1.5*10^5/Te)	cm^3/s
39	$e^- + O_3 \rightarrow e^- + O^- + O^+ + O$	8.4*10^-12*Te^0.5*(1+9.4*10^-6*Te)*exp(-2.1*10^5/Te)	cm^3/s
40	$e^- + O_3 \rightarrow O^- + O_2$	8.9*10^-12*(Tg/300)^1.5	cm^3/s
41	$e^- + O_3 \rightarrow O + O_2^-$	6.6* 10^-9*Te^1.75	cm^3/s
42	$e^- + O \rightarrow e^- + O$	7.46*10^-15*exp(-5.58/(Te)^1.47)	cm^3/s
43	$e^- + O \rightarrow e^- + e^- + O^+$	4.1*10^-11*Te^0.5*(1+1.3*10^-5*Te)*exp(-1.5*10^5/Te)	cm^3/s
44	e-+CO_2+=>CO+O	2.0*10^ - 5*Tg^ - 1*Te^ - 0.5	cm^3/s
45	e-+CO_2+=>C+O_2	3.939*10^ - 7*Te^ - 0.4	cm^6/s
46	e-+CO_4+=>CO_2+O_2	1.608*10^ - 7*Te^ - 0.5	cm^3/s
47	e-+CO+=>C+O	3.683*10^ - 8*Te^ - 0.55	cm^3/s
48	e-+C_2O_2+=>CO+CO	4.0*10^ - 7*Te^ - 0.34	cm^3/s
49	e-+C_2O_3+=>CO2+CO	5.4*10^ - 8*Te^ - 0.7	cm^3/s
50	e-+C_2O_4+=>CO_2+CO_2	2.0*10^ - 5*Tg^ - 1*Te^ - 0.5	cm^3/s
51	e-+O_2+M=>O_2-+M	3.0*10^ - 30	cm^6/s
52	e-+O_3+M=>O_3-+M	5.0*10^ - 31*Te^ - 0.5	cm^3/s
53	e-+O+M=>O-+M	1.0*10^ - 31	cm^3/s
54	e-+O_2++M=>O_2+M	1.0*10^ - 26	cm^3/s
55	e-+O2+=>O+O	6.0*10^ - 7*Tg^ - 0.5*Te^ - 0.5	cm^3/s
56	e-+O++M=>O+M	1.0*10^ - 26	cm^6/s

57	e-+O_4+=>O_2+O_2	2.251*10^ - 7*Te^ - 0.5	cm^6/s
58	O+CO_2=>CO+O_2	2.8*10^ - 11*exp(-26500/Tg)	cm^3/s
59	C+CO_2=>CO+CO_2	1.0*10^ - 15	cm^3/s
60	O+CO+M=>CO_2+M	8.2*10^ - 34*exp(-1510/Tg)	cm^6/s
61	O_2+CO=>CO_2+O	2.52 *10^ - 23	cm^3/s
62	O_3+CO=>CO_2+O_2	4.2*10^ - 12*exp(-24000/Tg)	cm^3/s
63	C+CO+M=>C_2O+M	4.0*10^ - 25	cm^3/s
64	O_2+C=>CO+O	6.5*10^ - 32	cm^3/s
65	O+C+M=>CO+M	3.0*10^ - 11	cm^3/s
66	O+C_2O=>CO+CO	2.136*10^ - 29*(Tg/300)^3.08*exp(-2114/Tg)	cm^6/s
67	O_2+C_2O=>CO_2+CO	5.0*10^ - 11	cm^6/s
68	O+O_3=>O_2+O_2	3.3*10^ - 13	cm^3/s
69	O_3+M=>O_2+O+M	3.1*10^ - 14*Tg^ - 0.75*exp(-1575/Tg)	cm^3/s
70	O+O_2+M=>O_3+M	4.1175*10^ - 10*exp(-11340/Tg)	cm^3/s
71	O+O+M=>O_2+M	1.81*10^ - 33*(Tg/300)^ - 1.2	cm^3/s
72	O_2++CO_2+M=>CO_4++M	1.27*10^ - 32*(Tg/300)^ - 1*exp(-170/Tg)	cm^3/s
73	O++CO_2=>O_2++CO	2.3*10^ - 29	cm^3/s
74	O++CO_2=>CO_2++O	9.4*10^ - 10	cm^3/s
75	C++CO_2=>CO++CO	4.5*10^ - 10	cm^3/s
76	CO++CO_2=>CO_2++CO	1.1*10^ - 9	cm^3/s
77	O-+CO_2+M=>CO_3-+M	1.0*10^ - 9	cm^3/s
78	O_2-+CO_2+M=>CO_4-+M	9.0*10^ - 29	cm^3/s
79	O_3-+CO_2=>O_2+CO_3-	1.0*10^ - 29	cm^3/s
80	O_4-+CO_2=>CO_4-+O_2	5.5*10^ - 10	cm^3/s
81	CO_2++CO_2+M=>C_2O_4++M	4.8*10^ - 10	cm^3/s
82	O++CO=>CO++O	3.0*10^ - 28	cm^3/s
83	O-+CO=> CO_2+e-	4.9*10^ - 12*(Tg/300)^0.5*exp(-4580/Tg)	cm^3/s
84	CO_3-+CO=>CO_2+ CO_2+e-	5.5*10^ - 10	cm^3/s
85	C_2O_3++CO=>CO_2+C_2O_2+	5.0*10^ - 13	cm^3/s
86	C_2O_4++CO=>C_2O_3++CO_2	1.1*10^ - 9	cm^3/s
87	C_2O_3++CO+M=>C_2O_3++CO_2+M	9.0*10^ - 10	cm^3/s
88	C_2O_4++CO+M=>C_2O_3++CO_2+M	2.6*10^ - 26	cm^3/s
89	C++CO=>CO++C	4.2*10^ - 26	cm^3/s
90	CO++C=>CO+C+	5.0*10^ - 13	cm^3/s
91	O_2++C=>CO++O	1.1*10^ - 10	cm^3/s
92	O_2++C=>C++O_2	5.2*10^ - 11	cm^3/s
93	O+CO_2+=>O_2++CO	1.1*10^ - 10	cm^3/s
94	O+CO_2+=>O++CO_2	1.64*10^ - 10	cm^3/s
95	O+CO_2+=>O_2++CO_2	9.62*10^ - 11	cm^3/s
96	CO_3-+CO_2+=>CO_2+CO_2+O	5.3*10^ - 11	cm^3/s
97	CO_4-+CO_2+=> CO_2+CO_2+O_2	5.0*10^ - 7	cm^3/s
98	O_2-+CO_2+=>CO+O_2+O	5.0*10^ - 7	cm^3/s
99	O+CO+=>CO+O	6.0*10^ - 7	cm^3/s
100	O_2+CO+=>O_2++CO	1.4*10^ - 10	cm^3/s
101	O_2+C_2O_2+=CO+CO+O_2+	1.2*10^ - 10	cm^3/s
102	C_2O_2++M=>CO++CO+M	5.0*10^ - 12	cm^6/s
103	CO_3-+C_2O_2+=>CO_2+ CO+CO+O	1.0*10^ - 12	cm^6/s
104	CO_4-+C_2O_2+=>CO_2+CO+CO+O_2	5.0*10^ - 7	cm^3/s
105	O_2-+C_2O_2+=>CO+CO+O_2	5.0*10^ - 7	cm^6/s
106	CO_3-+C_2O_3+=>CO_2+CO_2+CO+O	6.0*10^ - 7	cm^3/s
107	CO_4-+C_2O_3+=>CO_2+CO_2+CO+O_2	5.0*10^ - 7	cm^3/s
108	O_2-+C_2O_3+=>CO_2+CO+O_2	5.0*10^ - 7	cm^3/s
109	C_2O_4++M=>CO_2++CO_2+M	6.0*10^ - 7	cm^3/s
110	CO_3-+C_2O_4+=>3CO_2+O	1.0*10^ - 14	cm^3/s
111	CO_4-+C_2O_4+=> CO_2+ CO_2+CO_2+O_2	5.0*10^ - 7	cm^6/s
112	O_2-+C_2O_4+=> CO_2+ CO_2+O_2	5.0*10^ - 7	cm^3/s
113	O_2++CO_3-=>CO_2+O_2+O	6.0*10^ - 7	cm^3/s
114	O+CO_3-=>CO_2+O_2-	3.0*10^ - 7	cm^3/s
115	O_2++CO_4-=>CO_2+O_2+O_2	8.0*10^ - 11	cm^3/s
116	O+CO_4-=>CO_3-+O_2	3.0*10^ - 7	cm^3/s
117	O+CO_4-=>CO_2+O_2+O-	1.1*10^ - 10	cm^3/s

118	$O+CO_4$-=>CO_2+O_3-	1.4*10^ - 11	cm^3/s
119	O_3+CO_4-=>CO_2+O_3-+O_2	1.4*10^ - 11	cm^3/s
120	O_2+C+=>CO+O+	1.3*10^ - 10	cm^3/s
121	O_2+C+=>CO++O	6.2*10^ - 10	cm^6/s
122	O++O_2=>O_2++O	3.8*10^ - 10	cm^3/s
123	O_2++O_2+M=>O_4++M	1.9*10^ - 11*(Tg/300)^ - 0.5	cm^3/s
124	O_2-+O_2+M=>O_4-+M	4.4*10^ - 30	cm^3/s
125	O-+O_2=>O_3+e-	3.3*10^ - 31	cm^6/s
126	O-+O_2+M=>O_3-+M	1.0*10^ - 12	cm^3/s
127	O-+O_3=>O_3-+O	3.0*10^ - 28*(Tg/300)^ - 1	cm^3/s
128	O-+O_3=>O_2+O_2+e-	8.0*10^ - 10	cm^3/s
129	O_2-+O_3=>O_3-+O_2	3.0*10^ - 10	cm^3/s
130	O_3-+O_3=>$O_2+O_2+O_2$+e-	4.0*10^ - 10	cm^3/s
131	O++O_3=>O_2++O_2	3.0*10^ - 10	cm^3/s
132	O++O+M=>O_2++M	1.0*10^ - 10	cm^3/s
133	O-+O=>O_2+e-	1.0 *10^ - 29	cm^3/s
134	O_2-+O=>O_2+O-	2.3 *10^ - 10	cm^6/s
135	O_2-+O=>O_3+e-	3.3 *10^ - 10	cm^3/s
136	O_3-+O=>O_3+O-	3.3 *10^ - 10	cm^3/s
137	O_3-+O=>O_2+O_2+e-	1.0 *10^ - 13	cm^6/s
138	O_3-+O=>O_2-+O_2	1.0 *10^ - 13	cm^3/s
139	O_4-+O=>O_3-+O_2	2.5*10^ - 10	cm^3/s
140	O_4-+O=>O-+O_2+O_2	4.00 *10^ - 10	cm^3/s
141	O_4-+O=>O_2++O_3	3.00 *10^ - 11	cm^3/s
142	O++O_2-+M=>O_3+M	3.00 *10^ - 10	cm^3/s
143	O++O_2-=>O+O_2	2.00 *10^ - 25	cm^3/s
144	O_2++O_2-=>O_2+O_2	2.7*10^ - 7	cm^3/s
145	O_2++O_2-=>O_2+O+O	2.0*10^ - 7	cm^3/s
146	O_2++O_2-+M=>O_2+O_2+M	4.2*10^ - 7	cm^3/s
147	O_2+O_2-=>O_2+O_2+e-	2.00 *10^ - 25	cm^3/s
148	O_2-+M=>O_2+M+e-	2.18 *10^ - 18	cm^3/s
149	O_2++O_3-=>O_2+O_3	2.70*10^ - 10*(Tg/300)^0.5*exp(-5590/Tg)	cm^3/s
150	O_2++O_3-=>O+O+O_3	2.00*10^ - 7	cm^3/s
151	O++O_3-=>O_3+O	1.00*10^ - 7	cm^3/s
152	O_2+O_3-=>O_2+O_3+e-	1.00*10^ - 7	cm^3/s
153	O_3-+M=>O_3+e-	2.3*10^ - 11	cm^3/s
154	O++O-=>O+O	2.3*10^ - 11	cm^3/s
155	O++O-+M=>O_2+M	4.00*10^ - 8	cm^3/s
156	O_2++O-=>O_2+O	2.00*10^ - 25	cm^3/s
157	O_2++O-=>O+O+O	1.00*10^ - 7	cm^3/s
158	O_2++O-+M=>O_3+M	2.6*10^ - 8	cm^3/s
159	M+O-=> O+M + e-	2.00*10^ - 25	cm^3/s
160	M+O_4-=>O_2-+O_2+M	4.00*10^ - 12	cm^3/s
161	M+O_4+=>O_2++O_2+M	3.08*10^ - 12	cm^3/s
162	CO_2v1+CO_2=>CO_2+CO_2	1.73*10^ - 13	cm^3/s
163	CO_2v1+CO=>CO_2+CO	1.07* 10^ - 14	cm^3/s
164	CO_2v1+O_2=>CO_2+O_2	7.48* 10^ - 15	cm^3/s
165	CO_2v2+CO_2=>CO_2+CO_2	7.48* 10^ - 15	cm^3/s
166	CO_2v2+CO=>CO_2+CO	9* 10^ - 18	cm^3/s
167	CO_2v2+O_2=>CO_2+O_2	2.79* 10^ - 17	cm^3/s
168	CO_2v2+CO_2=>CO_2v1+CO_2	2.79* 10^ - 17	cm^3/s
169	CO_2v2+CO=>CO_2v1+CO	2.9* 10^ - 14	cm^3/s
170	CO_2v2+O_2=>CO_2v1+O_2	2.03* 10^ - 14	cm^3/s

171	$CO_2v3+CO_2=>CO_2v2+CO_2$	2.03* 10^ - 14	cm^3/s
172	$CO_2v3+CO_2=>CO_2v2+CO$	7.72* 10^ - 16	cm^3/s
173	$CO_2v3+O_2=>CO_2v2+O_2$	2.32* 10^ - 16	cm^3/s
174	$CO_2v3+CO_2=>CO_2v4+CO_2$	3.09* 10^ - 16	cm^3/s
175	$CO_2v3+CO=>CO_2v4+CO$	2.52 * 10^ - 23	cm^3/s
176	$CO_2v3+O_2=>CO_2v4+O_2$	6.05* 10^ - 15	cm^3/s
177	$CO_2v3+CO_2=>CO_2v1+CO_2v2$	1.81* 10^ - 15	cm^3/s
178	$CO_2v3+CO_2=>CO_2v1+CO_2$	2.42* 10^ - 15	cm^3/s
179	$CO_2v3+CO=>CO_2v1+CO$	2.42* 10^ - 15	cm^3/s
180	$CO_2v3+O_2=>CO_2v1+O_2$	1.7* 10^ - 18	cm^3/s
181	$CO_2v4+CO_2=>CO_2v2+CO_2$	5.1* 10^ - 19	cm^3/s
182	$CO_2v4+CO=>CO_2v2+CO$	6.8* 10^ - 19	cm^3/s
183	$CO_2v4+O_2=>CO_2v2+O_2$	4.33 * 10^ - 14	cm^3/s
184	$CO_2v4+O_2=>CO_2v1+CO_2$	3.03 * 10^ - 14	cm^3/s
185	$CO_2v4+CO=>CO_2v1+CO$	3.03 * 10^ - 14	cm^3/s
186	$CO_2v4+O_2=>CO_2v1+O_2$	9.08 * 10^ - 18	cm^3/s
187	$COv1+CO_2=>CO+CO_2$	6.18 * 10^ - 15	cm^3/s
188	$COv1+CO=>CO+CO$	6.18 * 10^ - 15	cm^3/s
189	$COv1+O_2=>CO+O_2$	1.34 * 10^ - 23	cm^3/s
190	$O_2v1+CO_2=>O_2+CO_2$	1.34 * 10^ - 23	cm^3/s
191	$O_2v1+CO=>O_2+CO$	4.78 *10^ - 24	cm^3/s
192	$O_2v1+O_2=>O_2+O_2$	7.55 *10^ - 23	cm^3/s
193	$O_2v2+CO_2=>O_2+CO_2$	2.52 *10^ - 23	cm^3/s
194	$O_2v2+CO=>O_2+CO_2$	2.52 *10^ - 23	cm^3/s

Appendix C

Table (C1) shows the TGA data profiles of the binary mixtures and pure of $(NH_4)_2CO_3$ and NH_4HCO_3 salts as a function of the temperatures

Temp. C	*EXPERIMENTAL RESULTS* : mass fraction of [Carbonate / Bicarbonate]						
	$(NH_4)_2CO_3$	NH_4HCO_3	0.2/0.8	0.4/0.6	0.5/0.5	0.6/0.4	0.8/0.2
20.06	1.0000	1.0000	1	1	1	1	1
23.24	0.9927	0.9999	0.9978	0.9979	0.9926	0.9928	0.9927
26.70	0.9840	0.9998	0.9948	0.9952	0.9835	0.9837	0.9840
30.09	0.9738	0.9997	0.9910	0.9919	0.9717	0.9723	0.9738
33.65	0.9620	0.9995	0.9861	0.9877	0.9575	0.9584	0.9483
37.21	0.9483	0.9993	0.9802	0.9767	0.9407	0.9419	0.9325
40.65	0.9325	0.9990	0.9728	0.9700	0.9205	0.9226	0.9143
44.14	0.9143	0.9986	0.9641	0.9624	0.8983	0.9009	0.8936
47.63	0.8936	0.9981	0.9556	0.9538	0.8747	0.8777	0.8701
51.04	0.8701	0.9974	0.9466	0.9441	0.8506	0.8532	0.8437
54.76	0.8437	0.9965	0.9351	0.9207	0.8264	0.8280	0.8142
58.10	0.8142	0.9952	0.9222	0.9068	0.8018	0.8014	0.7818
61.87	0.7818	0.9935	0.9076	0.8912	0.7765	0.7735	0.7487
65.50	0.7466	0.9912	0.8957	0.8742	0.7490	0.7440	0.7083
69.24	0.7087	0.9881	0.8844	0.8558	0.7203	0.7127	0.6757
72.78	0.6683	0.9840	0.8696	0.8359	0.6911	0.6799	0.6311
76.41	0.6257	0.9785	0.8573	0.8150	0.6621	0.6455	0.5848
80.11	0.5811	0.9714	0.8385	0.7841	0.6361	0.6093	0.5373
83.65	0.5348	0.9620	0.8178	0.7581	0.6200	0.5752	0.4888
87.19	0.4873	0.9498	0.8035	0.7441	0.6077	0.5531	0.4295
90.80	0.4388	0.9337	0.7840	0.7159	0.5922	0.5376	0.3304
94.26	0.2904	0.9142	0.7586	0.6577	0.5709	0.4969	0.2409
97.74	0.1912	0.8887	0.7262	0.6227	0.5424	0.4691	0.1912
101.14	0.1413	0.8596	0.6860	0.5409	0.5063	0.4335	0.1413

Table (C2) shows the forward model results data of the binary mixtures and pure of $(NH_4)_2CO_3$ and NH_4HCO_3 salts as a function of the temperature.

Temp. C	***The forward model* results: mass fraction of [Carbonate / Bicarbonate]**						
	$(NH_4)_2CO_3$	NH_4HCO_3	0.2/0.8	0.4/0.6	0.5/0.5	0.6/0.4	0.8/0.2
20.06	1.0000	1.0000	1.000	1.000	1.000	1.000	1.000
23.24	0.9927	0.9999	0.999	0.997	0.996	0.996	0.994
26.70	0.9840	0.9998	0.997	0.994	0.992	0.990	0.987
30.09	0.9738	0.9997	0.995	0.989	0.987	0.984	0.979
33.65	0.9620	0.9995	0.992	0.985	0.981	0.977	0.970
37.21	0.9483	0.9993	0.989	0.979	0.974	0.969	0.959
40.65	0.9325	0.9990	0.986	0.972	0.966	0.959	0.946
44.14	0.9143	0.9986	0.982	0.965	0.957	0.948	0.931
47.63	0.8936	0.9981	0.977	0.956	0.946	0.935	0.915
51.04	0.8701	0.9974	0.972	0.947	0.934	0.921	0.896
54.76	0.8437	0.9965	0.966	0.935	0.920	0.905	0.874
58.10	0.8142	0.9952	0.959	0.923	0.905	0.887	0.850
61.87	0.7818	0.9935	0.951	0.909	0.888	0.866	0.824
65.50	0.7466	0.9912	0.942	0.893	0.869	0.844	0.796
69.24	0.7087	0.9881	0.932	0.876	0.848	0.821	0.765
72.78	0.6683	0.9840	0.921	0.858	0.826	0.795	0.732
76.41	0.6257	0.9785	0.908	0.837	0.802	0.767	0.696
80.11	0.5811	0.9714	0.893	0.815	0.776	0.737	0.659
83.65	0.5348	0.9620	0.877	0.791	0.748	0.706	0.620
87.19	0.4873	0.9498	0.857	0.765	0.719	0.672	0.580
90.80	0.4388	0.9337	0.835	0.736	0.686	0.637	0.538
94.26	0.2904	0.9142	0.789	0.665	0.602	0.540	0.415
97.74	0.1912	0.8887	0.749	0.610	0.540	0.470	0.331
101.14	0.1413	0.8596	0.716	0.572	0.500	0.429	0.285

Table (C3) shows the TGA data profiles of the binary mixtures and pure of $(NH_4)_2CO_3$ and $NH_2COO\ NH_4$ salts as a function of the temperatures.

Temp. C	***EXPERIMENTAL RESULTS* : mass fraction of [Carbonate / Carbamate]**						
	$(NH_4)_2CO_3$	$NH_2COO\ NH_4$	0.2/0.8	0.4/0.6	0.5/0.5	0.6/0.4	0.8/0.2
20.06	1.0000	1.0000	1	1	1	1	1
23.48	0.9927	0.9850	0.988	0.987	0.987	0.99	0.99
26.94	0.9840	0.9669	0.973	0.971	0.971	0.977	0.977
30.41	0.9738	0.9453	0.955	0.951	0.951	0.962	0.961
34.00	0.9620	0.9198	0.934	0.927	0.927	0.943	0.941
37.47	0.9483	0.8900	0.908	0.898	0.898	0.92	0.918
41.06	0.9325	0.8559	0.878	0.865	0.865	0.892	0.889
44.66	0.9143	0.8172	0.844	0.826	0.826	0.86	0.857
48.35	0.8936	0.7740	0.805	0.782	0.782	0.824	0.82
51.78	0.8701	0.7265	0.763	0.734	0.734	0.784	0.779
55.29	0.8437	0.6751	0.718	0.684	0.684	0.74	0.734
58.68	0.8142	0.6203	0.671	0.632	0.632	0.694	0.686
62.32	0.7818	0.5628	0.622	0.579	0.579	0.644	0.633
65.89	0.7466	0.5038	0.57	0.525	0.525	0.59	0.577
69.53	0.7087	0.4446	0.515	0.469	0.469	0.533	0.517
73.14	0.6683	0.3864	0.458	0.41	0.41	0.472	0.453
76.76	0.6257	0.3303	0.398	0.35	0.35	0.408	0.386
80.33	0.5811	0.2763	0.336	0.287	0.287	0.342	0.317
83.94	0.5348	0.2237	0.271	0.223	0.223	0.274	0.248
87.47	0.4873	0.1716	0.203	0.158	0.158	0.203	0.179
91.13	0.4388	0.1193	0.133	0.094	0.094	0.133	0.111
94.73	0.2904	0.0687	0.069	0.038	0.038	0.073	0.05

Table (C4) shows the forward model results data of the binary mixtures and pure of $(NH_4)_2CO_3$ and $NH_2COO\ NH_4$ salts as a function of the temperature.

Temp. C	***The forward model* results : mass fraction of [Carbonate / Carbamate]**						
	$(NH_4)_2CO_3$	$NH_2COO\ NH_4$	0.2/0.8	0.4/0.6	0.5/0.5	0.6/0.4	0.8/0.2
20.06	1.0000	1.0000	1.000	1.000	1.000	1.000	1.000
23.48	0.9927	0.9850	0.987	0.988	0.989	0.990	0.991
26.94	0.9840	0.9669	0.970	0.974	0.976	0.977	0.981
30.41	0.9738	0.9453	0.951	0.957	0.960	0.962	0.968
34.00	0.9620	0.9198	0.928	0.937	0.941	0.945	0.954
37.47	0.9483	0.8900	0.902	0.913	0.919	0.925	0.937
41.06	0.9325	0.8559	0.871	0.887	0.894	0.902	0.917
44.66	0.9143	0.8172	0.837	0.856	0.866	0.876	0.895
48.35	0.8936	0.7740	0.798	0.822	0.834	0.846	0.870
51.78	0.8701	0.7265	0.755	0.784	0.798	0.813	0.841
55.29	0.8437	0.6751	0.709	0.743	0.759	0.776	0.810
58.68	0.8142	0.6203	0.659	0.698	0.717	0.737	0.775
62.32	0.7818	0.5628	0.607	0.650	0.672	0.694	0.738
65.89	0.7466	0.5038	0.552	0.601	0.625	0.650	0.698
69.53	0.7087	0.4446	0.497	0.550	0.577	0.603	0.656
73.14	0.6683	0.3864	0.443	0.499	0.527	0.556	0.612
76.76	0.6257	0.3303	0.389	0.449	0.478	0.508	0.567
80.33	0.5811	0.2763	0.337	0.398	0.429	0.459	0.520
83.94	0.5348	0.2237	0.286	0.348	0.379	0.410	0.473
87.47	0.4873	0.1716	0.235	0.298	0.330	0.361	0.424
91.13	0.4388	0.1193	0.183	0.247	0.279	0.311	0.375
94.73	0.2904	0.0687	0.113	0.157	0.180	0.202	0.246

Table (C5) shows the TGA data of the binary mixtures and pure of NH_4HCO_3 and NH_2COO NH4 salts as a function of the temperatures.

Temp. C	*EXPERIMENTAL RESULTS : mass fraction of [Bicarbonate / Carbamate]*						
	$NH_4H\ CO_3$	$NH_2COO\ NH_4$	0.2/0.8	0.4/0.6	0.5/0.5	0.6/0.4	0.8/0.2
20.26	**1.0000**	**1.0000**	**1.0000**	**1.0000**	**1.0000**	**1.0000**	**1.0000**
23.61	**0.9999**	**0.9850**	**0.9898**	**0.9933**	**0.9935**	**0.9956**	**0.9980**
27.16	**0.9998**	**0.9669**	**0.9774**	**0.9849**	**0.9855**	**0.9903**	**0.9956**
30.64	**0.9997**	**0.9453**	**0.9620**	**0.9747**	**0.9756**	**0.9838**	**0.9926**
33.99	**0.9995**	**0.9198**	**0.9437**	**0.9623**	**0.9634**	**0.9758**	**0.9889**
37.58	**0.9993**	**0.8900**	**0.9220**	**0.9474**	**0.9488**	**0.9664**	**0.9844**
41.27	**0.9990**	**0.8559**	**0.8964**	**0.9298**	**0.9321**	**0.9554**	**0.9787**
44.78	**0.9986**	**0.8172**	**0.8676**	**0.9095**	**0.9131**	**0.9431**	**0.9719**
48.52	**0.9981**	**0.7740**	**0.8359**	**0.8867**	**0.8926**	**0.9303**	**0.9639**
52.12	**0.9974**	**0.7265**	**0.8018**	**0.8618**	**0.8704**	**0.9166**	**0.9548**
55.69	**0.9965**	**0.6751**	**0.7657**	**0.8354**	**0.8464**	**0.9019**	**0.9441**
59.09	**0.9952**	**0.6203**	**0.7281**	**0.8077**	**0.8209**	**0.8860**	**0.9320**
62.63	**0.9935**	**0.5628**	**0.6893**	**0.7789**	**0.7945**	**0.8685**	**0.9183**
66.39	**0.9912**	**0.5038**	**0.6499**	**0.7487**	**0.7678**	**0.8492**	**0.9033**
69.84	**0.9881**	**0.4446**	**0.6103**	**0.7168**	**0.7396**	**0.8267**	**0.8874**
73.36	**0.9840**	**0.3864**	**0.5700**	**0.6833**	**0.7094**	**0.8002**	**0.8709**
76.91	**0.9785**	**0.3303**	**0.5276**	**0.6483**	**0.6764**	**0.7701**	**0.8539**
80.49	**0.9714**	**0.2763**	**0.4813**	**0.6112**	**0.6410**	**0.7377**	**0.8384**
84.16	**0.9620**	**0.2237**	**0.4306**	**0.5713**	**0.6035**	**0.7054**	**0.8244**
87.73	**0.9498**	**0.1716**	**0.3780**	**0.5285**	**0.5664**	**0.6730**	**0.8076**
91.33	**0.9337**	**0.1193**	**0.3290**	**0.4838**	**0.5296**	**0.6398**	**0.7863**
94.93	**0.9142**	**0.0687**	**0.2882**	**0.4431**	**0.4931**	**0.6050**	**0.7542**
98.46	**0.8887**	**0.0289**	**0.2525**	**0.4125**	**0.4548**	**0.5653**	**0.7175**
102.11	**0.8596**	**0.0060**	**0.2161**	**0.3856**	**0.4127**	**0.5194**	**0.6581**

Table (C6) shows the forward model results data of the binary mixtures and pure of NH_4HCO_3 and $NH_2COO\ NH_4$ salts as a function of the temperature.

Temp. C	***The forward model* results : mass fraction of [Bicarbonate / Carbamate]**						
	$NH_4H\ CO_3$	$NH_2COO\ NH_4$	0.2/0.8	0.4/0.6	0.5/0.5	0.6/0.4	0.8/0.2
20.26	1.0000	1.0000	1	1	1	1	1
23.61	0.9999	0.9850	0.988	0.991	0.9925	0.9939	0.9969
27.16	0.9998	0.9669	0.9735	0.9801	0.9834	0.9867	0.9933
30.64	0.9997	0.9453	0.9562	0.967	0.9725	0.9779	0.9888
33.99	0.9995	0.9198	0.9357	0.9517	0.9596	0.9676	0.9836
37.58	0.9993	0.8900	0.9119	0.9337	0.9447	0.9556	0.9775
41.27	0.9990	0.8559	0.8845	0.9131	0.9275	0.9418	0.9704
44.78	0.9986	0.8172	0.8535	0.8898	0.9079	0.9261	0.9623
48.52	0.9981	0.7740	0.8188	0.8637	0.8861	0.9085	0.9533
52.12	0.9974	0.7265	0.7807	0.8348	0.8619	0.889	0.9432
55.69	0.9965	0.6751	0.7393	0.8036	0.8358	0.8679	0.9322
59.09	0.9952	0.6203	0.6953	0.7702	0.8077	0.8452	0.9202
62.63	0.9935	0.5628	0.649	0.7351	0.7782	0.8212	0.9073
66.39	0.9912	0.5038	0.6013	0.6988	0.7475	0.7962	0.8937
69.84	0.9881	0.4446	0.5533	0.662	0.7163	0.7707	0.8794
73.36	0.9840	0.3864	0.5059	0.6254	0.6852	0.7449	0.8645
76.91	0.9785	0.3303	0.46	0.5896	0.6544	0.7192	0.8489
80.49	0.9714	0.2763	0.4153	0.5543	0.6238	0.6933	0.8323
84.16	0.9620	0.2237	0.3713	0.519	0.5928	0.6667	0.8143
87.73	0.9498	0.1716	0.3272	0.4829	0.5607	0.6385	0.7942
91.33	0.9337	0.1193	0.2822	0.4451	0.5265	0.6079	0.7708
94.93	0.9142	0.0687	0.2378	0.4069	0.4914	0.576	0.7451
98.46	0.8887	0.0289	0.2009	0.3728	0.4588	0.5448	0.7168
102.11	0.8596	0.0060	0.1767	0.3474	0.4328	0.5181	0.6889

Appendix D

Table (D1) illustrates the independent coded variables calculation of $\sum X_i^2$

	X_1	X_2	X_3	X_4	X_1X_2	X_1X_3	X_1X_4	X_2X_3	X_2X_4	X_3X_4	X_1^2	X_2^2	X_3^2	X_4^2
1	1	1	1	-1	1	1	-1	1	-1	-1	1	1	1	1
2	-1	1	1	-1	-1	-1	1	1	-1	-1	1	1	1	1
3	1	-1	1	-1	-1	1	-1	-1	1	-1	1	1	1	1
4	-1	-1	1	-1	1	-1	1	-1	1	-1	1	1	1	1
5	1	1	-1	-1	1	-1	-1	-1	-1	1	1	1	1	1
6	-1	1	-1	-1	-1	1	1	-1	-1	1	1	1	1	1
7	1	-1	-1	-1	-1	-1	-1	1	1	1	1	1	1	1
8	-1	-1	-1	-1	1	1	1	1	1	1	1	1	1	1
9	1	1	1	1	1	1	1	1	1	1	1	1	1	1
10	-1	1	1	1	-1	-1	-1	1	1	1	1	1	1	1
11	1	-1	1	1	-1	1	1	-1	-1	1	1	1	1	1
12	-1	-1	1	1	1	-1	-1	-1	-1	1	1	1	1	1
13	1	1	-1	1	1	-1	1	-1	1	-1	1	1	1	1
14	-1	1	-1	1	-1	1	-1	-1	1	-1	1	1	1	1
15	1	-1	-1	1	-1	-1	1	1	-1	-1	1	1	1	1
16	-1	-1	-1	1	1	1	-1	1	-1	-1	1	1	1	1
17	2	0	0	0	0	0	0	0	0	0	4	0	0	0
18	0	2	0	0	0	0	0	0	0	0	0	4	0	0
19	0	0	2	0	0	0	0	0	0	0	0	0	4	0
20	0	0	0	2	0	0	0	0	0	0	0	0	0	4
21	-2	0	0	0	0	0	0	0	0	0	4	0	0	0
22	0	-2	0	0	0	0	0	0	0	0	0	4	0	0
23	0	0	-2	0	0	0	0	0	0	0	0	0	4	0
24	0	0	0	-2	0	0	0	0	0	0	0	0	0	4
25	0	0	0	0	0	0	0	0	0	0	0	0	0	0
26	0	0	0	0	0	0	0	0	0	0	0	0	0	0
27	0	0	0	0	0	0	0	0	0	0	0	0	0	0
28	0	0	0	0	0	0	0	0	0	0	0	0	0	0
$\sum Xi^2$	24	24	24	24	16	16	16	16	16	16	48	48	48	48

Table (D2) illustrates the observed and predicted values for Electrical conductivity (mS) and Precipitated powder (g) as well as the sum of squared residuals.

	Electrical conductivity (mS)				Precipitated powder (g)			
	Observed	Predicted	Residuals	ei^2	Observed	Predicted	Residuals	ei^2
1	163.70	162.93	0.77	0.59	13.99	14.58	-0.59	0.34
2	160.40	160.02	0.38	0.14	12.80	13.33	-0.53	0.28
3	152.70	152.69	0.01	0.00	0.00	0.22	-0.22	0.05
4	151.20	151.30	-0.10	0.01	0.00	-0.59	0.59	0.35
5	159.10	160.19	-1.09	1.18	11.51	11.58	-0.07	0.01
6	156.20	157.65	-1.45	2.10	10.80	11.01	-0.21	0.04
7	146.90	146.02	0.88	0.78	4.43	3.94	0.49	0.24
8	144.90	145.00	-0.10	0.01	3.71	3.79	-0.08	0.01
9	167.80	168.49	-0.69	0.47	24.30	23.99	0.31	0.10
10	163.50	164.65	-1.15	1.32	22.16	22.40	-0.24	0.06
11	173.30	172.12	1.18	1.40	18.62	18.16	0.46	0.21
12	170.10	169.80	0.30	0.09	17.30	17.00	0.30	0.09
13	155.90	156.07	-0.17	0.03	12.46	12.80	-0.34	0.12
14	151.80	152.60	-0.80	0.65	12.33	11.88	0.45	0.20
15	154.60	155.77	-1.17	1.37	14.44	13.69	0.75	0.57
16	152.80	153.83	-1.03	1.07	14.03	13.19	0.84	0.70
17	163.20	163.60	-0.40	0.16	17.72	17.88	-0.16	0.02
18	160.60	159.03	1.57	2.47	15.22	14.37	0.85	0.72
19	170.00	170.88	-0.88	0.77	17.62	17.43	0.19	0.04
20	163.50	162.26	1.24	1.53	17.25	18.27	-1.02	1.05
21	160.20	158.75	1.45	2.11	15.82	16.14	-0.32	0.10
22	149.50	150.01	-0.51	0.26	0.00	1.33	-1.33	1.76
23	154.10	152.16	1.94	3.75	9.96	10.63	-0.67	0.45
24	147.70	147.88	-0.18	0.03	0.00	-0.55	0.55	0.30
25	158.50	158.35	0.15	0.02	12.20	12.14	0.06	0.00
26	158.20	158.35	-0.15	0.02	12.11	12.14	-0.03	0.00
27	158.30	158.35	-0.05	0.00	12.10	12.14	-0.04	0.00
28	158.40	158.35	0.05	0.00	12.15	12.14	0.01	0.00
	sum of squared residuals =			22.35	sum of squared residuals =			7.8

Appendix E

show the curves of pH values and temperature variations in the reactor with respect to time of the reaction (CO_2- aqueous NH_3) for the 28 experiments.

Figures (E1) For Experiments number (1 to 8)

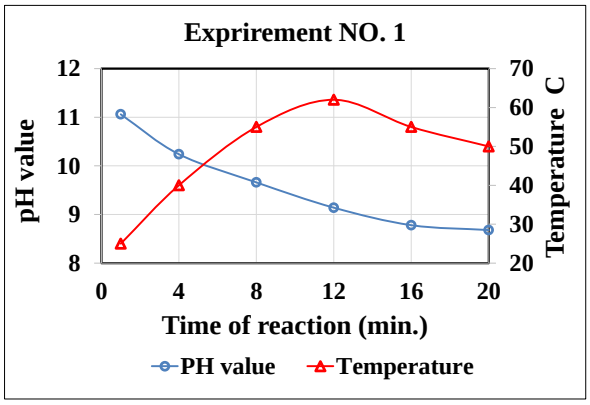

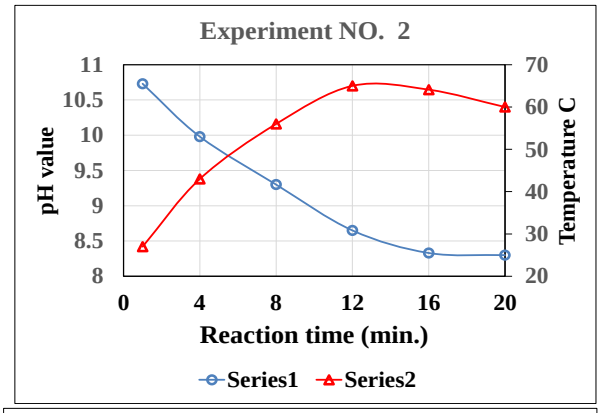

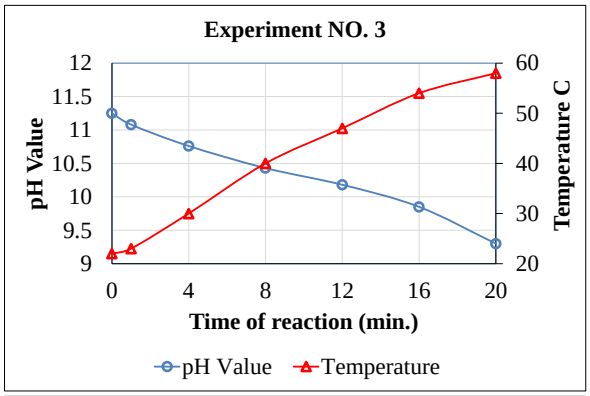

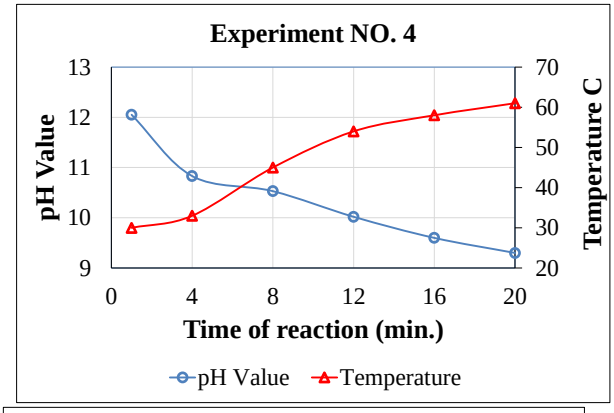

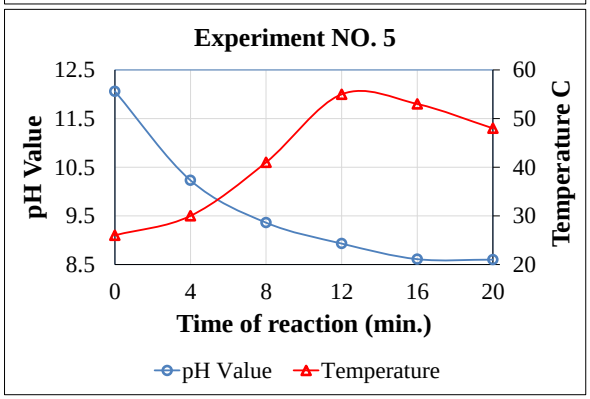

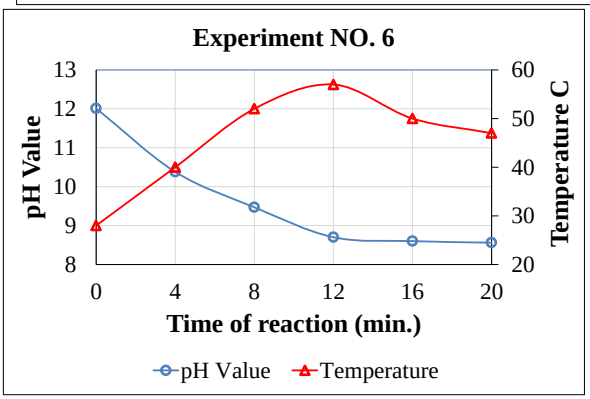

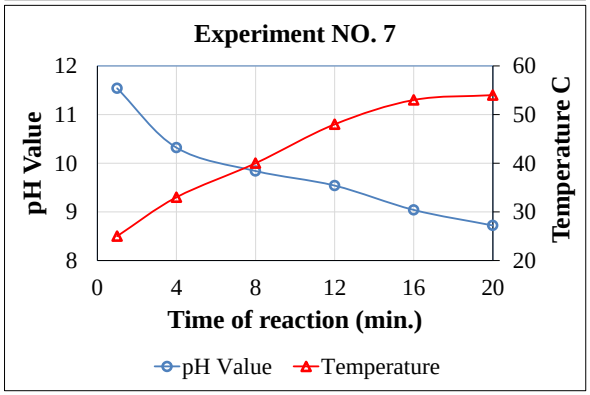

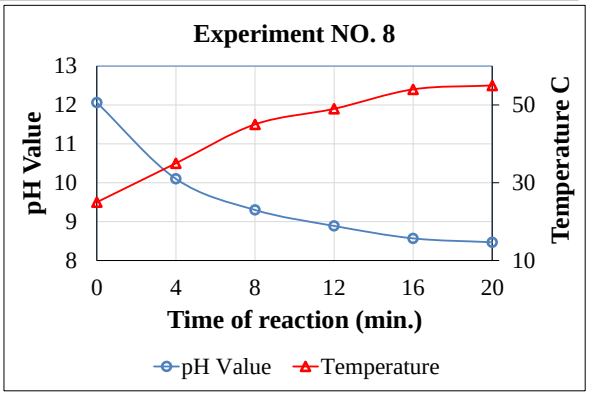

Appendix (E2): Figures for the xperiments number (9 to 16)

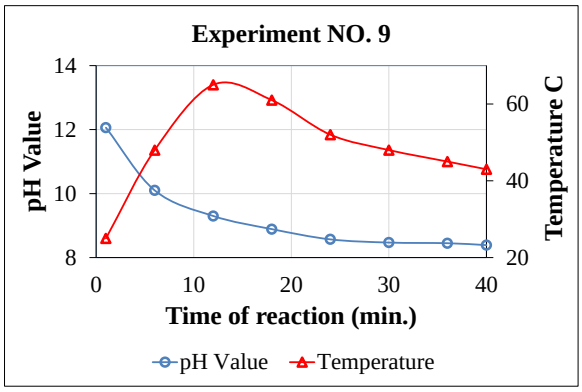

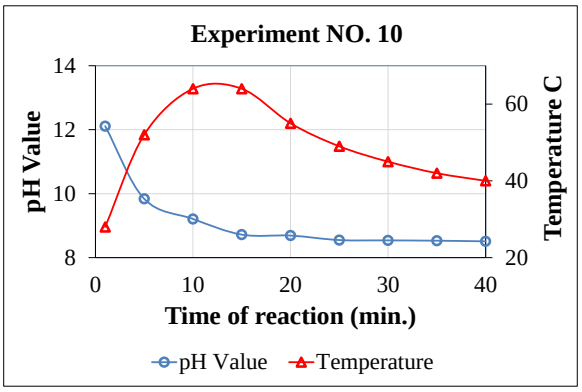

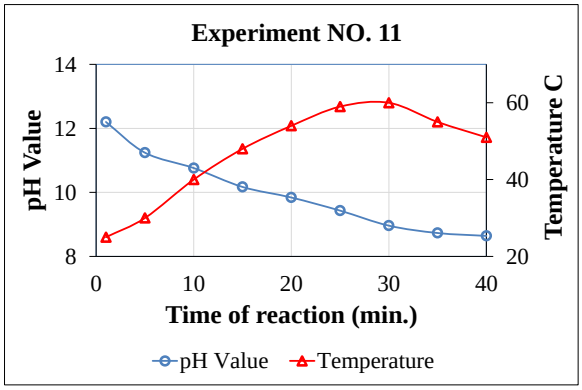

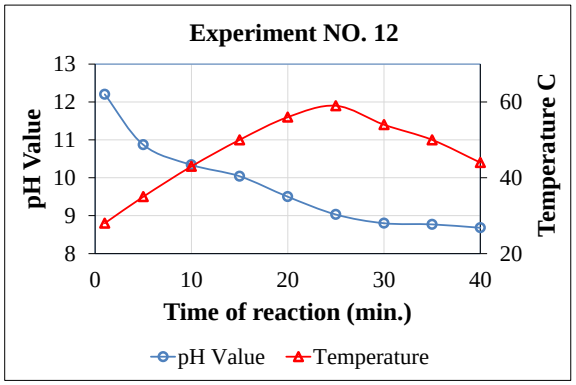

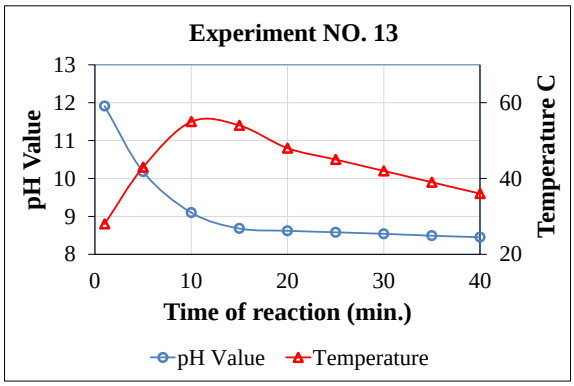

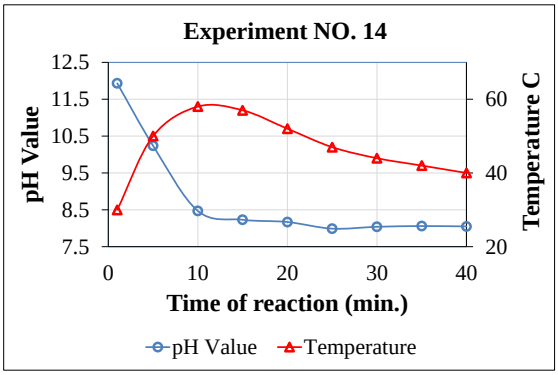

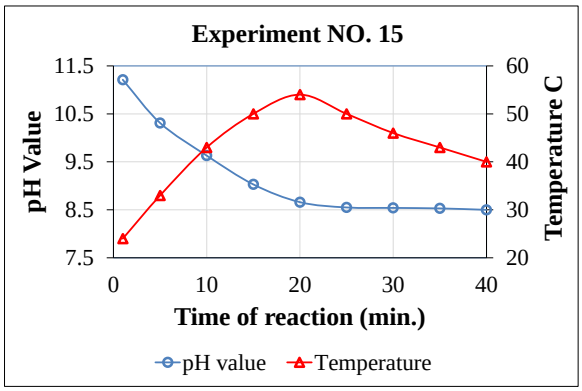

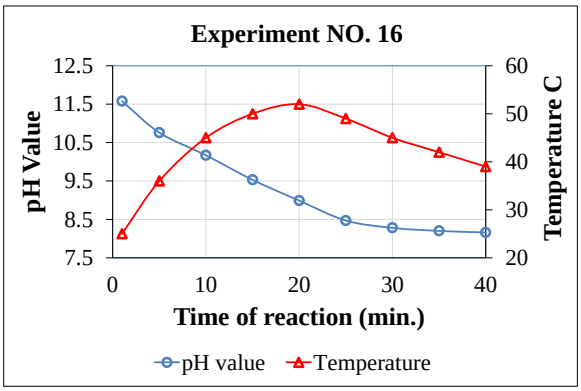

Appendix (E3): Figures for the xperiments number (17 to 24)

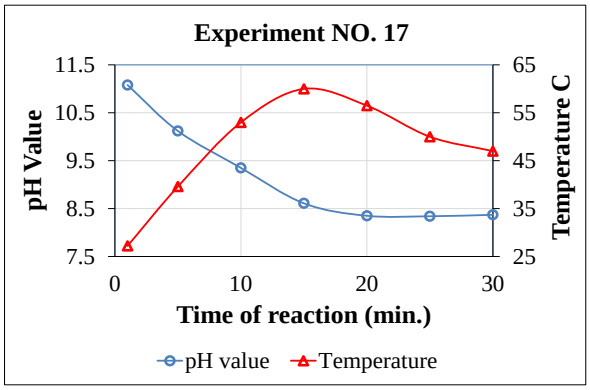

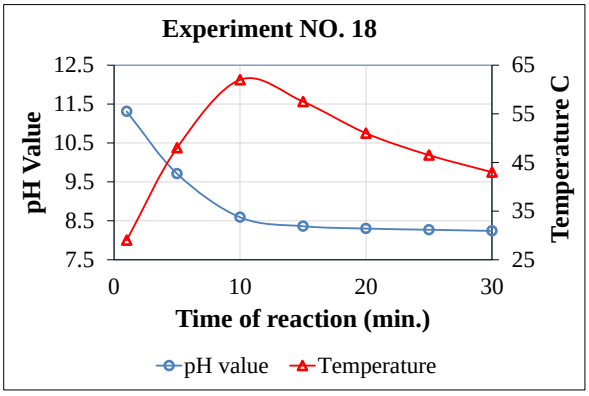

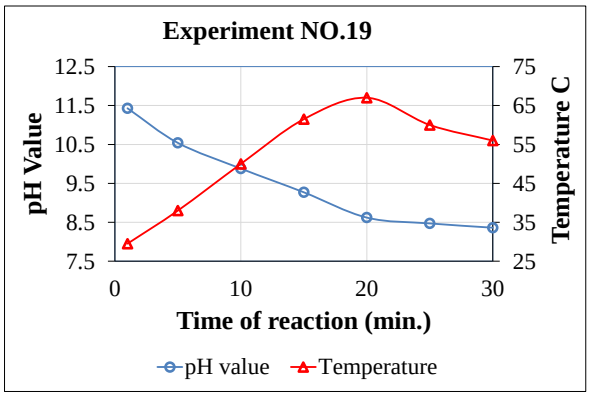

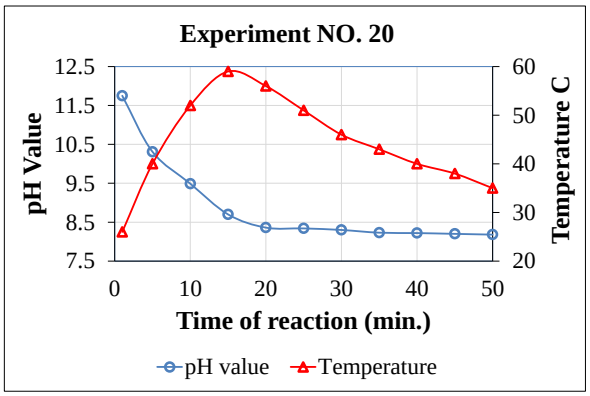

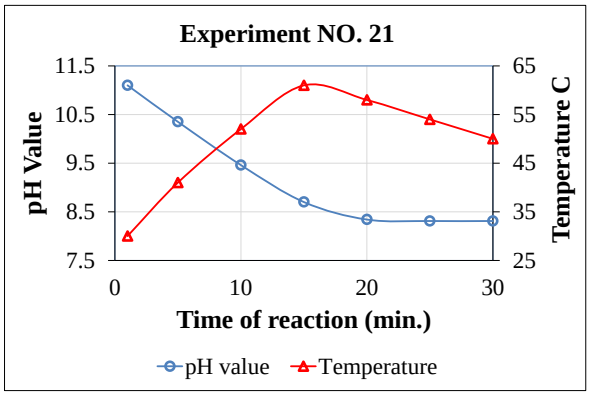

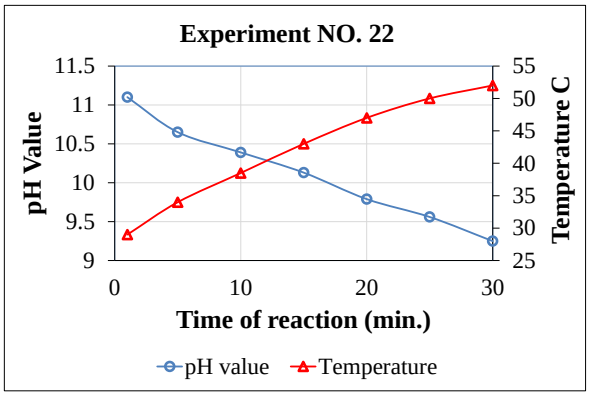

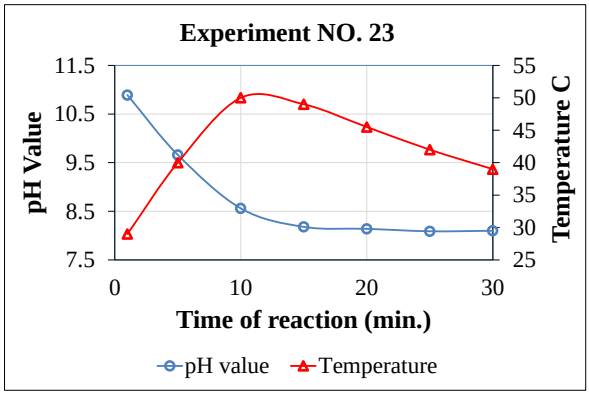

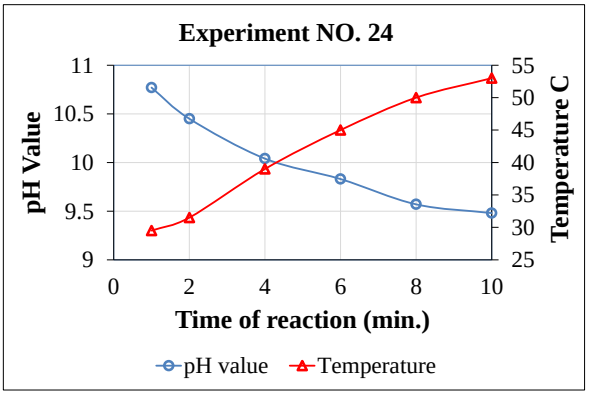

Appendix (E4): Figures for the xperiments number (25 to 28)

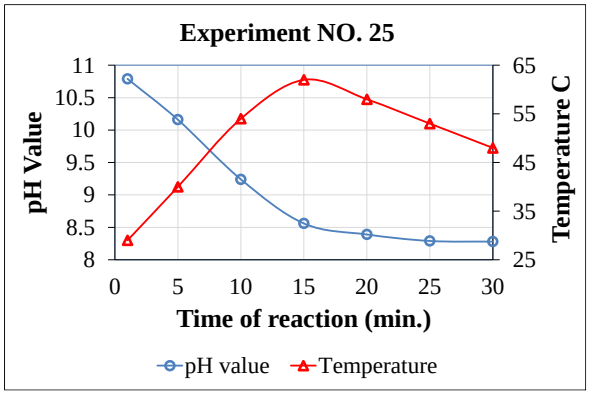

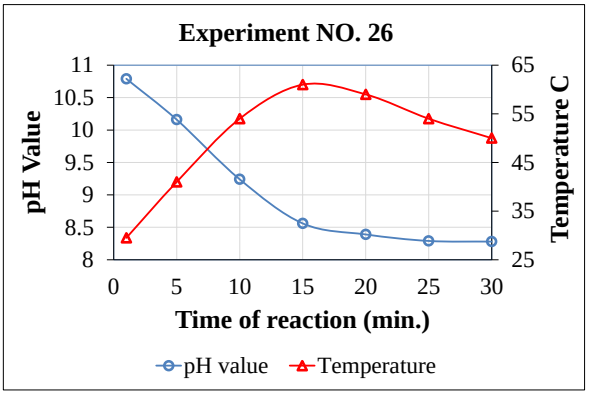

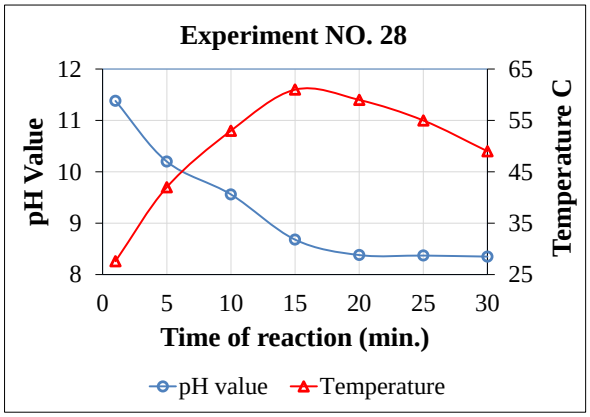

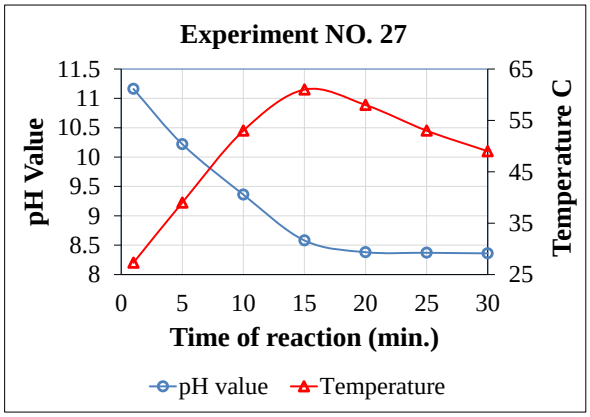

Appendix F

Figures show Spectra of C^{13} NMR for solid samples (experiments no. 17 to 20)

The solid sample test
of the experiment (17)

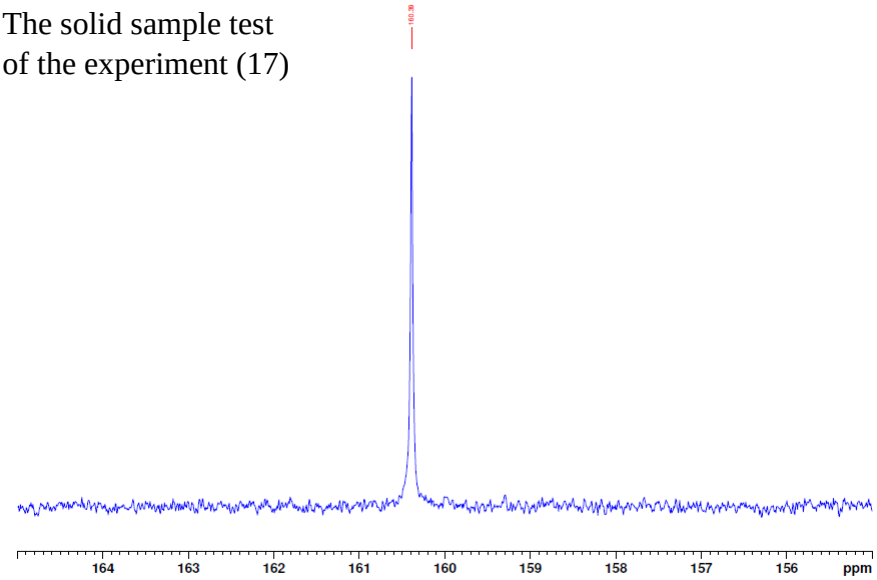

The solid sample test of
the experiment (18)

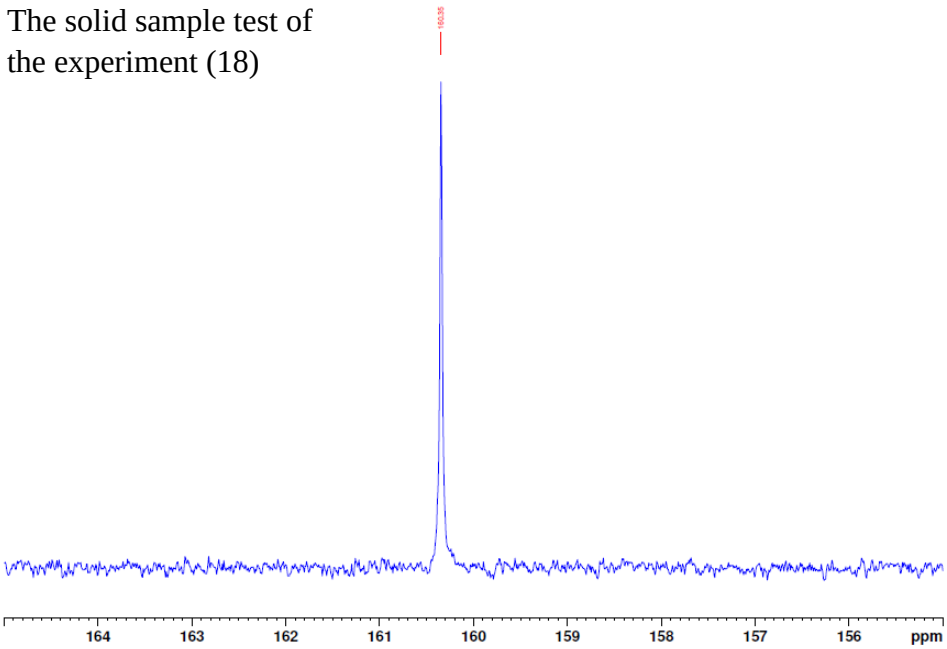

The solid sample test of the experiment (19)

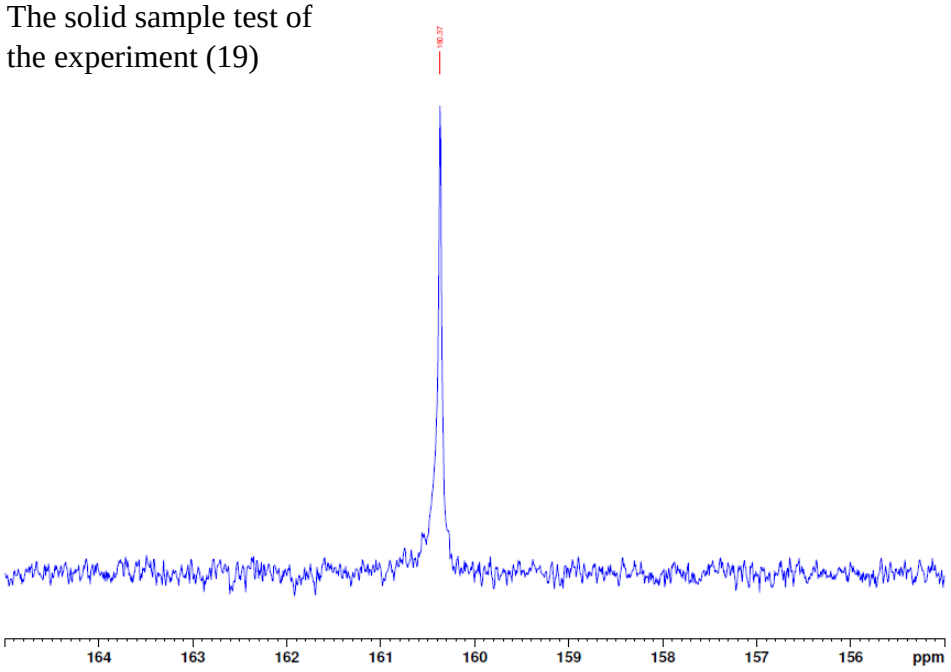

The solid sample test of the experiment (20)

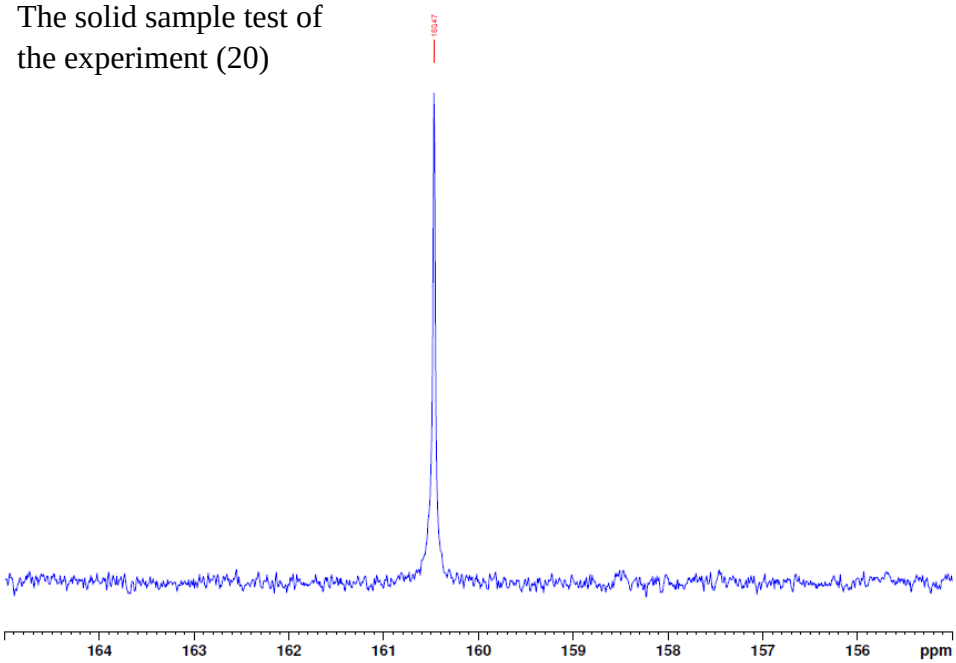

Appendix G

Figures G show the analysis data using FTIR for the precipitate solid from the experiments 1 to 28.

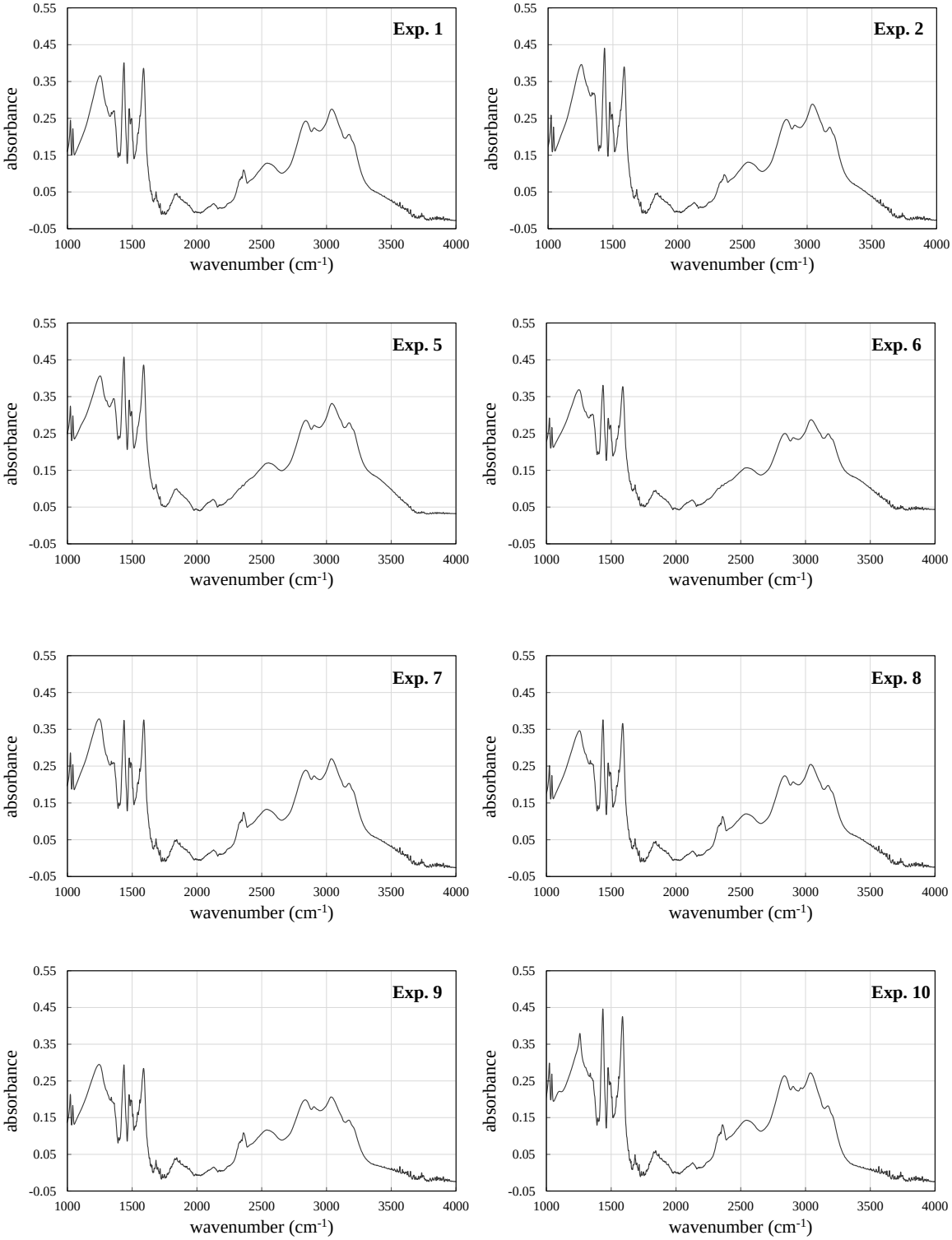

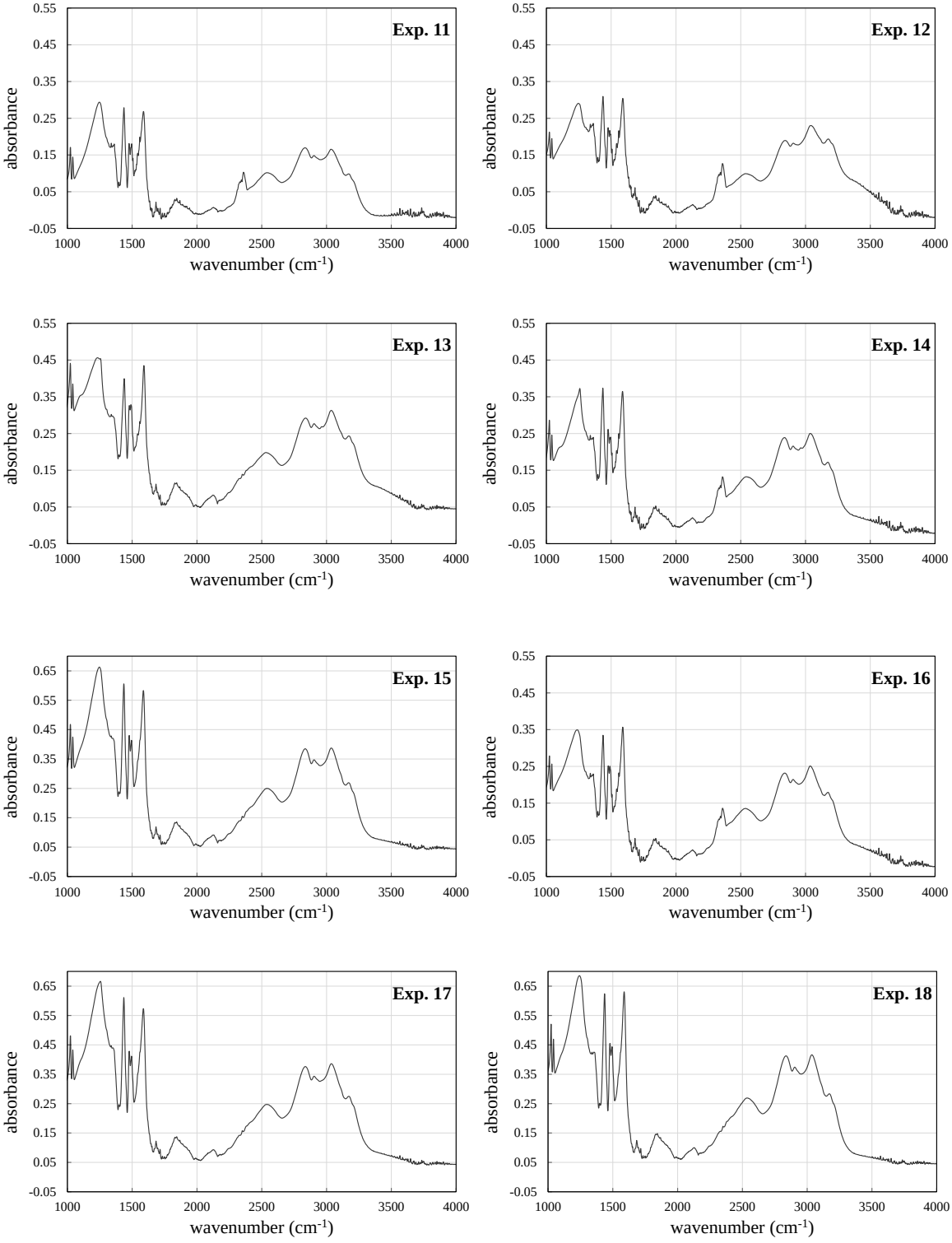
Exp. 11
Exp. 12
Exp. 13
Exp. 14
Exp. 15
Exp. 16
Exp. 17
Exp. 18
absorbance
wavenumber (cm-1)

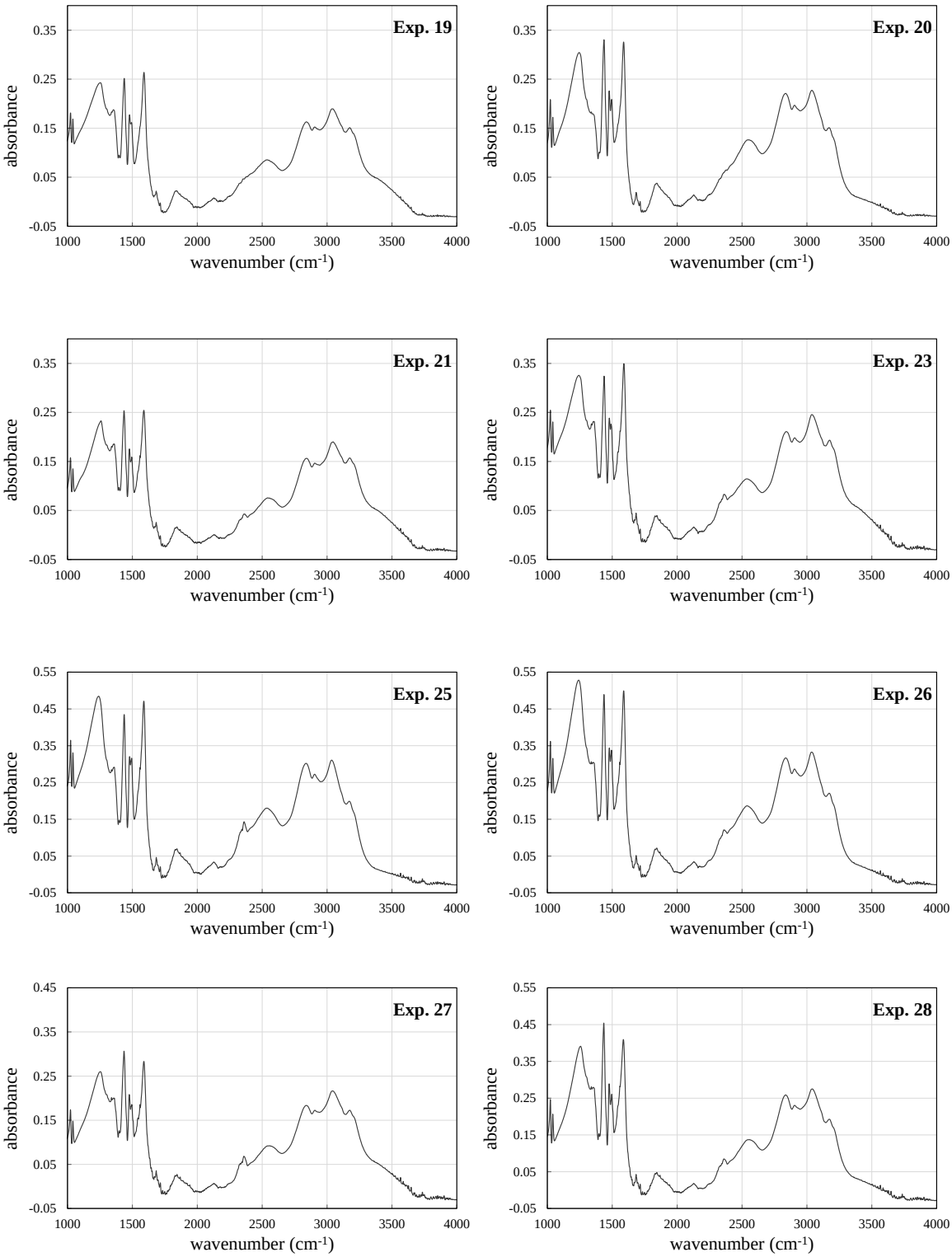
Exp. 19
Exp. 20
Exp. 21
Exp. 23
Exp. 25
Exp. 26
Exp. 27
Exp. 28
absorbance
wavenumber (cm-1)